Université de Liège

Integrated Layout Design of Multi-component Systems

ZHU Jihong

FACULTE DES SCIENCES APPLIQUEES

Thèse de doctorat 2008

Thèse défendue, avec succès, le 9 décembre 2008, pour l'obtention du grade scientifique de Docteur en Sciences appliquées de l'Université de Liège

Jury :

Pierre Duysinx, Professeur, Université de Liège, Président

Pierre Beckers, Professeur, Université de Liège, Promoteur

Weihong Zhang, Professeur, Northwestern Polytechnical University, Chine, Promoteur

Claude Fleury, Professeur, Université de Liège

Quentin Louveaux, Chargé de cours, Université de Liège

Van Hien Nguyen, Professeur, FUNDP, Namur

Mathias Stolpe, Professeur associé, Technical University of Denmark

Alain Remouchamps, Samtech sa, Liège

Acknowledgement

The dream of aerospace began at the end of 14th century, in Ming Dynasty, China, when Wanhoo tried to fly into the sky by tying 47 rockets and two big kites to his chair and finally sacrificed himself. During the years when the human beings struggle against the gravity of the earth, lightening the weight and strengthening the structure are always the main topics of the aeronautics and aerospace system design. The application of structural optimization has become a great religion.

All that is superfluous displeases God and Nature.
All that displeases God and Nature is evil.

Dante Alighieri, 1265-1321

I was so fortunate to be engaged in this challenging field since March, 2002, when I started to work with Prof. Zhang Weihong in the Laboratory of Aerospace Computing, Northwestern Polytechnical University. As a senior student, I was rather excited to have a chance of participating in a project of structural optimization design for a famous aircraft. Later, more works were carried out on the technical extensions of structural topology optimization and some practical applications in aeronautics and aerospace industries. In 2005, we had an in-depth discussion with Prof. Chen Yuze from Chinese Academy of Engineering Physics. We focused our topic on the application of layout optimization design in the aerospace systems. And finally during the coming spring festival, we concluded our common interest as the integrated layout design of multi-component systems. After some basic studies, I was accepted to continue the work on my PhD thesis by Prof. Pierre Beckers from LTAS, University of Liège, at the end of 2006. With the support from the professors in Liège, more new ideas are proposed and implemented, which helps me to finish the thesis.

First of all, I would like to express my deep and sincere gratitude to my two respectable supervisors, Prof. Pierre Beckers and Prof. Zhang Weihong, for their inspiring and encouraging way to guide me to a deeper understanding of knowledge, and their invaluable comments during the whole work with this dissertation. Mr. Beckers is a generous and kind old man. He will be retired from the university soon. I am very proud of being one of his students of the final batch. I just wish him a healthy and happy life in after years. Mr. Zhang has a rigorous scholarship. Even though I am in Belgium, he always tried to give me some long-range support by MSN, which are mentioned as the “Remote Control” from east to the west of Eurasia, the biggest continent on the earth. Since I am going to continue my research work with Prof. Zhang, the best way to show my appreciation is to keep on the study with greater passion.

I will also give special thanks to Prof. Claude Fleury and Prof. Pierre Duysinx from LTAS, University of Liège. They are the top experts in the field of structural

optimization. Thanks to the valuable discussions with them, I achieved a lot both theoretically and practically. It is my honor to have been working with them in LTAS.

I am very grateful to Prof. Chen Yuze and Dr. Guo Zhongze from Chinese Academy of Engineering Physics, and Dr. Alain Remouchamps from Samtech. They gave me a lot of technical supports and practical suggestions according to the requirements of aerospace engineering.

Many thanks to my office mates Mr. Gao Tong in China and Mr. Pierre Vueghs in Belgium, for our friendship and the academic atmosphere of the service. My life was not always boring during the work for PhD degree. Wish them great success in the research work and happiness in the family life.

This work is supported by LTAS-Infographie, National Natural Science Foundation of China (10676028, 50775184), Aeronautical Science Foundation of China (2006ZA53006, 04B53080), 973 Program (2006CB601205), 863 Project (2006AA04Z122), 111 Project (B07050), Shaanxi Province Science & Technology Project (2006K05-G25), Xi'an Applied Materials Innovation Fund (XA-AM-200705) and Doctorate Foundation of Northwestern Polytechnical University (CX200508).

Dedicated to my beloved grandpa, my parents, my girlfriend and my future parents-in-law,
for their constant support and unconditional love
I love you all dearly. ☺

Contents

Nomenclature

δ	Approximation error for FCM
APDL	ANSYS Parametric Design Language
BESO	Bi-directional Evolutionary Structural Optimization
C	Strain energy
C_{ij}	Strain energy of the jth element dominated by the ith density points
E	Elastic modulus
ESO	Evolutionary Structural Optimization
$\boldsymbol{f}$	Load vector
FCM	Finite-circle Method
GA	Genetic Algorithms
J	Moment of inertia
$\boldsymbol{K}$	Global stiffness matrix
$\boldsymbol{K}_{ij}$	the jth element stiffness matrix dominated by the ith density points
$O_{\varepsilon\varsigma}$	Center of the ςth circum-circle attached to the εth component
O_{τ}	Center of the τth circle describing the edge of the design domain
$P(\eta_i)$	Penalty function
RAMP	Rational Approximation of Material Properties
$R_{\varepsilon\varsigma}$	Radius of the ςth circum-circle attached to the εth component
R_{τ}	Radius of the τth circle describing the edge of the design domain
SIMP	Solid Isotropic Material with Penalty
TDF	Topology Description Function
$\boldsymbol{u}$	Nodal displacement vector/vibration shape vector
V	Total volume of the material
Γ_D	Global design domain
Γ_{ε}	Area occupied by the εth component
η_i	Value of the ith pseudo-density
ν	Poisson's ratio
ρ	Density
$\boldsymbol{M}$	Global mass matrix
$\boldsymbol{M}_{ij}$	The jth element mass matrix dominated by the ith density points
ω	Circular natural frequency
p	Penalty factor
$\boldsymbol{G}$	Gravity/inertial load vector
g	Gravity acceleration
R_{MK}	Ratio of the pseudo-density to the interpolation functions
x_G, y_G	Location of the gravity center

Chapter 1

Introduction

Overview

The purpose of the multi-component system layout design and state of the art are introduced in this chapter. The related studies as packing optimization, topology optimization, shape optimization etc are also reviewed here. An overview of the entire thesis is presented at last.

Contents

1.1 Basic concept of multi-component systems

A multi-component system consists of numbers of components, a container specifying the entire design domain and the supporting structures that interconnect the components and the container, e.g. an aircraft devices configuration as shown in Figure 1.1, is a basic form of structural systems.

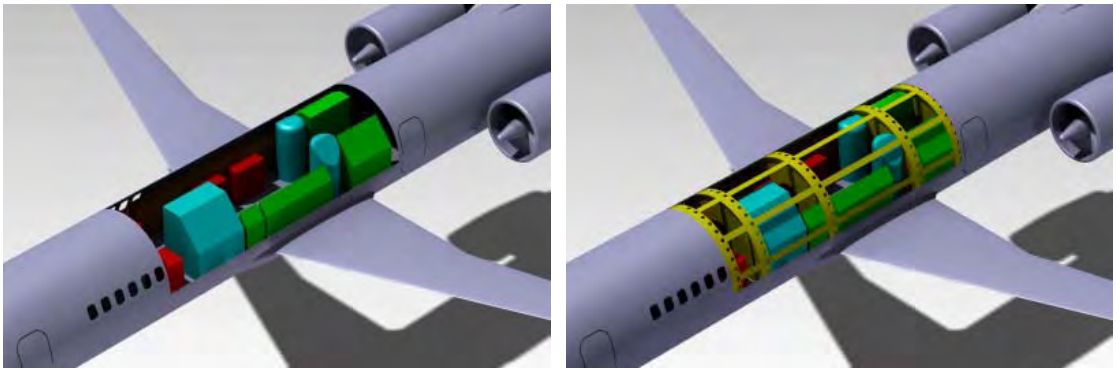

Figure 1.1: A multi-componnet system

According to the description, most of the industrial products like mechanism, automotive, marine, aeronautics and aerospace systems, as shown in Figure 1.2, can be regarded as different kinds of multi-components systems. The concerned problem is especially critical for aerospace engineering. On the one hand, different functional devices are required for the flight mission and should be installed in proper positions satisfying various design requirements. On the other hand, the structures supporting the devices have to be designed as a lightweight one and coordinate with the aircraft major airframe.

Airframe and components of Airbus A400M Cargo plane

“Rolling cage” of Thinkpad T61 laptop, Lenovo

Figure 1.2: Typical industrial multi-component systems

In the structural design of typical aerospace products, e.g. the satellite systems shown in Figure 1.3, the devices and the outer enclosure are modeled as the components and the container, respectively. To satisfy geometrical, physical needs and electromagnetic performances etc, the traditional approach is to carry out the packing design for which the

supporting structures and the locations of the components established are designed in a trial-and-error way to fix the components inside the container.

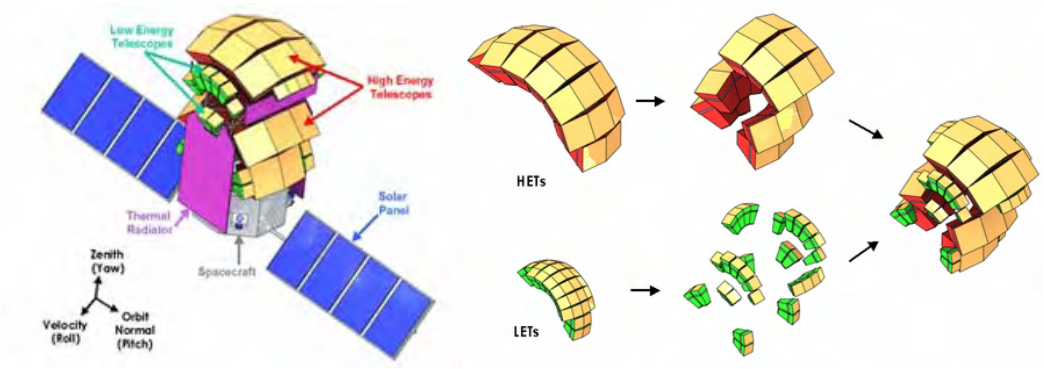

This is the satellite of the mission EXIST (Energetic X-ray Imaging Survey Telescope) of NASA. The total combined field of view of the HETs and LETs are almost identical. Ideally the HET and LETs can be arranged along the field of view of each telescope as shown below (left). In order to package both HETs and LETs inside the shroud of launching vehicle (possibly Delta IV-H or Altas V), the instruments are rearranged as shown below (right) and the fully coded field of view of each telescope is not interrupted. (http://exist.gsfc.nasa.gov/design/)

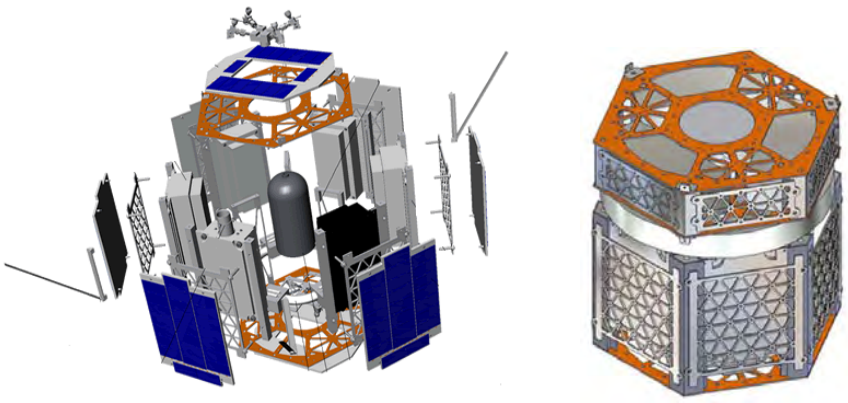

The structure and package design of the NanoSat by The University of Texas at Austin (http://artemis.ae.utexas.edu/)

Figure 1.3: Satellite systems configuration design

Since the mechanical performances of a multi-component system depend upon the layout of the components and the pattern of the structures, the drawbacks of the traditional design procedure are obvious, when the designs of the component layout and the structural pattern are separated as different stages. Actually, varieties of geometrical packing optimization techniques are developed. Meanwhile, more structural optimization techniques are oriented to sizing, shape and topology designs from concepts to details. But none has studied the multi-component system design as an integration of the components' layout design and the structural design.

In view of the common design requirements of aerospace structure systems, the integrated design of the component packing and the structural topology is studied as a simultaneous optimization procedure in this work. As shown in Figure 1.4, an illustrative multi-component system design is presented. A predefined design domain and several components to be located inside are firstly provided with all the loads and boundary conditions assigned. The design procedure consists of two general aspects: the packing optimization to find a proper layout of the components and the topology optimization to

generate a structural pattern ensuring the support and interconnection of the components, loads and the boundary conditions in the design domain.

Accordingly, the main topic of this thesis is the simultaneous packing optimization and topology optimization. Some related techniques, such as packing optimization, topology optimization and shape optimization are discussed in the following section.

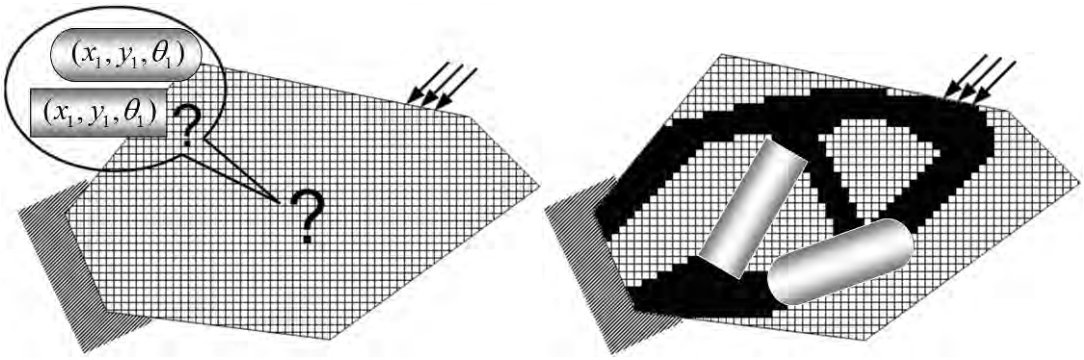

Figure 1.4: An illustrative multi-component system design

1.2 Related studies

Structural optimization and its multidisciplinary integrations are always active topics especially in the last two decades. More and more practical applications and improvements of structural performances can be found nowadays in engineering research and advanced industries like aerospace and aeronautics. However, more difficulties are involved in the integration of the packing optimization and topology optimization. The multi-component system design is still a challenging job.

In this section, the most related studies are introduced and discussed.

1.2.1 Packing optimization

In the field of aeronautics, aerospace and electronic engineering, it is essentially important to have a proper packing configuration. Packing optimization, also referred to as layout optimization and configuration optimization, deals with the configuration design of the multi-component system consisting of a number of components and a container which is also mentioned as a design domain or a packing area. Normally, by choosing the location and orientation of the components as design variables, the system compactness, center of gravity, configuration cost, etc are designed with respect to some geometrical constrains such as non-overlap and some functional and performance requirements (see Cagan et al. 2002, Blouin et al. 2004, Aladahalli et al. 2007 and Zhang et al. 2008).

However, the packing problem was still limited to a CAD-based design because some difficulties are generally involved, e.g., the modeling of the design constrains and objective function, the searching strategy for the optimization problem (see Cagan et al. 2002) etc. Among others, one of the key difficulties lies in that the geometry constraints have to be properly specified in order to avoid the components overlap and also the overlap with the design domain boundary. Although nonlinear programming was applied

to solve layout problems in some works (see Fujita et al 1991, Landon and Balling 1994), different shapes of components and design domain boundaries will lead to extreme nonlinearity and even discontinuity of the constraint functions, that limit the application of the gradient based optimization algorithms and the traditional formulation of packing problems. Therefore, non-deterministic gradient-free computational approaches such as Genetic Algorithms (GA), Simulated Annealing and some other extended patterns are mostly used in packing optimization problems, as shown in Figure 1.5 and 1.6.

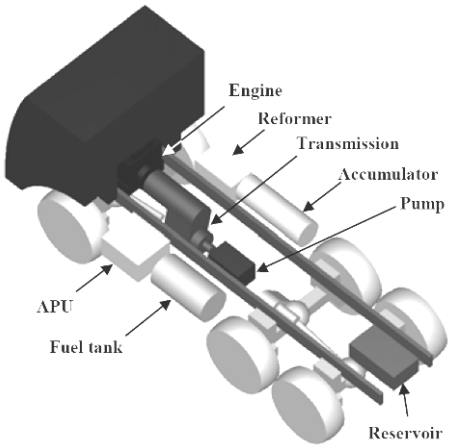

A Pareto front of two conflicting objectives, vehicle dynamics and ground clearance, is obtained through a single execution of the genetic algorithm to allow the decision-making process. The goal is to find optimal vehicle component configurations that achieve good vehicle performance behavior and satisfy design constraints. (Blouin et al. 2004)

Figure 1.5: Configuration design of a truck

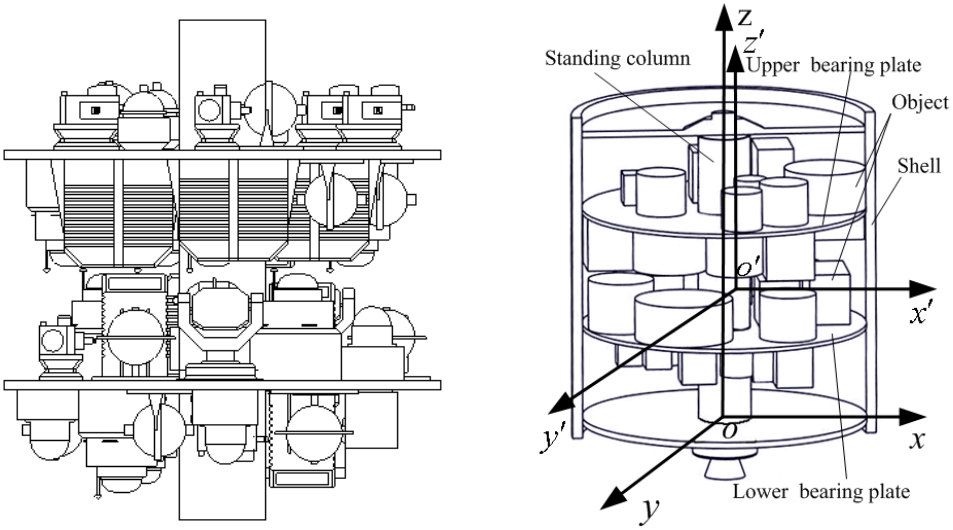

The design objective here is to optimize the inertia performance of the whole module, subjected to the following constraints: (1) all the objects should be contained within the module, with no overlap among the objects and no clash between the module wall and each object; (2) the centroid position error of the whole system should not exceed an allowable value, as small as possible; (3) equilibrium error of the system should be permissible and, of course, the smaller the better. (Zhang et al. 2008)

Figure 1.6: Layout optimization of satellite module

Theoretically, it is proved that the packing optimization is a kind of NP-hard problem (see De Bont et al. 1988). Much effort has been focused on the study of searching strategies by using the components of exact shapes. Among others, 2D rectangular and 3D cubic components layout problems which are also known as the bin-packing problems are mostly concerned, e.g., multichip module (MCM) layout design for circuit board, metal

cutting and product arrangement in containerized transport. To generate reasonable solutions, some heuristic rules were particularly applied together with the searching strategies as Genetic Algorithm and Simulated Annealing (see Pál 2006 and Huang et al 2007). Branch & bound methods and their improved versions were developed as well to solve the 2D bin-packing problem (Clautiaux et al. 2007). Miyazawa and Wakabayashi (2007) also presented an asymptotic approximation method for the packing optimization to find the maximum area usage, when numbers of rectangle or cubic components are placed vertically or horizontally in a larger rectangle area.

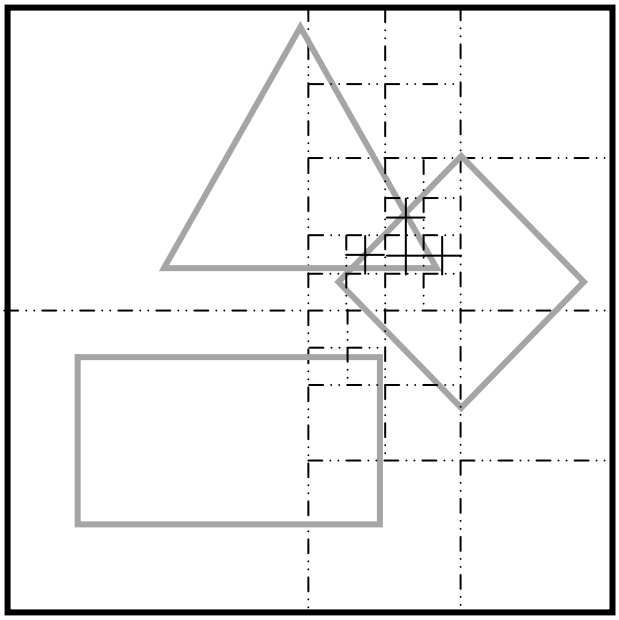

The packing space is subdivided by the tree method. If there are more than one component overlaps with one of the subspaces, there are possible collisions here and the subdivision will be carried on. The iterative subdivision will not stop until there is no possible overlap, which indicates no collision is found. If the possible overlap still appears when the space is subdivided to a predefined precision, the collision of the components is concluded. (An octree based collision detection ←)

Different tree methods are defined depending on the shape used in the subdivision. Alternatively, the components can also be subdivided with some tree methods. (An entity and 3 levels of its sphere-trees, http://isg.cs.tcd.ie/spheretree/ ↓)

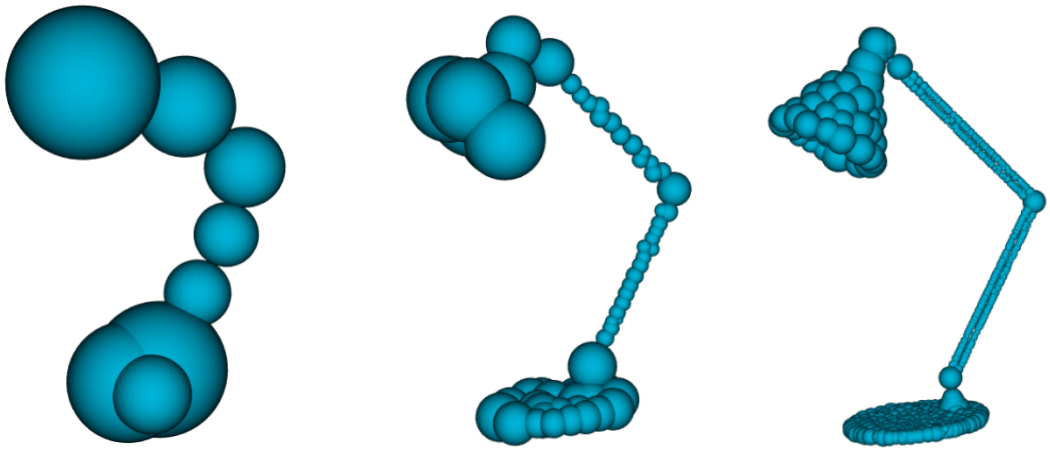

Figure 1.7: Collision detections using the tree methods

However, for a general packing problem, the shape of the components and the container are always more complex than rectangles, cubes or other regular shapes. Even for the simplest bin-packing problem with rectangular components, different overlapping cases are involved and should be considered respectively. Therefore, the overlap detection and avoidance between different components with arbitrary shapes are the key issues to be solved. To tackle this difficulty, numbers of methods were proposed as typical CAD modeling techniques to detect the collision between the components. Typically, some tree methods like octrees (see Meagher 1982 and Samet 1989), sphere-trees (Moore 2002 and 2003, O'Sullivan and Dingliana 1999, Hubbard 1993 and Quinlan 1994), S-bounds based

trees (Cameron 1991) and their variants have been developed. These techniques detect the overlaps by approximating the components with various levels of cubes or spheres and refining the model partition in an iterative way, as shown in Figure 1.7. Moreover, Cagan et al. (1998) proposed a collision detecting method based on octrees to solve the 3D packing optimization problems. More collision detecting methods have been reviewed by Lin and Gottschalk (1998).

The overlap detecting methods mentioned above can only detect whether the components overlap with each other or not. More information about the design sensitivities indicating the searching direction, in which the components shall move to escape from or avoid the overlap, cannot be obtained. As a result, typical packing optimization problems shall be solved with the gradient-free methods.

However, within the framework of the packing design integrated with topology optimization, although some gradient-free methods as Genetic Algorithm (see Missoum et al. 2000) are used to solve topology optimization problems, these methods are still not preferred due to their low efficiency.

1.2.2 Topology optimization

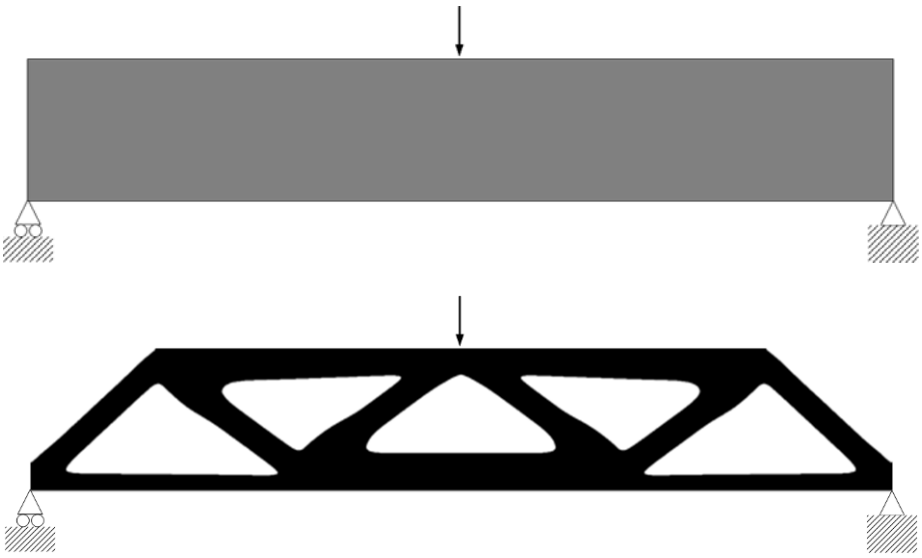

Figure 1.8: A typical topology optimization problem (Bendsøe and Sigmund 2003)

Topology optimization is originally considered as a 0-1 discrete problem. The major challenge is the solution of a large-scale integer programming problem. The high computing cost of function calls for these problems typically precludes the use of gradient free algorithms. The only successful application of Lagrangian duality to the large scale integer problem is found in the work of Beckers (1997, 1999) who proposed a dual method solving the topology optimization with discrete design variables. However, most of the approaches have been proposed to deal with the problem as a continuous one since Bendsøe and Kikuchi (1988) introduced the homogenization method into topology optimization. Now, topology optimization is developed as an effective technique for the concept design of material layout. Overviews were given by Bendsøe (1995, 2002), Eschenauer and Olhoff (2001) Bendsøe and Sigmund (2003). The basic approach is that the design procedure will start with a meshed design domain with given boundary conditions as shown in Figure 1.8. The structural topology will be optimized iteratively

with the proposed techniques.

Several typical topology optimization methods are proposed so far. For example, the homogenization based method (see Bendsøe and Kikuchi 1988, Guedes and Kikuchi 1990, Suzuki and Kikuchi 1991, Allaire et al. 2004) describes the structural material layout with different patterns of microstructures, as shown in Figure 1.9. The structural layout is actually built up with porous unit cells. The equivalent material properties of each unit cell e.g. the elastic modulus etc will be calculated using homogenization method. And the optimization is processed by modifying the porous size of each unit cell iteratively. However, the mathematical complexity of the homogenization calculation prevents the general application of this method.

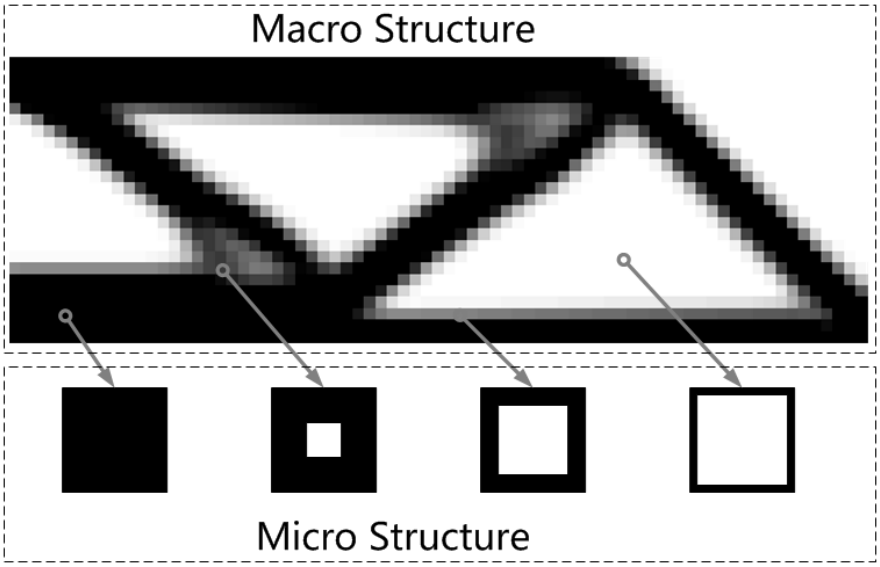

Figure 1.9: Material layout described with homogenization method

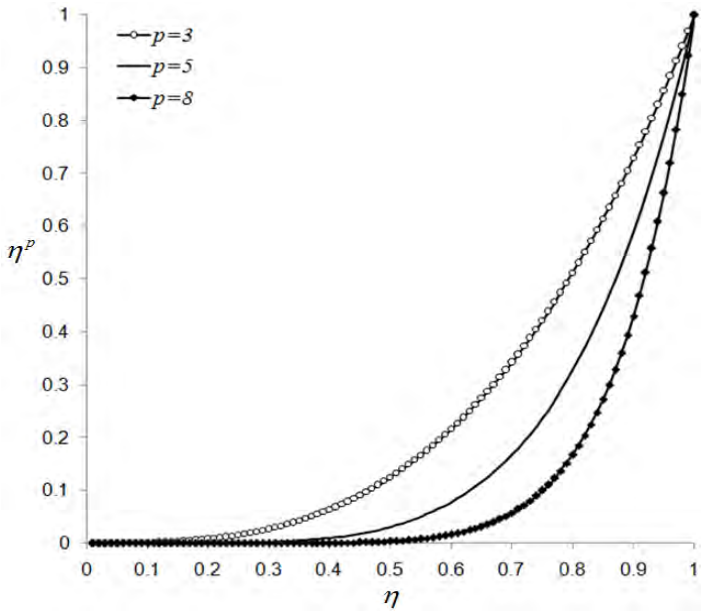

Figure 1.10: SIMP interpolation with different penalty factors

Among others, SIMP (Solid Isotropic Material with Penalty, see e.g., Bendsøe 1989,

Bendsøe and Sigmund 1999, Zhou and Rozvany 1991, Rozvany 2001) is the most popular method in topology optimization. Instead of the homogenization, it proceeds by penalizing exponentially isotropic material in terms of element density variables. The power law can be expressed as

$$E_i = E_0 \eta_i^p \tag{1-1}$$

where E_i is the elastic modulus of the ith element. E_0 is the elastic modulus of the solid material. η_i and p are the so-called pseudo-density and penalty factor, respectively. Compared with the amount of material for each element, a very low stiffness will be obtained even when element density variables take intermediate values between 0 and 1, as shown in Figure 1.10. The effect of penalization will drive the pseudo-densities vary towards 0 and 1 during the optimization. In the work of Bendsøe and Sigmund (1999), by comparing the interpolation scheme with the effective material properties of microstructures, the reliability of the power-law approach was proved theoretically provided that the power term satisfies the Hashin-Shtrikman bounds.

Normally, with the SIMP interpolation model, the topology optimization problems are non-convex. There will be possibly large number of local minima involved. To obtain a pure 0-1 or nearly a pure 0-1 optimal material layout, it is suggested to use stronger penalty, i.e. to use a greater exponent. Unfortunately, this leads to numerical instabilities due to the tiny values when the pseudo-densities vary towards zero.

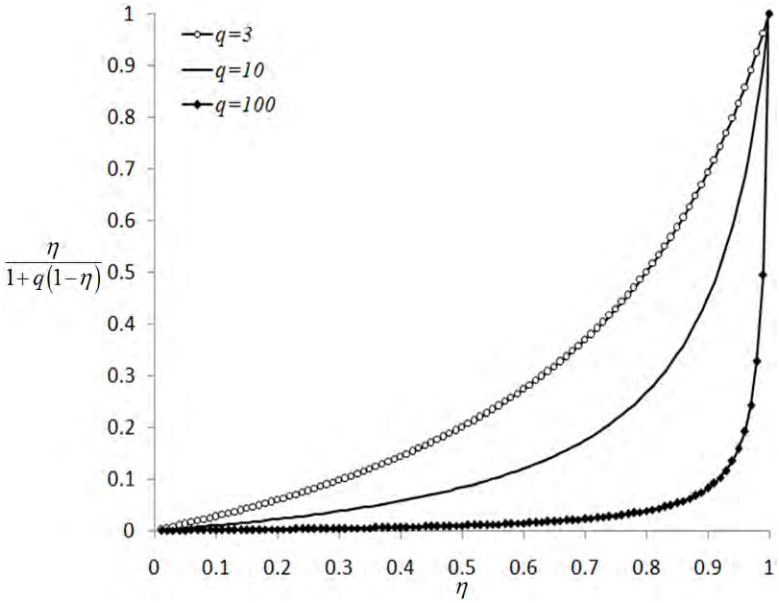

Figure 1.11: RAMP interpolation with different penalty factors

To ensure the numerical stability when a stronger penalty is used, the RAMP (Rational Approximation of Material Properties) was proposed by Stolpe and Svanberg (2001) as an alternative model

$$E_i = \frac{\eta_i}{1+q(1-\eta_i)} E_0 \tag{1-2}$$

where q is the penalty factor of the RAMP model. The interpolation is shown in Figure

1.11. The curves of SIMP and RAMP are similar to each other, but the RAMP model performs more stable when q takes a large value. Nevertheless, it proved theoretically that when q is greater than a certain value, the structural compliance becomes concave.

The evolutionary method is an engineering approach based on the simple concept that inefficient materials are gradually removed from the design domain to approach the optimal topology. Hard killing and soft killing methods discussed by Hinton and Sienz (1995). Mattheck (1997) realized the removal process by assuming a functional relationship between the elastic modulus and the strain energy density. Elements with the lowest level of the strain energy density will be killed iteratively.

ESO (Evolutionary Structural Optimization) described by Xie and Steven (1997), Kim et al. (2003) is another typical evolutionary approach. In most cases, optimal topologies are generated by deleting the group of elements with low strain energy values from the entire design domain systematically. The element efficiency evaluated from sensitivity analysis is used as an index for the determination of the element deletion. As the ESO method is devised as a unidirectional scheme only for removing elements, the restitution of the removed elements will be however unallowable during the iteration. Later, an improved bi-directional procedure named BESO was proposed by Querin and Yang (2000) and Yang et al. (1999a and 1999b). Materials are allowed to be added in those void areas with the highest efficiency, but it is required that an initial design configuration connecting the boundary conditions and loading locations shall be specified a priori.

Both ESO and BESO have the advantage of conceptual simplicity. Moreover, Tanskanen (2002) proved that, in some particular situations, these approaches basically correspond to a sequential linear programming approximate method. However, Sigmund (2001) believed that it is questionable to extend these approaches to other design cases such as multi-physics problems and those with multiple constraints. A critical view given by Zhou and Rozvany (2001), Rozvany (2001) also indicated some numerical failures. In fact, neither the stress level nor the sensitivity values of an element used till now has been able to describe exactly the criterion of the element deletion/growth, especially when the value of objective function varies significantly (see Zhu et al. 2007). Some papers are published to defend the ESO method from the criticism (Edwards 2007, Huang and Xie 2008, Tanskanen 2002, Rozvany and Querin 2002a and b, 2004). But this type of methods is still questionable.

Some other topology optimization methods were also proposed. Bubble method developed by Eschenauer et al. (1994) introduces new holes (or bubbles) into the design domain. The contour and position of the holes are optimized like a shape optimization problem. In the TDF (Topology Description Function) or Level Set Method (see De Ruiter and Van Keulen 2004, Mei and Wang 2004), the structural topology is described as a high dimension level set function, which is more flexible in describing some complex outer boundaries of the material layout.

It should be mentioned that in topology optimization, the presence of alternating solid and void elements over the design domain often occurs in a checkerboard-like fashion. The reason given in the theoretical framework of Jog and Haber (1996) is seemingly due to the finite element approximation or design optimization criteria. From this viewpoint, Rodrigues and Fernandes (1995) improved the interpolation accuracy by means of high-order elements in thermo-elastic optimization problems. However, the computing cost increases dramatically as the number of degrees of freedom of the structural system

expands. Later, Sigmund and Petersson (1998) developed the filtering scheme by smoothing the sensitivities of objective functions over the considered element and its eight neighbors based on image filtering techniques. Haber et al. (1996) proposed the perimeter control method to control the checkerboard pattern and some detailed structures between solid and void elements. Zhang and Duysinx (2003) also proposed a quadratic form of the improved perimeter control operational with the dual approach. Some detailed discussions of checkerboard control in the framework of ESO/BESO can be found in the paper by Yang and Xie (2003).

The idea of topology optimization has been extended to different territories. Numerical results show that a variety of problems including maximization designs of structural stiffness (Sigmund 2001), natural frequency (Pedersen 2000), buckling loads (Zhou 2004), thermal conduction (Gersborg-Hansen et al. 2006), CFD channel flow (Gersborg -Hansen et al. 2005) etc. can be solved. Furthermore, the concept of topology design domain is extended by introducing structural supports and joints modeled with spring elements. Some numerical examples of this type were presented by Jiang and Chirehdast (1997), Buhl (2001), Zhu and Zhang (2006) to solve structural stiffness, compliant mechanism and natural frequency problems. Other extended patterns of topology optimization are developed to solve the layout design of the microstructures (see Sigmund and Torquato 1999, Zhang and Sun 2006), and those with design-dependent loads (Chen and Kikuchi 2001, Bruyneel and Duysinx 2004).

When the eigenvalue problems like natural frequencies and buckling loads of considered structures are maximized with SIMP or some other similar material interpolation model, another important issue is on the artificial modes or localized deformations. These phenomena take place in areas where elements take the minimum density values. Compared with the solid region, these areas are too compliant to support themselves, which will then take the lowest vibration mode shape of the structure. Neves et al. (1995) investigated this phenomenon when optimizing the structural buckling loads. Pedersen (2000) and Bruyneel and Duysinx (2004) gave some improved SIMP interpolation models after analyzing the artificial modes numerically in natural frequency maximization and self-weight loading problems, respectively. By analyzing the material properties of the elements in low-density areas, Zhu et al. (2006 and 2007) gave the equivalent material properties of the orthotropic cellular microstructures that could be effective in avoiding the artificial modes. Detailed discussions of this problem can be found in Chapter 4 of this thesis.

More complexities are brought into the topology optimization by solving multi-component problems or multi-domain problems. For example, Ma et al. (2006) subdivided the design domain into several separated area with multiple material properties. Furthermore, in the works of Chickermane and Gea (1997), Li et al. (2001) and Qian and Ananthasuresh (2004), numbers of parts including the spring elements that interconnecting these parts are treated as different sub-domains for topology optimization. These sub-domains are defined with different volume fractions and evolved to the optima simultaneously.

The topology optimization with embedded rigid components was also discussed by Qian and Ananthasuresh (2004), which is the only paper we have found solving the similar problems with this thesis. They introduced some movable rigid components into the design domain and try to find their proper position and the supporting structures simultaneously. The exact shapes of the components are actually not included in the

design domain. They are simulated with a predefined material interpolation model, i.e., the geometrical movement of a component is actually simulated as a physical variation of the material properties. Elements with intermediate stiffness are found on the boundary of the components to interpolate the variation of the material properties. However, the authors were not aware of the meanings of the integration with the packing optimization. Only one component is taken into account in most of their tested examples. When the problem of more than one component was mentioned, the suggestion of avoiding the overlap was to use a single circle for the approximation of each component.

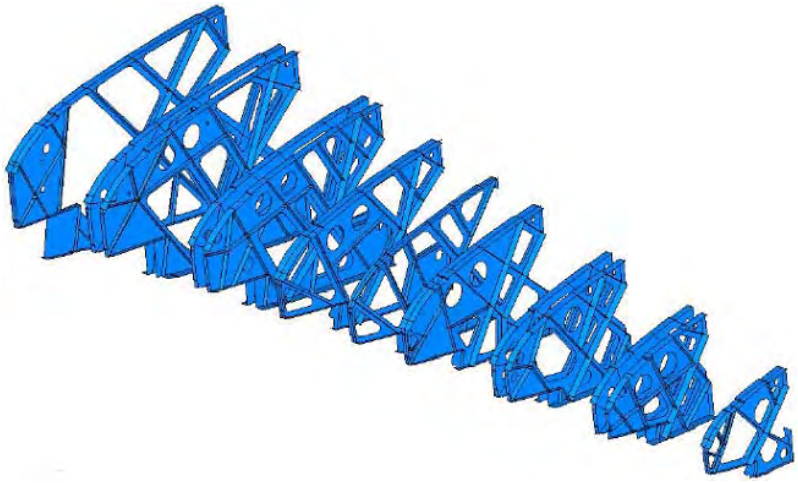

Topology optimization of Airbus A380 leading edge droop nose ribs. http://www.altairproductdesign.com/CaseStudy_Airbus.aspx ←

Combined bracket for alternator, air-conditioning compressor, and steering pump of Volkswagen. http://ak.fe-design.de/fileadmin/akweb/docs_meetings_public/2007-12-_MeyerPruessner_VW_BS_TopoOpt.pdf ↓

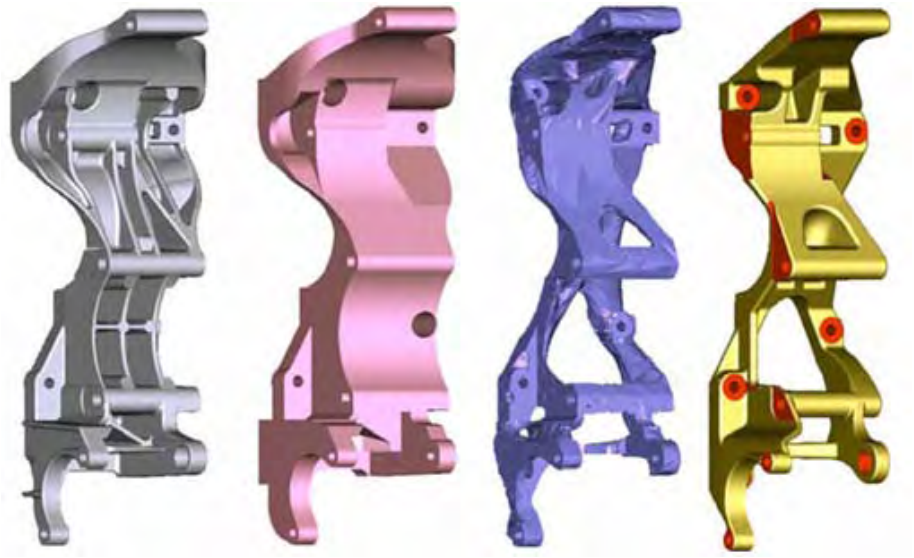

Figure 1.12: Practical design examples of topology optimization

Nowadays, numbers of practical applications of topology optimization can be found in the industrial field. Figure 1.12 shows two important examples. More manufacturing constrains for casting, forging, stamping, extrusion and specified symmetry shall be considered. More descriptions of topology optimization can be referred to the work of Rozvany (2001), Bendsøe and Sigmund (2003).

1.2.3 Shape optimization

Shape optimization techniques are developed maturely in recent years. By modifying the structural boundaries, e.g., detailed designs of notches, holes, and fillets etc., concerned

mechanical performances are improved during the optimization procedure, as shown in Figure 1.13.

Although Genetic algorithms, Simulated annealing etc. (see Rajan 1995, Atiqullah and Rao 1995) are sometimes used to deal with the shape optimization problem, the deterministic gradient-based methods associated with FE method are the most widely used algorithms (Bennet and Botkin 1985, Chen and Tortorelli 1997, Lindby and Santos 1997). The designable shape is multiform and the updating of the shape parameters probably leads to the remeshing of the FE model, which constituted one of key problems in the automatic computing of the design sensitivities. Therefore, much effort has been made to derive the efficient schemes of sensitivity analysis. So far, two approaches, i.e., the discretized method (Belegundu and Rajan 1988, Olhoff et al. 1993) and the continuum method (Belegundu and Rajan 1988, Tortorelli and Wang 1993) have been used to determine the response sensitivities. In fact, these two approaches are unified by their dependence on the velocity field. Accordingly, Laplacian smoothing was used to find the velocities of interior nodes (see Zhang 1991 and Kodiyalam et al. 1992). Later, profiting from the application of the Newton-Raphson method, Zhang et al. (1995) established a semi-analytical method for sensitivity analysis of independent shape variables.

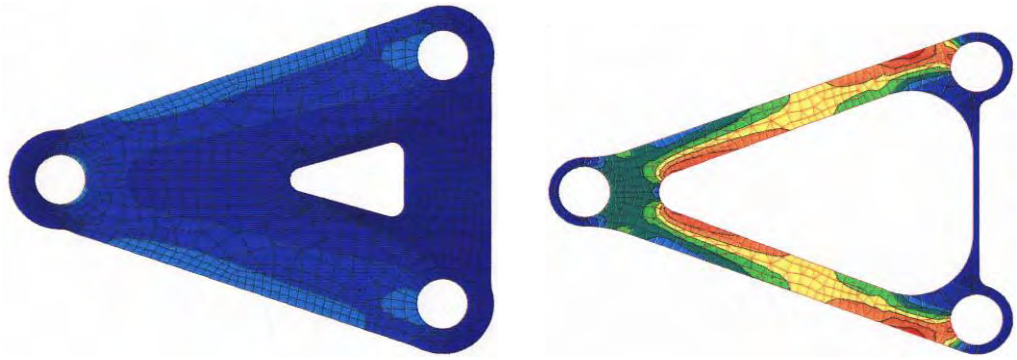

Figure 1.13: Typical shape optimization (Zhang 1991)

1.3 Overview of this thesis

In Chapter 2, the Finite-circle method is introduced to solve the packing problems. Some detailed discussions are made about the geometrical approximation, improved definition, local minimum and some numerical examples.

In Chapter 3, packing design and topology optimization are integrated in the standard compliance minimum problems. New techniques like density points and embedded meshing are proposed there. Several testing examples are solved and reasonable solutions are presented to illustrate the effect of integrated design.

In Chapter 4, discussions are made about localized phenomena in the low-density areas like localized modes and localized deformations which will lead to the numerical errors in eigenvalue maximization problems and design-dependent body load problems. Several material interpolation models are evaluated there. And a new effective model is presented. Meanwhile, we also find the interesting break-down problems of the ESO method can be

likely avoided when the low-density areas are properly treated.

In Chapter 5, the results from Chapter 4 are applied and the proposed integrated layout optimization is extended to problems with design-dependent inertial forces and natural frequency maximization. More constraints on the location of gravity center and moment of inertia are introduced to make the problems more practical.

In Chapter 6, boundary conditions related to the support layout and the surface loads are taken into account as design dependent items in the topology optimization, the proposed techniques of density points and embedded mesh are implemented.

In Chapter 7, the overall conclusion of the thesis is given. Some extended technical discussions are provided.

Chapter 2

Finite-circle Method

Overview

To integrate the packing optimization into the layout design of multi-component systems, the Finite-circle Method (FCM) is developed to adapt gradient-based algorithms to the packing design. The definition of the circum-circles, the geometrical constrains, different kinds of objectives are presented here. More discussions are presented about the advantages and the disadvantages of this method.

Contents

2.1 Basic formulation of FCM

Pure geometrical packing optimization is discussed in this chapter. As introduced previously, one of the key difficulties during the process of packing optimization is the collision detection and avoidance (Cagan et al. 2002). Most of the existing methods e.g. the category of the tree methods can only detect whether two components overlap with each other, rather than evaluating the overlap.

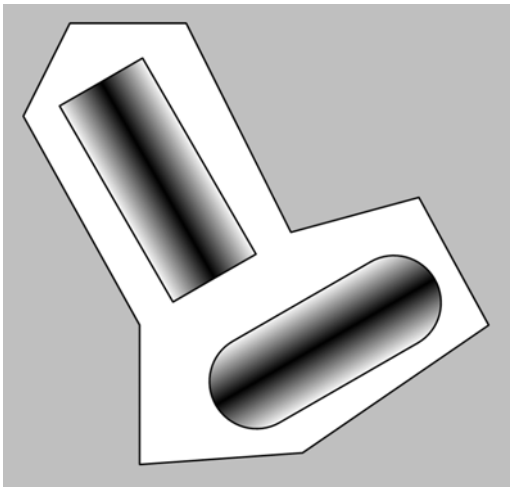

Figure 2.1: A 2D packing problem

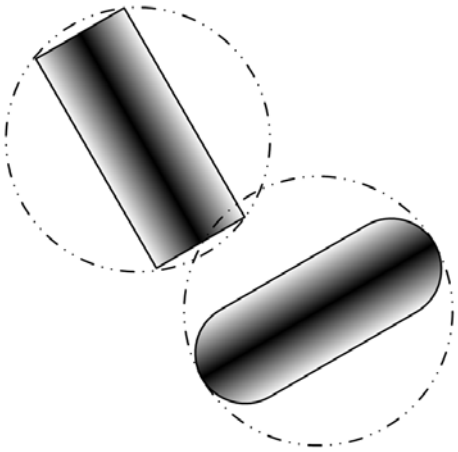

Figure 2.2: Components approximation with single circle

Consider a 2D packing problem as shown in Figure 2.1. Suppose several components will be located inside the design domain and no overlapping shall be found between different components. Mathematically, following conditions should be retained

$$\begin{cases} \forall \varepsilon = 1,2,...,n_c; \\ s.t.:\ \Gamma_\varepsilon(x_\varepsilon, y_\varepsilon, \theta_\varepsilon) \subset \Gamma_D \\ \forall \varepsilon 1 = 1,2,...,n_c;\ \varepsilon 2 = 1,2,...,n_c;\ \varepsilon 1 \neq \varepsilon 2 \\ s.t.:\ \Gamma_{\varepsilon 1}(x_{\varepsilon 1}, y_{\varepsilon 1}, \theta_{\varepsilon 1}) \cap \Gamma_{\varepsilon 2}(x_{\varepsilon 2}, y_{\varepsilon 2}, \theta_{\varepsilon 2}) = \varnothing \end{cases} \tag{2-1}$$

where Γ_ε and Γ_D denotes the area occupied by the εth component and the global design domain, respectively. Γ_ε is described as the function of the location and orientation of the component, i.e. (x_ε, y_ε, θ_ε). n_c is the number of the components. $\varepsilon 1$ and $\varepsilon 2$ denotes two different components. However, Equation (2-1) is a symbolic presentation. When gradient-based algorithms are applied, it is further necessary to understand how much the components are overlapped with each other, in which direction they should move to escape from the overlap or how far the component is from the current position to the situation of overlap and in which direction they should move to avoid the overlap.

In most cases, it is possible to detect the overlapping with some proposed methods like the trees listed in Chapter 1. Due to the geometric complexity of boundaries of the components and design domain, it is difficult to describe the exact Γ_ε in terms of (x_ε, y_ε, θ_ε) and Γ_D with some simple and explicit functions, This is one of the key reasons why only

some gradient-free methods like Genetic Algorithm, Simulated Annealing are mostly applied in the packing optimization problem.

2.1.1 Approximation of components

Although it is too difficult to describe the overlap for the components with arbitrary shapes, the overlap between circles and spheres can be easily calculated by comparing the distances of the centers to the summation of the radii. This is the idea of approximating all the components of arbitrary shapes with circles or spheres.

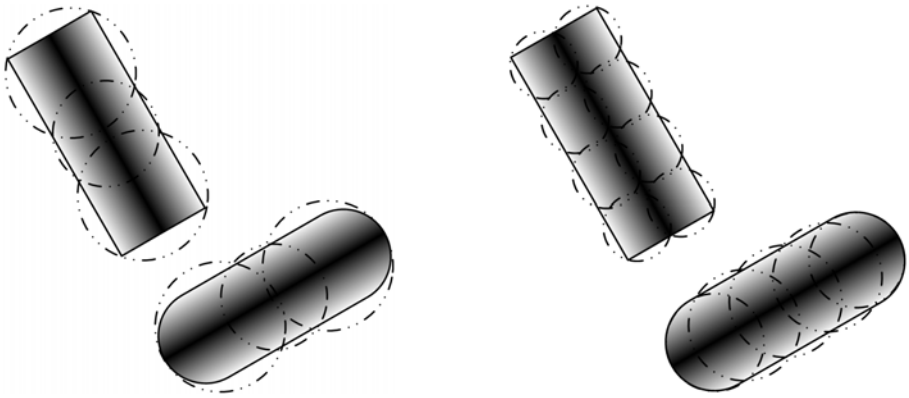

Figure 2.3: The FCM approximation of the components

For the clarity of presentation, only the formulation related to 2D components is discussed here. If only one single circle is used for the approximated definition of each component as shown in Figure 2.2, the approximation error will be large. Consequently, the two components are still far away from each other but the circles have already overlapped. Here, the idea similar to the sphere-trees is used. The components and the design domain are approximately modeled with numbers of circum-circles (2D) or spheres (3D) as shown in Figure 2.3. For each component, a family of circles may have different radii and be placed at different locations to cover the boundary of the components approximately. Clearly, the approximation accuracy can be properly improved by refining the FCM definition (locations, radii of the circles) or using more circum-circles.

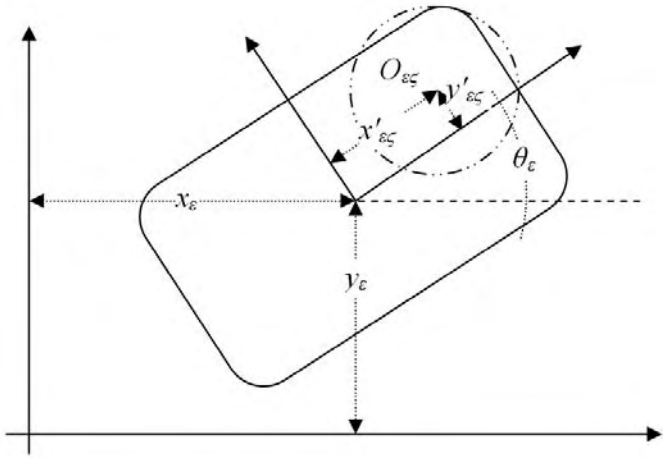

Figure 2.4: The global coordinate system and the local coordinate system of the component

In this way, the complex geometrical design constraints can be transformed and simplified into a standard form of non-overlap between the circles

$$\left\|O_{\varepsilon 1\varsigma 1}O_{\varepsilon 2\varsigma 2}\right\| \geq R_{\varepsilon 1\varsigma 1} + R_{\varepsilon 2\varsigma 2} \tag{2-2}$$

where $O_{\varepsilon 1\varsigma 1}$ is the center of the (ς1)th circum-circle attached to the (ε1)th component, $R_{\varepsilon 1\varsigma 1}$ is the corresponding radius. This relation refers to the distance condition between the circle centers.

In the global coordinate system shown in Figure 2.4, suppose the local coordinate system attached to the εth component is defined by (x_ε, y_ε, θ_ε) and the center of a certain circum-circle $O_{\varepsilon\varsigma}$ is located at ($x'_{\varepsilon\varsigma}$, $y'_{\varepsilon\varsigma}$) in the local coordinate system. The corresponding global coordinate can be calculated as

$$\begin{bmatrix} x_{\varepsilon\varsigma} \\ y_{\varepsilon\varsigma} \end{bmatrix} = \begin{bmatrix} x_\varepsilon \\ y_\varepsilon \end{bmatrix} + \begin{bmatrix} \cos\theta_\varepsilon & -\sin\theta_\varepsilon \\ \sin\theta_\varepsilon & \cos\theta_\varepsilon \end{bmatrix} \begin{bmatrix} x'_{\varepsilon\varsigma} \\ y'_{\varepsilon\varsigma} \end{bmatrix} \tag{2-3}$$

The distance $\|O_{\varepsilon 1\varsigma 1}O_{\varepsilon 2\varsigma 2}\|$ is then calculated as

$$\left(\left\|O_{\varepsilon 1\varsigma 1}O_{\varepsilon 2\varsigma 2}\right\|\right)^2 = (x_{\varepsilon 1\varsigma 1} - x_{\varepsilon 2\varsigma 2})^2 + (y_{\varepsilon 1\varsigma 1} - y_{\varepsilon 2\varsigma 2})^2 \tag{2-4}$$

which can be expressed as explicit and differentiable functions according to Equation (2-3). The design constraint of the non-overlap between the components can be thus written as

$$(x_{\varepsilon 1\varsigma 1} - x_{\varepsilon 2\varsigma 2})^2 + (y_{\varepsilon 1\varsigma 1} - y_{\varepsilon 2\varsigma 2})^2 \big/ (R_{\varepsilon 1\varsigma 1} + R_{\varepsilon 2\varsigma 2})^2 \geq 1 \tag{2-5}$$

With this kind of formulation, the gradients with respect to the involved design variables can be easily calculated by differentiating the equation. From this viewpoint, FCM can be seen as a unified approach for packing optimization problems with components and design domain of arbitrary shapes.

Compared with the sphere-trees methods, the iterative approximation refinements of the circles discretization are not employed in FCM, which implies that the FCM uses a fixed number of design constraints during the packing optimization. In fact, FCM is more than a collision detection method. It finds out how to relocate the components to avoid the overlap by calculating the sensitivities of the distances between the circles with respect to the location and orientation of the components. Note that although FCM is proposed to favor the gradient-based algorithms, it doesn't limit the application of the gradient-free methods.

2.1.2 Approximation of design domain

Another kind of geometrical constraints is the overlap avoidance between the components and the boundaries of the design domain, i.e. the container's constraints. Since the components are approximately defined by the families of circles, the design domain shall be described properly for the easy definition of the container's constraints and ensuring all the circles belonging to a component are located inside the design domain. To simplify

the illustration, the design domains of arbitrary shapes are described with polygons.

Actually, different methods are available to define the container's constraints. Here we just use one circle approximating the components for easy illustration.

The first version of the constraints definition is based on the exact polygon shape of the design domain. As shown in Figure 2.5, the direction of the contour is defined anticlockwise. Any point located always on the left side of each edge of the contour can be proved to be located inside a convex polygon design domain.

Accordingly, the following two different kinds of constraints must be satisfied to keep the circle inside the design domain.

- the circle center is kept on the left side of each edge of the design domain;
- the distance between the circle center and any contour edge is greater than the radius of the corresponding circle.

$$\begin{cases} \sin\angle JIO_{\varepsilon\varsigma} > 0 \\ \sin\angle KJO_{\varepsilon\varsigma} > 0 \\ \sin\angle LKO_{\varepsilon\varsigma} > 0 \\ \sin\angle ILO_{\varepsilon\varsigma} > 0 \end{cases} \quad \text{and} \quad \begin{cases} d\left(O_{\varepsilon\varsigma}, \overline{IJ}\right) > R_{\varepsilon\varsigma} \\ d\left(O_{\varepsilon\varsigma}, \overline{JK}\right) > R_{\varepsilon\varsigma} \\ d\left(O_{\varepsilon\varsigma}, \overline{KL}\right) > R_{\varepsilon\varsigma} \\ d\left(O_{\varepsilon\varsigma}, \overline{LI}\right) > R_{\varepsilon\varsigma} \end{cases} \tag{2-6}$$

Now there are two groups of design constraints defining each pair of circle center and edge of design domain. Obviously, such a definition is still too complex and too many constrains are involved.

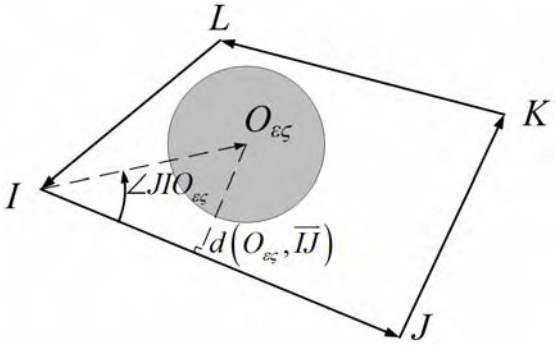

Figure 2.5: Direction of the contour

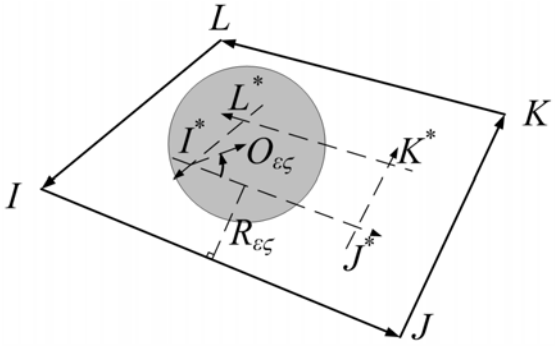

Figure 2.6: Container's constraints with an inner contour

To reduce the constraint number, an inner contour of the design domain can be introduced, whose distance to the real contour of the design domain is assigned as the radius of the corresponding circle. As shown in Figure 2.6, the constraints expressed in Equation (2-6) can be simplified in such a way that the center of the circle is limited inside the inner contour.

$$\begin{cases} \sin\angle J^*I^*O_{\varepsilon\varsigma} > 0 \\ \sin\angle K^*J^*O_{\varepsilon\varsigma} > 0 \\ \sin\angle L^*K^*O_{\varepsilon\varsigma} > 0 \\ \sin\angle I^*L^*O_{\varepsilon\varsigma} > 0 \end{cases} \tag{2-7}$$

Although the number of constraints is reduced, the problem definition becomes complex. As the radii of the circles are not the same, inner contour segments would be defined by different radii of the circles.

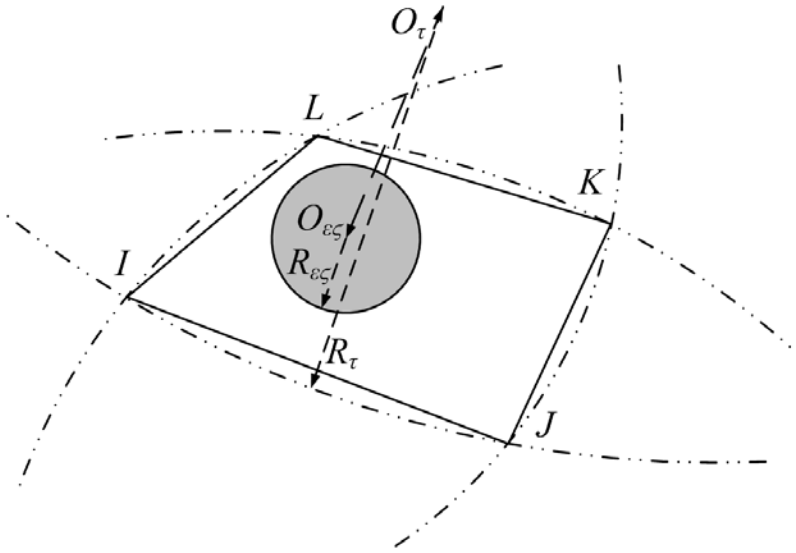

Figure 2.7: Relaxed approximation of the design domain with big circles

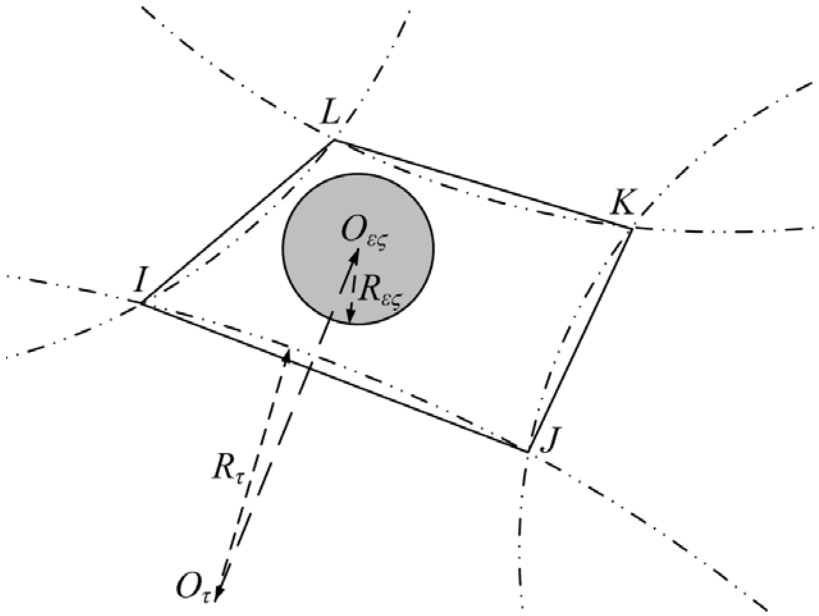

Figure 2.8: Conservative approximation of the design domain with big circles

Since the circle approximation can simplify the non-overlap constraints between the components, it can also be used to approximate the contour of the design domain. As

shown in Figure 2.7 and 2.8, the design domain is approximated by several big circles in two different ways. Now the container's constraints are also transformed into the distance constraints between the circle centers.

With the relaxed approximation, the components are located in all the big circles so that we have

$$\left\| O_{\varepsilon\varsigma} O_{\tau} \right\| \le R_{\tau} - R_{\varepsilon\varsigma} \tag{2-8}$$

where O_τ is the center of the τth circle describing the edge of the design domain and R_τ is the corresponding radius.

With the conservative approximation, the components are located outside all the big circles so that we have

$$\left\| O_{\varepsilon\varsigma} O_{\tau} \right\| \ge R_{\tau} + R_{\varepsilon\varsigma} \tag{2-9}$$

The conservative approximation provides a general way of avoiding the overlap. The approximation error is easily adjusted by changing the radii and centers of the big circles. It is thus used in this thesis.

For the circles approximating the components, two situations that satisfy the Equation (2-9) may exist. As shown in Figure 2.9, although the dark circle is far away from the design domain, practically in the optimization, the design constraints are functional with the lower and upper bounds of the design variables. The movements of the components are actually limited in a rectangle like areas which is just a little bigger than the design domain.

The component is totally located inside the design domain if all the circles describing it are kept inside. However, this is not a necessary condition. It can be proved that in a convex polygon design domain, we only have to keep some selected circles inside, e.g. the circles located at the vertices of a polygon component, which can further reduce the number of the design constraints.

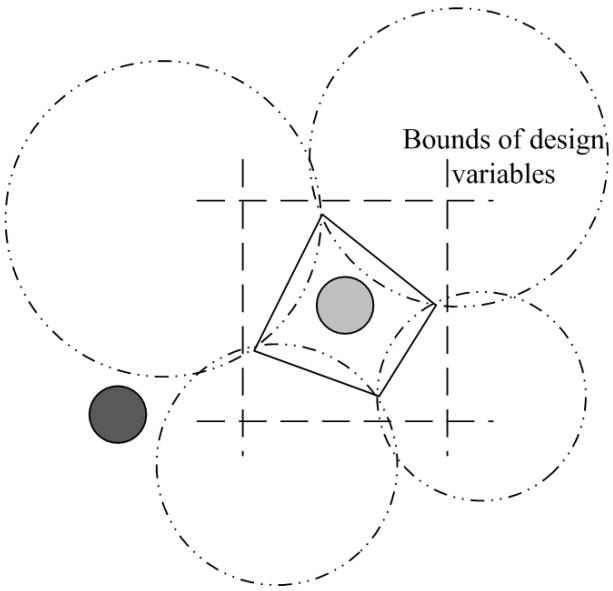

Figure 2.9: Two situations of the component's location and the bounds of the design variable

2.1.3 Non-convex polygon design domain

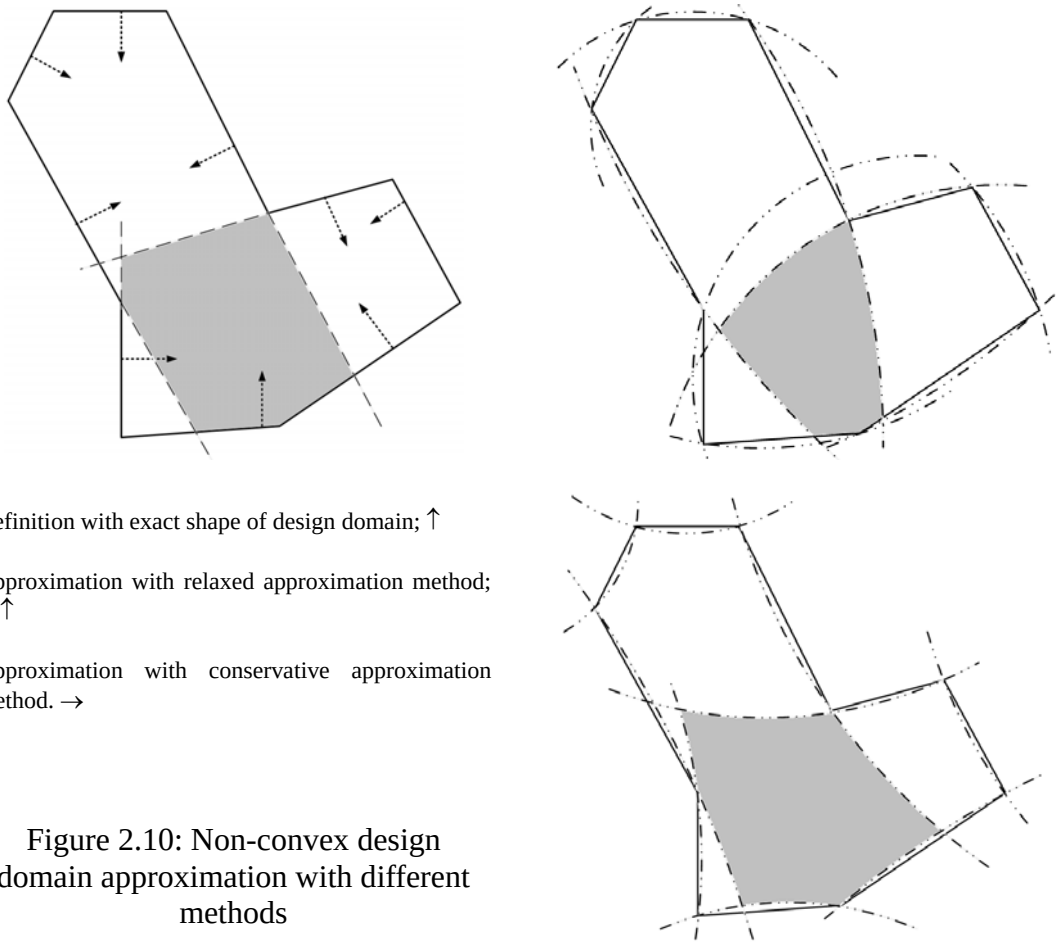

Definition with exact shape of design domain; ↑

Approximation with relaxed approximation method; →↑

Approximation with conservative approximation method. →

Figure 2.10: Non-convex design domain approximation with different methods

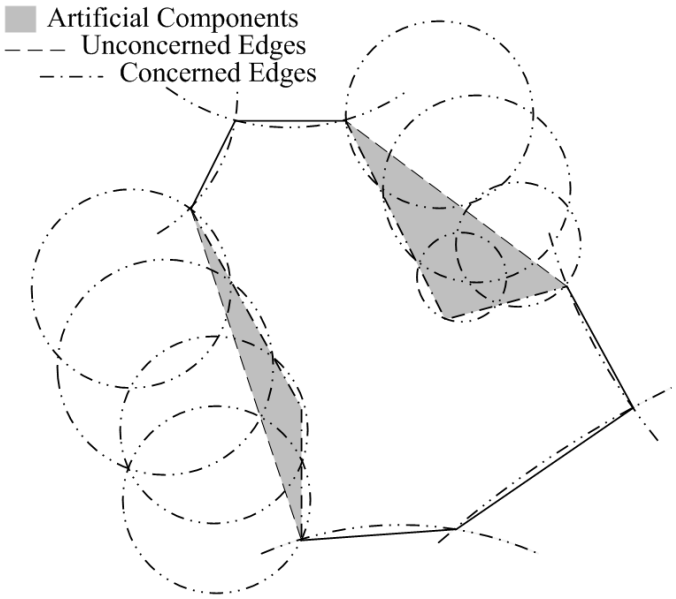

Figure 2.11: Introduction of the artificial components and their approximations

Although the approximation methods proposed above work well for the convex polygon design domain, they fail to describe the non-convex packing area shown typically in Figure 2.10. For this reason, new ideas are proposed to work with the conservative approximation of the design domain. As shown in Figure 2.11, artificial components are introduced as fixed ones to convexify the area and only those edges of the artificial

components that contact the design domain will be approximated in a conservative way to avoid the overlap. During the collision detection, the artificial components are considered as non-designable ones with fixed positions and orientations.

Thus, for the non-convex design domain, the geometrical design constraints are generally formulated as

$$\begin{cases} \forall \varepsilon,\ \varsigma,\ \tau \\ s.t.:\ \left\| O_{\varepsilon\varsigma} O_{\tau} \right\| \geq R_{\varepsilon\varsigma} + R_{\tau} \\ \forall \varepsilon 1,\ \varepsilon 2,\ \varepsilon 1 \neq \varepsilon 2 \\ \forall \varsigma 1,\ \varsigma 2 \\ s.t.:\ \left\| O_{\varepsilon 1\varsigma 1} O_{\varepsilon 2\varsigma 2} \right\| \geq R_{\varepsilon 1\varsigma 1} + R_{\varepsilon 2\varsigma 2} \end{cases} \tag{2-10}$$

where the circles of the artificial components are included in the group of circles O_τ approximating the edges.

2.2 Circle discretization

2.2.1 Uniform discretization

As mentioned already, the refinement of the circle discretization can improve the approximation precision of the Finite-circle Method. The simplest way is to discretize the contour of the component uniformly. A simple packing problem consisting of six identical equilateral triangle components and an equilateral hexagon design domain is illustrated in Figure 2.12. The characteristic length l is now assigned as the edge length of the triangular component and each component is approximated with nine identical circles with a maximum approximation error of 7.22%l. Likewise, the design domain is approximated with six big circles and the maximum error is 3%l. The problem is now to find the optimal locations of all components inside the design domain with a minimum packing area. Mathematically, the problem can be stated as the height minimization of the equilateral hexagon.

$$\begin{cases} \text{find: } (x_\varepsilon, y_\varepsilon, \theta_\varepsilon)\ \varepsilon \in \{1,2,3,4,5,6\} \\ \text{min: } h \\ \forall \varepsilon \in \{1,2,3,4,5,6\} \\ s.t.: \Gamma_\varepsilon(x_\varepsilon, y_\varepsilon, \theta_\varepsilon) \subset \Gamma_D \\ \forall \varepsilon 1 \in \{1,2,3,4,5,6\}, \varepsilon 2 \in \{1,2,3,4,5,6\}, \varepsilon 1 \neq \varepsilon 2 \\ \Gamma_{\varepsilon 1}(x_{\varepsilon 1}, y_{\varepsilon 1}, \theta_{\varepsilon 1}) \cap \Gamma_{\varepsilon 2}(x_{\varepsilon 2}, y_{\varepsilon 2}, \theta_{\varepsilon 2}) = \varnothing \end{cases} \tag{2-11}$$

Finally, 1215 constraints are retained to avoid the overlap between the components and 324 constraints to keep all the components inside the design domain. Based on the initial configuration shown in Figure 2.13(a), the optimization problem is programmed and sensitivity analysis is carried out in the framework of Boss-Quattro^{TM}, the design process converges to the configuration shown in Figure 2.13(d) after 13 iterations. Because of the

conservative approximation of the design domain, there is always a safety gap between the domain contour and the circles of the components.

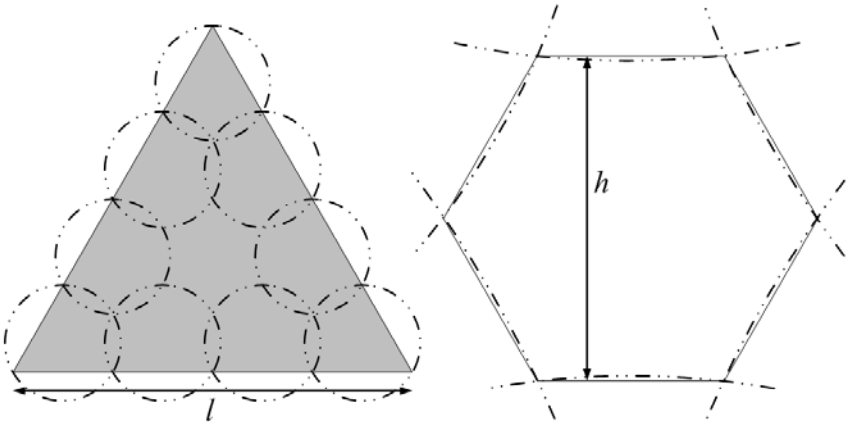

Figure 2.12: The triangle component and the design domain

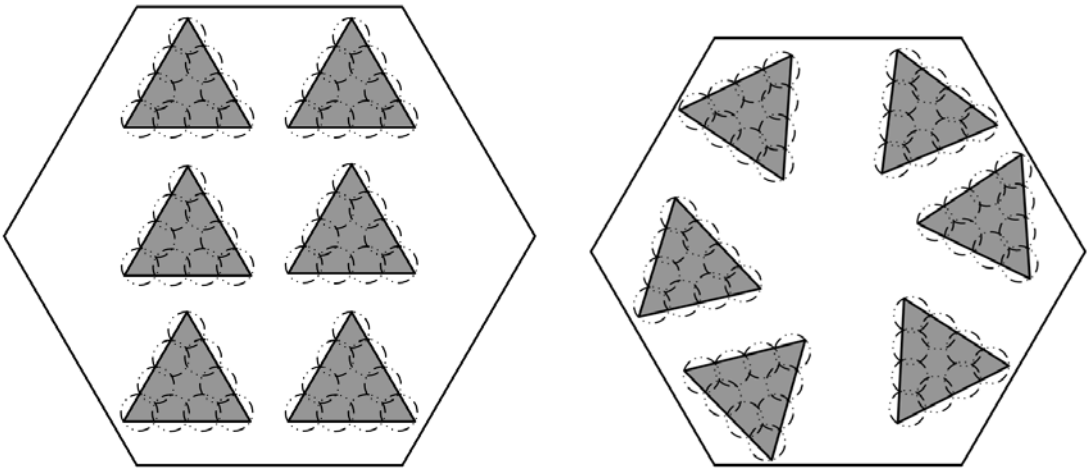

(a) The initial configuration (b) Iteration 4

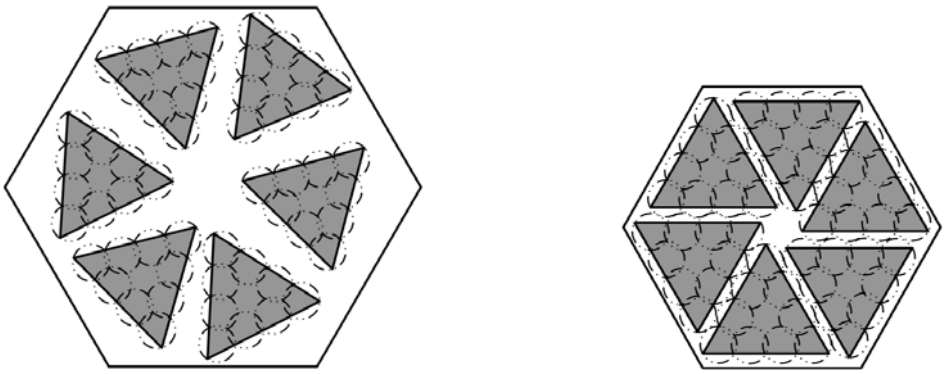

(c) Iteration 8 (d) The final configuration

Figure 2.13: The design iteration and the optimal result

To improve the approximation accuracy, more circles are used as shown in Figure 2.14 with the uniform discretization. Although the approximation error is reduced, the great number of the circles leads to a large number of design constrains which cost tremendous

computing time.

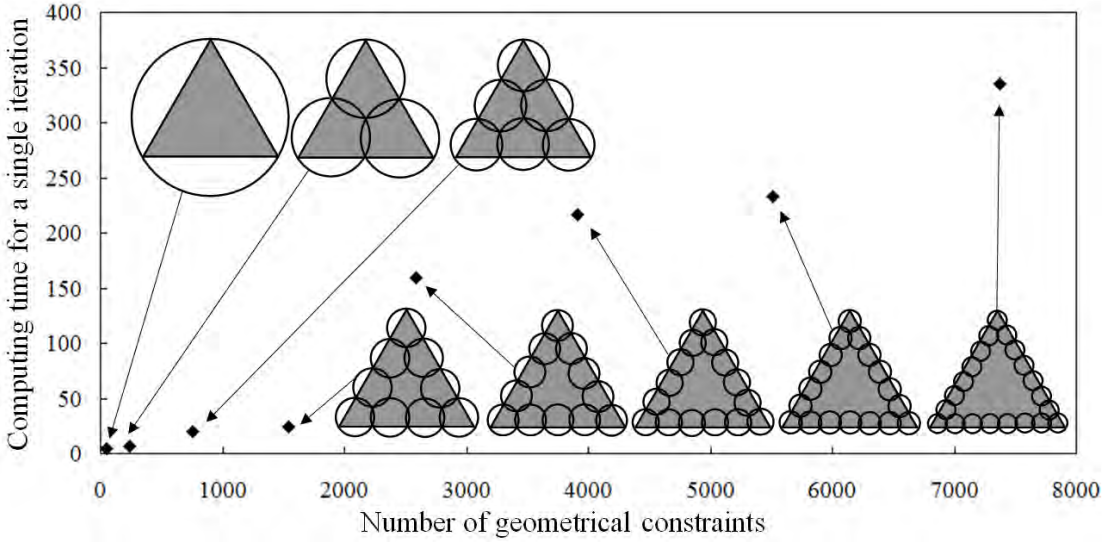

Number of circles	1	3	6	9	12	15	18	21
Number of constraints	51	243	756	1539	2592	3915	5508	7371
Computing time for one iteration (s)	4.906	6.688	19.483	24.718	158.797	216.462	232.828	335.281

Figure 2.14: Effects of circle and constraint numbers upon the computing time for one single iteration

2.2.2 Improved component discretization

The uniform discretization is easily performed and the refinement is very convenient to be carried out because of the identical circles, but a huge computing cost is obviously needed for an acceptable approximation precision when the packing optimization problem is solved iteratively. It is therefore necessary to use fewer circum-circles while maintaining the approximation precision.

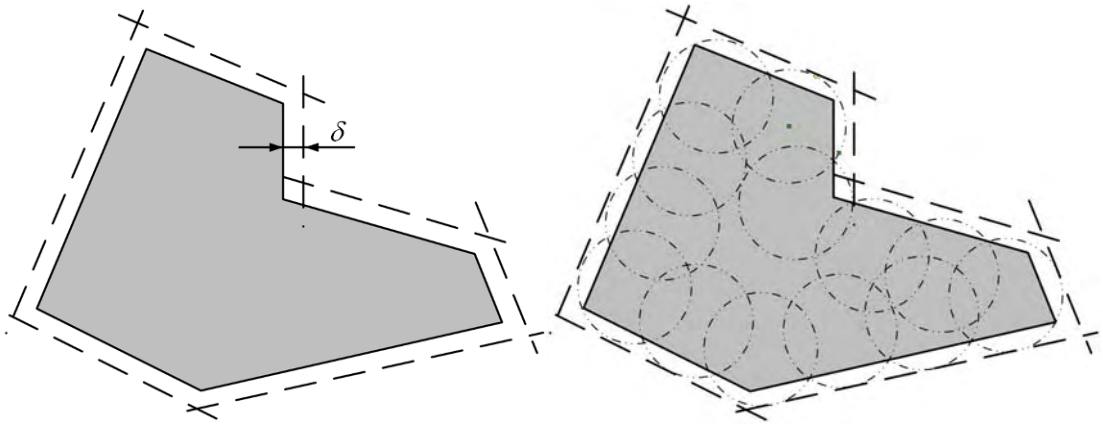

Figure 2.15: The approximation error and the circle definition by uniform discretization

In this section, some semi-heuristic rules are used to reduce the number of circles with a satisfactory approximation error by adjusting the radii and positions of circles. For the purpose of comparison, an illustrative component is shown in Figure 2.15. Suppose the approximation error is predefined as δ, all the circles have to be located in the area delimited by the dashed line referred to as the tolerance contour. The uniform discretization leads to 13 circles is used for this component.

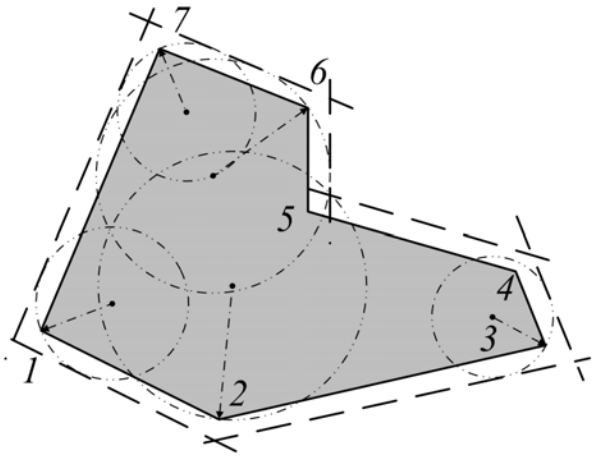

Figure 2.16: The corner approximation

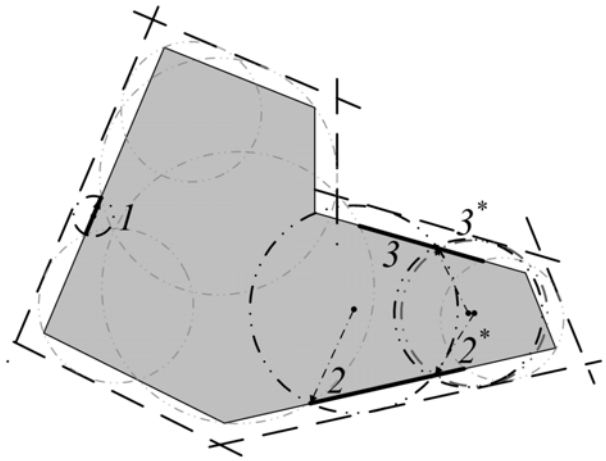

(a) The first step of edge approximation

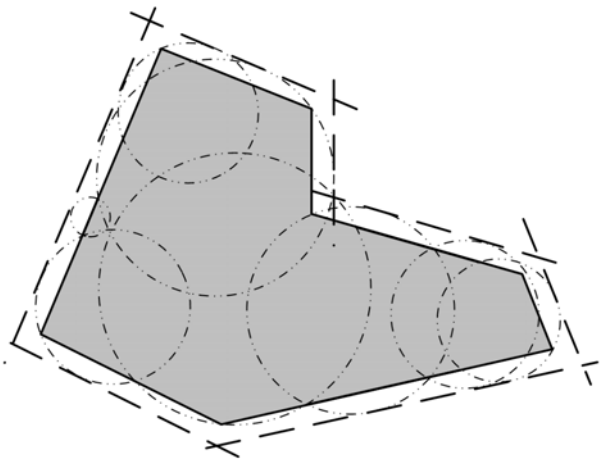

(b) Circle definition covering all sections

Figure 2.17: The edge approximation

The improved semi-heuristic discretization method proceeds as follows.

1) The corner approximation. As shown in Figure 2.16, the circle definition starts from each convex vertex of the component. The circle center is located on the bisector of this corner angle and the circle is tangent with the tolerance contour on both sides of the corner. The radius of each circle will be defined as big as possible to cover more parts of the contour. For example at the 2nd and 6th corner, circles with large radii are used here as long as the circles will not exceed the tolerance contour. Sometimes, the circle at one corner is big enough to cover another corner. For example, the 4th corner is covered by the circle at the 3rd corner and no more circles are needed.

2) The edge approximation. Uncovered sections of the contour are identified and then approximated with circles. If the considered section cannot be covered by one single circle, it will be subdivided into 2 or even more sections from one end until each of them can be covered by one circle. Note that all the circles will be defined as large as possible to cover more sections. When all the sections are covered, the circles will be checked to avoid the duplicated coverage.

Now the circle definition is shown in Figure 2.17. Only 8 circles are used with the approximation error satisfied. Normally, this kind of definition can be used in the FCM right now.

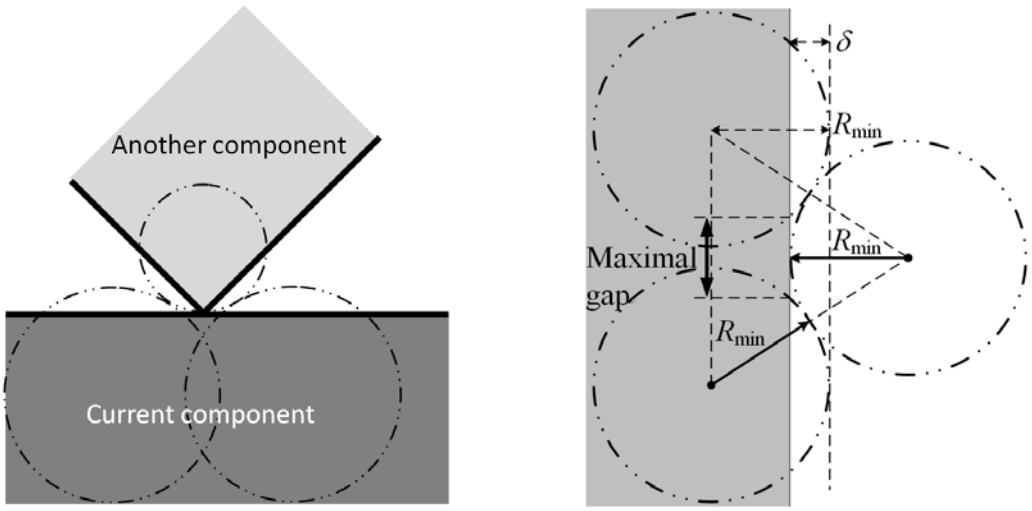

Figure 2.18: The critical situation and the maximal gap estimation

3) Circle shrink. In fact, the approximation error of the current circle definition in Figure 2.17 can be further reduced. As shown in Figure 2.18, because the circles do not need to be distributed one after another, a small gap is allowed between two circles on the section. The critical condition is that the minimum circle from other components is tangent to the gap. Therefore, when the radius of the minimal circle, R_{min}, and the approximation error, δ, are given, the maximum gap can be estimated.

Based on the current discretization, some circles will be removed when the contour section to be covered is shorter than the critical maximum gap. Meanwhile, the rest circles will shrink until the critical situation is reached. For the circles at the corner, the radii are reduced by moving the center towards the corner along the angle bisector. For other circles on the edges, the radii shrink directly without moving the center as shown in Figure 2.19. The final improved circle is shown in Figure 2.20.

The introduction of the gap is proved to be effective in improving the approximation and reducing the number of circles. However, it is still heuristic and when the approximation becomes more and more rigorous, the gap becomes less useful (See Fang 2008).

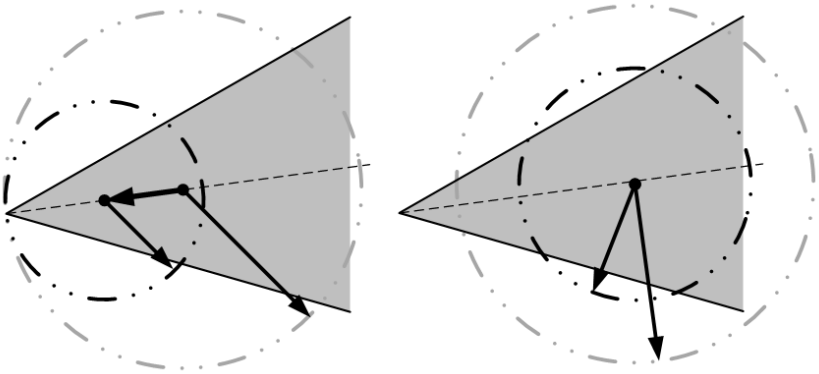

Figure 2.19: Circle shrink

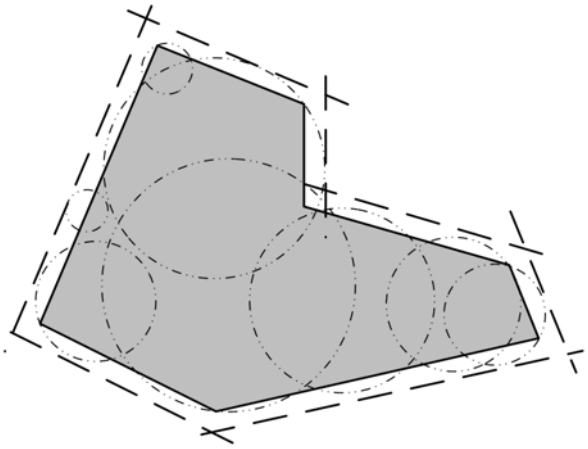

Figure 2.20: Finial circle discretization after the circle shrinking

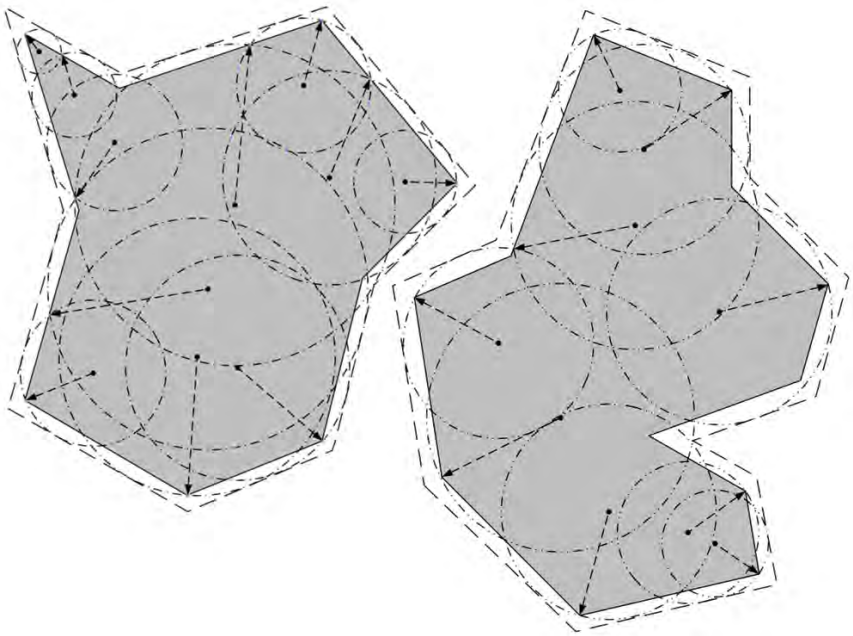

Figure 2.21: Circle discretization for the components with arbitrary shapes

2.2.3 Design domain discretization

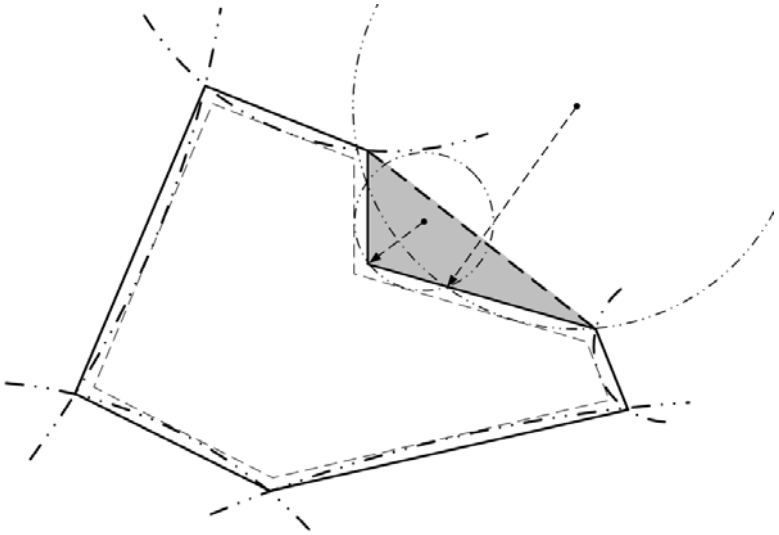

Figure 2.22: Design domain discretization

The circle definition of the design domain is much easier. A design domain and its acceptable approximation error are shown in Figure 2.22. As indicated before, the edges of the design domain except those situated in the non-convex part of the design domain can be approximated with one big circle. The centers of the circles are located on the perpendicular bisectors of the edges. The approximation error can be adjusted by modifying the distances between the center of the circle and the edge of the design domain. The concave parts of the design domain are filled with the artificial components that are in turn approximated except the unconcerned edges.

2.3 Packing examples

Several 2D and 3D examples are tested here to evaluate the FCM for pure geometrical packing problems.

2.3.1 Equilateral hexagon

The example tested in Section 2.2.1 is further designed here. As shown in Figure 2.23, suppose the proposed discretization rule generates only 4 circles for the triangle with the approximation error of 6.11%l. Consequently, 240 constraints are generated to avoid the component overlap and 144 constraints to keep the components inside the design domain.

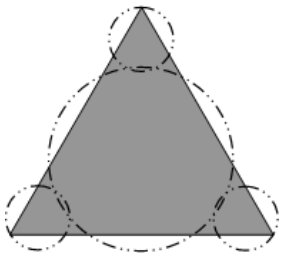

Figure 2.23: The improved circum-circle approximation with 4 circles

With the initial configuration shown in Figure 2.24(a), the optimization is carried out with the same design objective. The final configuration figured out in Figure 2.24(d) is obtained after 13 iterations. The packing layout is identical to the previous solution although a simplified discretization is used. However, due to the circle approximation, it

is impossible to find an ideal packing design without gap between components.

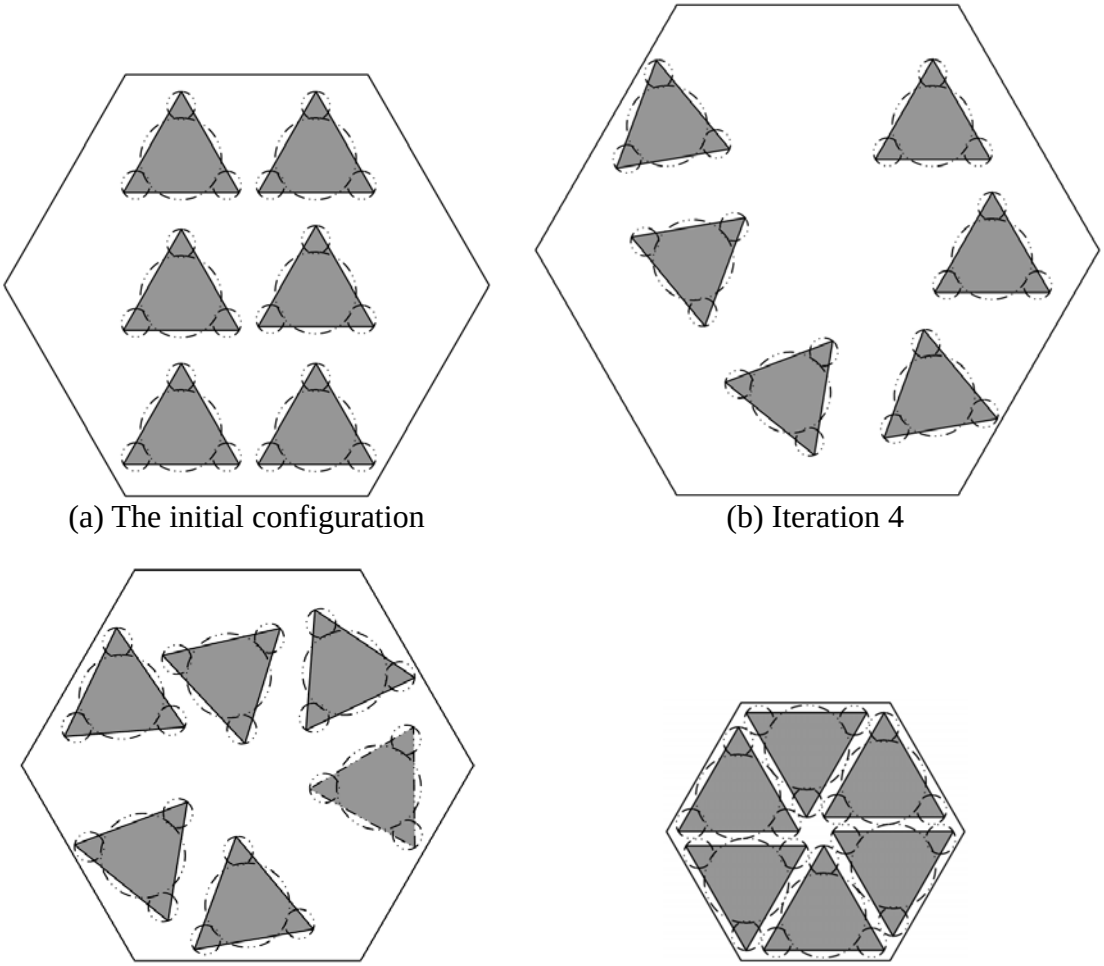

(a) The initial configuration (b) Iteration 4

(c) Iteration 8 (d) The final configuration

Figure 2.24: The design iteration and the optimal result

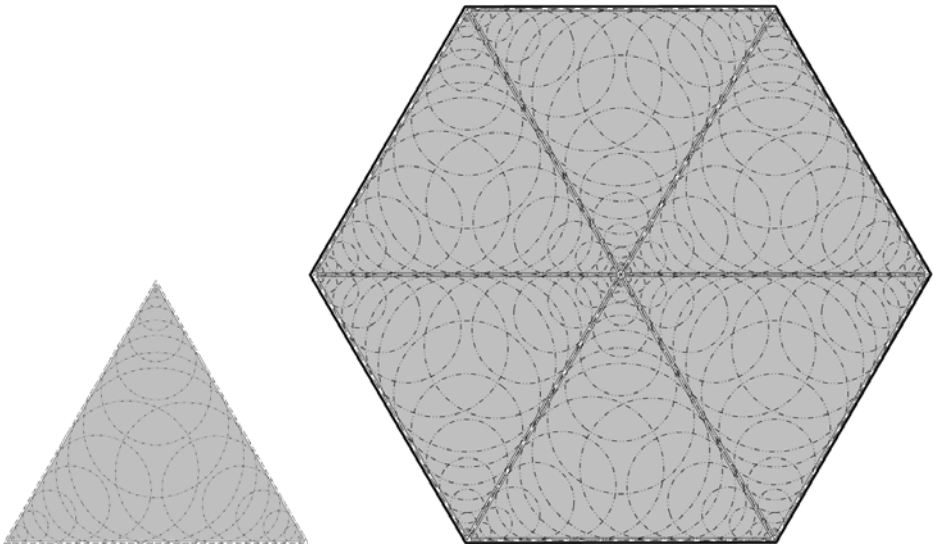

Figure 2.25: Equilateral hexagon packing with more precise approximation

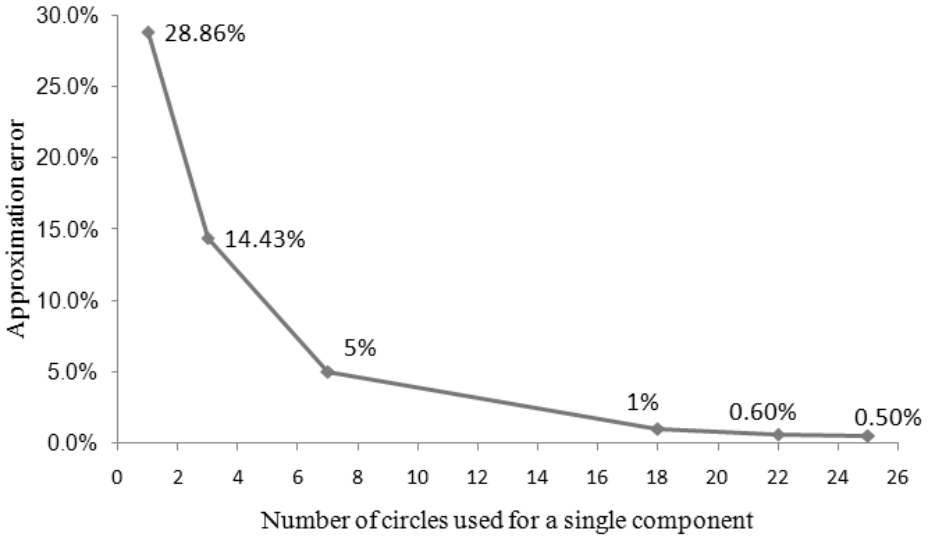

Figure 2.26: Number of the circles versus the approximation error

If the approximation error is further reduced by using more circles for the components, the final design is nearly compact. As shown in Figure 2.25, 22 circles are used for one single component and the approximation error is 0.62%. The approximation errors are plotted in Figure 2.26 versus the circle number. More and more circles are needed if a tiny approximation error is required.

2.3.2 Packing with more components

Another 2D packing problem is tested with more complex components. As shown in Figure 2.27, 14 components of 7 different shapes need to be located in a hexagonal design domain. The problem is to minimize the area of the design domain in 4 different ways of compactness as shown in Figure 2.28. Firstly, suppose components having the same shape are overlapping with each other and are located outside the design domain. Different layouts of the components are obtained to adapt to the outer contour of the design domain.

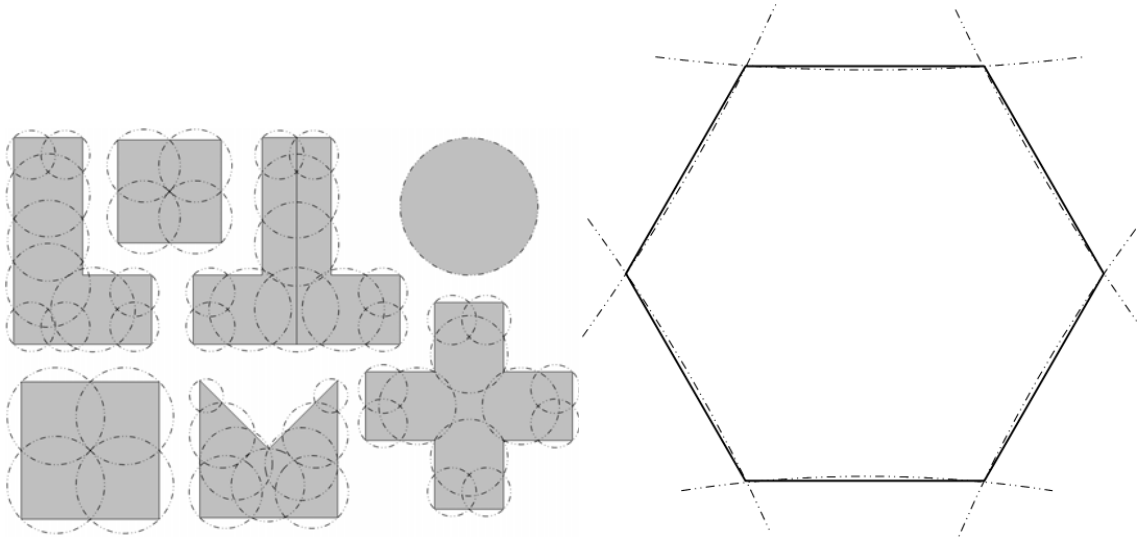

Figure 2.27: Different shapes of the components and the design domain

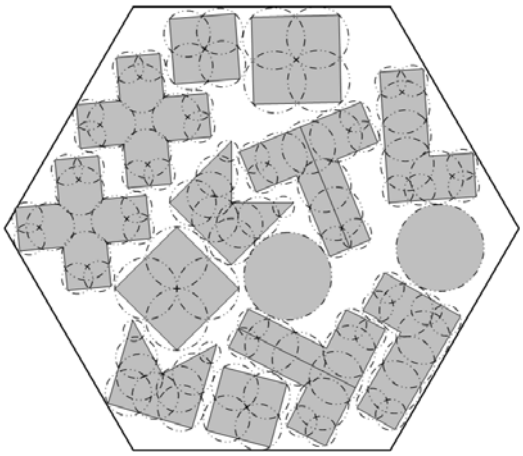

(a) The design domain remains to be a equilateral hexagon

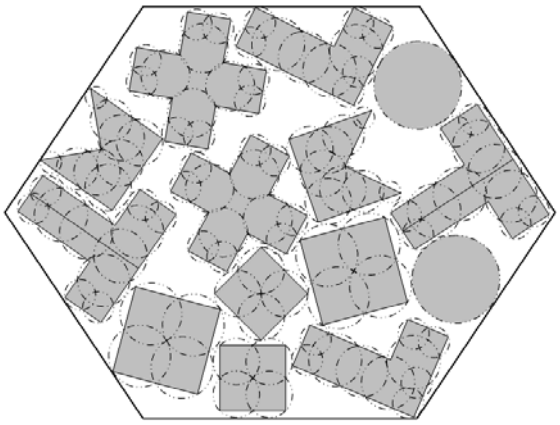

(b) Compact in vertical direction

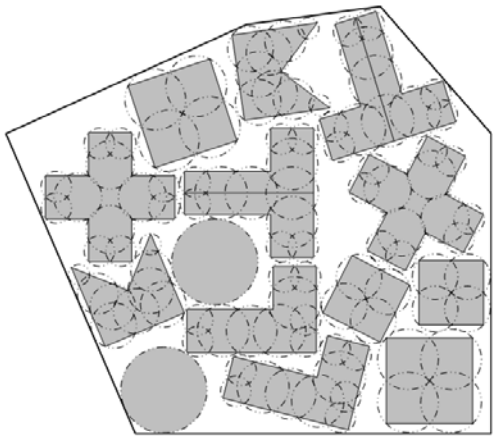

(c) All vertexes move freely

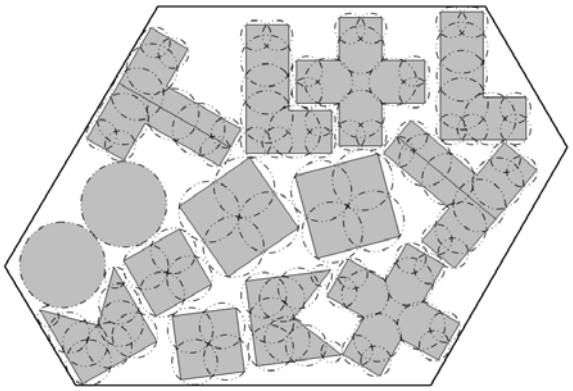

(d) All edges vary in parallel with the initial ones

Figure 2.28: Packing with different kinds of compactness

2.3.3 Packing in a cube

In this example, a 3D packing optimization problem is tested. 4 identical cubic components and 2 cuboids shown in Figure 2.29 will be located into a bigger cube. 21 and 35 spheres are used to approximate each cube and cuboid, respectively. 6 big spheres are used to define the cubic design domain.

With the FCM approximation, the 3D packing problem is just an extended version of the 2D one. Both the location and orientation of a 3D component are described by 6 design variables indicating 6 degrees of freedom. Initially, suppose the components are located freely outside the design domain as shown in Figure 2.30(a). The optimization will find a minimum cubic container to envelop the components inside. Finally, the optimization process takes 23 iterations to reach the convergence and the 6 components are located as shown in Figure 2.30(b). Obviously, with the gradient-based algorithm, this is a typical local minimum rather than the most compact design.

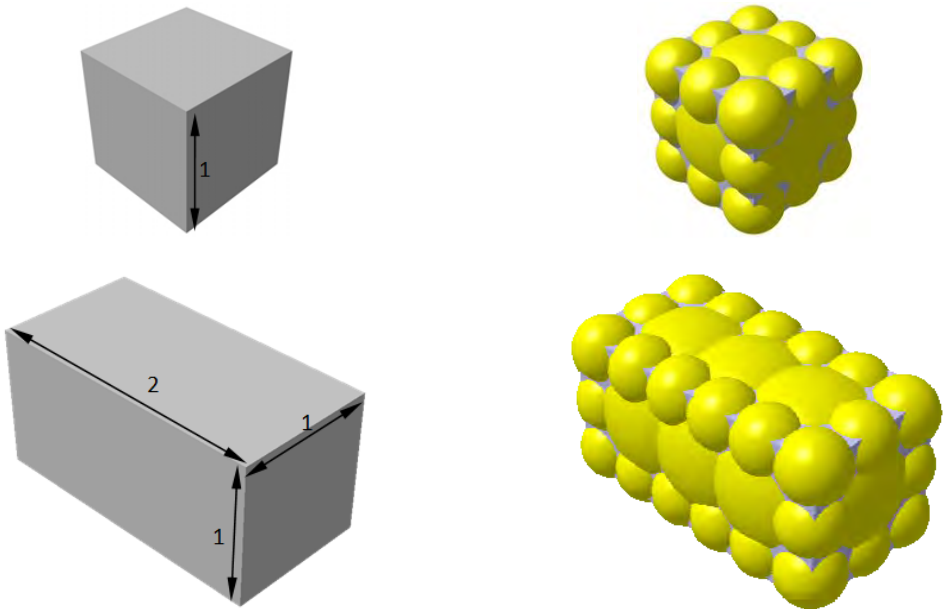

Figure 2.29: The cubic and cuboid components and their finite-circle definition

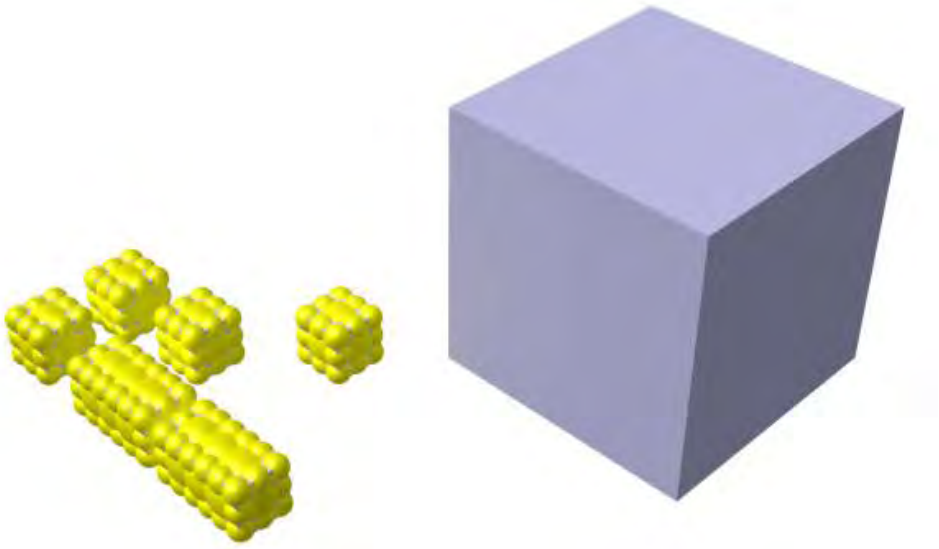

(a) The initial configuration

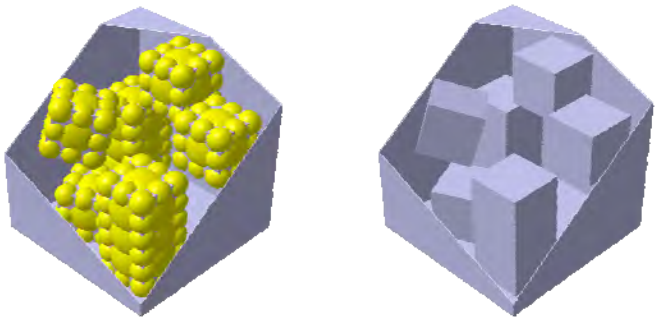

(b) The optimal configuration

Figure 2.30: Design iteration and the optimal result

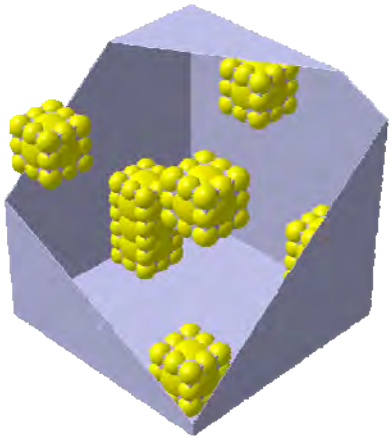

Figure 2.31: A loose packing configuration

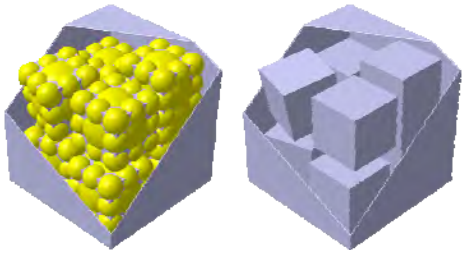

Figure 2.32: The optimal configuration

If we start from a different initial design as shown in Figure 2.31, the optimization will lead to another local optimum. Here, the cubic components are firstly relocated as a loose packing that can be obtained by starting from a packing design maximizing the summation of all distances between spheres with the non-overlap constraints.

Obviously, the benefit of a loose packing configuration is twofold. First, the initial design is a feasible one with all the design constraints satisfied. Second, a loose packing actually forms a larger searching space. Both are favorable for the optimum searching with gradient-based algorithms. In this example, a new packing configuration is obtained with 25 iterations as shown in Figure 2.32. It is more compact than the previous one.

2.3.4 Packing design with moment of inertia

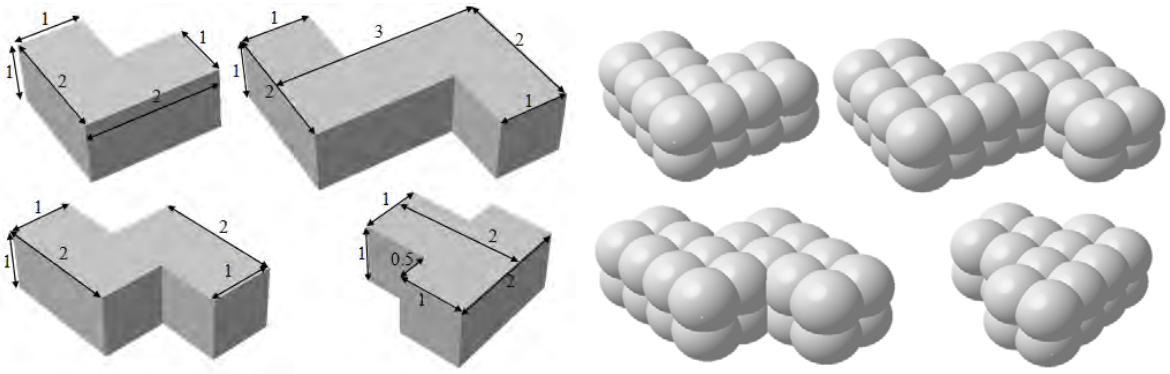

Figure 2.33: Dimensions and the FCM definition of the components

In aerospace structural systems, e.g., rockets and satellites, it is a critical subject to design the moment of inertia for the system stability. Illustrative examples are tested here to show how the packing optimization is performed with FCM method. Suppose 4 components with different shapes are located in a cylinder. Dimensions of the components and their sphere definition are shown in Figure 2.33.

Suppose the components are composed of solid material of density ρ. By calculating the integral moment of inertia of each component and then using the parallel axis theorem,

the global moment of inertia with respect to the system axis, i.e. the central axis of the cylinder can be obtained and assumed as the objective function to be minimized here.

$$
\begin{aligned}
&\text{find: } (x_\varepsilon, y_\varepsilon, z_\varepsilon, \theta_{xy\_\varepsilon}, \theta_{yz\_\varepsilon}, \theta_{zx\_\varepsilon})\ \varepsilon \in \{1,2,3,4\} \\
&\text{min: } J = \int \rho \left(\Delta d\right)^2 dv \\
&\forall \varepsilon \in \{1,2,3,4\}, \varepsilon 1 \in \{1,2,3,4\}, \varepsilon 2 \in \{1,2,3,4\}, \varepsilon 1 \neq \varepsilon 2 \\
&\text{s.t.: } \Gamma_\varepsilon (x_\varepsilon, y_\varepsilon, z_\varepsilon, \theta_{xy\_\varepsilon}, \theta_{yz\_\varepsilon}, \theta_{zx\_\varepsilon}) \subset \Gamma_D \\
&\quad \Gamma_{\varepsilon 1} (x_{\varepsilon 1}, y_{\varepsilon 1}, z_{\varepsilon 1}, \theta_{xy\_\varepsilon 1}, \theta_{yz\_\varepsilon 1}, \theta_{zx\_\varepsilon 1}) \\
&\qquad \cap \Gamma_{\varepsilon 2} (x_{\varepsilon 2}, y_{\varepsilon 2}, z_{\varepsilon 2}, \theta_{xy\_\varepsilon 2}, \theta_{yz\_\varepsilon 2}, \theta_{zx\_\varepsilon 2}) = \varnothing
\end{aligned}
\tag{2-12}
$$

where J is the global moment of inertia and Δd is the distance between the current particle and the central axis of the system. It should be noted that the sphere approximations are only used to define the geometrical constraints while the moment of inertia is calculated with the exact body shape of the components.

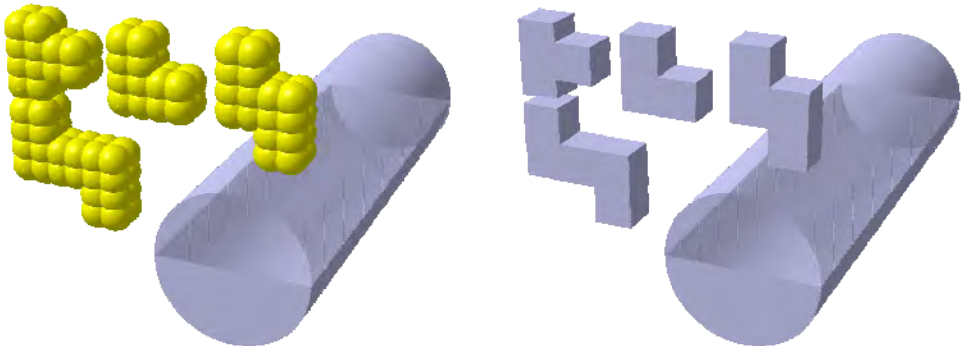

Figure 2.34: Initial configuration of the components

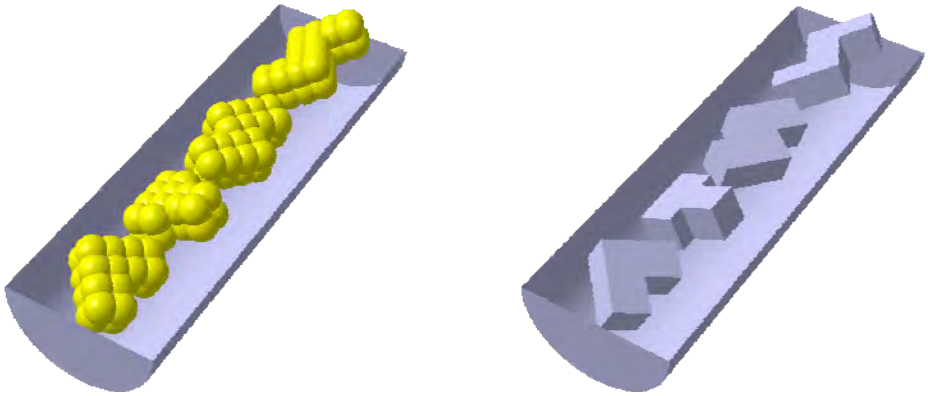

Figure 2.35: Final configuration with minimal moment of inertia

The components are first located outside the design domain that has a radius of 2.13 and a height of 14.14 as shown in Figure 2.34. For the purpose of a clearer view, half of the design domain is transparent and the spheres for the components are hided.

The global moment of inertia is minimized. The final configuration is shown in Figure 2.35. As expected, all the components are finally located along the central axis of the cylinder with the optimal moment of inertia being 4.229ρ.

Another test is carried out here with the same components but a different cylinder design domain. As shown in Figure 2.36, the radius and height of the cylinder are set to be 2.6 and 3.5, respectively. And the components are initially located outside the design domain as well. The final result is shown in Figure 2.37 with the moment of inertia being 25.157ρ. Although the design domain is not high enough to locate all the components on the central axis of the cylinder, all of them crowd into the cylinder as close as possible to the axis.

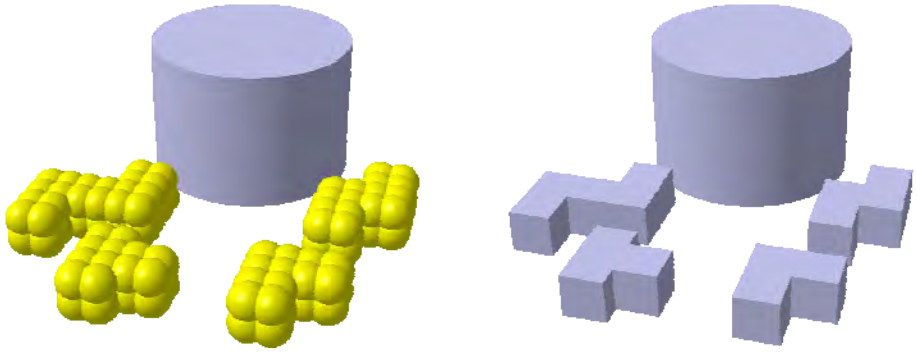

Figure 2.36: Initial configuration of the components

Figure 2.37: Final configuration with minimal moment of inertia

2.4 Local minima in FCM

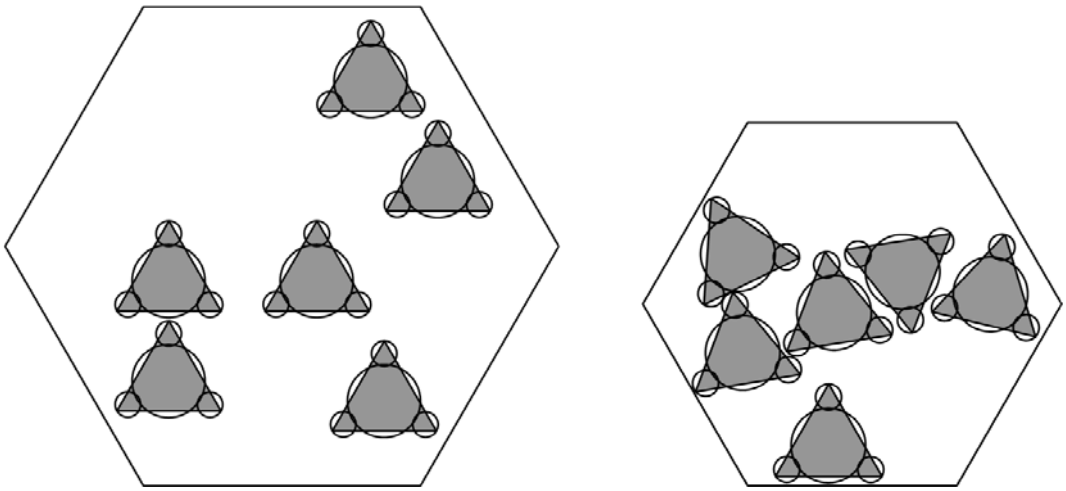

(a) The initial configuration

(b) 4th iteration

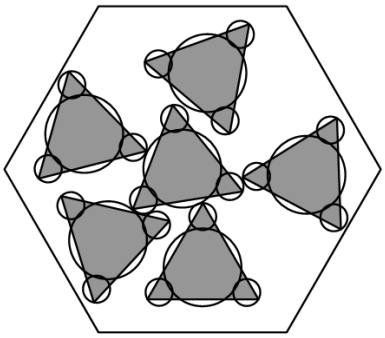

(c) 8th iteration

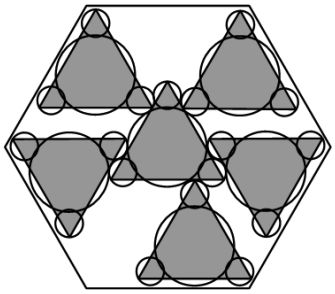

(d) The final configuration

Figure 2.38: The design evolution of the local minimum

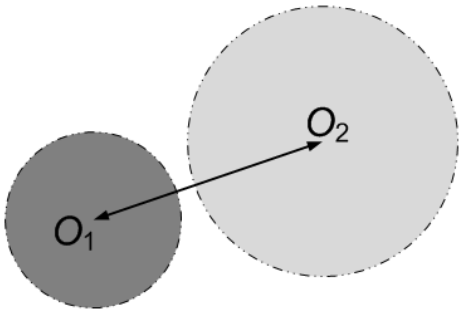

(a) Distance between two circle centers

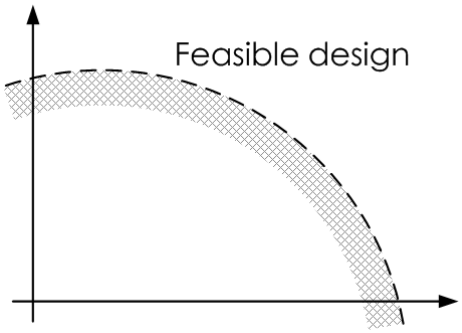

(b) Reverse convex constraint

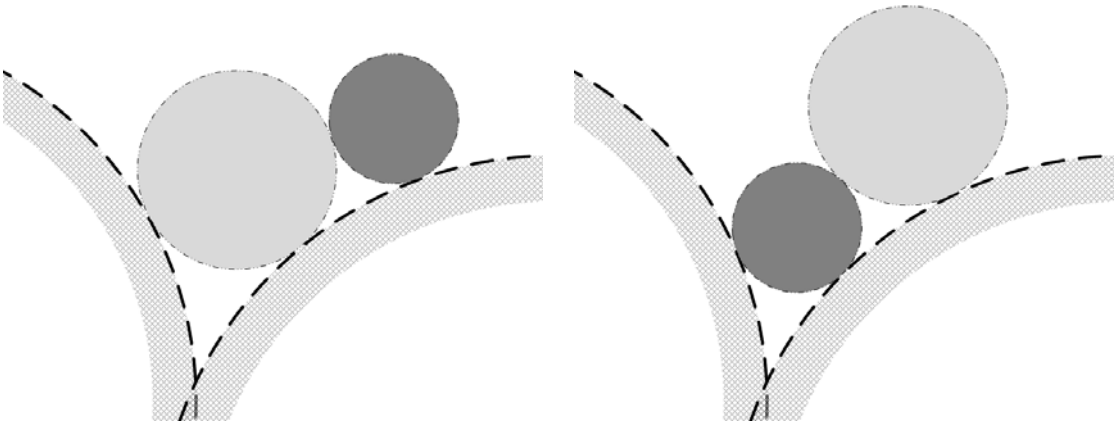

(c) Possible local minima

Figure 2.39: Non-overlap constraints with single circles

The reason is analyzed based on the non-overlap constraint functions. Suppose only two circular components are concerned and the design variables are assigned to the center positions of the circles as shown in Figure 2.39(a), the non-overlap constraint is expressed as

$$\left\|O_1O_2\right\| = \sqrt{\left(x_1 - x_2\right)^2 + \left(y_1 - y_2\right)^2} \geq R_1 + R_2 \qquad (2\text{-}13)$$

where O_1 and O_2 are the centers of two different circles with the coordinates (x_1, y_1) and (x_2, y_2), respectively. R_1 and R_2 are the radii of both circles. As the square root brings more complexities in calculation, the expression can be equivalently simplified as

$$\left\|O_1O_2\right\|^2 = \left(x_1 - x_2\right)^2 + \left(y_1 - y_2\right)^2 \geq \left(R_1 + R_2\right)^2 \tag{2-14}$$

The Hessian matrix of the squared distance with respect to the design variables (x_1, x_2, y_1, y_2) is calculated as

$$\nabla^2\left(\left\|O_1O_2\right\|^2\right) = \begin{bmatrix} 2 & -2 & 0 & 0 \\ -2 & 2 & 0 & 0 \\ 0 & 0 & 2 & -2 \\ 0 & 0 & -2 & 2 \end{bmatrix} \tag{2-15}$$

which can be easily proved to be positive semi-definite. This implies that the distance function between two single circles is always convex. But the constraint itself is actually non-convex as shown in Figure 2.39(b) because of the sign of the inequality. As shown in Figure 2.39(c), if the two circles are put into a corner to minimize geopotential energy, several local minima may exist for the final design.

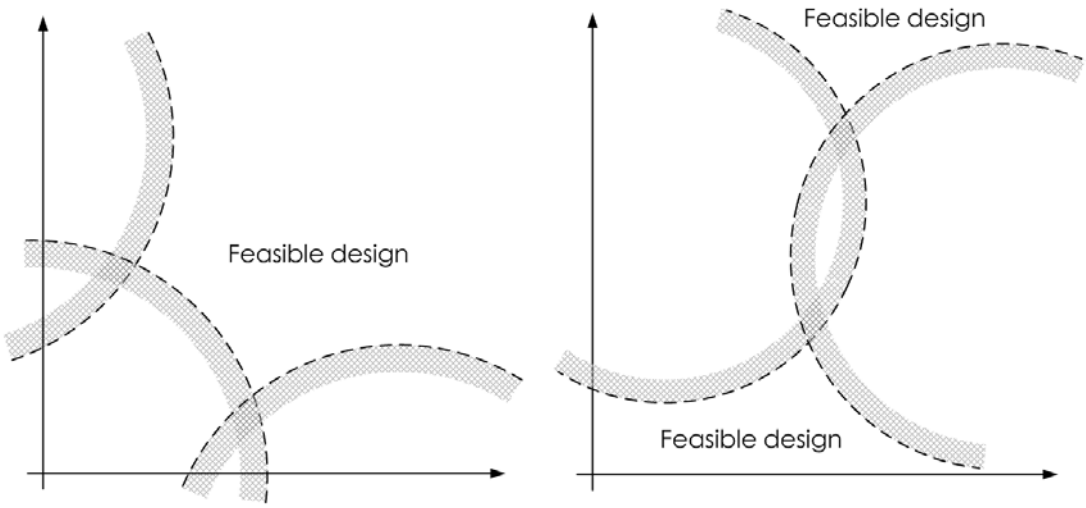

Figure 2.40: Feasible design space for multiple reverse convex constraints

In fact, this problem is rather complicated when more constraints are involved. This situation can be explained in Figure 2.40. These constraints create a non-convex or even discontinuous feasible design space. The design point will not be changed from one local minimum to another one unless it goes across the infeasible design space, which is not allowed by the gradient based algorithms. Some examples of circle packing can be found in the work of Fang (2008).

Unfortunately, a single circle cannot approximate the component of arbitrary shape very well. In FCM, the centers of the circles have to be calculated by the coordinate transformation by Equation (2-3). As a result, the Hessian matrix of the original Equation (2-5) with respect to the locations and orientations of the components becomes too complex to be expressed. To makes things clear, consider a simplified FCM example

shown in Figure 2.41. Two identical components are located into a rectangle design domain. Each of the components is composed of 2 circles with the same radius R=1. And the design objective is to find a minimal height of the rectangular design domain.

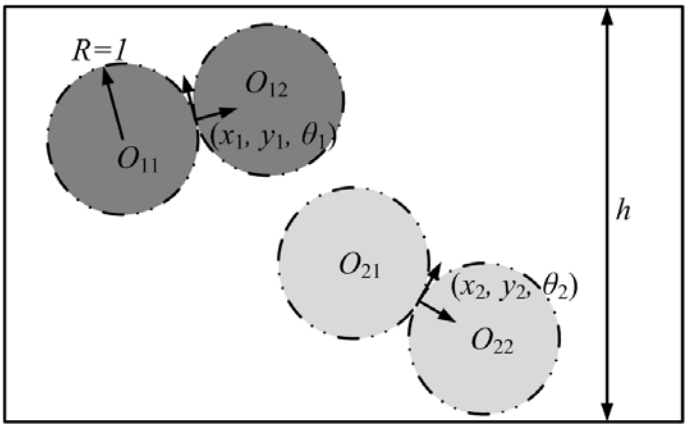

Figure 2.41: A simplified FCM packing problem

Here, the centers of the four circles are calculated as the functions of the locations and orientations of the components and the non-overlap constraints are formulated. For example,

$$\begin{aligned} x_{11} &= x_1 + R\cos\left(\theta_1 + 180^\circ\right) = x_1 - \cos\theta_1 \\ y_{11} &= y_1 + R\sin\left(\theta_1 + 180^\circ\right) = y_1 - \sin\theta_1 \\ &\vdots \end{aligned} \tag{2-16}$$

$$\begin{aligned} \left\|O_{11}O_{21}\right\|^2 &= \left(x_{11} - x_{21}\right)^2 + \left(y_{11} - y_{21}\right)^2 \\ &= \left(x_1 - \cos\theta_1 - x_2 + \cos\theta_2\right)^2 + \left(y_1 - \sin\theta_1 - y_2 + \sin\theta_2\right)^2 \\ &\geq 4 \\ &\vdots \end{aligned} \tag{2-17}$$

For simplicity, suppose only the 1st component is movable while the 2nd one is fixed. Consequently, (x_2, y_2, θ_2) are set to be (0, 0, 0) and the Hessian matrix of one of the constraint functions with respect to the design variables (x_1, y_1, θ_1) can be written as

$$\nabla^2\left(\left\|O_{11}O_{21}\right\|^2\right) = \begin{bmatrix} 2 & 0 & 2\sin\theta_1 \\ 0 & 2 & -2\cos\theta_1 \\ 2\sin\theta_1 & -2\cos\theta_1 & 2x_1\cos\theta_1 + 2y_1\sin\theta_1 + 2\cos\theta_1 \end{bmatrix} \tag{2-18}$$

This matrix is much more complex than that in Equation (2-15) due to the non-convex trigonometric functions. As (x_1, y_1, θ_1) is involved, it can be easily proved that the matrix is not always positive semi-definite. The situation will be even more complicated than those shown in Figure 2.40, which indicates that the constraint functions will lead to extremely non-convex problems and local minima may most likely take place.

We can also draw the 3D surface of the equation (2-17) with (x_2, y_2, θ_2) to be (0, 0, 0),

$$\begin{aligned}\left\|O_{11}O_{21}\right\|^2 &= \left(x_{11}-x_{21}\right)^2+\left(y_{11}-y_{21}\right)^2 \\ &= \left(x_1-\cos\theta_1+1\right)^2+\left(y_1-\sin\theta_1\right)^2 \\ &= \left[x_1-f_1(\theta_1)\right]^2+\left[y_1-f_2(\theta_1)\right]^2 \geq 4\end{aligned} \tag{2-19}$$

Note that the function has a form of circle with its center varying with θ_1 and radius equal to 2, and the surface is actually a pipe with circular cross sections. It is also found that

$$\left[f_1(\theta_1)+1\right]^2+f_2^2(\theta_1)=\cos^2\theta_1+\sin^2\theta_1=1 \tag{2-20}$$

which denotes that the centers of the cross sections compose a spiral going up with θ_1. As shown in Figure 2.42(a), a single constraint of Equation (2-19) is drawn. The constraint is satisfied only if (x_1, y_1, θ_1) are located outside the pipe.

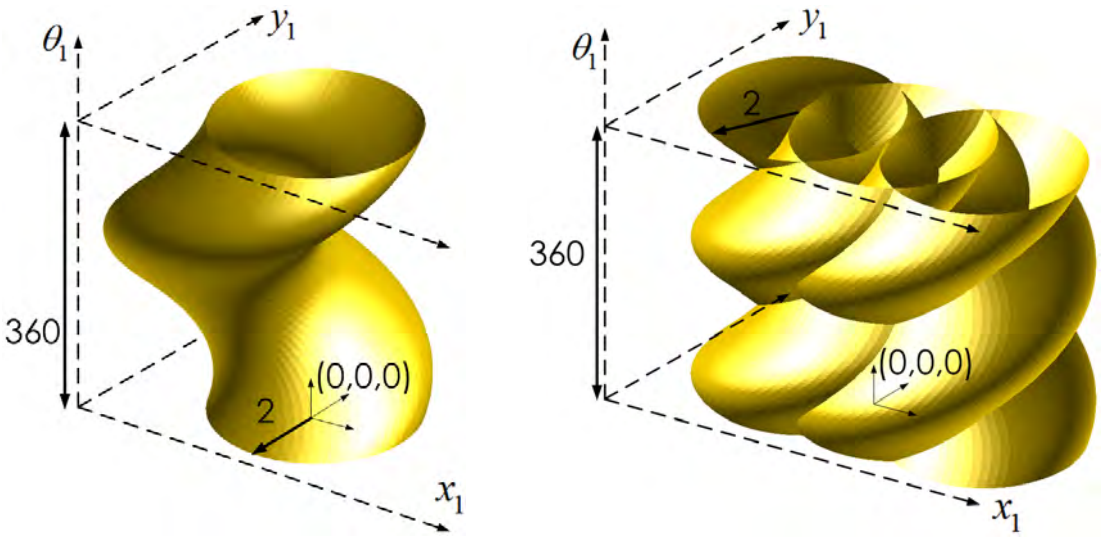

(a) A single distance constraint (b) Multiple distance constraints

Figure 2.42: Surfaces of distance constraints

Surfaces of all the 4 non-overlap constraints are put together in Figure 2.42(b). More complex details are found on the multiple surfaces which make the design space extremely non-convex. Design variables (x_1, y_1, θ_1) have to be located outside all of the surfaces to satisfy the 4 constrains, which makes the gradient based algorism easily fall into the local minimum.

Besides, it is also possible that the packing optimization problems have multiple solutions with identical values of objectives, which bring more difficulties in packing design. As shown in Figure 2.43, this is due to the symmetry or the local incompactness of the design domain. Maybe several or even infinite numbers of optimal solutions exist in the packing problems. These multiple solutions can be global minima local minima. Therefore, for most of the packing problems, it is not sure that the solution is globally optimal.

Furthermore, the number of the constraints will increase tremendously as more components and circum-circles are used. And the design space will be indescribably more complex. Incredible difficulties will be involved in gradient-based algorithms which are

not preferred in solving these problems. Until now no methods can guarantee global optima for packing problems. To make the gradient-based algorithms more applicable, more improvements have to be carried out and probably some ideas of the gradient free methods shall be implemented in a mixed way.

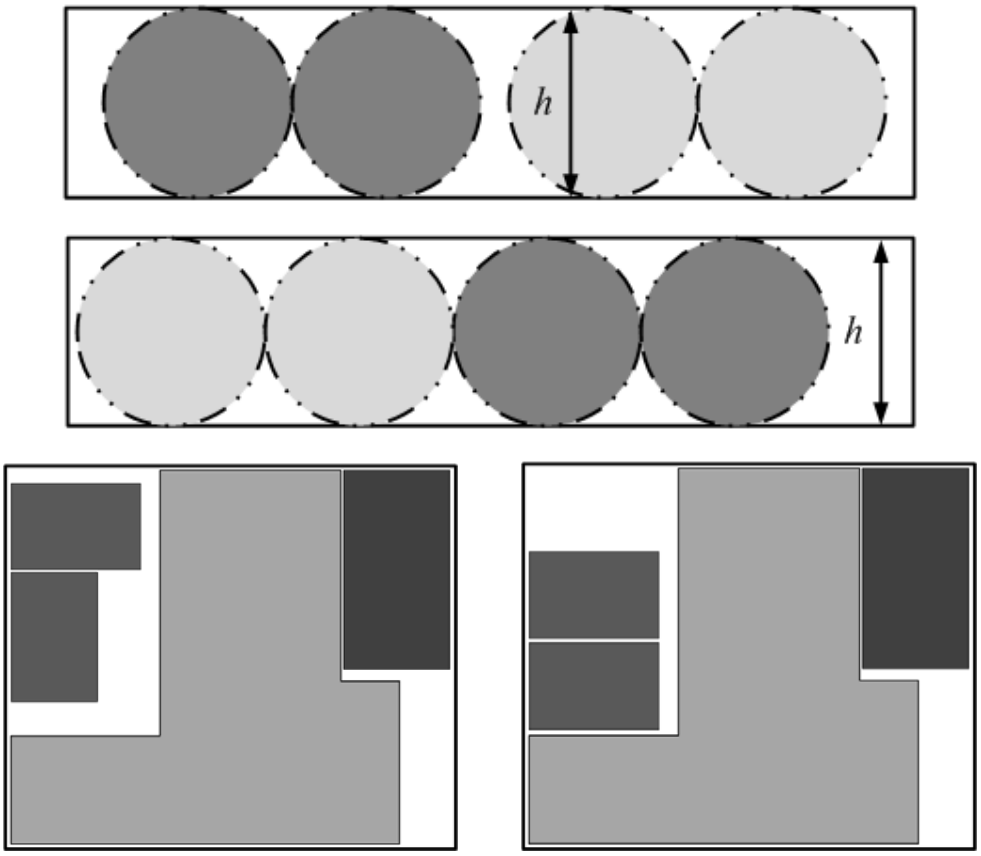

Figure 2.43: Multiple solutions for packing problems

As a result, the FCM technique of the current state is not effective in solving a pure compactness packing optimization. However, it was not developed for the pure packing optimization at the very beginning. In this work, its implementation with the gradient-based algorithms is a basic support technique to avoid the component overlap in the integrated layout design to be discussed in the following chapters.

2.5 Conclusion

The Finite-circle Method (FCM) is presented in this chapter. To generate an optimal packing solution, the overlap of the components shall be avoided. Because of the shape complexity of the components and design domain, many difficulties are involved in the definition and sensitivity analysis of geometrical constraints. Therefore, numbers of circles are used in FCM to approximate their contours and the constraints are now transformed into the distances limitations between the circles' centers. Meanwhile, some semi-heuristic rules are presented to find a better circum-circle approximation with fewer circles and better precision, which will improve the quality of the optimization and reduce the number of constraints. With the simplified design constraints, gradient-based algorithms are applied in some 2D and 3D packing design examples. Reasonable local

minimum are found with different design objectives.

However, the FCM is still a primary method suffering from the local minimum when the gradient-based algorithms are used. Therefore, improvements have to be carried out for practical packing problems.

Chapter 3

Integrated Packing and Topology Design

Overview

The components packing and structural topology are designed simultaneously in this chapter. By studying the standard minimal compliance topology design, the components are embedded into the design domain and the problems are solved as an integrated optimization. More techniques as density points and embedded meshing are proposed to avoid the conflictions involved in the simultaneous design.

Contents

3.1 Problem statement

The problem can be introduced with a practical example. As shown in Figure 3.1, the pylons on the wing are used to hang the turbine engine. Pipes, control mechanisms and some other devices are located inside the shrouds.

Figure 3.1: Pylon on the wing and the handed turbine engine (Airbus 380)

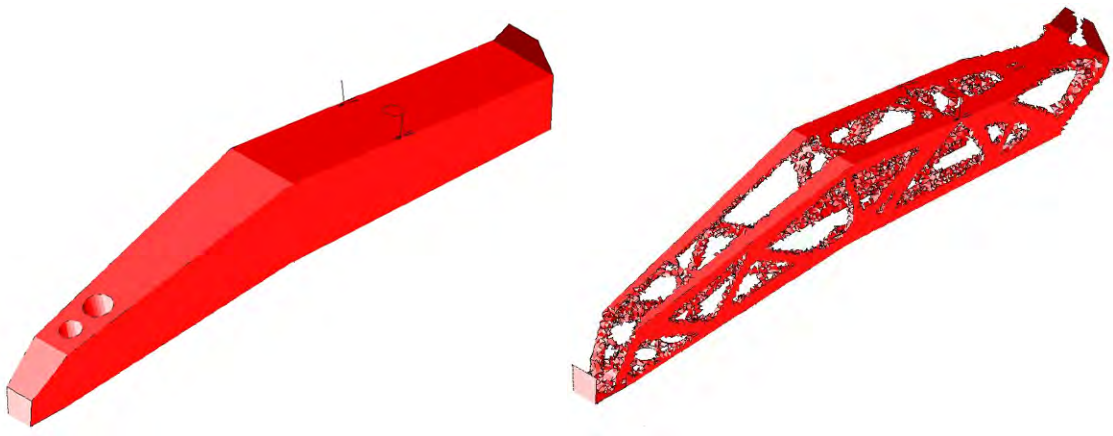

(a) (b)

Figure 3.2: Pylon model in Samcef Field™ and the topology optimization (Remouchamps et al. 2007)

A typical layout design of the pylon structure is carried out as follows. The global design domain is assigned firstly, which indicates the feasible design space for the structural layout, as shown in Figure 3.2(a). The design domain is then discretized into finite elements. The weight and thrust of the engine are assigned to the joint points as the external loads. The global structure is clamped at the fixation to the wing. As introduced in Chapter 1, the topology optimization results in a clear structure pattern (Remouchamps et al. 2007) with a proper set of 0/1pseudo-densities, as shown in Figure 3.2(b).

Suppose the equipments will be further arranged as numbers of components into the pylon

structure. In this packing design process, the location and orientation of the components are assigned as geometrical design variables. The final configuration is required to satisfy the geometrical and other functional requirements. Finally, structural supports and fixations of the components are designed in details.

The integrated packing and topology design is to put two steps together. In fact, the layouts of both the structure and the components can impact the mechanical performances of structural system significantly. Here, the mechanical properties of the pylon may be degraded when the equipment is assembled inside it. The structural patterns obtained by the topology optimization are probably not optimal any more.

The purpose of this section is to carry out the integrated layout design of the components and structures. As shown in Figure 3.3, a simplified pylon model is presented for illustration. A rectangle design domain is defined and meshed with finite elements. The loads and boundary conditions are assigned to the proper positions. Till now, a standard topology optimization problem is to minimize the global compliance.

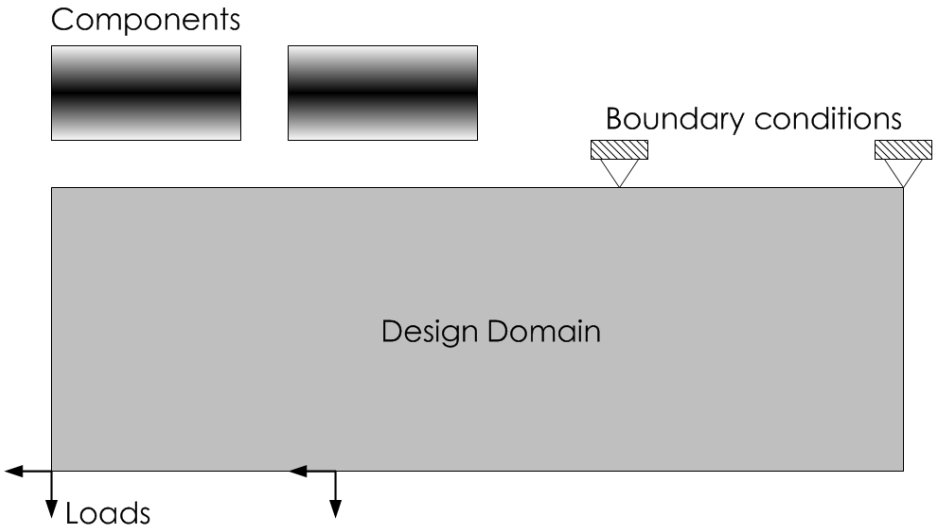

Figure 3.3: Problem illustration of the simplified pylon

Then, two rectangle devices, referred to as the components in this thesis, are involved in the integrated layout design. To carry out the packing design and the topology design simultaneously, the location and orientation of the components are assigned as the geometrical design variables while the pseudo-densities describing the material distribution are assigned as the density variables. Both kinds of variables can be expressed as

$$\begin{aligned} \text{find}: \quad & 0 < \eta_i \le 1,\ i = 1,2,...,n_d; \\ & (x_\varepsilon, y_\varepsilon, \theta_\varepsilon),\ \varepsilon = 1,2,...,n_c. \end{aligned} \tag{3-1}$$

where η_i is the pseudo-density variables describing a solid or a void finite element when it is 1 or 0 respectively. n_d is the number of density variables. Meanwhile, the minimization of the global compliance is set as the design objective function in this chapter. The design constrains which will limit the total cost of the material and avoid the geometrical overlap are included. The mathematical formulation can be written as

$$\begin{aligned} \min: \quad & C = \frac{1}{2} \boldsymbol{f}^T \boldsymbol{u} \\ \text{s.t.:} \quad & \text{Eq.(2-10);} \\ & V \le V^{(U)} \end{aligned} \tag{3-2}$$

where C is the strain energy calculated by the load vector $\boldsymbol{f}$ and the nodal displacement vector $\boldsymbol{u}$. V is the total volume of the material used for the supporting structure with a prescribed upper limit. To make sure all the components are located inside the design domain and no overlap is found during the optimization, the geometrical constraints defined by the FCM have to be satisfied.

If the above optimization problem is solved right now, it can be imagined that the two components will move inside the design domain to find proper positions and the supporting structure will be figured out with a clearer and clearer pattern as in a classical topology optimization. However, as seen below, the integrated layout design is much more sophisticated than a mathematical formulation. More difficulties are involved in the simultaneous design and more techniques have to be proposed.

3.2 Density points

In topology optimization, the material distribution is mostly described by pseudo-density variables related to the elements in the design domain. Based on the interpolation models of material properties, the distribution can be updated by modifying the density variables.

Like the SIMP method, the pseudo-densities are attributed to each finite element in the design domain and the finite element mesh is fixed during the iteration. Therefore, the number of the elements and the number of the pseudo-density variables are always kept identical.

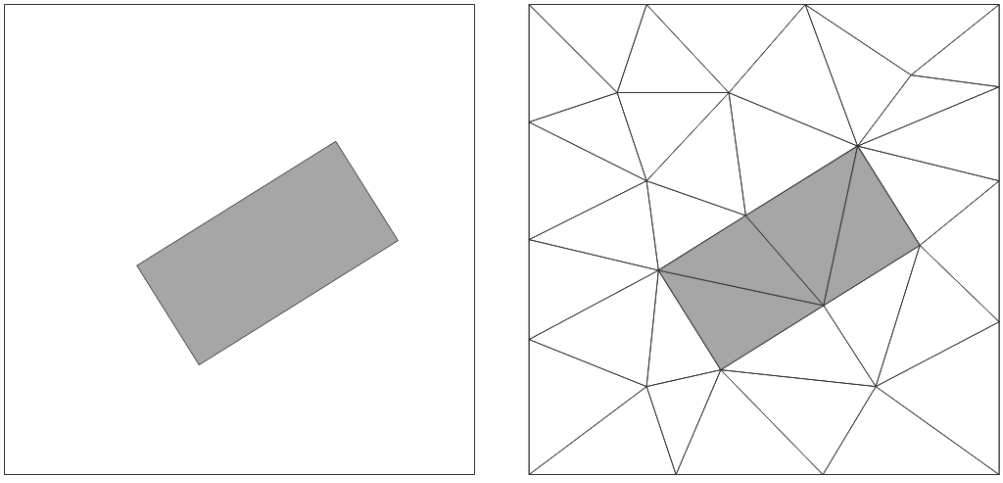

Figure 3.4: Element mesh embedding the components inside the design domain

However, in the integrated layout design, the first encountered problem is the confliction between the geometrical variables and the density variables. As shown in Figure 3.4, when the components are fully embedded in the design domain, the finite element mesh

shall be properly generated to join the components and structure together as a whole system.

Suppose an intermediate topology pattern is generated as shown in Figure 3.5. The black and white colors denote the solid and void material properties, respectively. The optimization is to update the geometrical variables and pseudo-densities simultaneously. The problem occurs when the locations and orientations of the components are changed during the iteration. A new finite element mesh has to be generated to make sure the components are still embedded and joint with the structure in the model. However, after the remeshing, the total element number may be changed. The pseudo-densities cannot find the previous corresponding elements. As a result, the structural material layout cannot be further updated.

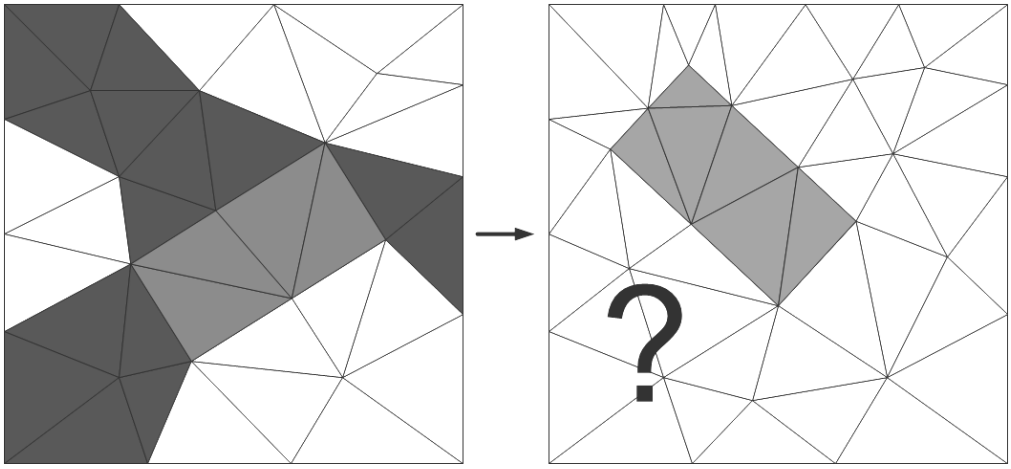

Figure 3.5: Layout updating with illustrative design patterns

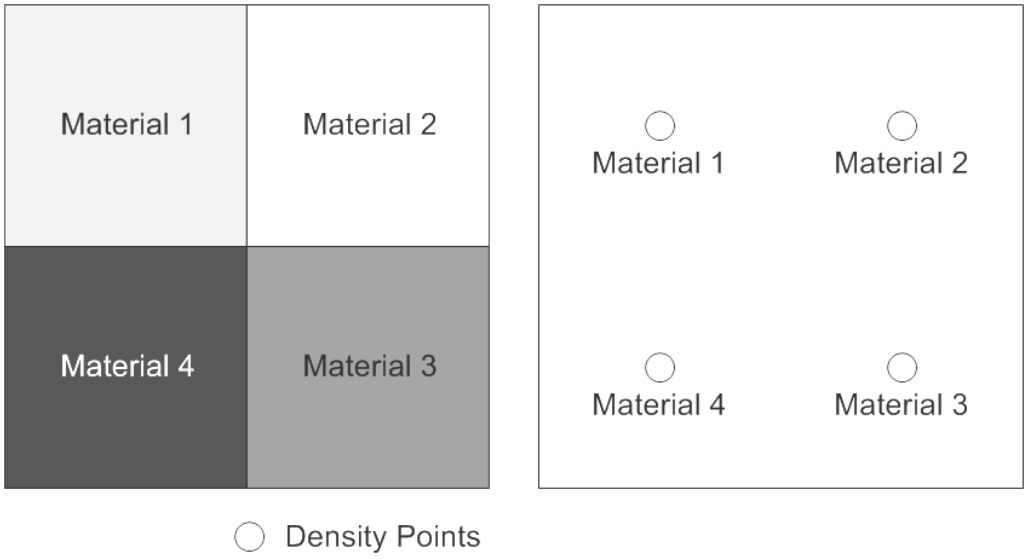

Figure 3.6: Definition of the density points

Accordingly, the method of density points is proposed here to solve this confliction. The idea is to relate the pseudo-densities with the location points rather than elements. To do this, some fixed points named density points are firstly defined in the design domain and

the pseudo-densities are then attributed to these points. The material properties will be, in turn, spread out from these points to the neighborhood elements.

The method is practically as follows. Firstly the density points are defined in the design domain to dominate the overall area. As shown in Figure 3.6, four density points are defined to describe the four material properties in this square area.

Later, the design domain is meshed with elements of proper sizes as shown in Figure 3.7. By calculating the distance between each density point and the centroids of the corresponding elements, each element will find the nearest density point and receive the information of the material properties. Note that several numbers of elements may share the same material property. The material layout is actually approximated by the density points if it is compared with the original one in Figure 3.6.

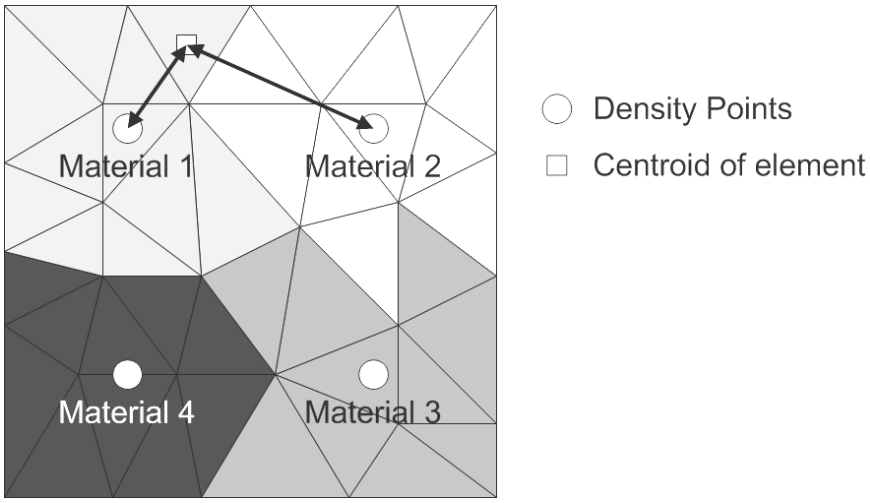

Figure 3.7: Material properties received from the density points

Several material layout patterns are shown in Figure 3.8, which are described with original fine element mesh and density points, respectively. The design domain is first meshed by 25×25 fine quadrangular elements with the size 0.04m×0.04m. The original material layout is shown in Figure 3.8(a). Later, the density points are defined according to the original layout as shown in Figure 3.8(b) while the design domain is meshed freely with triangular elements of two different sizes, respectively in Figure 3.8(c and d).

Globally, the density points can describe approximately the original layout with acceptable precision as shown in Figure 3.8(c and d). The precision of the material layout can be improved by refining the finite element mesh.

However, slight changes of the element mesh sometimes cause the variation of the material layout. As shown in Figure 3.9, a one-node connection is found in the original layout. But with the density points, the two solid parts are totally connected in one of the layouts while disconnected in the other one. This will cause incorrect calculations of the design sensitivities during the perturbation of geometrical variables. Although the refined mesh can be used to improve the precision, it costs much more computing time. As a result, the element mesh has to be further improved with some restriction.

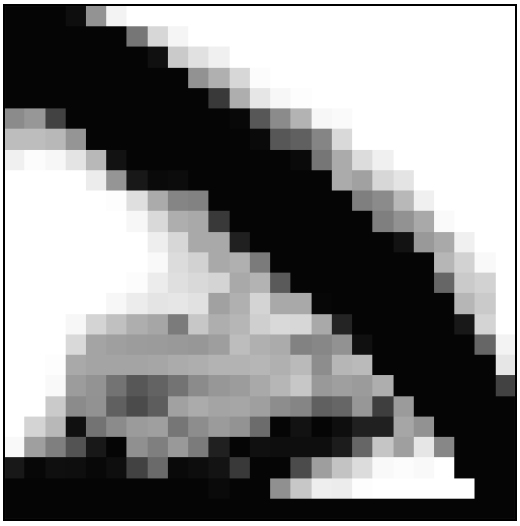

(a) Fine quadrangular mesh

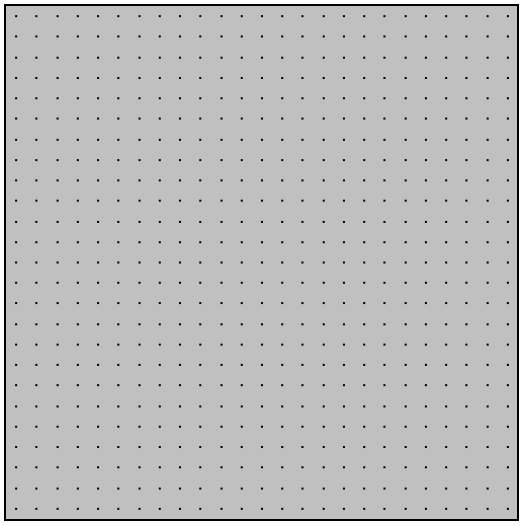

(b) Definition of density points

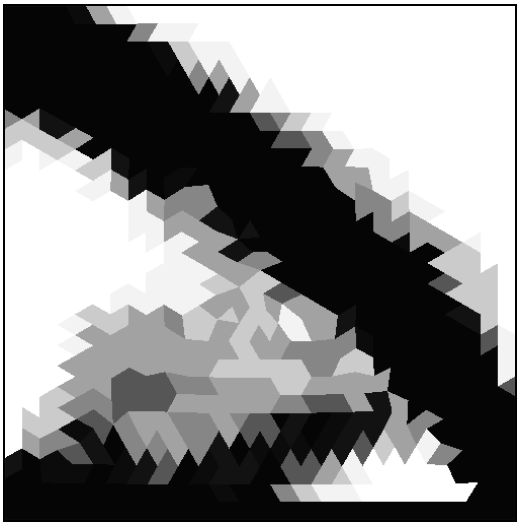

(c) Material layout with density points, element size 0.04m

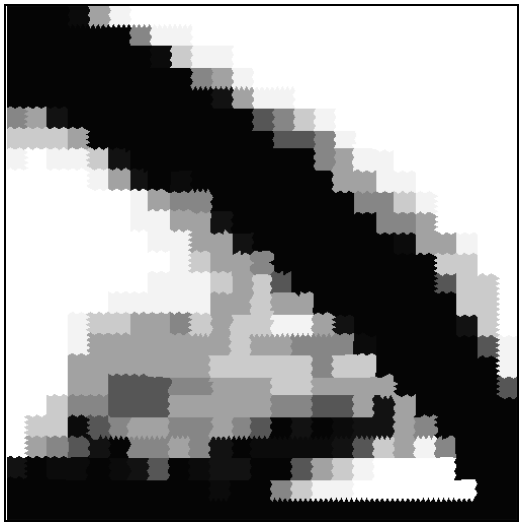

(d) Material layout with density points, element size 0.01m

Figure 3.8: Material layout description with density points

As shown in Figure 3.10, for a typical 2D problem, the finite element mesh is restricted inside numbers of small square areas corresponding to the density points and the original material layout. In this way, the material layout will be always identical with the one shown in Figure 3.6 regardless of the mesh. Clearly, the shape of the restricted areas depends on the problem. For a 3D problem, the elements dominated by a single density point will be restricted inside a small cube.

Obviously, the number of the elements used in the design domain has to be much larger than the number of the pseudo-density variables i.e. the number of the density points. If a fixed mesh of quadrangular elements is used, the method of density points will be identical with the ordinary topology optimization. The method of density points is thus effective to solve some special topology optimization problems with mesh variation like multi-component system design discussed in this thesis.

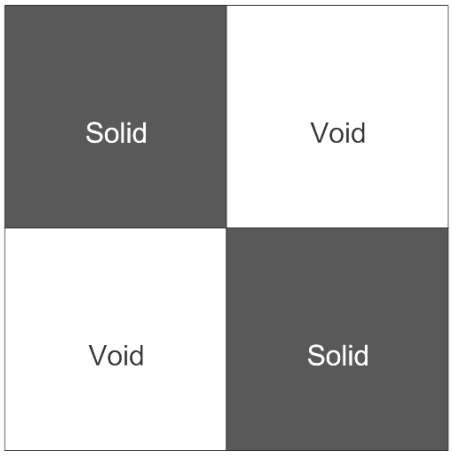

(a) Original material layout

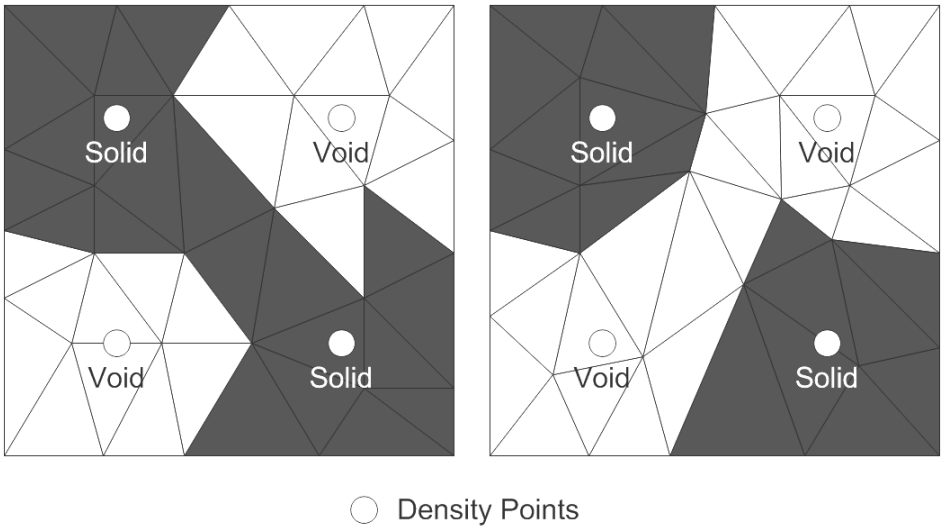

(b) Two different material layouts with the same density points

Figure 3.9: An incorrect material layout description with density points

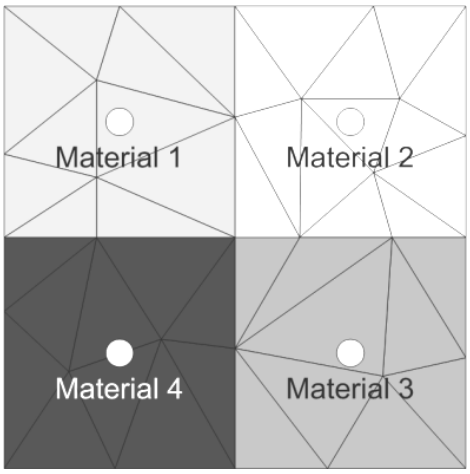

Figure 3.10: Material layout described by density points with mesh restriction

3.3 Embedded meshing

With the proposed technique of density points, the finite element mesh can be updated during the iteration of topology optimization. As shown in Figure 3.11, a structural system consisting of a square design domain and a rectangle component is meshed here. With the Boolean operation employed, the component is embedded in the design domain.

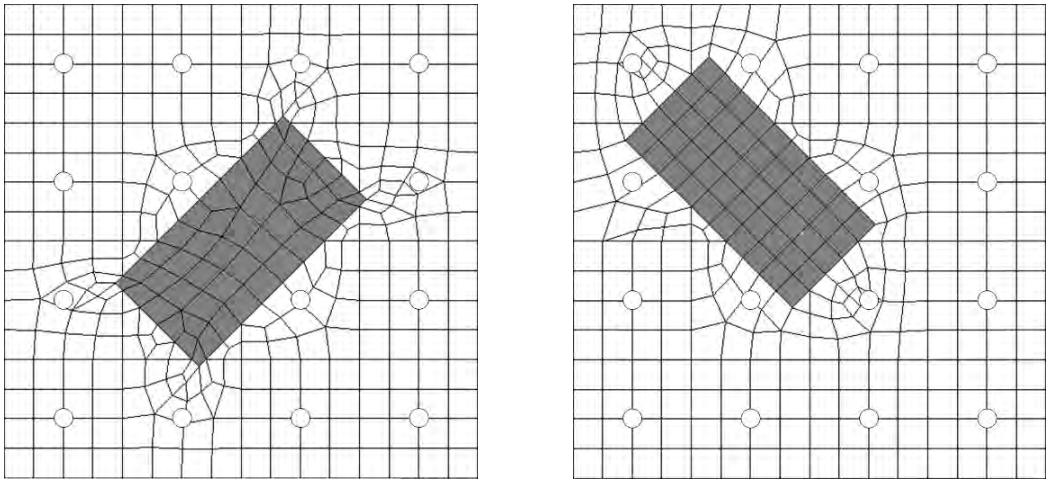

(a) The original element mesh (b) An updated element mesh

Figure 3.11: Element mesh with density points and restriction

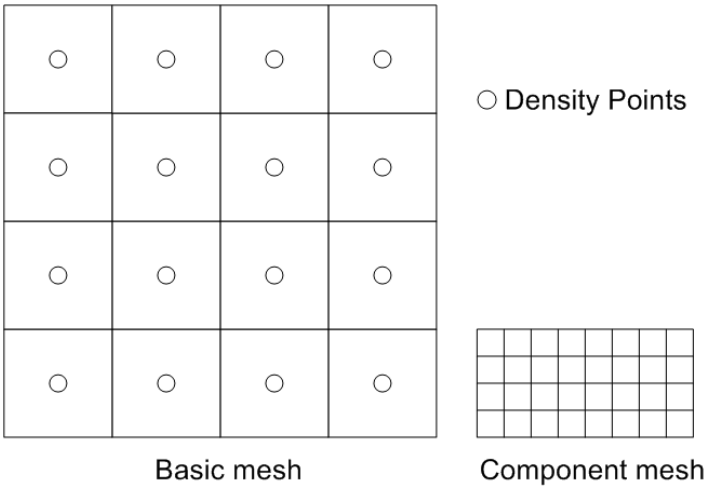

Figure 3.12: Basic mesh with density points and the component mesh

To ensure the element quality at the interconnection interface between the component and the surrounding structure, a proper element size control has to be specified, i.e. normally less than 1/4 of the distance between the adjacent density points. The domain is meshed as shown in Figure 3.11(a), where 336 elements are generated and restricted in the small squares. Later when the location and orientation of the component are updated, the same process of the Boolean operation and element mesh will be carried out, as shown in Figure 3.11(b), where 324 elements are included, 20 times more than the number of density points defining design variables.

The drawbacks of this kind of element mesh are however twofold. On the one hand, a

large quantity of elements will be generated in the finite element model. On the other hand, the whole system has to be remeshed along with the perturbations of the geometrical variables and the design iteration. Both of them will cost much more computing time and resources.

For this reason, the technique of embedded meshing is introduced to embed the components of designable locations and orientations in the design domain with fewer elements and easier mesh updating. As shown in Figure 3.12, similarly to the mesh restriction and the definition of the density points, the initial mesh of the design domain referred to as the basic mesh is firstly created by fine quadrangular elements. The components are also meshed with refined element size.

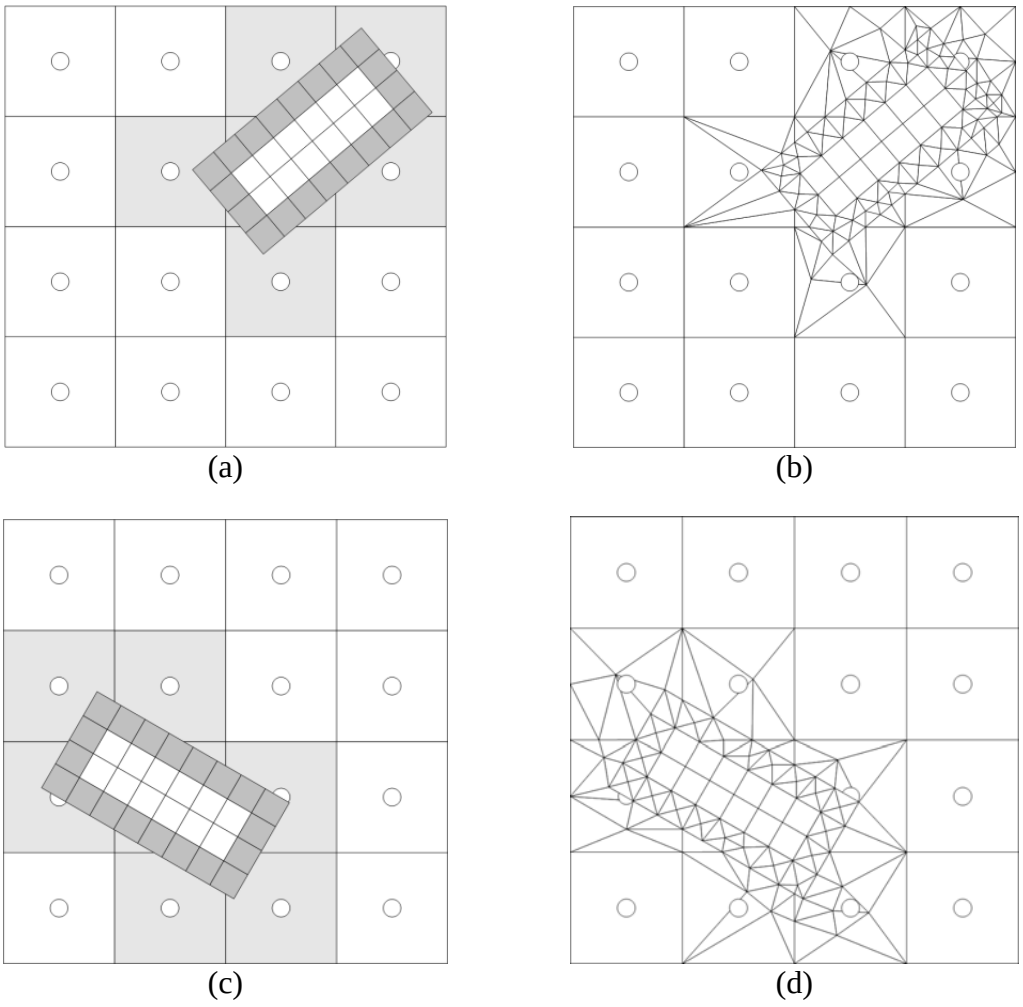

Figure 3.13: Process of embedded meshing

When the component is located in the design domain, as shown in Figure 3.13(a), Boolean operations have to be carried out in such a way that some elements of the basic mesh overlapping with the component, as indicated with gray color, will be refined locally to ensure the elements of the component are embedded in the design domain. And the modified elements belonging to the design domain will also be restricted in the small square elements of the basic mesh as shown in Figure 3.13(b). The modified elements are generated by the free mesh of ANSYS (ANSYS Release 9.0 Documentation) with refined element size. Material properties of these elements will still be dominated by the proper density points except those belonging to the components. In this way, only a few density

points that are located around the component have more than one dominated elements, which avoids using a large number of the elements to mesh the whole structural system. Furthermore, when the component changes its location and orientation as shown in Figure 3.13(c), the basic mesh is simply restored and only the Boolean operations and modification of the affected elements will be repeated at the new position, rather than remeshing the global system. The final element mesh is shown in Figure 3.13(d).

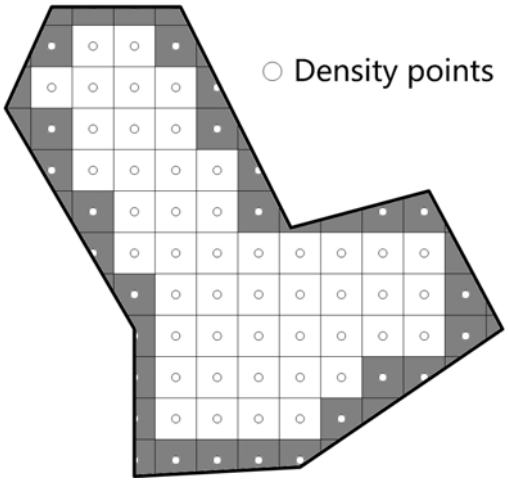

Figure 3.14: Basic mesh of an irregular design domain

According to our numerical tests, the embedded meshing reduces the number of the elements significantly and thus saves much computing time in mesh generation and FE analysis when large quantities of density points are defined in a topology optimization.

The basic mesh with fine quadrangular elements is easily conducted. Furthermore, only slight modifications have to be made for the irregular design domains. For example, the gray areas as shown in Figure 3.14 have to be refined to ensure the precision of the elements generated on the irregular boundaries. It should be noted that, the modified basic mesh still complies with the mesh restriction and remains unchanged during the optimization iteration.

3.4 Sensitivity analysis

The key to the application of gradient-based algorithms is the derivation of the design sensitivities with respect to the design variables. Here, sensitivity analysis consists of evaluating the gradient of the global strain energy with respect to the shape parameters of the components and the pseudo-density design variables.

For a static FE model, the static equation of the structure is

$$\boldsymbol{f} = \boldsymbol{K}\boldsymbol{u} \tag{3-3}$$

where $\boldsymbol{f}$ is the load vector. And the global strain energy is calculated as

$$C = \frac{1}{2}\boldsymbol{f}^T\boldsymbol{u} = \frac{1}{2}\boldsymbol{u}^T\boldsymbol{K}\boldsymbol{u} \tag{3-4}$$

3.4.1 Geometrical design variables

Suppose s_ε is one of the three geometrical parameters (x_ε, y_ε, θ_ε). Considering the complexities of the geometrical design variables related to the different shapes and finite element models, it is difficult to derive an analytical form of the sensitivities. As a result, the sensitivities of the global strain energy with respect to the geometrical design variables are calculated by finite difference

$$\frac{\partial C}{\partial s_\varepsilon} \approx \frac{\Delta C}{\Delta s_\varepsilon} \tag{3-5}$$

The perturbed step size of s_ε is chosen to be

$$\Delta s_\varepsilon = 10^{-5} \left| s_\varepsilon^{(U)} - s_\varepsilon^{(L)} \right| \tag{3-6}$$

where $s_\varepsilon^{(U)}$ and $s_\varepsilon^{(L)}$ are the upper and lower bounds of s_ε, respectively.

However, in some simple problems, the geometrical parameters (x_ε, y_ε, θ_ε) can be considered as special geometrical design variables in shape optimization. The gradients can be derived with a semi-analytical sensitivity form as presented by Zhang et al. (1995) to avoid the finite difference calculation.

The differentiation of the above equation with respect to s_ε leads to

$$\frac{\partial \boldsymbol{K}}{\partial s_\varepsilon}\boldsymbol{u} + \boldsymbol{K}\frac{\partial \boldsymbol{u}}{\partial s_\varepsilon} = 0 \tag{3-7}$$

While the derivative of the global strain energy with respect to s_ε can be put down as

$$\frac{\partial C}{\partial s_\varepsilon} = \frac{1}{2}\boldsymbol{f}^T\frac{\partial \boldsymbol{u}}{\partial s_\varepsilon} = \frac{1}{2}\boldsymbol{u}^T\boldsymbol{K}\frac{\partial \boldsymbol{u}}{\partial s_\varepsilon} = -\frac{1}{2}\boldsymbol{u}^T\frac{\partial \boldsymbol{K}}{\partial s_\varepsilon}\boldsymbol{u} \tag{3-8}$$

Here, the derivative of the global stiffness matrix is approximated by finite difference calculations.

$$\frac{\partial \boldsymbol{K}}{\partial s_\varepsilon} \approx \frac{\boldsymbol{K}^* - \boldsymbol{K}}{\Delta s_\varepsilon} \tag{3-9}$$

where $\boldsymbol{K}^*$ is the structural stiffness matrix after the perturbation. Therefore, the final semi-analytical shape sensitivity scheme can be written as

$$\frac{\partial C}{\partial s_\varepsilon} \approx -\frac{1}{2}\boldsymbol{u}^T\frac{\boldsymbol{K}^* - \boldsymbol{K}}{\Delta s_\varepsilon}\boldsymbol{u} = -\frac{\boldsymbol{u}^T\boldsymbol{K}^*\boldsymbol{u} - 2C}{2\Delta s_\varepsilon} \tag{3-10}$$

In this method, the stiffness matrices $\boldsymbol{K}^*$ and $\boldsymbol{K}$ are in the same order. This implies that both the number of degrees of freedom and the mesh topology of the structural system are unchangeable after the perturbation.

Similarly to the shape optimization as well, the requirement of identical number of

degrees of freedom can be satisfied by implementing the perturbation of the geometrical parameters as the slight movement of the related nodes in the model, i.e. the Morphing technique. The global mesh remains unchanged. However, the movements of the components are much more complex than the contour perturbations in the standard shape optimization. The material layout described by the pseudo-densities shall not be affected by the shape perturbation, which makes the modification of the nodal positions strictly limited in the affected areas i.e. the gray area in Figure 3.13. Although the perturbation of the stiffness matrix avoids the finite difference calculation and saves the computing time significantly, it brings more complexity into the modeling of the embedded meshing. Much effort is needed in this study.

3.4.2 Pseudo-density variables

Sensitivities with respect to the pseudo-density variables which are now defined at the density points are derived analytically. Suppose η_i is the pseudo-density at the *i*th density point, which dominates a number of surrounding elements at the neighborhood. The elastic modulus and the element stiffness matrix attached to η_i can be written as

$$E_{ij} = P(\eta_i)E_{ij0} = \eta_i^p E_{ij0} \tag{3-11}$$

$$\boldsymbol{K}_{ij} = P(\eta_i)\boldsymbol{K}_{ij0} = \eta_i^p \boldsymbol{K}_{ij0} \tag{3-12}$$

where $j \in \left\{(1,2,...,n_{e1}),(n_{e1}+1,...,n_{e2}),...,(n_{e(i-1)}+1,...,n_{ei})...\right\}$, $n_{e0}=0$, $i=1,2,...n_d$ identify each element of the supporting structure. *p* is the penalty factor set to be 3 in this thesis. E_{ij} and $\boldsymbol{K}_{ij}$ are the elastic modulus and stiffness matrix of the *j*th element dominated by the *i*th density point, while $\boldsymbol{K}_{ij0}$ and E_{ij0} are the stiffness matrix and elastic modulus when it is solid.

Likewise, the sensitivity is also formulated by differentiating the static equation.

$$\frac{\partial \boldsymbol{K}}{\partial \eta_i}\boldsymbol{u} + \boldsymbol{K}\frac{\partial \boldsymbol{u}}{\partial \eta_i} = 0 \tag{3-13}$$

The derivative of the strain energy can be expressed as

$$\frac{\partial C}{\partial \eta_i} = \frac{1}{2}\boldsymbol{f}^T\frac{\partial \boldsymbol{u}}{\partial \eta_i} = \frac{1}{2}\boldsymbol{u}^T\boldsymbol{K}\frac{\partial \boldsymbol{u}}{\partial \eta_i} = -\frac{1}{2}\boldsymbol{u}^T\frac{\partial \boldsymbol{K}}{\partial \eta_i}\boldsymbol{u} \tag{3-14}$$

Bacause only the stiffness matrices of the elements dominated by the *i*th density point are related to η_i, this equation can be further developed as

$$\begin{aligned}\frac{\partial C}{\partial \eta_i} &= -\frac{1}{2}\boldsymbol{u}^T\frac{\partial\left(\sum_{j=n_{e(i-1)}+1}^{n_{ei}}\boldsymbol{K}_{ij}\right)}{\partial \eta_i}\boldsymbol{u} = -\frac{1}{2}\boldsymbol{u}^T\frac{\partial\sum_{j=n_{e(i-1)}+1}^{n_{ei}}\eta_i^p\boldsymbol{K}_{ij0}}{\partial \eta_i}\boldsymbol{u} \\ &= -\frac{p}{2}\boldsymbol{u}^T\frac{\sum_{j=n_{e(i-1)}+1}^{n_{ei}}\boldsymbol{K}_{ij}}{\eta_i}\boldsymbol{u} = -\frac{p}{\eta_i}\sum_{j=n_{e(i-1)}+1}^{n_{ei}}C_{ij}\end{aligned} \tag{3-15}$$

where C_{ij} is the strain energy of the jth element dominated by the ith density point.

Meanwhile, the technique of mesh-independency filter (see Sigmund and Petersson 1998) is applied here to avoid the checkerboard problem. But the filter is carried out with respect to the density points rather than the elements in the following way.

The sensitivities obtained are modified with the weighted average of the neighborhood density points.

$$\left(\frac{\partial C}{\partial \eta_i}\right)^* = \frac{\sum_l \left\{ \eta_l \left[r_{\min} - \mathrm{dis}(l,i) \right] \frac{\partial C}{\partial \eta_l} \right\}}{\eta_i \sum_l \left[r_{\min} - \mathrm{dis}(l,i) \right]} \tag{3-16}$$

$$\eta_l \in \left\{ \eta_l \middle| \mathrm{dis}(l,i) \le r_{\min} \right\} \tag{3-17}$$

where dis(l,i) indicates the distance between the lth and ith density points. All the density points located within the predefined distance $r_{\min}$ are accounted in the filter scheme.

However, the filter on the sensitivities is not appropriate for the current searching strategies because the modified sensitivities do not completely correspond to the objective function, which may lead to some divergence problems. As a result, further developments are made on the density filter by Bruns and Tortorelli (2001) and Bourdin (2001). The modifications are directly implemented on the updated design variables. More descriptions and improvements on the topic of density filter can be found in the works of Wang and Wang (2005), Sigmund (2006), Sigmund (2007) and Lemaire et al. (2007). But this is not the problem mainly concerned in this thesis. As we are using the sensitivity filter technique, the convergence difficulties are only reported in a few tested examples in Chapter 6.

3.5 Iteration control

3.5.1 Problem modeling

Now, the proposed density points and embedded meshing techniques are programmed and integrated in the software platform to perform the packing and the topology design simultaneously. Take the simplified pylon shown at the beginning of this chapter as an example. The geometrical model shown in Figure 3.15 is composed of numbers of circum-circles approximating the components and the design domain. Only the geometrical design variables i.e. the locations and orientations of the components are imported in the model to compute all the geometry constraints.

The finite element model is the second model used to calculate the mechanical and physical responses, e.g. the strain energy, natural frequencies, position of the gravity center, moment of inertia with respect to a prescribed axis etc. The meshed components and design domain with the applied loads and boundary conditions will be properly modeled. All the pseudo-densities and geometrical variables have to be imported by using the techniques of density points and the embedded meshing to describe the layout of structure and the components, as shown in Figure 3.16.

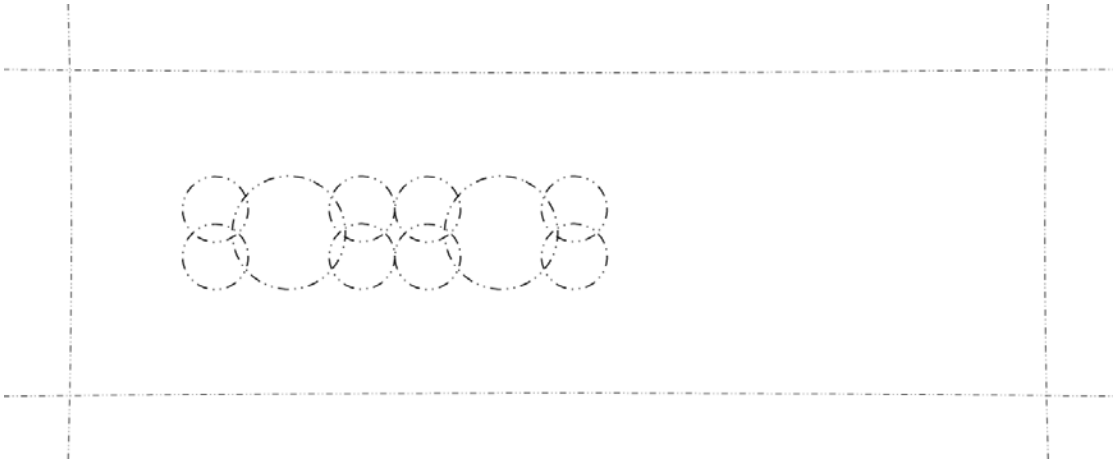

Figure 3.15: Geometrical model of the pylon

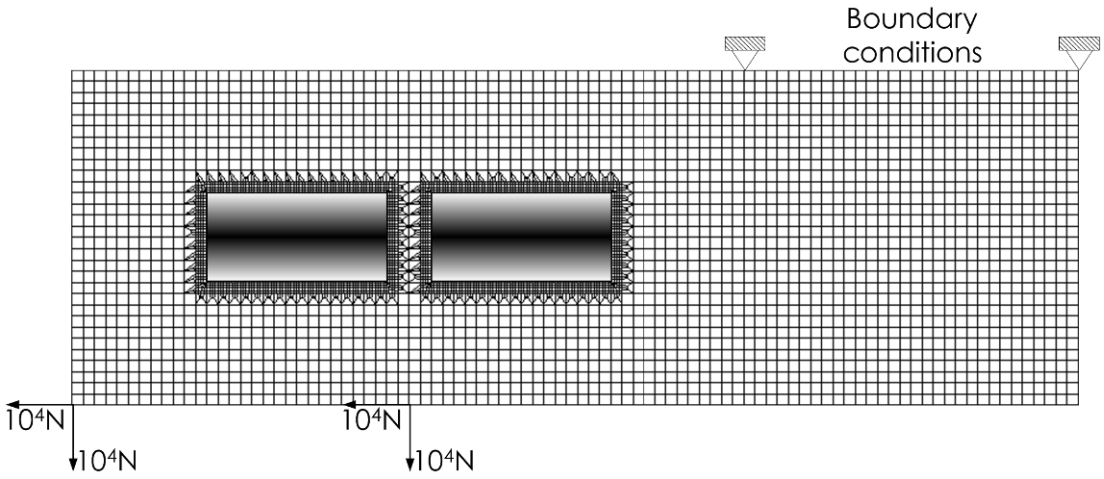

Figure 3.16: Finite element model of the pylon

3.5.2 Software platform

The global analysis and optimization processes are programmed within the platform of ANSYS™ (ANSYS Inc) and Boss-Quattro™ (Samtech Inc), as shown in the flowchart of Figure 3.17. Although the programming is essential and time-consuming, this thesis will be focused on the methods developed for the integrated layout design. Only a brief description of the software and programming is presented here.

The modeling, solving and post-processing are mostly programmed using the ANSYS command lines and the language APDL (ANSYS Parametric Design Language). APDL is a scripting language that enables the batch execution of the finite element analysis by automating common tasks of the model built in terms of parameters. Since APDL encompasses a wide range of other features such as repeating a command, macros, if-then-else branching, do-loops, scalar, vector and matrix operations and text file processing etc, it provides more flexibilities and conveniences in complex system modeling and analysis. However, the command line and the APDL are inefficient for scientific computing. Some tasks, e.g. the sensitivity filtering, are programmed alternatively and compiled in the language C++. Furthermore, the data exchanging between different executions is realized by writing and reading ASCI files or binary files.

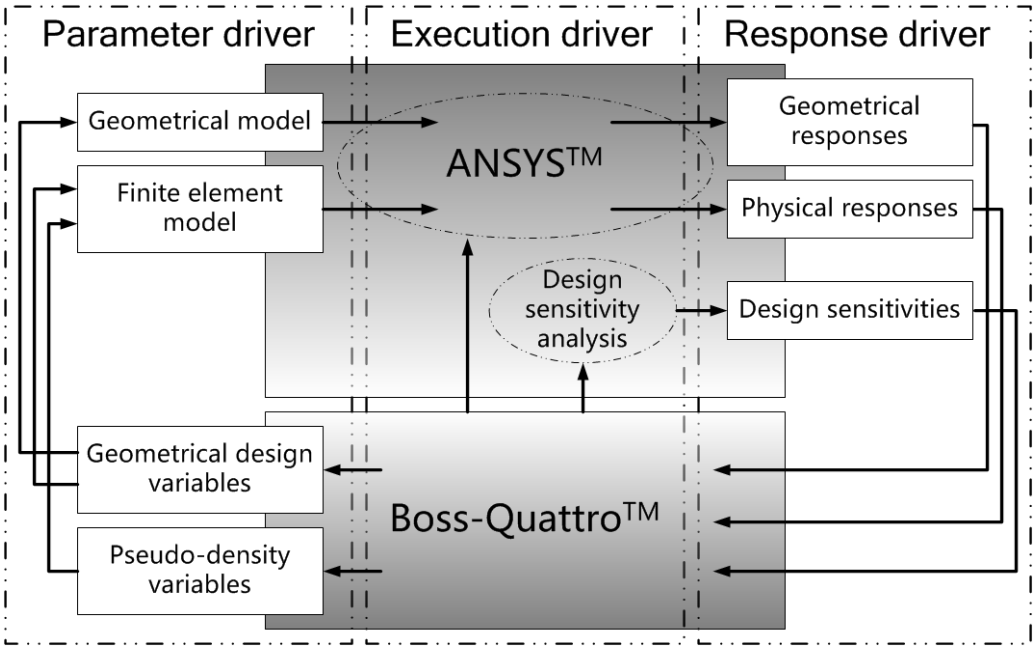

Figure 3.17: Flowchart and platform of the integrated layout optimization

Boss-Quattro is an open optimization platform that works with executable analysis. Normally, the analysis procedure will be run automatically in batch by inputting a parametric model and then results or responses yield. As described in the documentation of Boss-Quattro 5.0, Boss-Quattro can be viewed as an application manager: it builds and runs chains of tasks involving different applications, and collects results automatically. Actually, more utilities are offered. Besides some available interfaces for the parameter and result files with MSC-Nastran™, Samcef™ etc, it is easy to integrate external programs by programming user's customized scripts. Furthermore, the neutral form of the parameters' definition, results and sensitivities list makes it possible to realize the deep customization of external software without further development of interface.

To have a full control of the iteration, three interfaces connecting Boss-Quattro and ANSYS are built, i.e. the parameter driver, execution driver and the response driver.

The parameter driver is dedicated to read and edit the definition of design variables at the beginning of the optimization. The initial value, lower and upper bounds of the design variables are introduced here with a prescribed form which can be recognized by both Boss-Quattro and ANSYS.

The two models, i.e. the geometrical model and the finite element model are sent to ANSYS and the calculations are carried out respectively within the control of the execution driver. The first analysis is to generate the responses that will be defined later as the objective function and constraints by the response driver. Meanwhile, the analytical sensitivities with respect to the pseudo-density design variables are calculated within the first analysis. Later, the finite difference is carried out to obtain the sensitivities with respect to the geometrical design variables, as shown in the flowchart of the execution diver in Figure 3.18.

When the objective function and constraints are defined, all the values of the responses and the corresponding sensitivities are asked to be output in a specified form which will

be received by Boss-Quattro. According to these data, values of design variables will be updated and transferred to the parameter driver to modify the two design models.

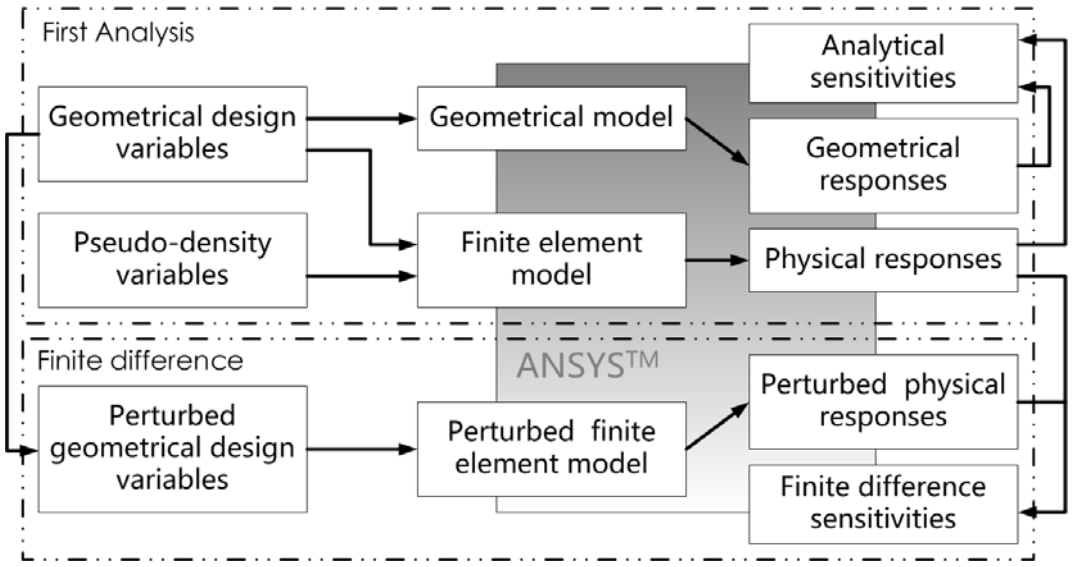

Figure 3.18: Flowchart of the execution diver

Finally, the optimization process will stop if the selected convergences test is satisfied. In Boss-Quattro, three convergence tests are provided, i.e.

1) On the variation of design variables. The process will stop if the maximum variation of all design variables is less than the prescribed precision;

2) On the variation of objective function. The process will stop if the maximum variation of the objective function is less than the prescribed precision;

3) Find admissible point. The process will stop when all constraints are satisfied.

For all the examples shown in this thesis, the convergence tests on objective variation and variable variation are applied simultaneously with the convergence precision to be 0.1%.

3.5.3 Note on the optimization algorithms

To choose a proper optimization algorithm for the integrated layout design, several popular algorithms are evaluated in this section.

In fact, most of the functions e.g. the strain energy, natural frequencies etc involved in the optimization are neither linear non explicit with respect to the design variables. Only the values and sometimes the derivatives of the responses are available at the current design point. Therefore, it is necessary to build approximated expressions of explicit form, e.g. the Taylor expansion, for the gradient based algorithms. The general strategy is to expand the objective function and the constraint functions approximately with the current values of the functions and their derivatives obtained. Then, a series of sub-problems are solved iteratively to find the next design point until the convergence is reached.

Conlin (See Fleury and Braibant 1986, Fleury 1989) is a first order method based on the convex linearization. The approximation of a given function $g(\boldsymbol{x})$ can be expressed as

$$\begin{aligned}
&\boldsymbol{x} = \left[x_1, x_2, ..., x_n \right]^T \\
&g\left(\boldsymbol{x}\right) \approx g\left(\boldsymbol{x}^{(k)}\right) + \sum_i p_i^{(k)} \left(x_i - x_i^{(k)} \right) - \sum_i q_i^{(k)} \left(\frac{1}{x_i} - \frac{1}{x_i^{(k)}} \right) \\
&\text{if } \frac{\partial g}{\partial x_i}|_{\boldsymbol{x}^{(k)}} > 0,\ p_i = \frac{\partial g}{\partial x_i},\ q_i = 0 \\
&\text{if } \frac{\partial g}{\partial x_i}|_{\boldsymbol{x}^{(k)}} < 0,\ p_i = 0,\ q_i = \frac{\partial g}{\partial x_i}\left(x_i^{(k)}\right)^2
\end{aligned} \tag{3-18}$$

where $\boldsymbol{x}^{(k)}$ is the current design point at the kth iteration. The terms of direct linearization or inverse linearization are used when the gradient is positive or negative respectively. By evaluating the second order derivatives, it can be easily demonstrated that the approximated function is always convex and conservative compared with the direct linearization.

Conlin is suitable to sizing optimization and standard topology optimization minimizing the structural compliance because the design functions are monotonous. However, for non-monotonous functions, the oscillation may occur iteratively. As a result, unconstrained problems cannot be solved by Conlin.

Another monotonous approximation is the standard MMA (Method of Moving Asymptotes, see Svanberg 1987) inspired by Conlin. The approximation function is expressed as

$$\begin{aligned}
&\boldsymbol{x} = \left[x_1, x_2, ..., x_n \right]^T \\
&g\left(\boldsymbol{x}\right) \approx g\left(\boldsymbol{x}^{(k)}\right) + \sum_i p_i^{(k)} \left(\frac{1}{u_i^{(k)} - x_i} - \frac{1}{u_i^{(k)} - x_i^{(k)}} \right) \\
&\qquad + \sum_i q_i^{(k)} \left(\frac{1}{x_i - l_i^{(k)}} - \frac{1}{x_i^{(k)} - l_i^{(k)}} \right) \\
&\text{if } \frac{\partial g}{\partial x_i}|_{\boldsymbol{x}^{(k)}} > 0,\ q_i = 0 \\
&\text{if } \frac{\partial g}{\partial x_i}|_{\boldsymbol{x}^{(k)}} < 0,\ p_i = 0
\end{aligned} \tag{3-19}$$

where the parameters $p_i^{(k)}$ and $q_i^{(k)}$ are determined by the first order derivatives as in Conlin. $u_i^{(k)}$ and $l_i^{(k)}$ indicate the upper and lower asymptotes, respectively. They are introduced to further ensure the convexity of the approximation functions. Obviously, under the assumption of l_i=0 and u_i to ∞, MMA is reduced to the convex linearization scheme.

In addition, a move-limit strategy proposed by Svanberg (1987) is needed to restrict the variation range of the design variables during the optimization process. Similarly to Conlin, MMA is widely used in topology optimization problems.

As shown above, the same asymptotes are used for different functions in MMA. In fact, each function may have its own proper moving asymptotes u_i and l_i with respect to each design variable x_i. A modified version named GMMA (Generalized Method of Moving Asymptotes, See Zhang et al. 1996) was developed. The GMMA proved to be more flexible.

The SQP (Sequential Quadratic Programming) (see Nocedal and Wright 1999) is a basic second order* algorithm that builds up each subproblem using the Hessian matrix of the Lagrangian function and linear approximations of the constraints. This yields a sequence of QP (Quadratic Programming) problems that are solved iteratively until the convergence.

With a proper definition of the subproblem, SQP can be viewed as an extension of the Newton method. Both share some common characteristics, i.e. rapid convergence when the iteration is near the final solution but the iteration may be erroneous when it is far from the solution. Moreover, the initial design does not have to be necessarily feasible.

Since the first order derivative of the quadratic approximation may be negative or positive with respect to the design variables, non-monotonous problems e.g. some shape optimization problems may be well dealt with.

MDQA (Method of Diagonal Quadratic Approximations, see Zhang and Fleury 1997) is another algorithm in which the diagonal terms of the Hessian matrix i.e. the second order derivatives are approximated using the preceding iteration result. With the curvature of the functions obtained, the approximations of the functions are generally better. This benefits the optimization iteration when it is near the final solution.

The global convergent version of MMA (GCMMA) is further proposed by Svanberg (1995). More discussions on this method can be found in Bruyneel et al (2002), Svanberg (2007). Each function can be approximately expressed as

$$\begin{aligned} &\boldsymbol{x} = \left[x_1, x_2, ..., x_n \right]^T \\ &g\left(\boldsymbol{x}\right) \approx g\left(\boldsymbol{x}^{(k)}\right) + \sum_i p_i^{(k)} \left(\frac{1}{u_i^{(k)} - x_i} - \frac{1}{u_i^{(k)} - x_i^{(k)}} \right) \\ &\qquad + \sum_i q_i^{(k)} \left(\frac{1}{x_i - l_i^{(k)}} - \frac{1}{x_i^{(k)} - l_i^{(k)}} \right) \end{aligned} \tag{3-20}$$

Although the approximation function looks like the standard MMA and GMMA, both of the asymptotes are always strictly positive. Both the parameters $p_i^{(k)}$ and $q_i^{(k)}$ are computed based on the first-order derivatives, the asymptotes $u_i^{(k)}$ and $l_i^{(k)}$ and another non-monotonic factor $\rho^{(k)}$ which will is updated on the basis of a rule proposed by Svanberg (1995) to ensure the globally convergent character of the approximation. Therefore, the approximation functions of GCMMA are now non-monotonous.

The benefits of GCMMA are obvious. It inherits the property of stability from the family of MMA and the non-monotonous approximation is helpful in solving some optimization

* The so-called "second order" here is an engineering concept. The diagonal terms of the Hessian matrix are not directly obtained by computing the second order derivatives but approximated based on the information from the precedent iteration (See Boss-Quattro Documentation, Samtech).

problems with non-monotonous functions.

As the component layout will be designed simultaneously with the structural topology, the problem with movable components inside the design domain is similar to a shape optimization design. Non-monotonous approximations have to be used to generate reasonable component layout.

Furthermore, it should be mentioned that the comparison between the algorithms with non-monotonous approximation has shown the iteration stabilities are in conflict with the convergence speed. As indicated by Samtech who has plenty of experience in testing these algorithms, a rough rule is: the GCMMA holds more stability in finding the final solution than SQP that is, in turn, more stable than MDQA. But if all of them can find a solution, MDQA is faster than SQP that is, in turn faster than GCMMA (See Radovcic and Remouchamps 2002 and Boss-Quattro Documentation, Samtech).

As a result, considering the characteristics of the integrated layout design and ignoring the drawback of slow convergence, GCMMA is generally used in solving the examples in this thesis.

3.6 Numerical examples

Several examples are presented here to illustrate the integrated layout optimization. As the first step into the multi-component system design, the global strain energy is chosen as the design objective like the simplest standard topology optimization.

3.6.1 Simplified pylon

As shown in Figure 3.3, the basic mesh of the design domain (0.6m×1.8m) is discretized with 30×90 quadrangular elements. The size of the components is 0.16m×0.32m.

The material properties of the supporting structures are set to be:

elastic modulus, $E_0=7\times10^{10}$pa, density $\rho_0=2700$kg/m^3 and Poisson's ratio $v=0.3$.

And the material properties for the components are:

elastic modulus, $E_0=2\times10^{11}$pa, density $\rho_0=7800$kg/m^3 and Poisson's ratio $v=0.3$.

A standard topology optimization without components is firstly solved with classic SIMP method to obtain a first impression of the structural layout.

The volume fraction is prescribed as 50% of the total material cost. The checkerboard problem is avoided by applying the sensitivity filter by Sigmund (1998). After 32 iterations, the optimization converges quickly. The final structural pattern and the convergence history of the objective function are shown in Figure 3.19.

Later, the components are put back into the design domain. The integrated layout optimization starts from the initial design as shown in Figures 3.15 and 3.16, where the components are firstly located horizontally in the design domain. Five circles are used to approximate each of them.

The global strain energy is chosen as the design objective as well. 50% of the total

material cost is used for the supporting structure. The iteration history of the structural and components layout is shown in Figure 3.20.

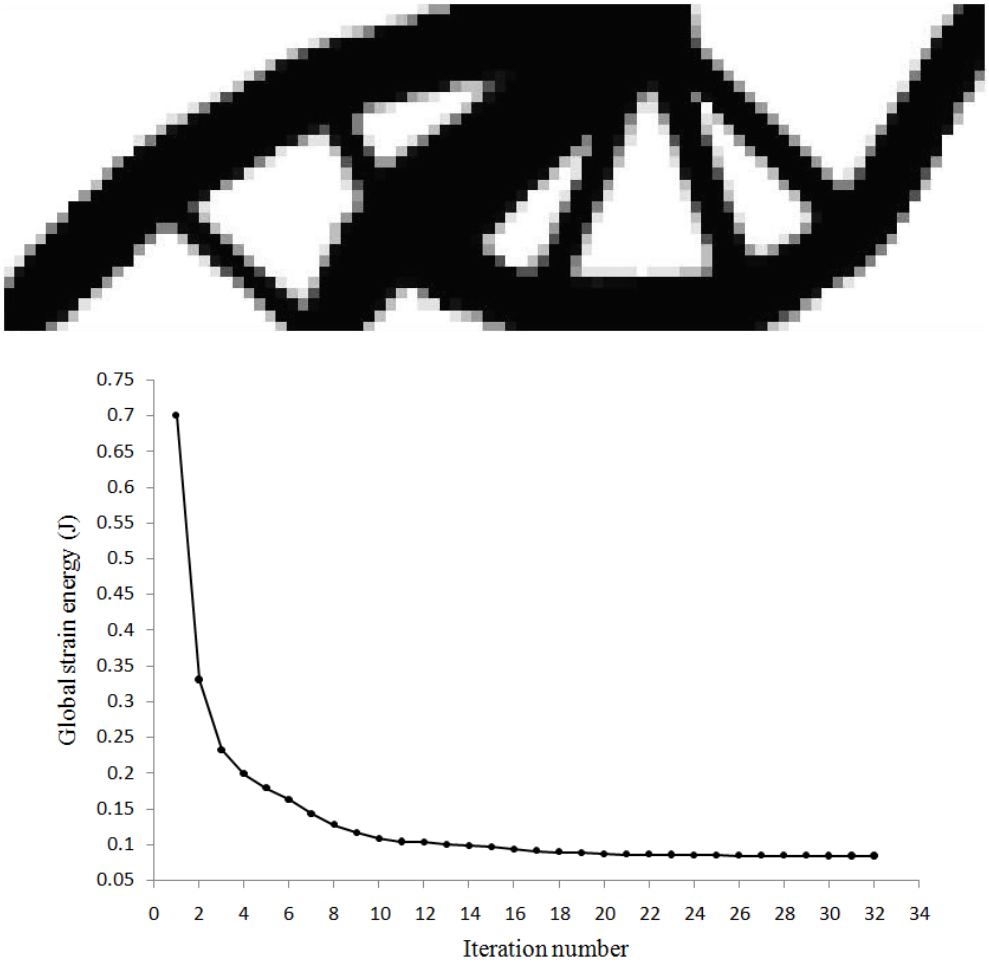

Figure 3.19: A standard topology design without components and the convergence history

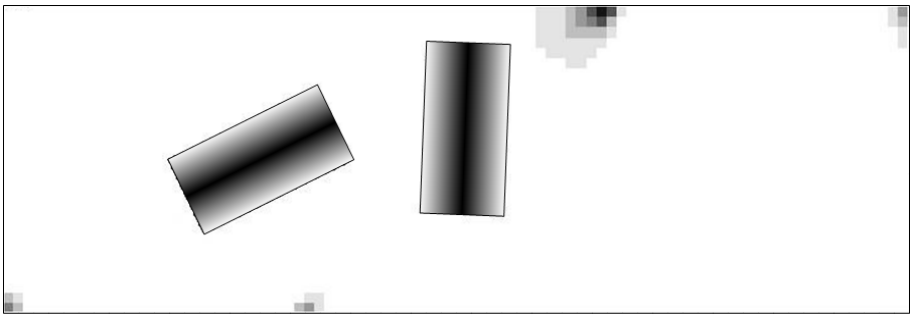

(a) 5th iteration

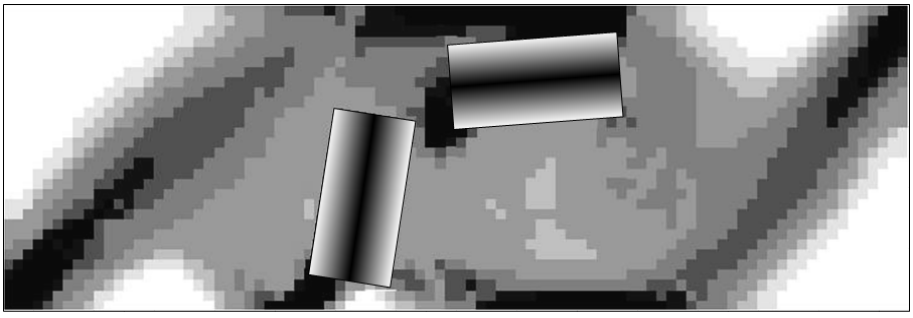

(b) 10th iteration

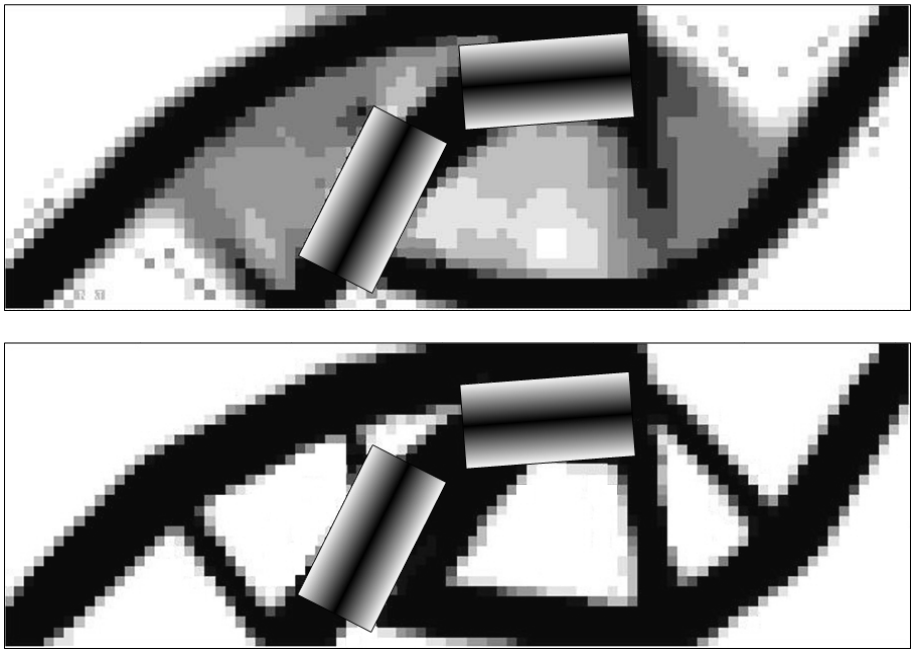

(c) 20th iteration

(d) The final design C=0.074J

Figure 3.20: Iteration history of the design patterns

Because more complexities are involved with the introduction of the movable components in the design domain, the optimization costs 65 iterations and finally converges. This consumes much more computing time than the pure structural topology design without components. During the iteration, the components move inside the design domain and try to find the proper positions. Meanwhile, the structural layout generated by the topology optimization becomes clearer and clearer.

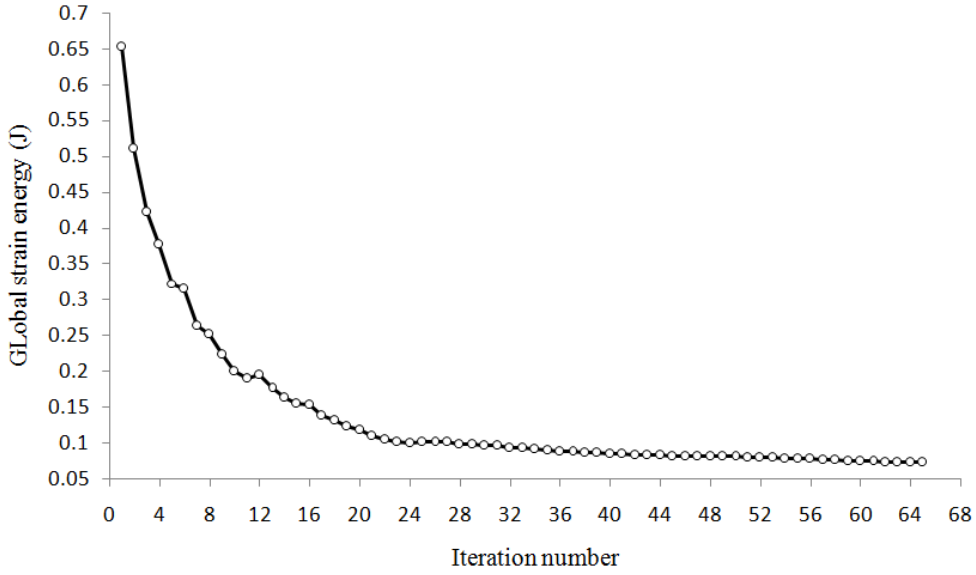

Figure 3.21: The convergence history of the objective function

Although introducing the components brings more limitations to the material layout design, the components material is much stronger than that of the structure in this example. That's the reason why the final strain energy is lower than that without components. In the final design, the two components are finally found to be embedded in

the design domain as some key parts of the loading structure. The convergence of the objective function is plotted in Figure 3.21.

The structural pattern in Figure 3.20 is not completely identical with that in Figure 3.19 where no component is involved. Obviously, the integrated layout design for structure and components is not a method simply embedding the components into the optimal structural topology. The simultaneous updating of the components' positions and structural patterns implies their coupled effects on the design objective.

3.6.2 Effect of component material

Practically, the equipments assembled in a structural system are not always stronger than the supporting structure. Therefore, the integrated layout optimization of the pylon is further discussed by exchanging the material properties of the components and the supporting structures, i.e.
for the components:

elastic modulus, $E_0=7\times10^{10}$pa, density $\rho_0=2700$kg/m^3 and Poisson's ratio $v=0.3$;

for the structures:

elastic modulus, $E_0=2\times10^{11}$pa, density $\rho_0=7800$kg/m^3 and Poisson's ratio $v=0.3$.

The same loads and boundary conditions as the previous ones are used here. By removing 50% of the total material cost, the iteration of the topology design is shown in Figure 3.22.

During the iteration, the optimizer also tries to find proper positions for the two components. But they are not strong enough to be located at the main load path of the structure.

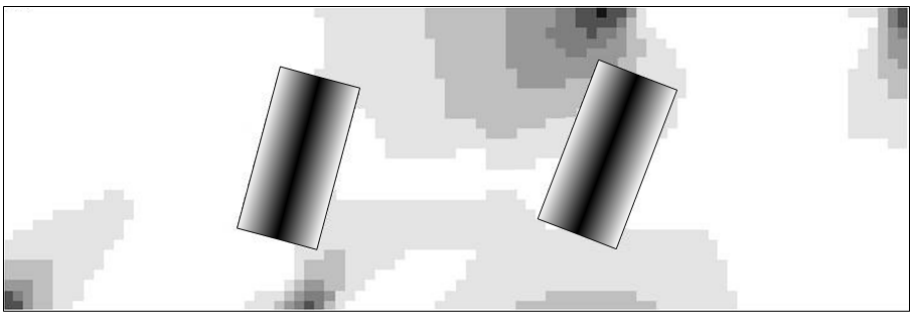

(a) 5th iteration

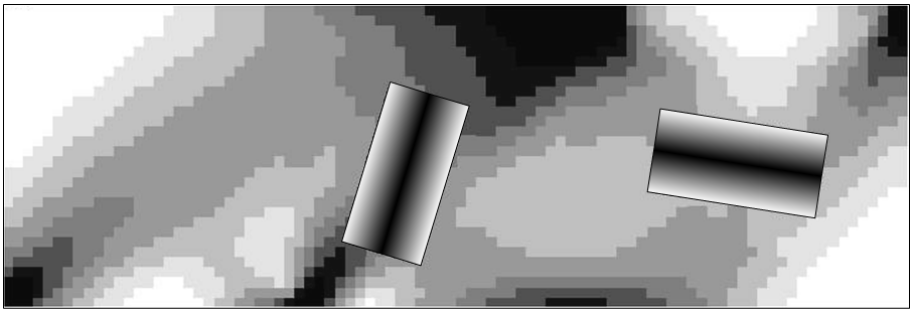

(b) 10th iteration

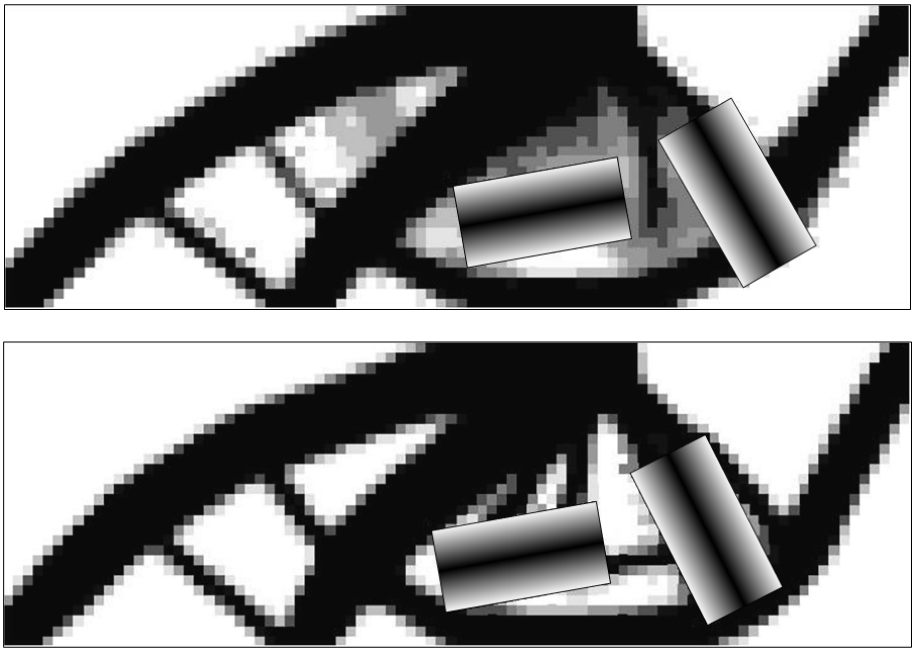

(c) 20th iteration

(d) The final design *C*=0.030J

Figure 3.22: Iteration history of the design patterns

After 41 iterations, the optimization converges to the final design configuration. Compared with the previous design, the structural layout is similar. The relatively weaker components are also embedded as parts of the loading structure, but the positions are not as critical as before. The iteration history of the objective function is shown in Figure 3.23. The strain energy is quite lower in this example because stronger material properties are used for the supporting structure.

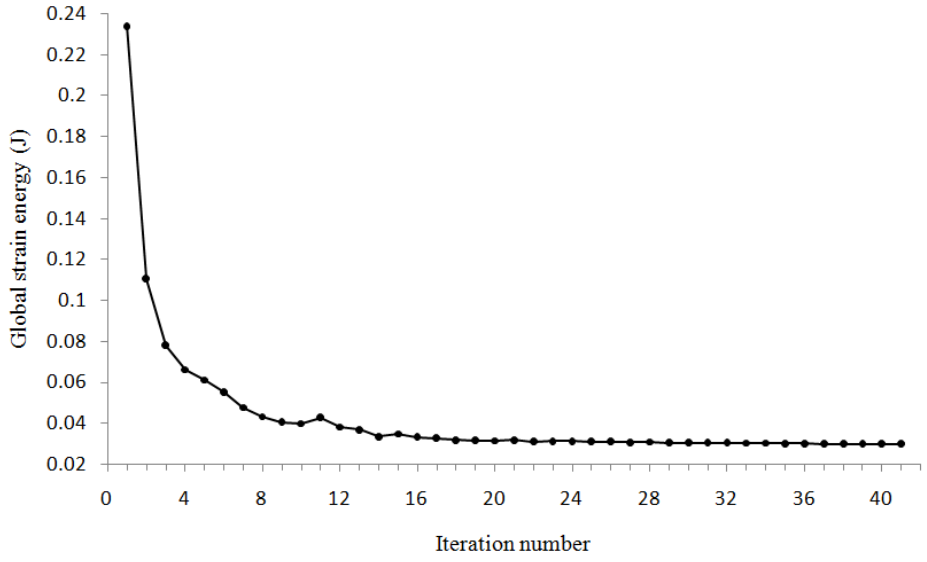

Figure 3.23: The convergence history of the objective function

In the extreme case when the equipments are easily broken or too weak to carry some loads, some void areas of the design domain have to be reserved for their protection. Actually, we just need to assign rather weak material properties to the components, e.g., for the components:

elastic modulus, E_0=1pa, density ρ_0=1kg/m^3 and Poisson's ratio v=0.3;
and for the structures:
elastic modulus, E_0=7×10^{10}pa, density ρ_0=2700kg/m^3 and Poisson's ratio v=0.3.

The components are now rectangular holes reserved in the design domain. Iterative design patterns are shown in Figure 3.24. These holes occupy proper positions which should not affect the main load path while the structural layout has to avoid passing through the locations of the components. When the void components break the structural layout instantaneously, unsatisfactory instabilities occur in the convergence history shown in Figure 3.25.

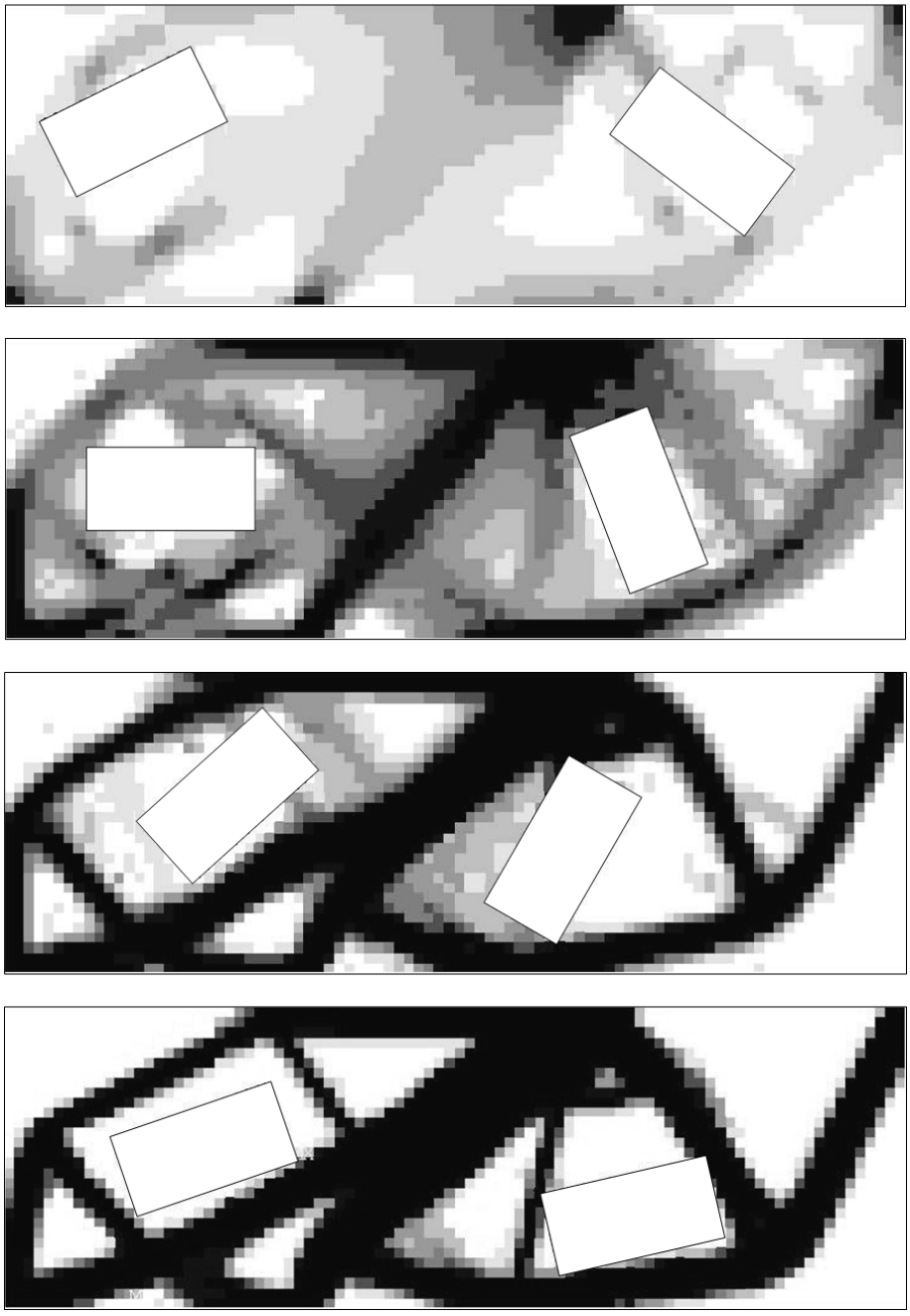

(a) 5th iteration

(b) 10th iteration

(c) 20th iteration

(d) The final design C=0.098J

Figure 3.24: Iteration history of the design patterns

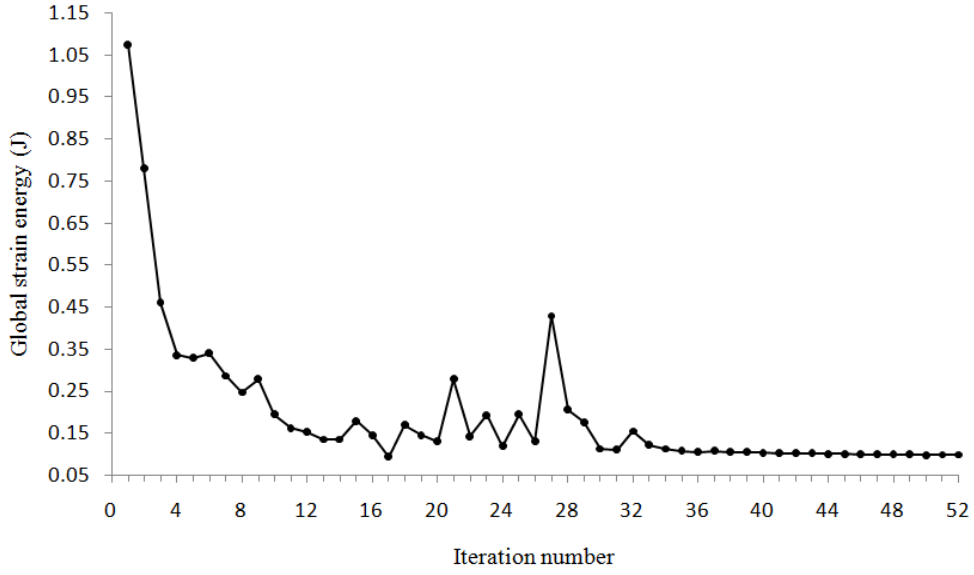

Figure 3.25: The convergence history of the objective function

The optimization takes about 52 iterations to reach the convergence. The material layout and the configuration of the components are actually rather different from the previous designs.

3.6.3 Non-convex design domain

In this section, two examples with solid components are tested to illustrate how the integrated layout design works with a non-convex design domain. The material properties are defined as follows:
for the components:

elastic modulus, $E_0=2\times10^{11}$pa, density $\rho_0=7800$kg/m^3 and Poisson's ratio $v=0.3$;

and for the structures:

elastic modulus, $E_0=7\times10^{10}$pa, density $\rho_0=2700$kg/m^3 and Poisson's ratio $v=0.3$.

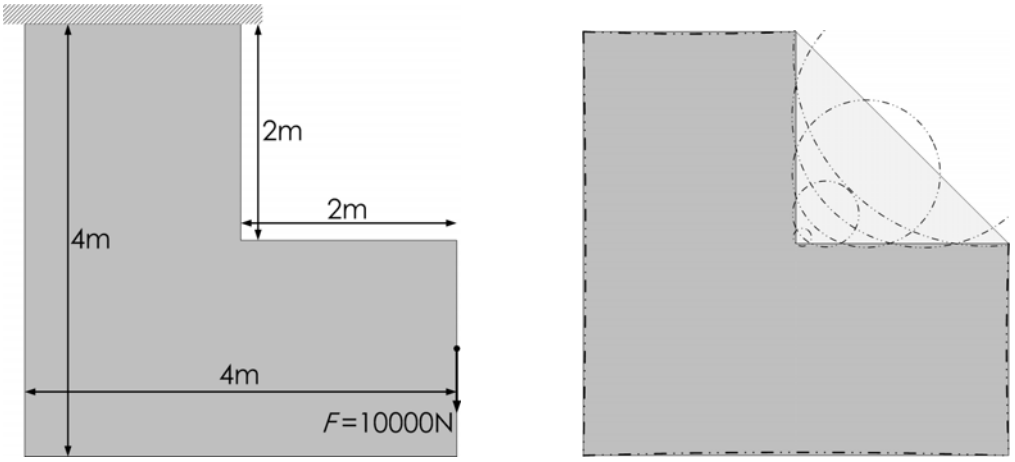

(a) Dimension, load and boundary conditions

(b) FCM approximation for the design domain

Figure 3.26: The definition of the design domain

The components are much stronger than the supporting structure. The design domain and its dimension are shown in Figure 3.26(a). An L-shaped beam is modeled with its upper side fixed and one concentrated force assigned at the right side. The basic mesh consists of quadrangular elements with a size of 0.1m×0.1m. 1200 density points are defined in total. The design domain is shown in Figure 3.26(b) where the concave part is modeled as a fictive triangular component approximated with 5 circles.

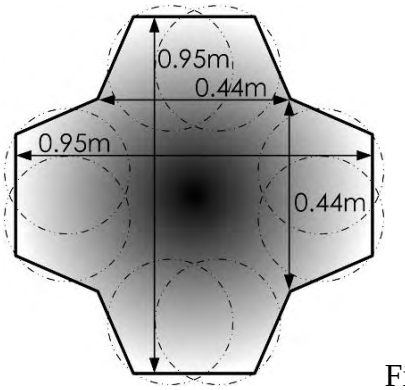

Figure 3.27: The definition of the component

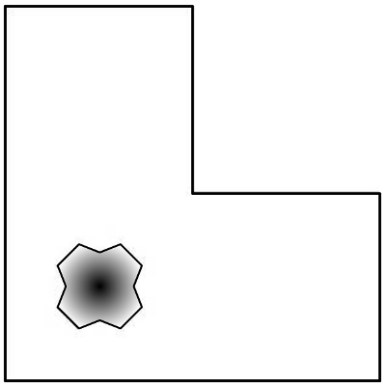

(a) The initial design

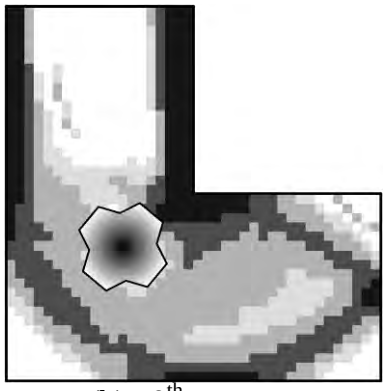

(b) 10th iteration

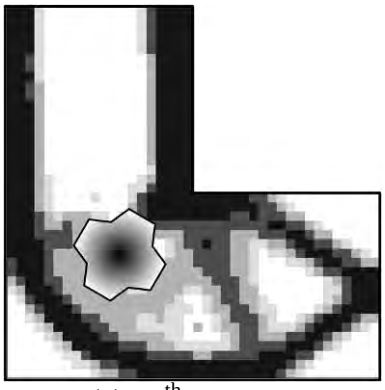

(c) 25th iteration

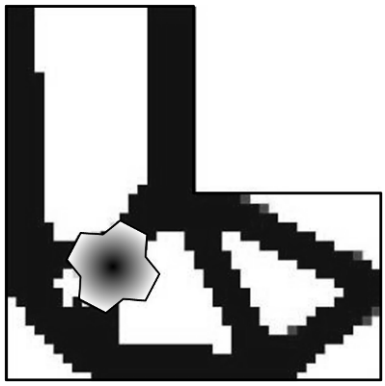

(d) The final design *C*=0.050J

Figure 3.28: Iteration history of the design patterns

In the first case, one component is concerned and is approximated with 8 circles as shown in Figure 3.27. By minimizing the strain energy and constraining the volume of the supporting structure to 50% of the total volume, several iterations of the configurations and the convergence history of the design objective are shown in Figures 3.28 and 3.29, respectively. The component is finally located as a part of the structure after 58 iterations.

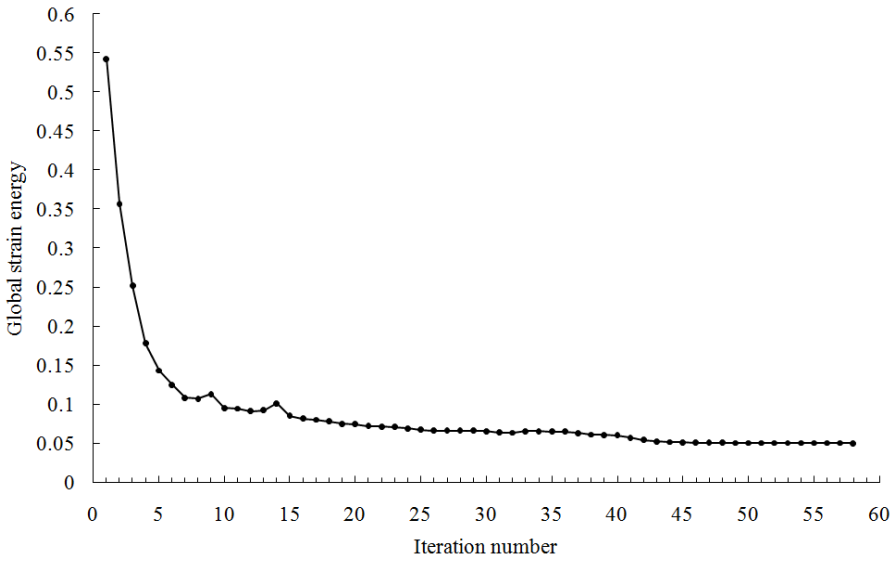

Figure 3.29: The convergence history of the objective function

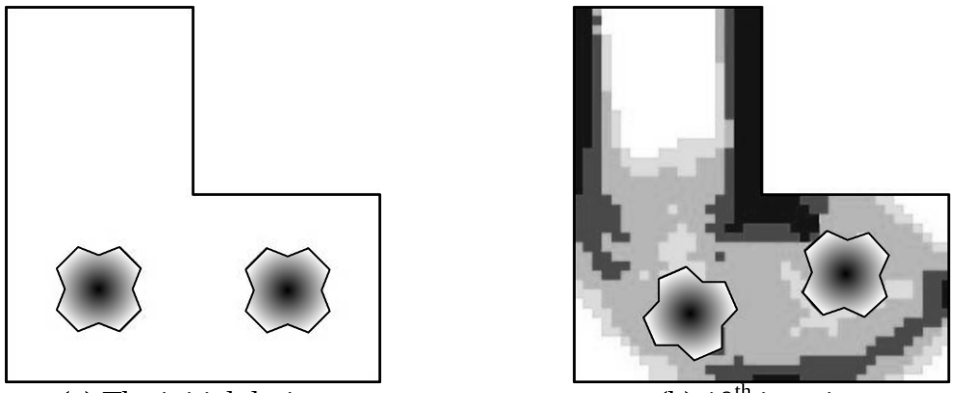

(a) The initial design

(b) 10th iteration

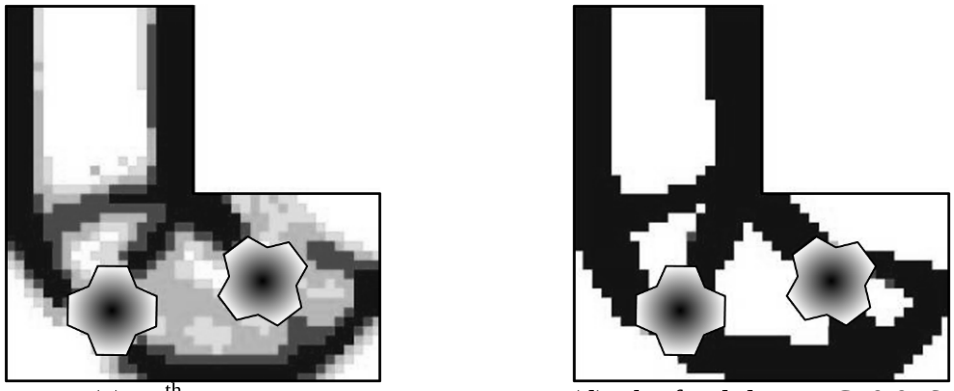

(c) 25th iteration

(d) The final design C=0.046J

Figure 3.30: Iteration history of the design patterns

The second case is about two identical components in the same design domain. Figure 3.30 shows the iteration histories. And the objective function converges as shown in Figure 3.31. It is also found that both two components are now integrated as parts of the structure and demonstrate their existence for the rigidity maximization of the system.

In both tests, the complexity of the components shape and the design domain are

considered. Although more geometrical design constraints are involved in the iteration process, the optimization gives rise to a reasonable design pattern.

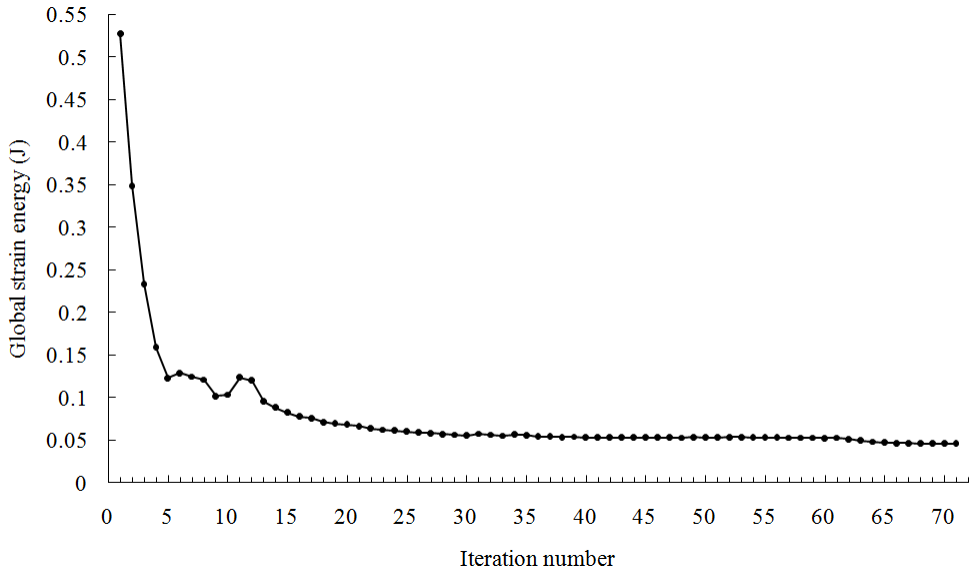

Figure 3.31: The convergence history of the objective function

3.6.4 An aircraft structure

In this problem, an illustrative part of an aircraft structure is designed. As shown in Figure 3.32, two identical groups of holes with thick edges are defined as components in the original design. Therefore, both solid and void material properties are employed in the components which are more complex than previous examples. Material properties of aluminum are assigned to both components and the structure:

elastic modules $E_0=7\times10^{10}$pa; Poisson's ratio v = 0.3.

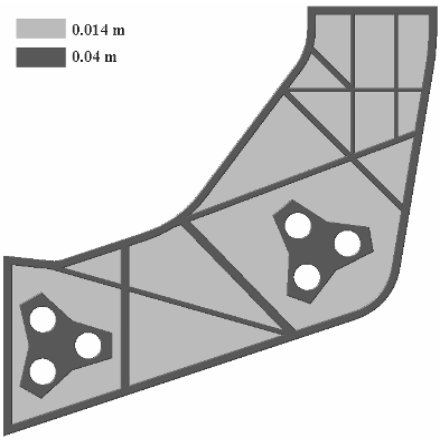

Figure 3.32: Original design of the part, 28.7kg, C=0.0826J(3D) C=0.0938J(2D)

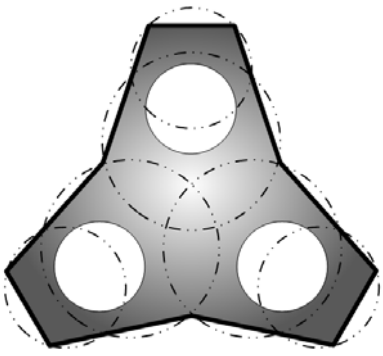

Figure 3.33: Component with a group of holes and its circles

Different thicknesses are assigned to the components and the structure as shown in different colors. The part is supported at the left side and a pressure 2.87×10^5pa is applied on the upper bound. The original design is meshed with 3D solid elements and then simplified into 2D membrane elements and analyzed for the purpose of comparison. The

strain energies as well as the total mass including the mass of the structure and the components are also shown in Figure 3.32.

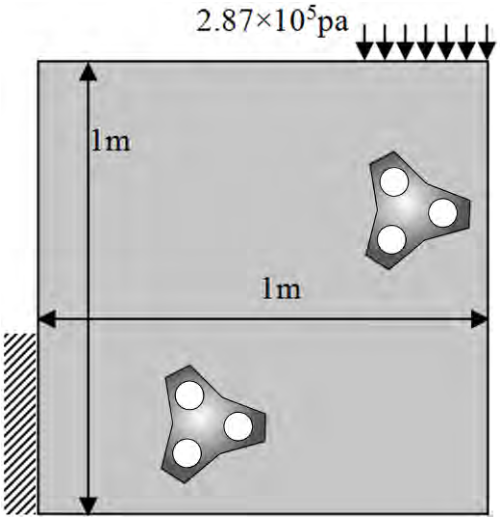

Figure 3.34: Initial design configuration

Figure 3.35: A regular topology optimization, 28.7kg, C = 0.0636J(2D)

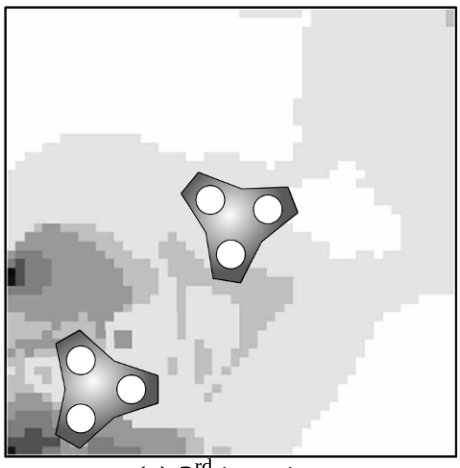

(a) 3rd iteration

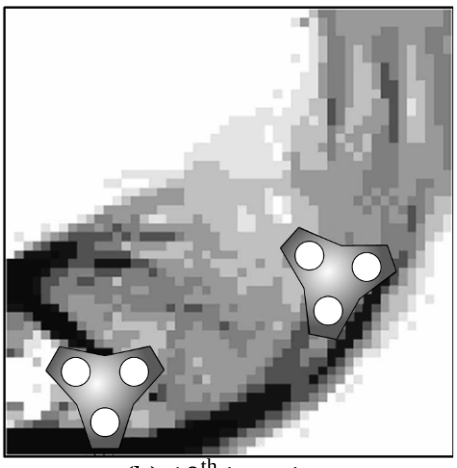

(b) 10th iteration

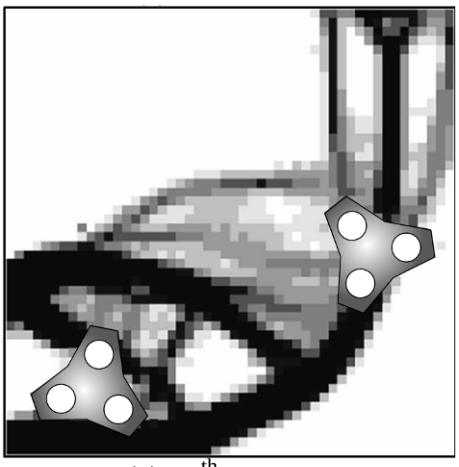

(c) 25th iteration

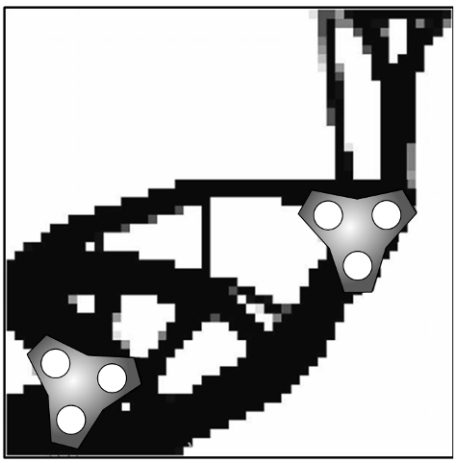

(d) The final design 28.0kg
C=0.0730J(2D)

Figure 3.36: Iteration history of the design patterns

The 2D model is adopted in the integrated layout optimization. 6 circles are used to approximate the geometry of each component as shown in Figure 3.33. The design domain, loads and boundary conditions can be found in Figure 3.34. The element size is 0.02m and the basic mesh of the design domain is discretized into 50×50 elements.

A standard topology optimization without any components is carried out first. The material cost is set to the total mass of the original part. The optimal result is shown in Figure 3.35. The optimal structural layout is rather different from the original design. Most of the material is distributed on the left side near the fixation. However, we don't know where to locate the two groups of holes yet.

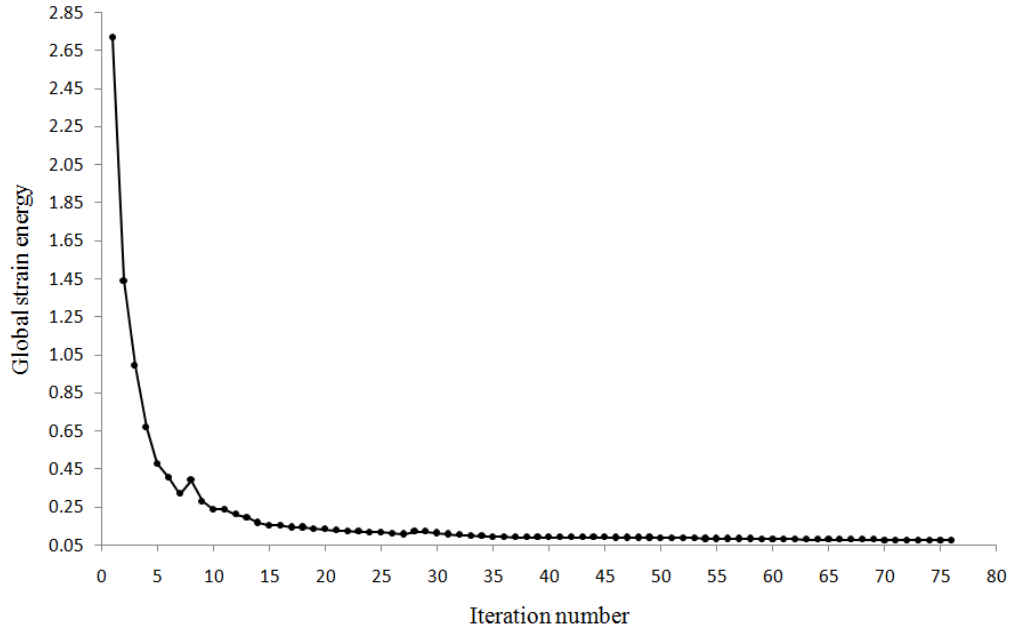

Figure 3.37: The convergence history of the objective function

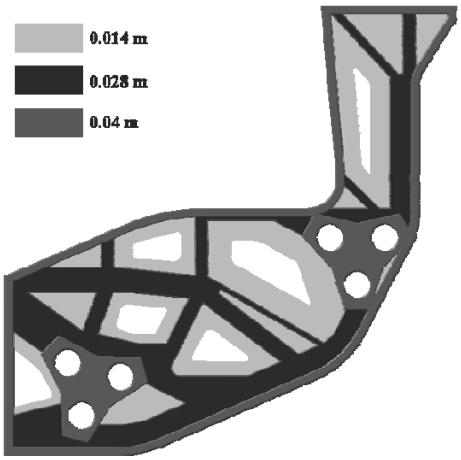

Figure 3.38: The redesigned optimal part. 28.7kg *C*=0.0511J (3D)

In the integrated design, the same design objective and constraint of material cost are assigned. The two components find the optimal positions very quickly but it takes much more iterations to reach the convergence. The iteration history and the final design are shown in Figure 3.36. Two components are finally located as a part of the structure after 76 iterations. The convergence of the objective function is shown in Figure 3.37.

In comparison, it is found the optimal structure obtained by the integrated design have a

similar structural configuration to the result without component. However, the latter has a smaller value of objective function because all materials are freely distributed. Furthermore, the optimal result in Figure 3.36 saves 2.5% of the weight and reduces the strain energy by 22% compared with the 2D solution of the original structure.

Finally, the refined design of the part is shown in Figure 3.38 according to the optimized design pattern. Compared with the original one with 3D analysis, the optimal part reduces the strain energy by 38% and the maximum von-mise stress by 27% while holding the same weight.

3.6.5 Partially supported components

Figure 3.39: A power facility and its fixation positions

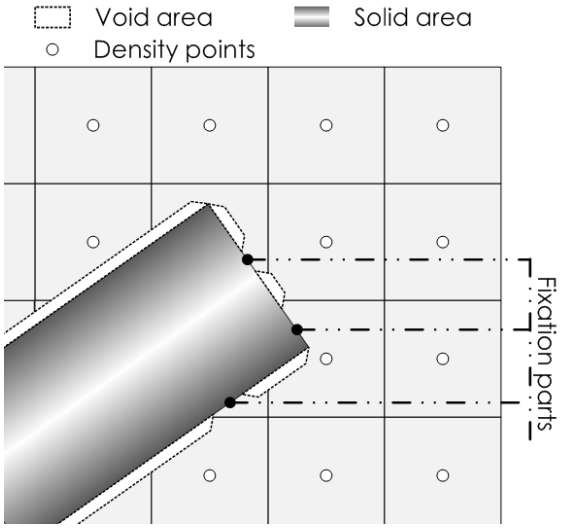

Figure 3.40: Definition of the partially supported component

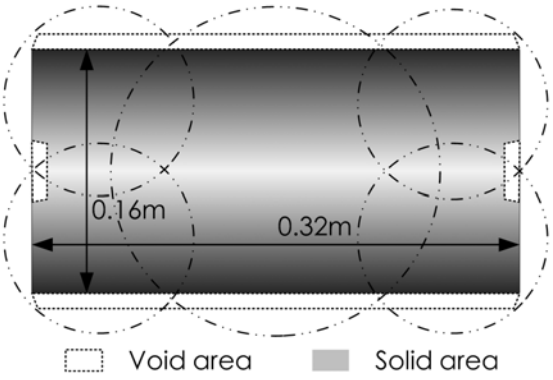

Figure 3.41: Definition of the component

In most of the practical cases, only some specified sections and flanges on the contour of the components are allowed to be supported by the structure. For example, the power facility as indicated in Figure 3.39 can only be fixed at the two ends.

This is the situation of partially supported components that can be modeled by employing two different material properties in one component like in section 3.6.4. As shown in Figure 3.40, the fixation positions of the component are directly in contact with the surrounding elements of the supporting structure, while the rest parts of the component are cut apart from the supporting structure with a small gap defined with a thin layer of void area. However, both the solid and void areas belong to the component and will move together with the attached local coordinate system during the iteration.

Here, the example of the pylon is further tested with partially supported components. Suppose the two components have 4-supported positions as shown in Figure 3.41. The circles have to cover both the solid and void areas of the components. The material properties of the solid parts are defined as:
for the components:

elastic modulus, $E_0=2\times10^{11}$pa, density $\rho_0=7800$kg/m^3 and Poisson's ratio $v=0.3$;

for the structures:

elastic modulus, $E_0=7\times10^{10}$pa, density $\rho_0=2700$kg/m^3 and Poisson's ratio $v=0.3$.

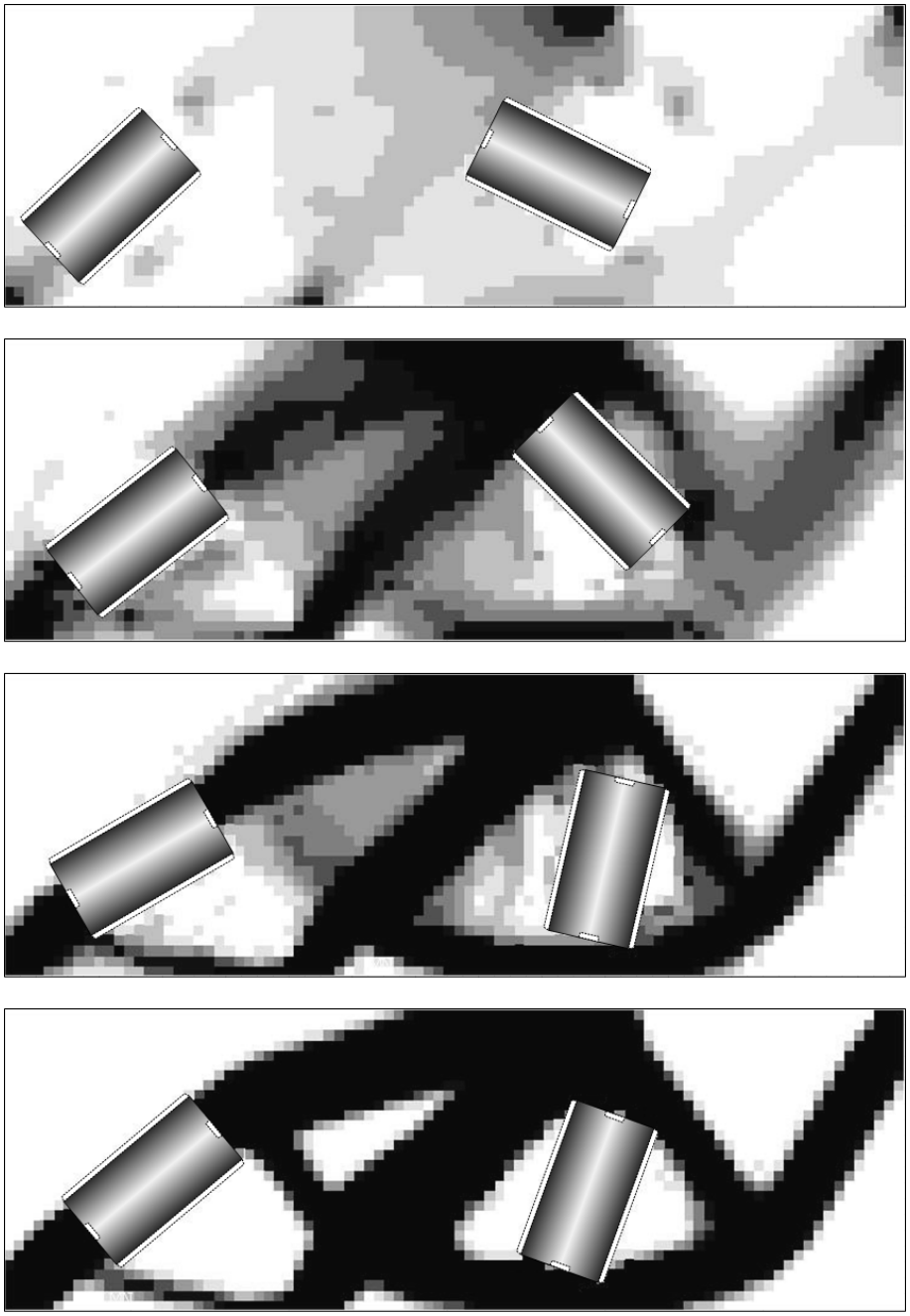

(a) 5th iteration

(b) 10th iteration

(c) 25th iteration

(d) The final design C=0.078J

Figure 3.42: Iteration history of the design patterns

The two components are initially located horizontally in the design domain. The same loads and boundary conditions are used here. The optimization converges at the 42nd iteration. The convergence history of the objective function is shown in Figure 3.43.

The two components are now located directionally in the structure to make sure the supporting structure is connected at the specified fixation positions. Compared with the optimal design in Figure 3.20, the strain energy is higher here because the partially supported components bring more constraints to material layout design. Further comparisons of the detailed structural layout are carried out with the optimal design without component, as shown in Figure 3.44. The structural layouts are generally similar. The components are not wide enough to be located on the main loading structure as in Figure 3.20. As a result, the structure on the left side has to be slightly modified to create a section long enough for one component. Meanwhile, some of the structure members on the right side are replaced by the other component.

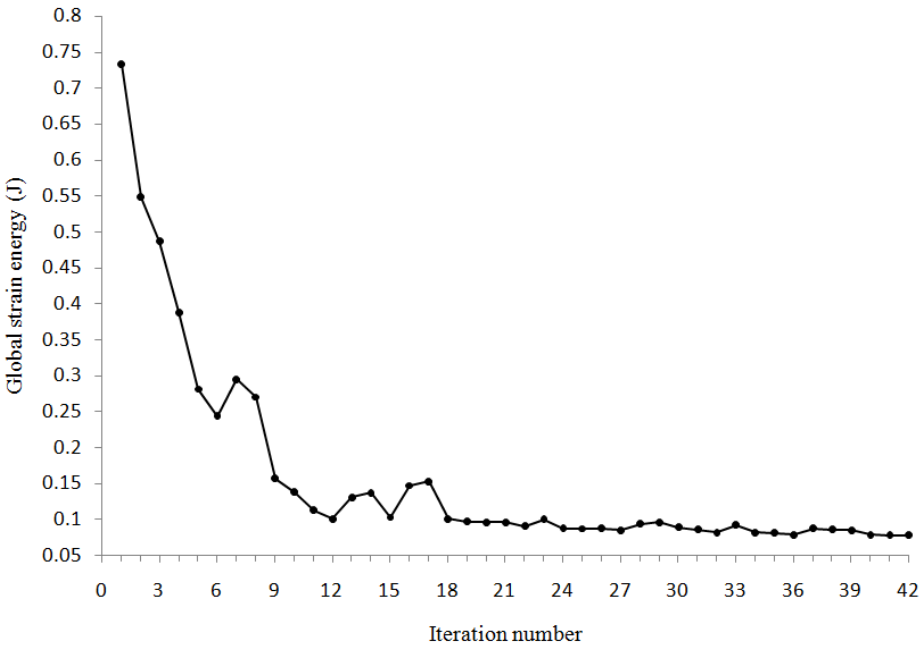

Figure 3.43: The convergence history of the objective function

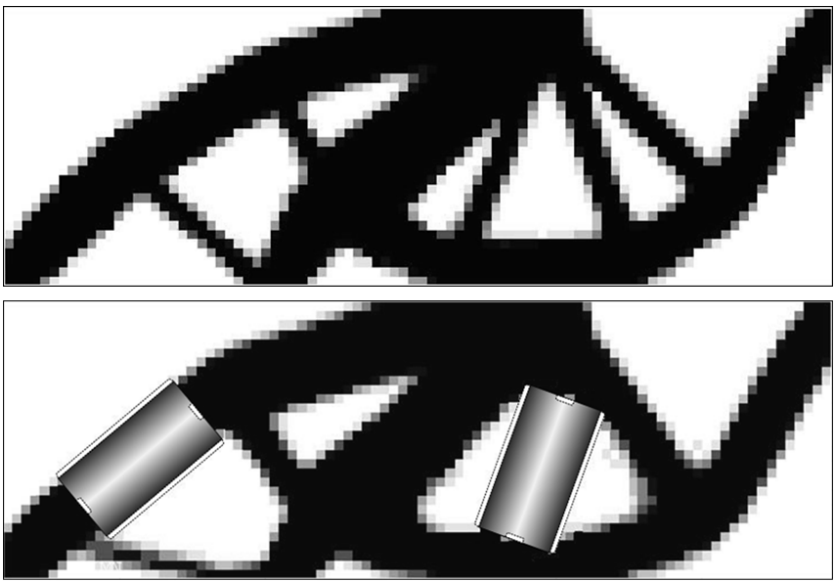

Figure 3.44: Comparison of the standard topology optimization and integrated layout design with partially supported components

Finally, components of a cross shape that are partially supported at the four ends are further tested. As shown in Figure 3.45, the void areas are defined at the four concave parts and 8 circles are used to approximate the contour of each component.

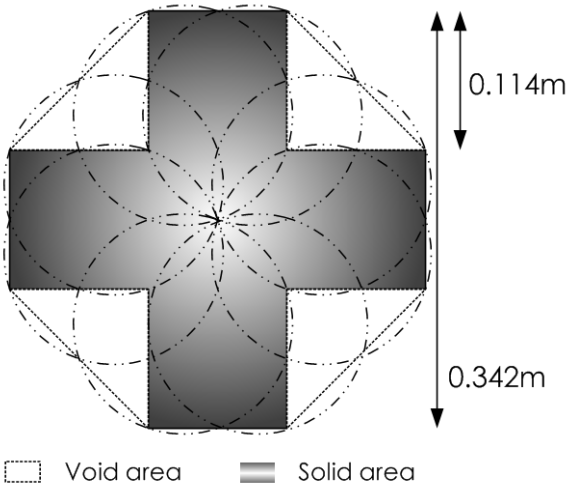

Figure 3.45: Definition of the component

The design domain, material properties and boundary conditions are the same as used above. The optimization consumes 78 iterations as shown in Figure 3.46. However, the design process costs more computing time because it is rather difficult to find proper locations of the components that have four fixation positions.

The convergence of the objective function is plotted in Figure 3.47. Much more instabilities are found during the iteration history when the void areas cut the loading path. In the final solution, only three of the four fixation positions are firmly supported. In this design, although the component has a material stronger than that in Figure 3.42, the strain energies in both final designs are close to each other.

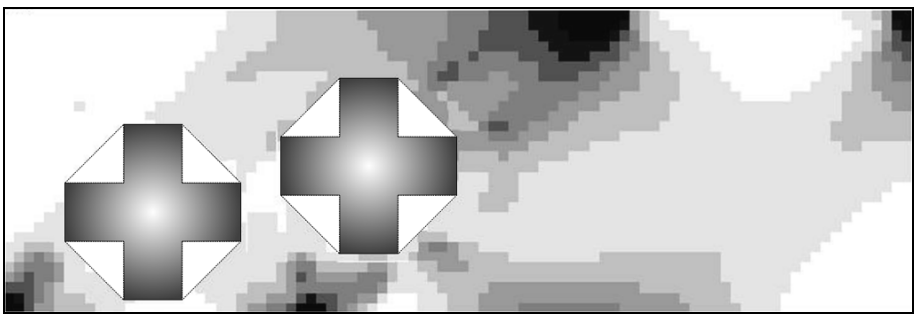

(a) 5th iteration

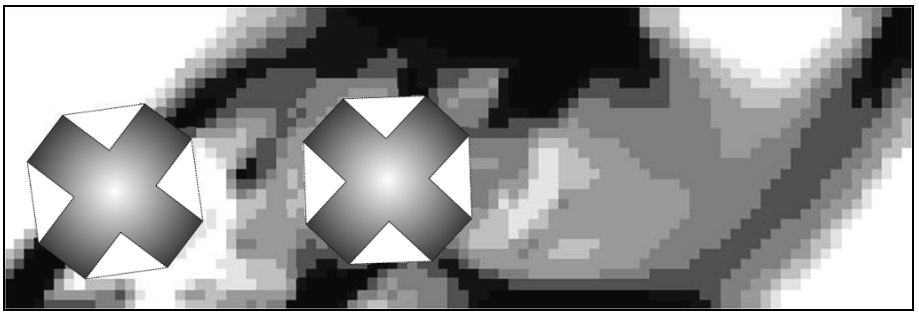

(b) 10th iteration

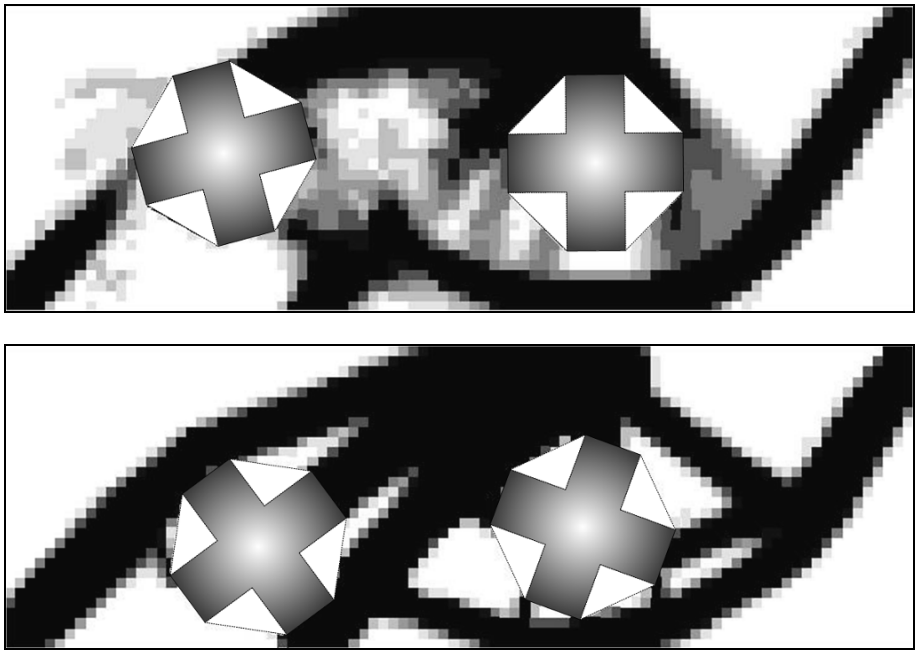

(c) 25th iteration

(d) The final design *C*=0.079J

Figure 3.46: Iteration history of the design patterns

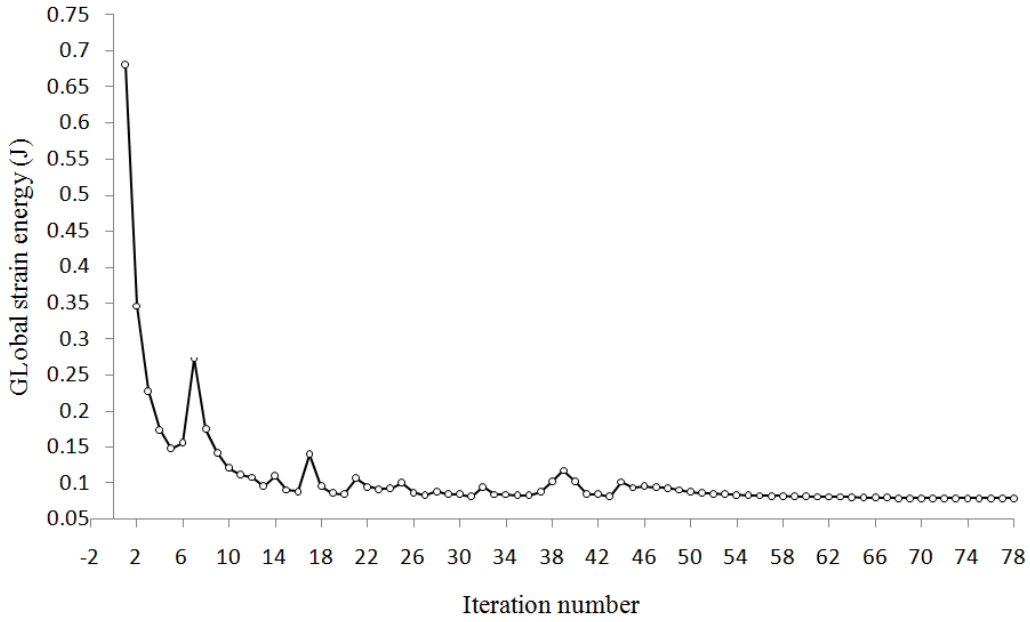

Figure 3.47: The convergence history of the objective function

3.6.6 Pylon with three components

The purpose of the final example in this chapter is to demonstrate the integrated layout optimization with one more component and more convergence details. The definitions of the design domain, components, material properties, loads and boundary conditions are identical with those in the Section 3.6.1.

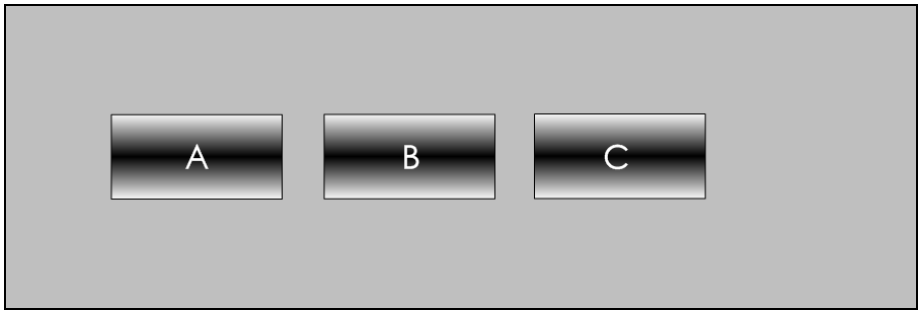

Figure 3.48: Initial configuration of the pylon with three components

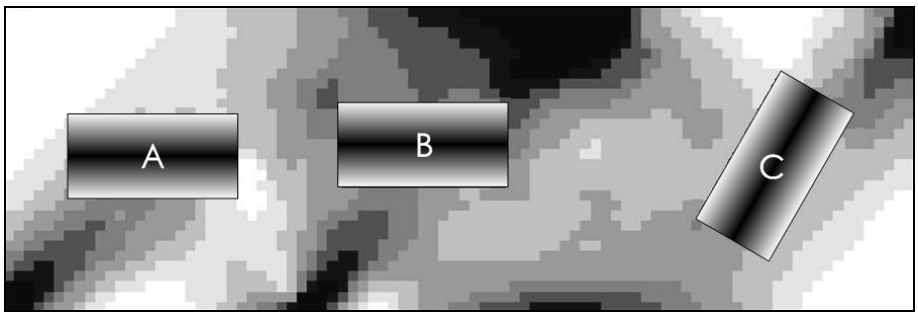

(a) 5th iteration

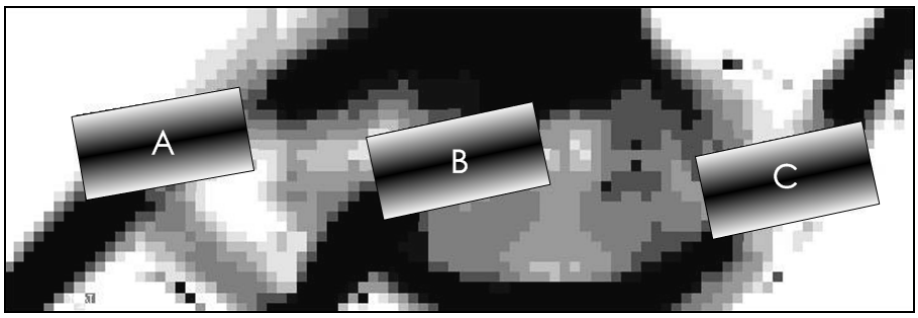

(b) 10th iteration

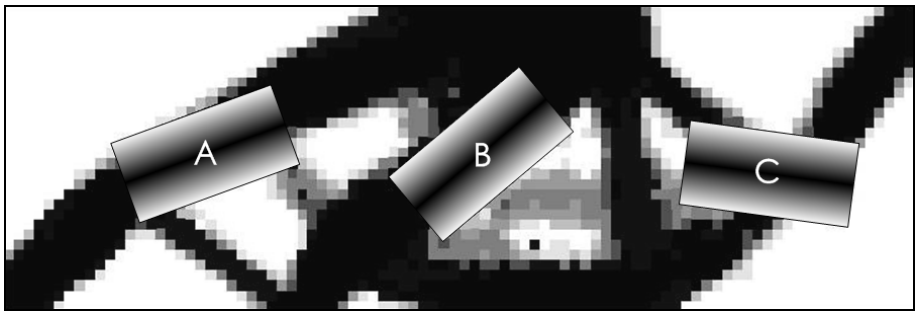

(c) 25th iteration

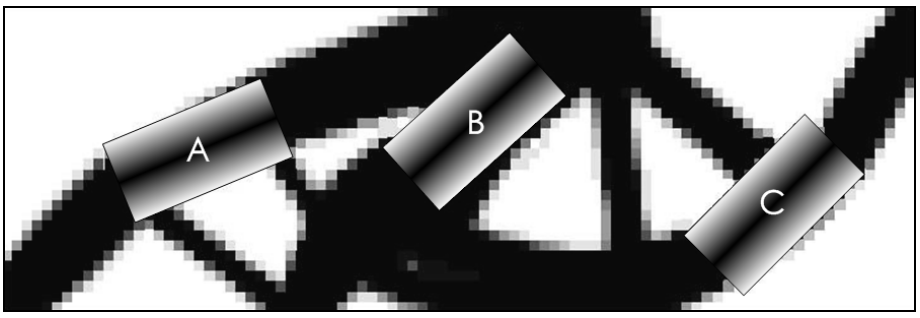

(d) The final design C=0.069J

Figure 3.49: Iteration history of the design patterns

The initial configuration is shown in Figure 3.48, where the three components are located horizontally in the design domain. These components in the figure are marked as A, B and C to be identified.

The optimization process converges at the 84th iteration as shown in Figure 3.49. 50% of the structural material is distributed similar to the previous examples. Three components are located on the main loading structure as expected. However, the integrated layout design still suffers from the problem of local minima inherited from the packing optimization with FCM. On the one hand, the components can hardly exchange their positions all through the entire iteration. On the other hand, when the structural layout becomes clearer, the components will be clamped by the structure and never move far away.

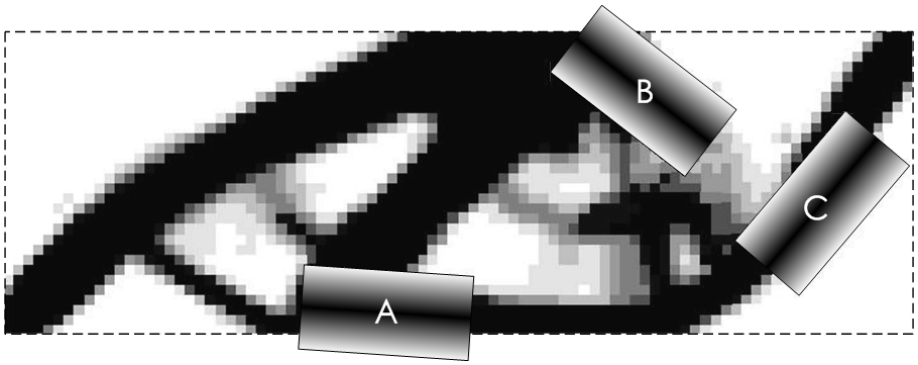

(a) Design configuration obtained at 25th iteration when the geometrical constraints are disabled at the 20th iteration

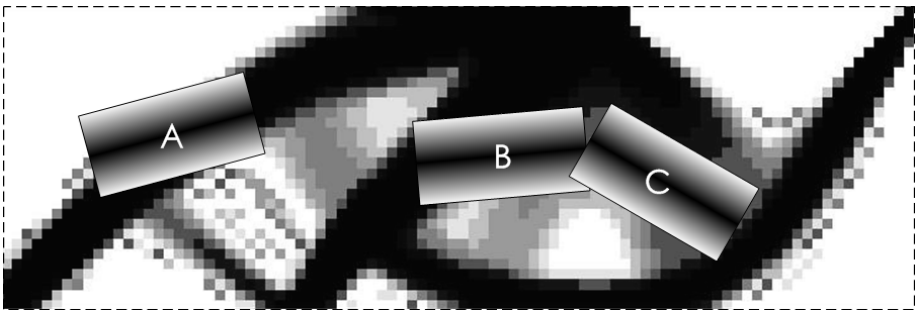

(b) Design configuration obtained at 17th iteration when the geometrical constraints are disabled at the 10th iteration

Figure 3.49: Design configurations obtained without geometrical constraints

The geometrical constraints are normally not active in the final design because in the feasible design space the objective functions are non-monotonous with respect to the geometrical design variables. But these constraints are still necessary to prevent the possible overlapping during the design iteration. Figure 3.49 shows two design configurations obtained without geometrical constraints. In Figure 3.49(a), two of the components are found located partially outside the design domain. This situation is not fatal to the optimization procedure because it is still a correctly defined FE model. But when the components overlap with each other as shown in Figure 3.49(b), we have no idea to define the elements and their material properties in the overlapped area. The optimization procedure will be terminated.

To have a global view of the detailed convergence process, the convergence histories of the objective function and maximum variations of the design variables are shown in Figure 3.50. The optimization design will be converge when all these values below 0.1%.

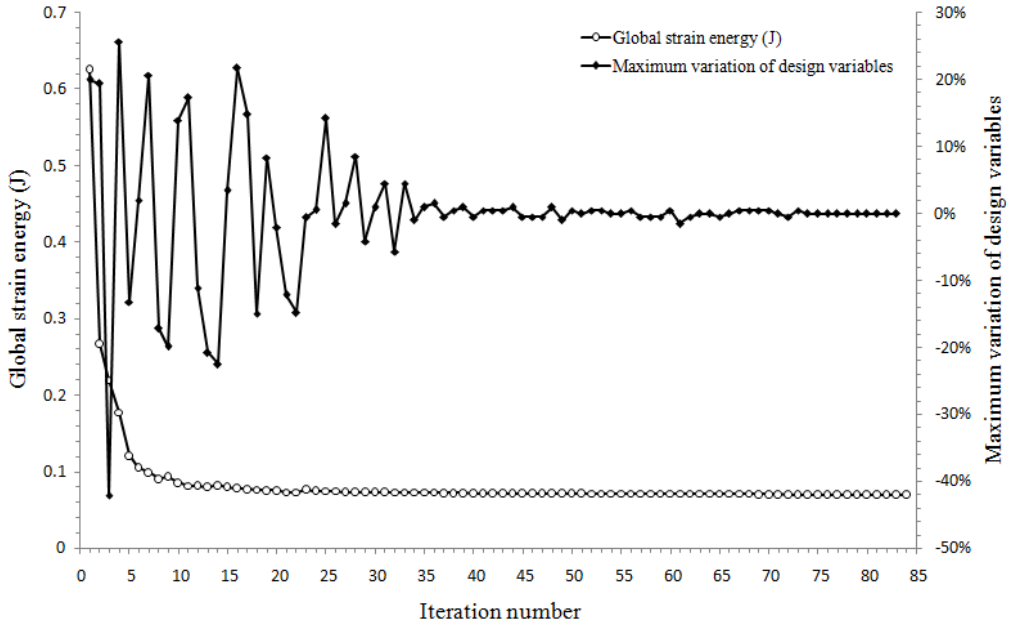

Figure 3.47: The convergence history of the objective function and maximum variation of the design variables

The objective function trend to steady very quickly but it takes more iterations for the design variables especially the geometrical variables to reach the convergence.

Introducing more components into the integrated layout design brings problems in two fold. Firstly, more geometrical design variables have to be defined for new introduced components, which further need more computing time consumed by large numbers of geometrical constraints and FE analysis involved in finite difference. Secondly, if the components take up much space in the design domain, they cannot move in the design domain as free as in a loose package. Some less optimal configuration may be obtained.

3.7 Conclusion

In this chapter, components and their supporting structure are simultaneously designed with the proposed layout design method that integrates the FCM, density point and embedded meshing techniques. The FCM aims at simplifying the complex overlap constraints involved in a pure geometry model. The technique of density points is used to avoid the conflict between the geometrical design variables and pseudo-densities. Meanwhile, the combination of density point and embedded meshing techniques can save the computing cost of the remeshing procedure. Several compliance minimization examples are tested. Components with different shapes, material properties and partially supported positions are taken into account. Numerical results show that integrated layout design is efficient to achieve reasonable design configurations. Compared with the traditional topology optimization, the introduction of the components into the layout design brings more complexities but also demonstrates more practical significance in

multi-component system design.

Chapter 4

Low-density Areas in Topology Optimization

Overview

Several interesting problems involved in low-density areas of topology optimization are discussed in this chapter, which will benefit the extension of the integrated layout optimization. The phenomena of localized deformations occurring in topology optimization with eigenvalue maximization or design dependent body loads are firstly analyzed here. It is shown that these problems will numerically lead to an erroneous solution and undesired results. Then, from the viewpoint of low-density elements, the breakdown problem of the Evolutionary Structural Optimization (ESO) is also discussed.

Contents

4.1 Localized modes

The localized modes are found in the eigenvalue optimization problems e.g. maximizing the natural frequencies or buckling loads in topology optimization (see Neves 1995, Pedersen 2001 and Zhou 2004). It is generally recognized that this phenomenon is actually a numerical error due to the improperly defined material properties for the void elements, especially in the popularly used SIMP model.

When the localized modes appear, the vibration or buckling takes place only in the low-density areas which are actually supposed to be void areas without mechanical effects. As a result, this problem will probably lead to the incorrect calculation of the design response, sensitivities and further the iteration failure of the design optimization.

4.1.1 Sensitivity analysis

The sensitivities used in topology optimization of eigenvalue maximization are firstly derived here. The problem is described as the solution of the general eigenvalue problem

$$\left(\boldsymbol{K} - \omega^2 \boldsymbol{M}\right)\boldsymbol{u} = 0 \tag{4-1}$$

where $\boldsymbol{K}$ and $\boldsymbol{M}$ are the stiffness matrix and mass matrix of the structural system, respectively. ω is one of the circular natural frequencies and $\boldsymbol{u}$ is the corresponding mode shape. This equation can be transformed to a buckling problem by replacing ω^2 with the buckling eigenvalue that indicates the minimum buckling load, $\boldsymbol{M}$ with the geometric stiffness matrix which depends on the displacement vector of a given unified static load case. However, due to the similarity, only the natural frequency maximization is discussed here.

Based on the interpolation model, the stiffness and mass matrices can be related to the pseudo-densities.

$$\begin{aligned} \boldsymbol{M}_i &= \eta_i \boldsymbol{M}_{i0} \\ \boldsymbol{K}_i &= P(\eta_i)\boldsymbol{K}_{i0} \end{aligned} \tag{4-2}$$

where $\boldsymbol{M}_i$ and $\boldsymbol{K}_i$ are the mass matrix and stiffness matrix of the ith element, respectively. $\boldsymbol{M}_{i0}$ and $\boldsymbol{K}_{i0}$ are the corresponding mass and stiffness matrices, respectively when the element is solid. $P(\eta_i)$ is the penalty function. A topology optimization problem of maximizing the natural frequencies is defined as

$$\begin{aligned} &\text{Find: } 0 < \eta_i \le 1 \\ &\max: \ \omega^2 \\ &\text{s.t.: } V \le V^{(U)} \end{aligned} \tag{4-3}$$

It should be noticed that the eigenvalue maximization problems are actually non-differentiable because the eigenmodes may switch the modal order during the optimization. In such a case, the sensitivities of the objective function become

discontinuous which may cause oscillation and divergence in the iterative optimization process. In order to overcome this problem, several mean-eigenfrequency functions, e.g. the max-min formulation, weighted formulation, reciprocal formulation, Euclidean norm formulation etc are introduced to smooth out the frequency objective (See Seyranian et al 1994, Lund 1994 and ANSYS 9.0 Documentation, ANSYS Inc). However, this is not the topic concerned in this thesis.

The sensitivities are then derived by differentiating the eigenequation:

$$\left(\frac{\partial \boldsymbol{K}}{\partial \eta_i}-\frac{\partial \omega^2}{\partial \eta_i}\boldsymbol{M}-\omega^2\frac{\partial \boldsymbol{M}}{\partial \eta_i}\right)\boldsymbol{u}+\left(\boldsymbol{K}-\omega^2\boldsymbol{M}\right)\frac{\partial \boldsymbol{u}}{\partial \eta_i}=0 \tag{4-4}$$

$$\boldsymbol{u}^T\left(\frac{\partial \boldsymbol{K}}{\partial \eta_i}-\frac{\partial \omega^2}{\partial \eta_i}\boldsymbol{M}-\omega^2\frac{\partial \boldsymbol{M}}{\partial \eta_i}\right)\boldsymbol{u}+\boldsymbol{u}^T\left(\boldsymbol{K}-\omega^2\boldsymbol{M}\right)\frac{\partial \boldsymbol{u}}{\partial \eta_i}=0 \tag{4-5}$$

Note that the second term of Equation (4-6) is zero. With the introduction of the interpolation model, the sensitivities can be further derived as

$$\begin{aligned}\frac{\partial \omega^2}{\partial \eta_i}&=\frac{\boldsymbol{u}^T\frac{\partial \boldsymbol{K}}{\partial \eta_i}\boldsymbol{u}-\omega^2\boldsymbol{u}^T\frac{\partial \boldsymbol{M}}{\partial \eta_i}\boldsymbol{u}}{\boldsymbol{u}^T\boldsymbol{M}\boldsymbol{u}}\\&=\frac{1}{\boldsymbol{u}^T\boldsymbol{M}\boldsymbol{u}}\left(\frac{P'\left(\eta_i\right)}{P\left(\eta_i\right)}\boldsymbol{u}^T\boldsymbol{K}_i\boldsymbol{u}-\frac{\omega^2\boldsymbol{u}^T\boldsymbol{M}_i\boldsymbol{u}}{\eta_i}\right)\end{aligned} \tag{4-6}$$

4.1.2 Problem occurrence

A simple example of a cantilever beam clamped at the left end is analyzed here to explain the occurrence of the localized modes. As shown in Figure 4.1, the beam is meshed with two elements. Typical material properties are assumed according to the SIMP interpolation model as

Element №1: elastic modulus $E_1=\eta_1^p\times10^6$pa, density $\rho_1=\eta_1\times100$kg/m^3 and Poisson's ratio v=0.3

Element №2: elastic modulus $E_2=\eta_2^p\times10^6$pa, density $\rho_1=\eta_2\times100$kg/m^3 and Poisson's ratio v=0.3.

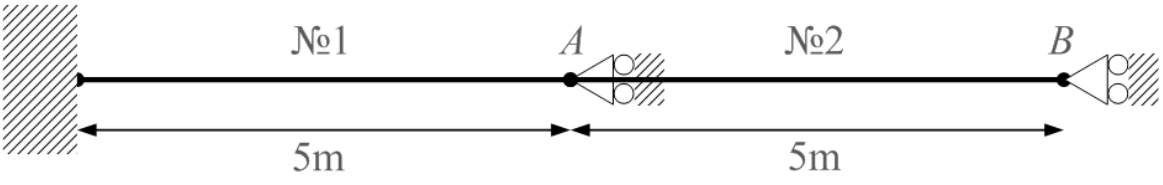

Figure 4.1: A cantilever beam with two elements

The cross section of the beam is a square with the size 0.05m×0.05m. Suppose the element №1 is solid with the pseudo-density η_1=1.

The first analysis is carried out by assuming element №2 to be solid as well, i.e. η_2=1 and

p=3. Only the nodes A and B are free and 4 degrees of freedom are taken into account altogether, i.e. the vertical displacement and the rotation of the two nodes (u_A, θ_A, u_B, θ_B).

The global stiffness and mass matrices are assembled and put down here

$$\boldsymbol{K} = \begin{bmatrix} 0.1000 & 0 & -0.0500 & 0.1250 \\ 0 & 0.8333 & -0.1250 & 0.2083 \\ -0.0500 & -0.1250 & 0.0500 & -0.1250 \\ 0.1250 & 0.2083 & -0.1250 & 0.4167 \end{bmatrix}$$

$$\boldsymbol{M} = \begin{bmatrix} 0.9286 & 0 & 0.1607 & -0.1935 \\ 0 & 0.5952 & 0.1935 & -0.2232 \\ 0.1607 & 0.1935 & 0.4643 & -0.3274 \\ -0.1935 & -0.2232 & -0.3274 & 0.2976 \end{bmatrix} \quad (4\text{-}7)$$

By solving the eigenequation, the first 4 eigenvalues and their corresponding eigenvectors can be obtained as

$$\left[\omega_1^2, \omega_2^2, \omega_3^2, \omega_4^2\right] = \left[0.0026 \quad 0.1029 \quad 1.1768 \quad 9.9134\right] \quad (4\text{-}8)$$

$$\left[\boldsymbol{u}_1, \boldsymbol{u}_2, \boldsymbol{u}_3, \boldsymbol{u}_4\right] = \begin{bmatrix} 0.3395 & -0.7194 & 0.1017 & 0.2531 \\ 0.1163 & 0.0433 & -0.7647 & 0.5204 \\ 1 & 1 & 1 & 1 \\ 0.1377 & 0.4799 & 0.9644 & 1.9329 \end{bmatrix} \quad (4\text{-}9)$$

The eigenvectors are normalized by assuming the vertical displacement of node B to be 1. According to the eigenvectors, the 1st to 4th order vibration shapes can be drawn as shown in Figure 4.2. Nothing abnormal is found in obtained natural frequencies and vibration shapes.

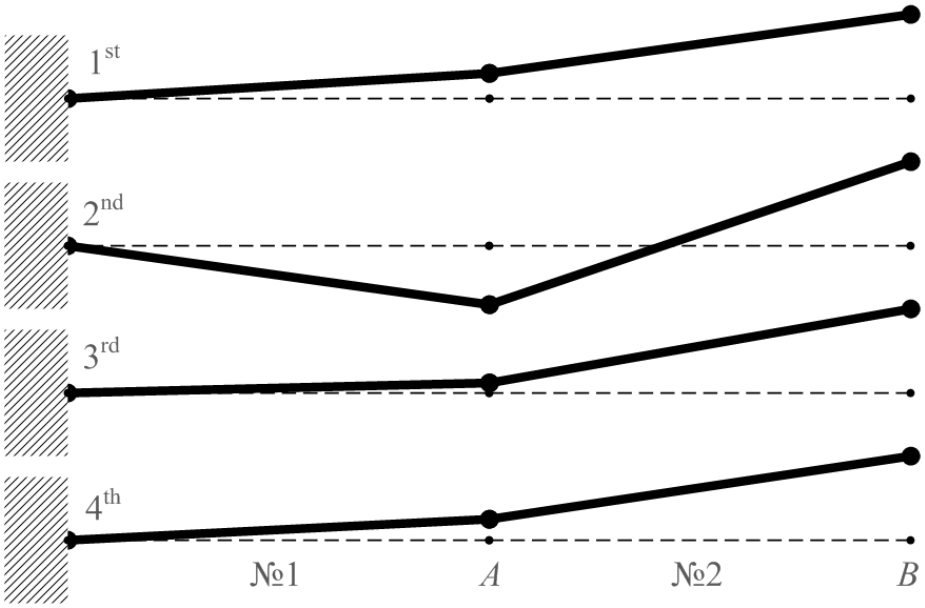

Figure 4.2: 4 Mode shapes of the cantilever beam

Now modify the material property of element №2 by setting η_2=0.01 and p=3, which simulate a void element in topology optimization. The global stiffness and mass matrices are

$$\boldsymbol{K}=\begin{bmatrix} 0.0500 & -0.1250 & -5.0\times10^{-8} & 1.3\times10^{-7} \\ -0.1250 & 0.4167 & -1.3\times10^{-7} & 2.1\times10^{-7} \\ -5.0\times10^{-8} & -1.3\times10^{-7} & 5.0\times10^{-8} & -1.3\times10^{-7} \\ 1.3\times10^{-7} & 2.1\times10^{-7} & -1.3\times10^{-7} & 4.2\times10^{-7} \end{bmatrix}$$

$$\boldsymbol{M}=\begin{bmatrix} 0.4689 & -0.3241 & 0.0016 & -0.0019 \\ -0.3241 & 0.3006 & 0.0019 & -0.0022 \\ 0.0016 & 0.0019 & 0.0046 & -0.0033 \\ -0.0019 & -0.0022 & -0.0033 & -0.0030 \end{bmatrix} \quad (4\text{-}10)$$

The absolute values of terms in the stiffness matrix of element №2 are found decreasing much faster than those in mass matrix because of the power-law penalization. Then the eigenequation are solved. The eigenvalues and the eigenvectors are obtained as

$$\left[\omega_1^2,\omega_2^2,\omega_3^2,\omega_4^2\right]=\begin{bmatrix} 4.2\times10^{-6} & 0.0004 & 0.0411 & 3.7938 \end{bmatrix} \quad (4\text{-}11)$$

$$\left[\boldsymbol{u}_1,\boldsymbol{u}_2,\boldsymbol{u}_3,\boldsymbol{u}_4\right]=\begin{bmatrix} 3.31\times10^{-6} & -7.29\times10^{-5} & 1.5345 & 0.7839 \\ 1.14\times10^{-6} & -2.37\times10^{-5} & 0.4234 & 1.2158 \\ 1 & 1 & 1 & 1 \\ 0.2755 & 1.5245 & 2.4250 & 2.5214 \end{bmatrix} \quad (4\text{-}12)$$

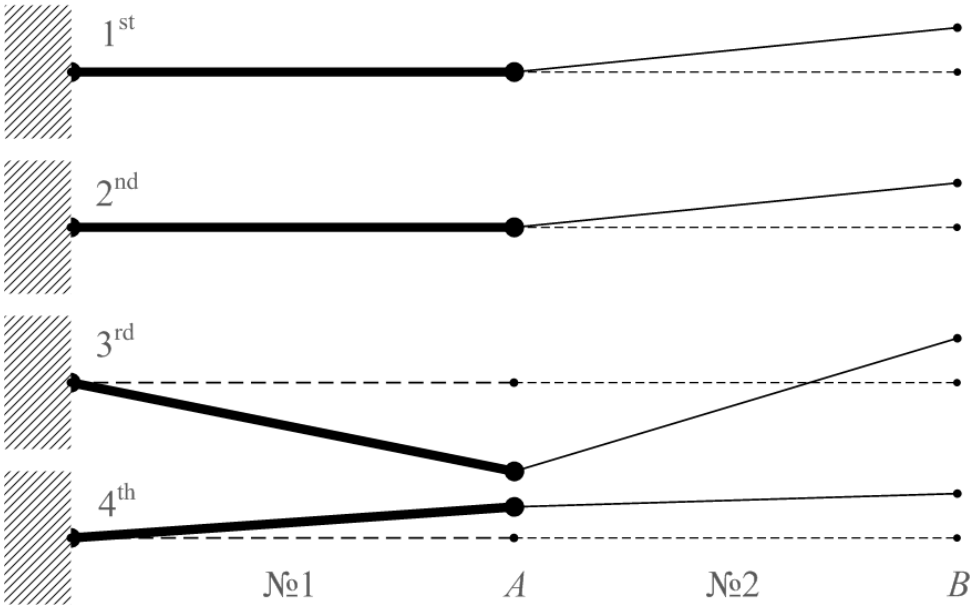

Figure 4.3: 4 Mode shapes of the cantilever beam including localized modes

Small values are significantly found for the 1st and 2nd eigenvalues because of the great difference between the stiffness and mass matrices. Meanwhile in the 1st and 2nd

eigenvectors, the values of displacements of node *A* are very small as well, which indicates that the node *A* stops vibrating and the total mode shapes are concluded as localized modes, as shown in Figure 4.3.

The 1st and 2nd order vibration shapes in the modal analysis results are typical localized modes, where the natural frequencies are rather low and the vibration takes place only in the low density area. The great difference between the stiffness and mass matrices due to the material interpolation model is concluded as the reason of this phenomenon.

To have a detailed view of the occurrence of the localized modes, the material property of the element №2 is modified step by step between η_2=1 and η_2=0.01. The modal analysis is carried out iteratively to show the variation of the eigenvalues and the mode shapes.

Since the localized modes appear in the 1st and 2nd order, only these two modes are analyzed. As shown in Figures 4.4 and 4.5, the variation of the two eigenvectors and eigenvalues are plotted in the curves versus the pseudo-density of element №2.

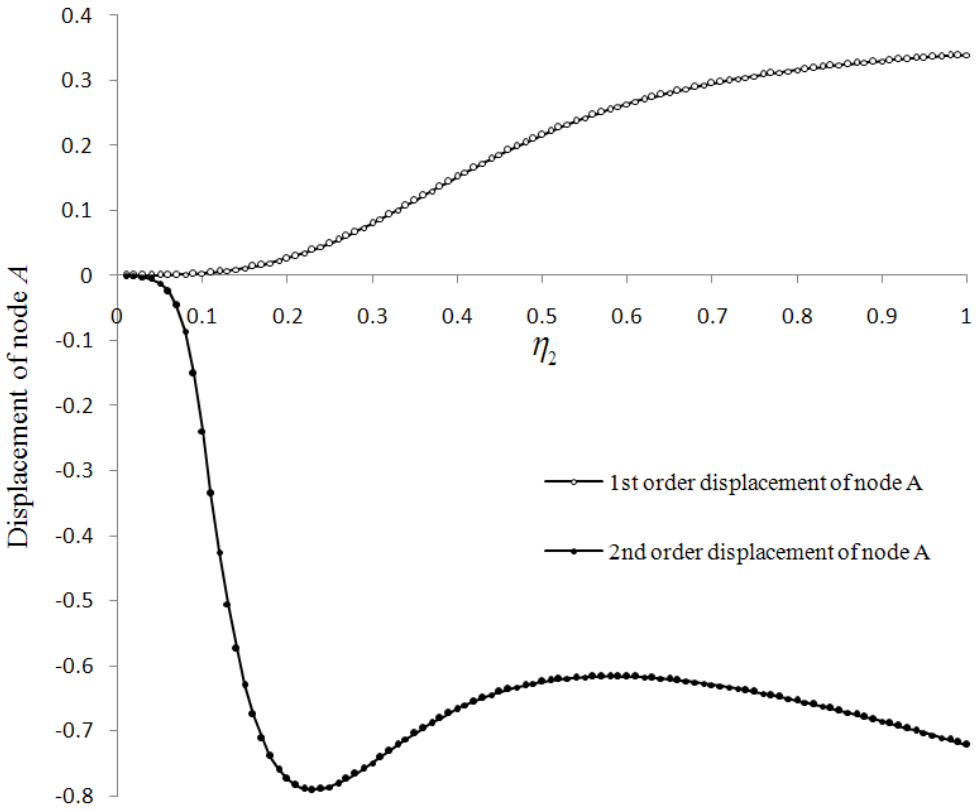

Figure 4.4: Displacement of Node *A* versus the material property of element №2

As shown in Figure 4.4, the vibrations of element №1 gradually stop when the material property of element №2 tends towards void. Meanwhile, although the eigenvalues are found decreasing quickly in Figure 4.5 as the pseudo-density decreases, the occurrence of the localized mode is actually continuous.

It is obvious that the curves will be divided into three sections from right to left, i.e. the normal modes, the generation of localized modes and completely localized modes. However, no clear bounds can be defined for these sections. Since there is no explicit form for the solution of eigenequation, it is difficult to describe the variation of the

eigenvalues and eigenvectors in a closed form.

Moreover, it is found that for the completely localized modes, which decreases of the eigenvalues depend on the material interpolation model. When the elements in the low-density area are compliant enough, the solid elements stop their vibration and act as approximately a rigid part which can be removed from the stiffness and mass matrices like the boundary conditions. Thus in this problem the eigenequation can be expressed as

$$\left(\boldsymbol{K}_2 - \omega^2 \boldsymbol{M}_2\right)\boldsymbol{u} = 0 \tag{4-13}$$

$$\begin{aligned}\omega^2\boldsymbol{u} &= \boldsymbol{M}_2^{-1}\boldsymbol{K}_2\boldsymbol{u} = \left(\eta_2\boldsymbol{M}_{20}\right)^{-1}\eta_2^3\boldsymbol{K}_{20}\boldsymbol{u} \\ &= \eta_2^2\boldsymbol{M}_{20}{}^{-1}\boldsymbol{K}_{20}\boldsymbol{u}\end{aligned} \tag{4-14}$$

where $\boldsymbol{K}_2$ and $\boldsymbol{M}_2$ are the stiffness matrices of the element №2, $\boldsymbol{K}_{20}$ and $\boldsymbol{M}_{20}$ are the corresponding stiffness and mass matrices when it is solid. The equation (4-15) shows the eigenvalues decrease in a parabolic way because of the SIMP interpolation. As shown in Figure 4.6, the refined variations of the eigenvalues in the completely localized modes and the interpolated parabolas are plotted.

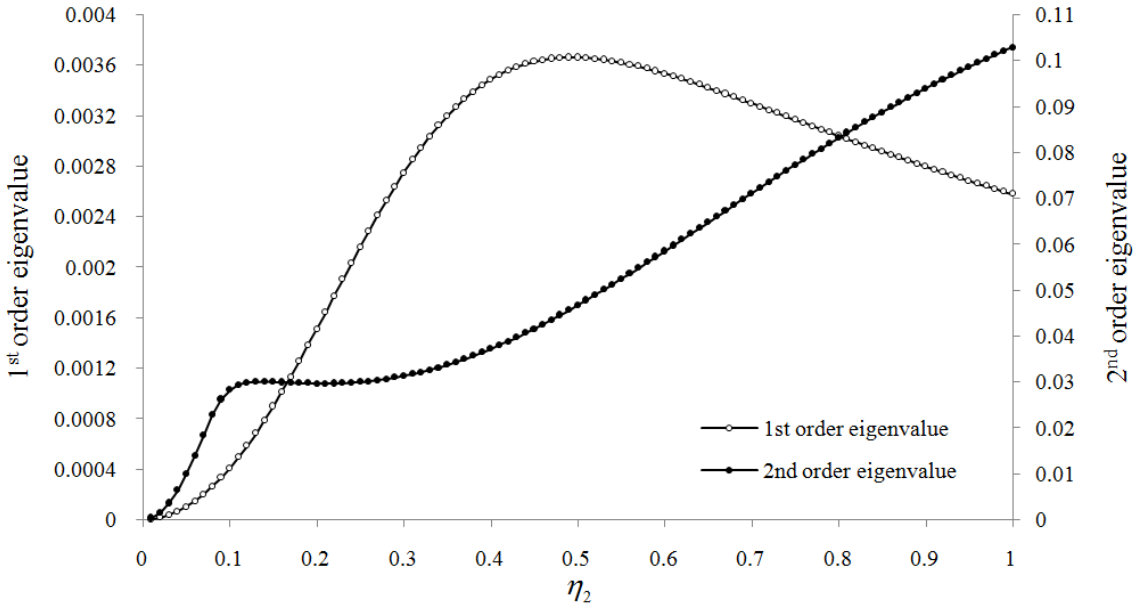

Figure 4.5: 1st and 2nd eigenvalues versus the material property of element №2

The 1st and 2nd eigenvalues and the interpolated parabola start to coincide at around η_2=0.12~0.15 and η_2=0.04~0.06, respectively. It is further validated by the variation of vibration shape in Figure 4.4, where the node *A* stops vibrating around these values.

According to the analysis, the lower bound of the pseudo-density design variables in SIMP must be greater than 0.1 or ever higher to ensure the stiffness of the low-density areas. But the low-density areas will not be void at all. Alternatively, although the difference between the stiffness and mass matrices can be controlled by using a lower penalty factor in SIMP, this will unfortunately weaken the penalty effect which is the key of SIMP method in generating clear black and white structural patterns. As a conclusion, the standard SIMP interpolation model with the power-law penalization cannot be used in

the topology optimization of eigenvalues maximization.

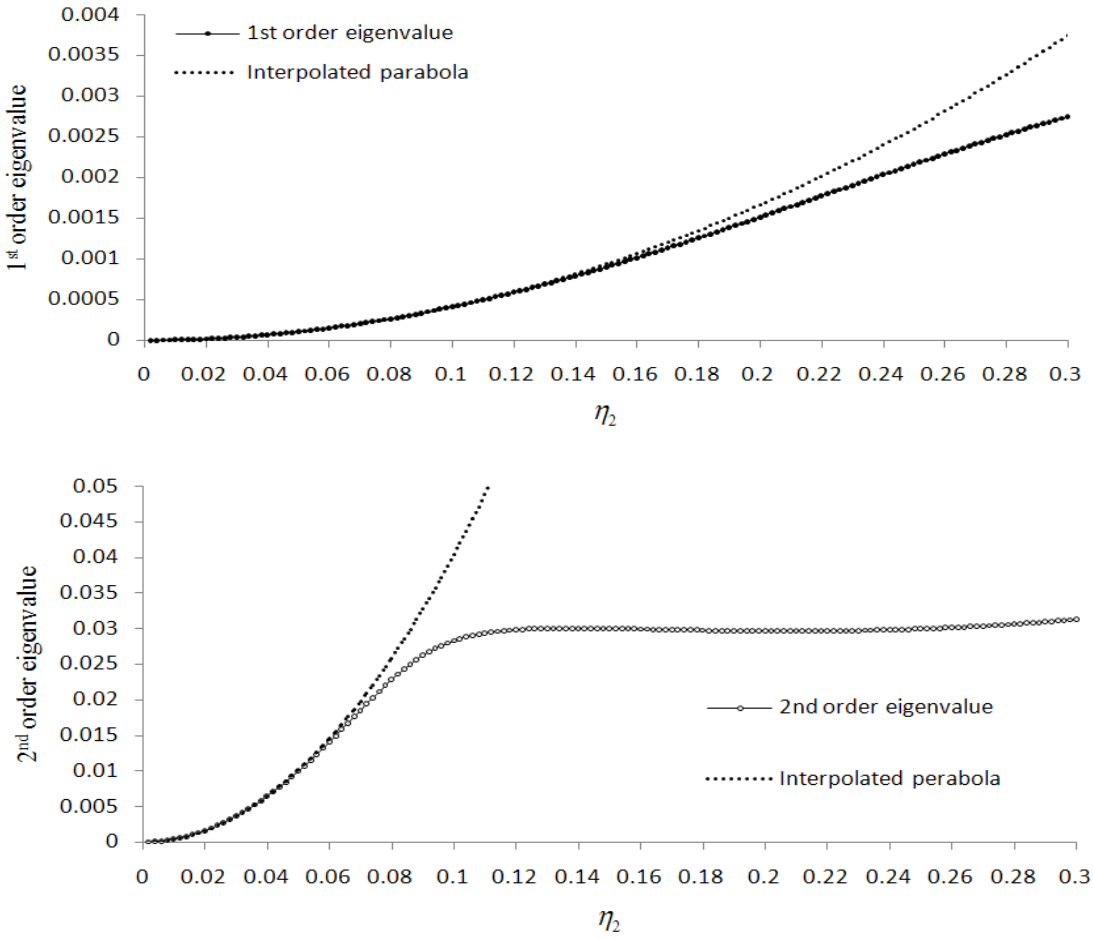

Figure 4.6: Variation of the eigenvalues versus the interpolated parabola

4.1.3 Numerical test with localized modes

A test of maximizing the fundamental frequency is carried out here to show how the localized modes influence the design. As shown in Figure 4.7, a 4m×4m square plate is divided into 40×40 fine quadrangular shell elements. A 0.8m×0.8m square area at the center of the plate is assigned as the non-designable part. All the four edges are completely clamped.

The material properties for the solid structure and the non-designable part are defined as:
elastic modulus E_0=7×10^{10}pa, density ρ_0=2700kg/m^3 and Poisson's ratio v=0.3

The SIMP model with the penalty factor p=3 is used here and 50% of the material is to be removed. The localized modes start to appear at the 8th iteration with the objective function decreases sharply. Later at the 16th and 17th iterations, some unsupported materials appear near the right corners on the top and bottom as shown in Figure 4.8.

The vibration shape at the 16th iteration is shown in Figure 4.9, where localized modes are obviously seen at the two corners. This will lead to high sensitivities of the neighborhood elements and create the unsupported material at the 17th iteration. Due to the incorrect calculation of the design objective and its sensitivities, these iterations are actually

meaningless.

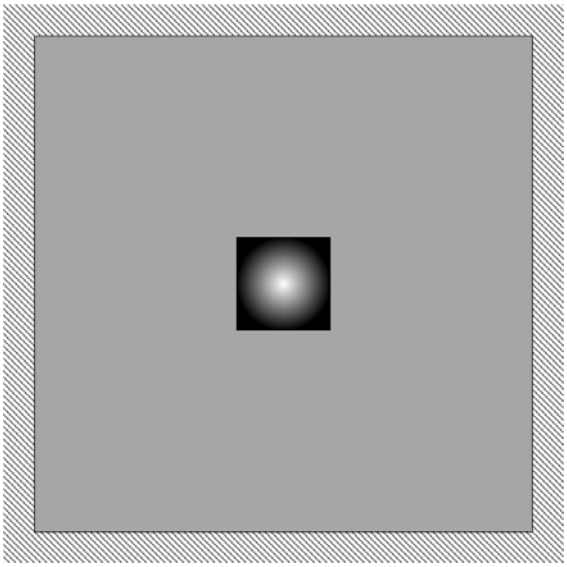

Figure 4.7: Design domain of the square plate

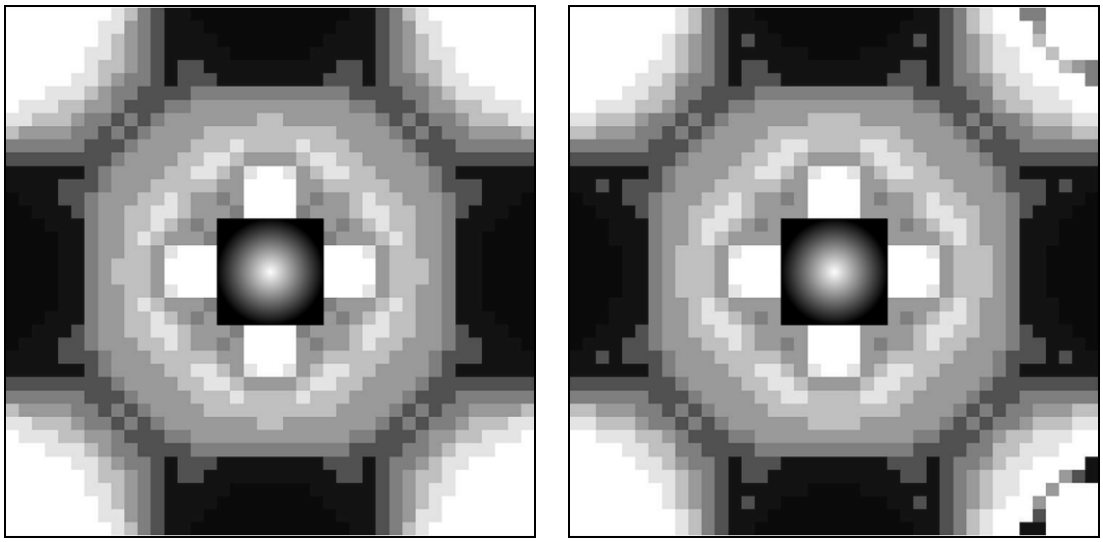

Figure 4.8: The material layout at the 16th (left) and 17th (right) iteration

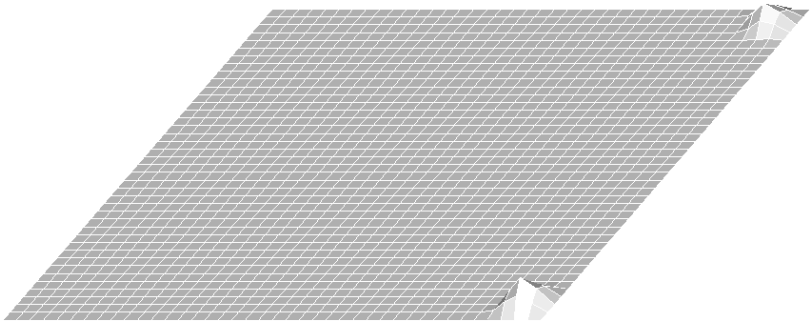

Figure 4.9 Vibration shape at the 16th iteration

Figure 4.10 shows the variation of the 1st natural frequency during the iteration. A sudden decrease of the frequency value occurs at the 8th iteration. Meanwhile the vibration mode

occurs in local areas, which is very different from the normal shape. The low-density areas are so compliant that rather low frequencies are obtained and the vibration takes up the lowest orders of the modes. Therefore, the phenomenon of localized modes is an ill-posed problem caused by the improperly defined material models. More discussions will be presented in section 4.3 to show the improved material interpolation models.

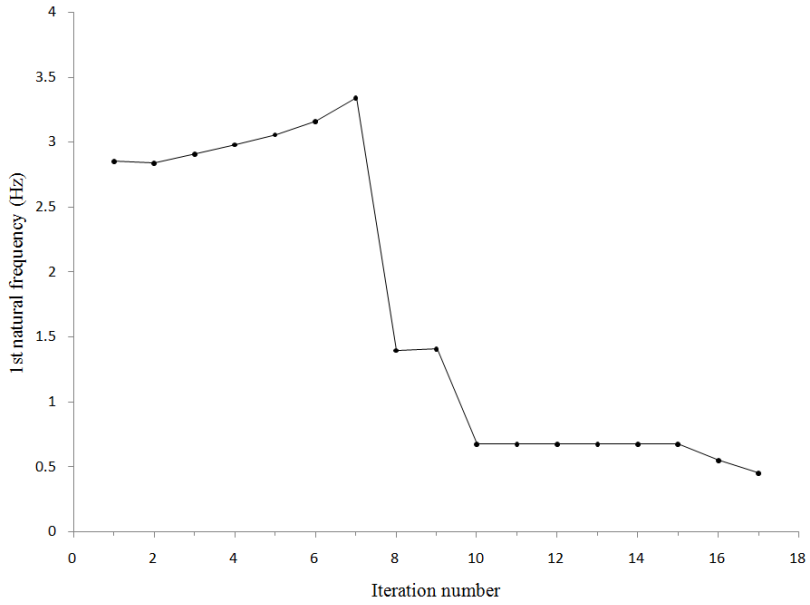

Figure 4.10: The iteration history of the 1st natural frequency

4.2 Localized deformation

In topology optimization with design dependent loads, the localized deformation is similar to the localized modes in eigenvalue problems. But this problem is easily understood and more descriptions can be found in Bruyneel and Duysinx (2004). Here, design dependent loads are those that change with respect to the variation of design variables, e.g. body force and pressure loads on a moving surface. Due to their existence, the low-density parts are too weak to support themselves. Consequently, deformations in the low-density areas become much larger than those in the solid parts. Here, new formulations are derived and numerical tests are made to address the problem.

4.2.1 Sensitivity analysis

With design dependent body forces, the design sensitivities of the strain energy with respect to the pseudo-densities are calculated on account of the derivatives of the loading vector. The finite element equation is expressed as

$$\boldsymbol{f} + \boldsymbol{G} = \boldsymbol{K}\boldsymbol{u} \tag{4-15}$$

And the total strain energy is

$$C = \frac{1}{2}\left(\boldsymbol{f} + \boldsymbol{G}\right)^T \boldsymbol{u} \tag{4-16}$$

where $\boldsymbol{G}$ is the inertial load vector that distributes and assembled to each node in the design domain with the inertial acceleration applied. A single load vector on the Ith node belonging to the ith element is expressed as

$$\boldsymbol{G}_i^{(I)} = \iint N_I \cdot \frac{\boldsymbol{G}_i}{S_i} \cdot dxdy = N_I \boldsymbol{G}_i \tag{4-17}$$

where N_I is the shape function at the Ith node of the ith element, S_i is the area of the element. $\boldsymbol{G}_i$ is the vertical and negative gravity vector of the ith element which can be written as

$$\boldsymbol{G}_i = \begin{bmatrix} 0 \\ -\eta_i \rho_0 g V_i \end{bmatrix} \tag{4-18}$$

where ρ_0 is the density of the solid material. g is the acceleration. V_i is the volume of the ith element. The global gravity load vector $\boldsymbol{G}$ is assembled at each node as

$$\boldsymbol{G} = \sum_i \sum_I \boldsymbol{G}_i^{(I)} \tag{4-19}$$

The derivative of the strain energy is put down as

$$\frac{\partial C}{\partial \eta_i} = \frac{1}{2}\left[\frac{\partial \boldsymbol{G}^T}{\partial \eta_i} \boldsymbol{u} + \left(\boldsymbol{f} + \boldsymbol{G} \right)^T \frac{\partial \boldsymbol{u}}{\partial \eta_i} \right] \tag{4-20}$$

The derivative of $\boldsymbol{G}$ with respected to ith pseudo-density can be transformed to the derivative of the corresponding $\boldsymbol{G}_i$ as

$$\frac{\partial \boldsymbol{G}}{\partial \eta_i} = \sum_I \frac{N_I \partial \boldsymbol{G}_i}{\partial \eta_i} \tag{4-21}$$

Note that the derivative of the displacement vector can be found in the last chapter when we derive the design sensitivity with respect to the pseudo-densities defined at the density points. The final sensitivity is very similar to that in the eigenvalue maximization problems.

4.2.2 Problem occurrence

The same beam in section 4.1.2 is used here with a vertical gravity acceleration g=10m/s^2 applied. Suppose the material properties of the solid element are

Elastic modulus E= 10^{11}pa, density ρ= 1000kg/m^3 and Poisson's ratio v=0.3

The gravity of the beam is discretized into nodal loads as shown in Figure 4.11.

The material properties of the element №2 is interpolated with the SIMP model and the penalty factor is set to be p=3. Although the gravity of the element №2 decreases linearly with the value of η_2, the elastic modulus decreases much faster. As shown in Figure 4.12, the nodal displacement is plotted versus the decreasing of η_2.

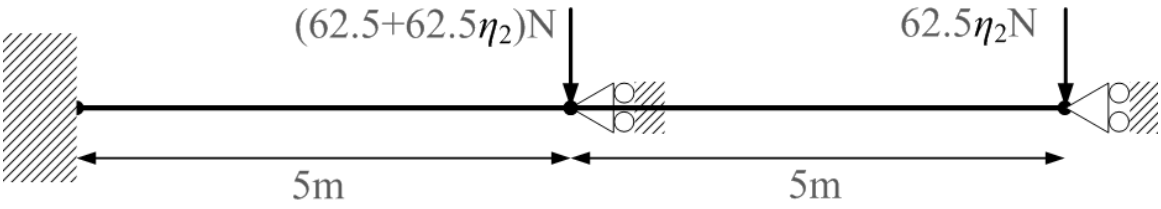

Figure 4.11: The equivalent nodal loads when gravity is applied

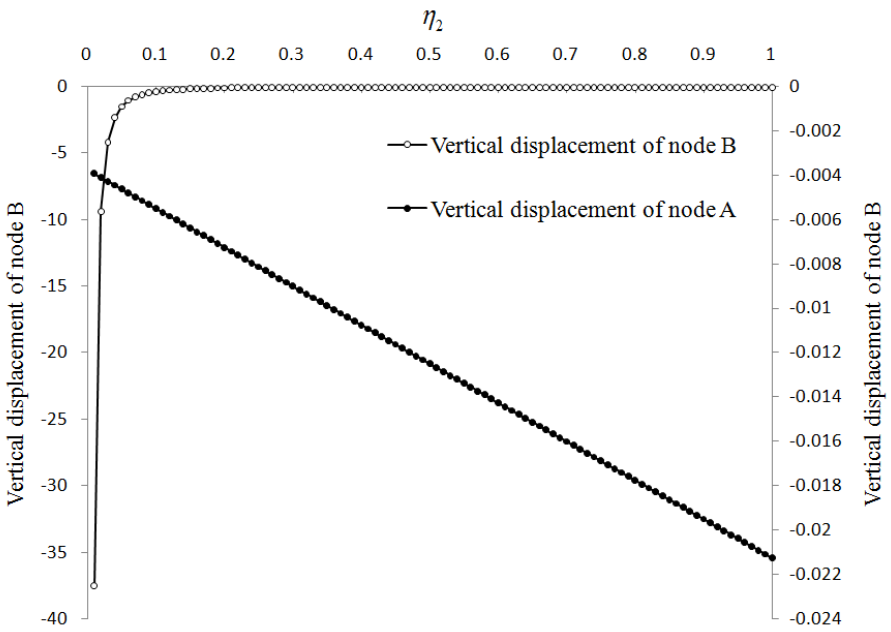

Figure 4.12: Nodal displacements versus the pseudo-density of element №2

Both nodal loads vary linearly with η_2. As the material properties of element №1 remain unchanged, a linear relation is obtained between the displacement of node *A* and η_2. Comparatively, as the stiffness of element №2 varies with the cubic exponent of η_2, the absolute displacement of node *B* increases sharply around η_2=0.05, which generates a relatively large localized deformation.

Unlike the vibration shapes obtained in localized modes, the localized deformation of the solid area is actually correct. However, the incredibly large displacements may cause erroneous design sensitivities which will further lead to the non-preferred topology design solution.

4.2.3 Numerical test with localized deformations

A test problem of topology optimization with inertial loads is firstly carried out. The standard SIMP model is used here. The penalty factor *p* is set to be 3. The design domain as shown in Figure 4.13 consists of 50×100 quadrangular finite elements. Only half of the area is taken into account because of the symmetry. The material properties are defined as elastic modulus E_0=7×10^{10}pa, density ρ_0=2700kg/m^3 and Poisson's ratio ν=0.3

Problems occur at the 13th iteration as shown in Figure 4.14. Because of the power-law interpolation for the material properties, the low density areas are too compliant to support themselves. Localized deformations appear at the bottom center as shown in

Figure 4.14(b). And the result of the calculation has shown that the most sensitive elements are located around the area with large deformation, which further generates some unconnected structures in the following iterations. As a result, the optimization stops at the 19th iteration with an ill-posted pattern as shown in Figure 4.14(c).

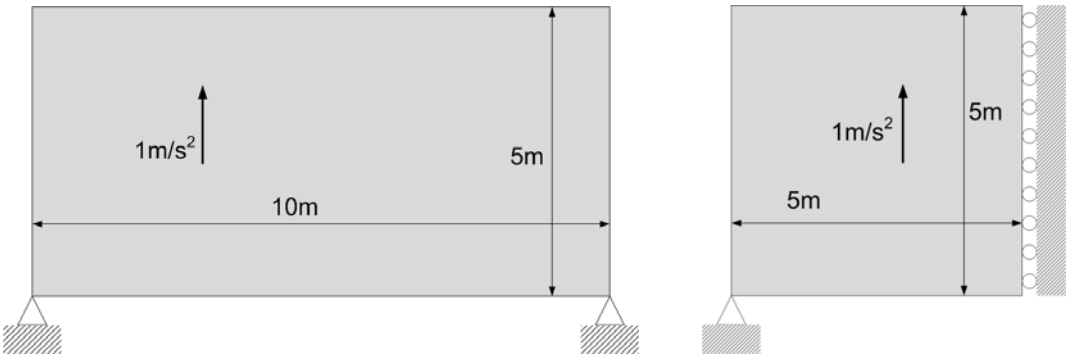

Figure 4.13: Design domain of the test example

(a) Material layout at 13th iteration

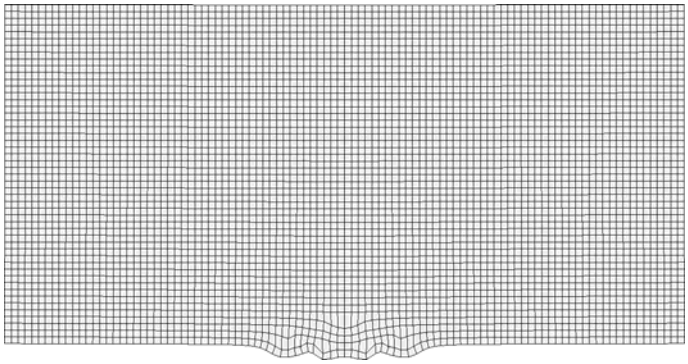

(b) Localized deformation at 13th iteration

(c) Material layout at 19th iteration

Figure 4.14: Solutions obtained with standard SIMP model

4.3 Modified interpolation model

The most popular power-law interpolation of SIMP for the stiffness and mass matrix is expressed as

$$\begin{aligned} \boldsymbol{K}_i &= P(\eta_i)\boldsymbol{K}_{i0} = \eta_i^p \boldsymbol{K}_{i0} \\ \boldsymbol{M}_i &= \eta_i \boldsymbol{M}_{i0} \end{aligned} \tag{4-22}$$

where the stiffness matrix and the mass matrix are proportional to the elastic modulus and material density, respectively. As analyzed in the last section, the SIMP interpolation model is not proper in topology optimization of maximizing the eigenvalues or those with design dependent loads.

To evaluate the difference between the stiffness and mass, a ratio of the pseudo-density value to the penalty function (also seen in Pedersen 2000) is introduced as

$$R_{MK} = \frac{\eta_i}{P(\eta_i)} \tag{4-23}$$

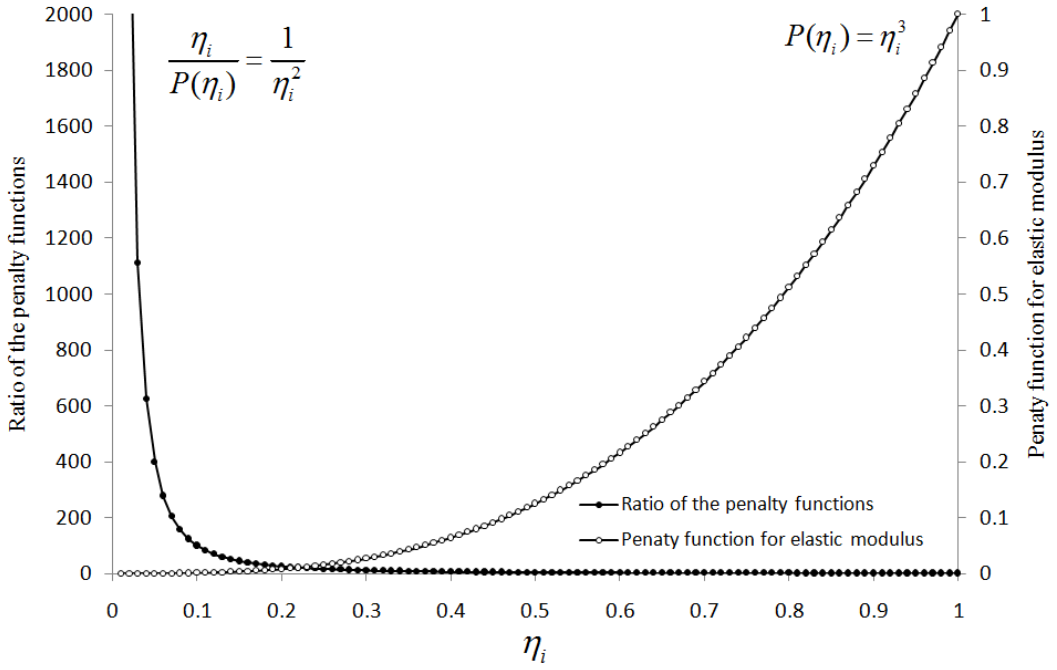

Figure 4.15: Interpolation model and ratio of the penalty functions of standard SIMP

Both the SIMP interpolation model with the penalty factor p=3 and the ratio R_{MK} are plotted with respect to the pseudo-density as shown in Figure 4.15. The value of the ratio trends towards infinity when the pseudo-density goes to zero, which indicates a great difference between the stiffness and mass matrices.

As indicated before, this difference can be partially improved by using a higher value for the lower bound of the pseudo-density or assigning a weaker penalty factor. However, these implementations bring more problems in topology optimization and are not

preferred here. More improvements on the penalty function have to be proposed.

The first improved model discussed here was presented in Pedersen (2000), which constrains the lower bound of the elastic modulus to be 1/1000 of the solid one, i.e.

$$\begin{aligned} P(1) &= 1 \\ P(0) &= 0.001 \end{aligned} \tag{4-24}$$

A cubic function is built accordingly as

$$P(\eta_i) = \eta_i^3 + 0.001\left(1-\eta_i^3\right) \tag{4-25}$$

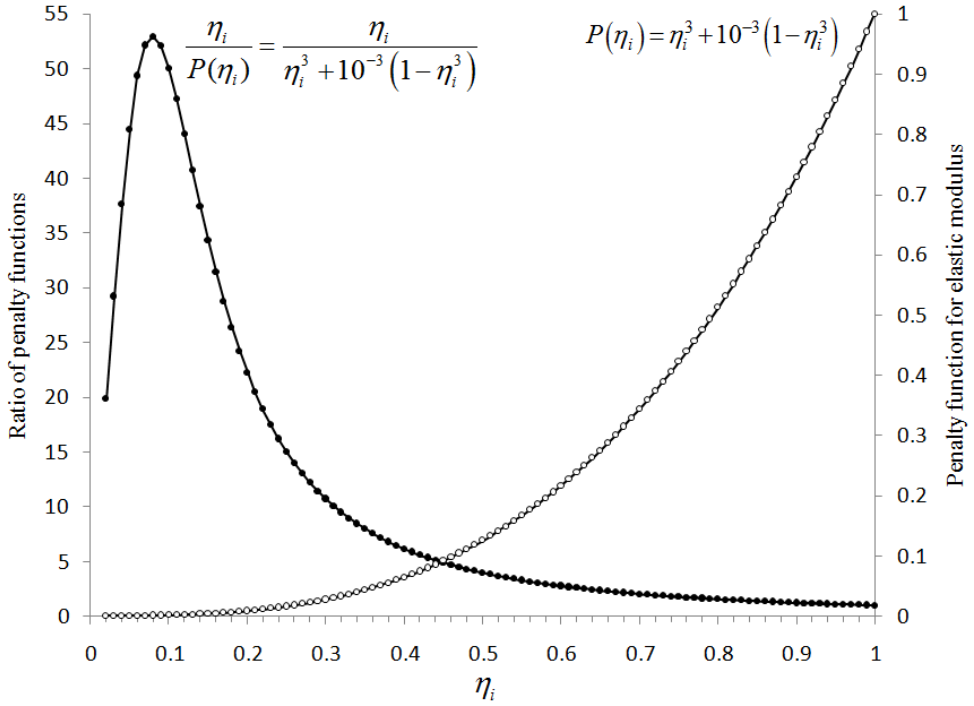

Figure 4.16: Improved model constraining the lower bound of the elastic modulus

This function and the ratio R_{MK} are plotted in Figure 4.16. Although only a slight modification is made to the penalty function, the value of the ratio will not trend towards infinity when the pseudo-density goes near zero.

This interpolation model can be used to solve some eigenvalue maximization problems and avoid the localized modes. However, there is still an unsatisfied peak value of the ratio around $\eta_i = 0.1$, which will possibly lead to localized modes in some cases.

Later, it is found that the low-density material properties described by the microstructures can retain more stiffness than those by the SIMP model. Take the "□" shape microstructure for example, the equivalent tensile stiffness is calculated here with the strain energy based method (see Pedersen and Tortorelli 1998, Zhang et al. 2007), which was proved to be equivalent to the homogenization method in predicting the effective elastic material properties (Hori & Nemat-Nasser 1999). The boundary conditions are defined as shown in Figure 4.17. The horizontal displacements on the left edge are constrained. A uniform horizontal displacement u is assigned on the right edge. The

volume fraction of the microstructure is calculated as

$$\eta = \frac{l_1^2 - l_2^2}{l_1^2} \tag{4-26}$$

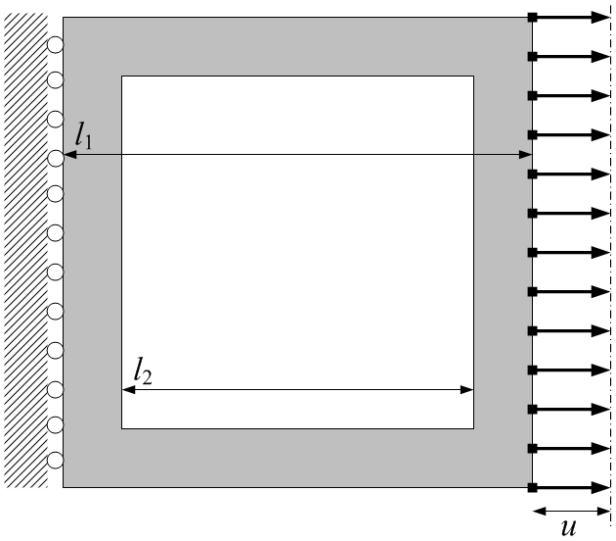

Figure 4.17: Definition of the microstructure and the boundary conditions

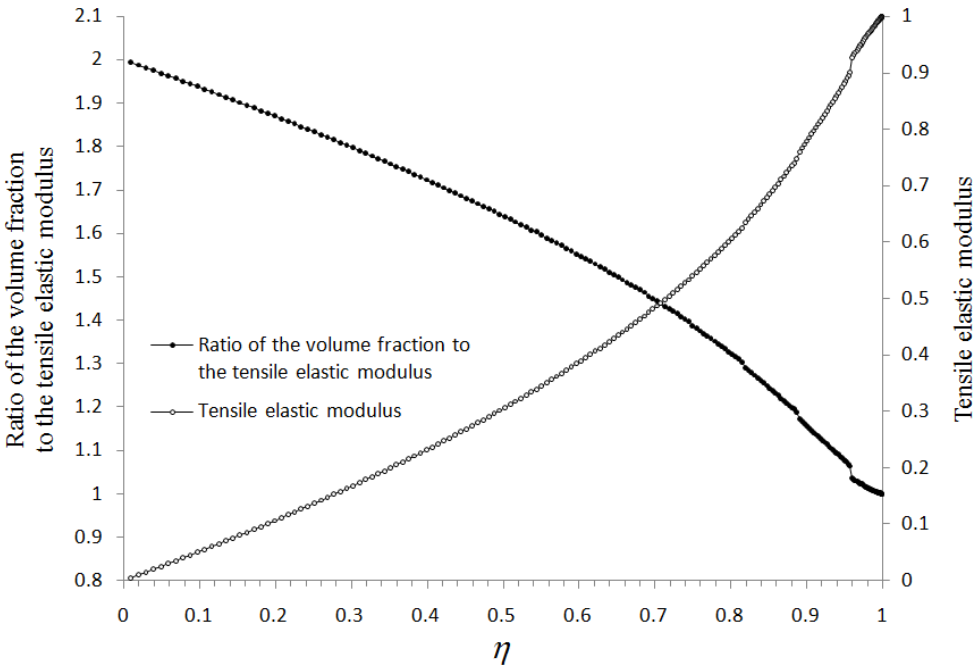

Figure 4.18: The horizontal tensile elastic modulus versus the volume fraction of the "□" shaped microstructure

After the finite element analysis, the horizontal tensile elastic modulus is calculated as

$$\frac{Eu}{l_1} = \frac{f_R}{l_1 t} \tag{4-27}$$

$$E = \frac{f_R}{ut} \tag{4-28}$$

where E is the equivalent tensile elastic modulus, f_R is the summation of the nodal reaction forces on the left edge. t is the thickness of the microstructure. We assume l_1=u=t=1 and l_2 varies from 0.005 to 0.995 in the test. The relation between the horizontal tensile elastic modulus and the volume fraction are plotted in Figure 4.18. And the ratio here just corresponds to the ratio R_{MK} in the pseudo-density interpolation models.

Compared with the curves of SIMP in Figure 4.15, apparently when η = 0, the slope of the tensile elastic modulus is positive and the ratio of the volume fraction to the tensile elastic modulus is limited to a small value which is approximately equal to 2.

The maximum value of the ratio can be proved by ignoring the two vertical edges of the microstructure when η is rather small. As a result, the summation of nodal reaction forces is approximately calculated as the inner tensile forces of the two horizontal edges.

$$\frac{f_R}{(l_1 - l_2)t} = \frac{E_0 u}{l_1} \tag{4-29}$$

where E_0 is the elastic modulus of the solid material forming the microstructure. The equivalent tensile elastic modulus is then calculated by

$$\frac{Eu}{l_1} = \frac{f_R}{l_1 t} = \frac{E_0 u(l_1 - l_2)}{l_1^2} \tag{4-30}$$

$$E = \frac{E_0(l_1 - l_2)}{l_1} \tag{4-31}$$

And the ratio of the volume fraction to the tensile elastic modulus is expressed as

$$\lim_{\eta \to 0} \frac{\eta}{E} = \lim_{l_2 \to l_1} \frac{(l_1^2 - l_2^2)}{l_1^2} \cdot \frac{l_1}{E_0(l_1 - l_2)} = \lim_{l_2 \to l_1} \frac{l_1 + l_2}{l_1 E_0} = \frac{2}{E_0} \tag{4-32}$$

where E_0 is predefined as 1 in this example. At η = 0, it is further derived that the derivative of E with respect to η is 0.5, which makes the curve so different from that of the SIMP model.

However, the computational complexities of homogenization are involved when the microstructures are used as the equivalent elements in topology optimization. It is better to construct new simplified interpolation models according to the analysis result of microstructure.

The RAMP (Stolpe and Svanberg 2001) presented in Chapter 1 is an interpolation model of this kind. It controls the derivative of the penalty function when the pseudo-density nears zero.

The penalty function and its derivative at η_i = 0 can be expressed as

$$P(\eta_i)=\frac{\eta_i}{1+q(1-\eta_i)} \tag{4-33}$$

$$\lim_{\eta_i\to 0} P'(\eta_i)=\lim_{\eta_i\to 0}\frac{1+q-(1+q)\eta_i}{(1+q-q\eta_i)^2}=\frac{1}{1+q} \tag{4-34}$$

where q is the penalty factor of RAMP, which is always positive. The penalty function and the ratio R_{MK} are plotted in Figure 4.19, where we set q=5. It is obvious that the ratio R_{MK} is actually linear with respect to the pseudo-density.

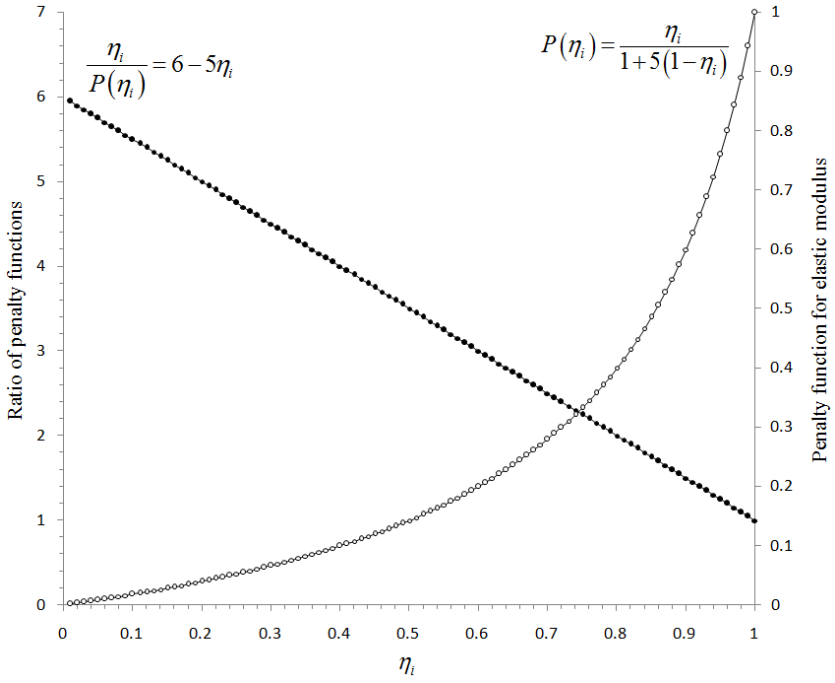

Figure 4.19: Interpolation model and ratio of the penalty functions of RAMP

With the RAMP model, it is theoretically proved that the design objective function of structural compliance is concave when q is greater than a certain value. More numerical examples of compliance minimization, compliant mechanisms and natural frequency maximization problems using RAMP can be found in Luo et al. (2004). However, a strong penalty, e.g. q can be greater than 100, which will generate a large value of the ratio.

Another improved interpolation model presented by Pedersen (2000), Bruyneel and Duysinx (2004) is defined as a modification of the SIMP model

$$E_i=P(\eta_i)E_{i0}=\begin{cases}(\eta_i/\alpha)E_{i0}; & \eta_i\le\alpha^{\frac{1}{1-p}}\\ \eta_i^p E_{i0} & ;\ \eta_i>\alpha^{\frac{1}{1-p}}\end{cases} \tag{4-35}$$

where the interpolation model is composed of two sections, i.e. a linear penalty with a slope $1/\alpha$ and the standard SIMP model with a power law interpolation. The linear penalty is defined to ensure the positive derivative near η_i=0. Two parameters α and p are

independent, which can separate the modification of the ratio R_{MK} and the penalty effect.

As shown in Figure 4.20, the penalty function and the ratio R_{MK} are plotted, respectively. The linear penalty actually has the ratio R_{MK} cut at the value α, which limits the maximum value.

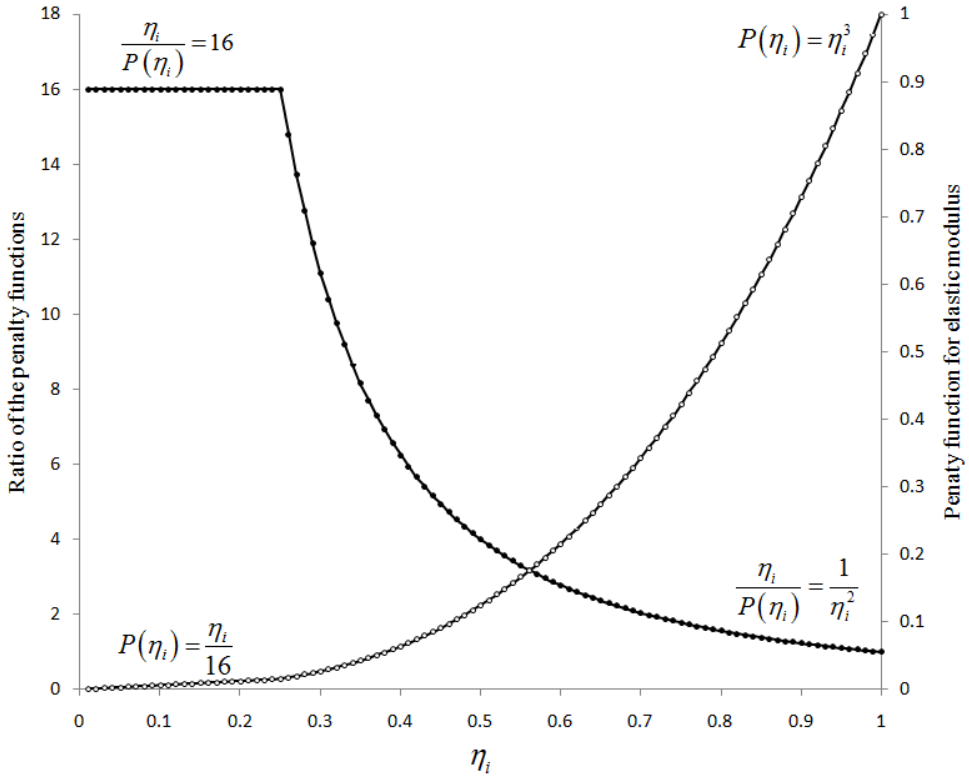

Figure 4.20: Improved SIMP model with linear penalty

The improved interpolation model is effective for topology optimization problems with self-weight or natural frequencies maximization. However, critical comments are received that the design sensitivities are discontinuous at $\eta_i = \alpha^{1/(1-p)}$.

Therefore, further improvements are carried out in this work. Based on the SIMP model and the derivative control at η_i=0, a penalty function has to satisfy the following requirements:

1) The value at two end points

$$P(0)=0,\ P(1)=1; \tag{4-36}$$

2) The derivative value at η_i=0

$$\lim_{\eta_i \to 0} P'(\eta_i)=\frac{1}{\alpha},\ \alpha>0; \tag{4-37}$$

3) To ensure a convex penalty function, the 2nd derivatives shall also satisfy

$$P''(\eta_i)>0,\ \forall\ 0<\eta_i \le 1 \tag{4-38}$$

4) The 1st derivative continuity will be guaranteed at least

Obviously, only the 2nd condition i.e. the control of the derivative value at η_i=0 is different from the standard SIMP. That's why only a slight change has to be made. The modified function can be expressed as

$$P(\eta_i) = \frac{\alpha - 1}{\alpha}\eta_i^p + \frac{1}{\alpha}\eta_i \qquad (4\text{-}39)$$

As shown in Figure 4.21, the new penalization function and its ratio R_{MK} are plotted, respectively. It takes a simple form of polynomial function and satisfies all the required conditions. The ratio R_{MK} is limited to the value α, and the derivative of the penalty function is continuous everywhere. Moreover, compared with the function presented by Pedersen (2000) and Bruyneel and Duysinx (2004), it is more convenient to program and to evaluate material properties and the design sensitivities because no if-else condition is included.

In Figure 4.21, the two examples given in Sections 4.1 and 4.2 are tested here with such a new polynomial interpolation model. For the vibrating square plate, the optimization is carried out by removing 50% of the material. One intermediate iteration of the material layout as well as the corresponding vibration shape are shown in Figure 4.22(a) and Figure 4.22(b), respectively. It is obvious that the vibration shape is a global deformation and the problem of localized modes is avoided.

The optimization is further processed and the convergence attains at the 42nd iteration. The non-designable area is finally supported as shown in Figure 4.22(c). Similar topology design problem and optimal material layout can be found in Pedersen (2000). The convergence history of the objective function is rather stable as shown in Figure 4.23.

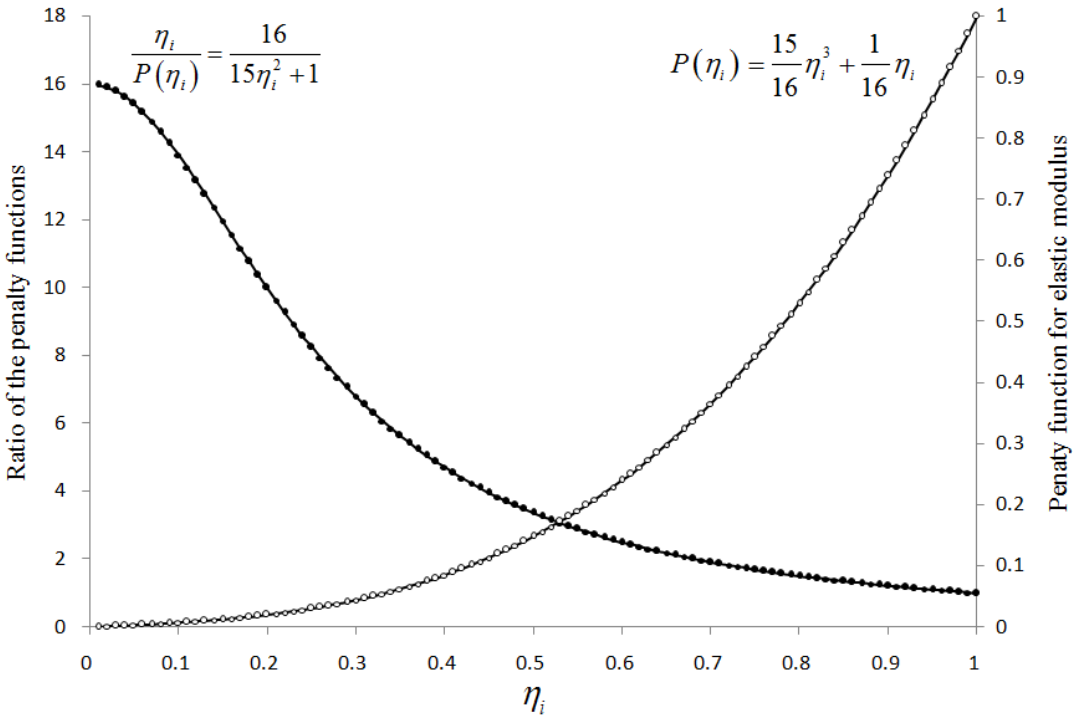

Figure 4.21: Further improved polynomial interpolation model based on SIMP

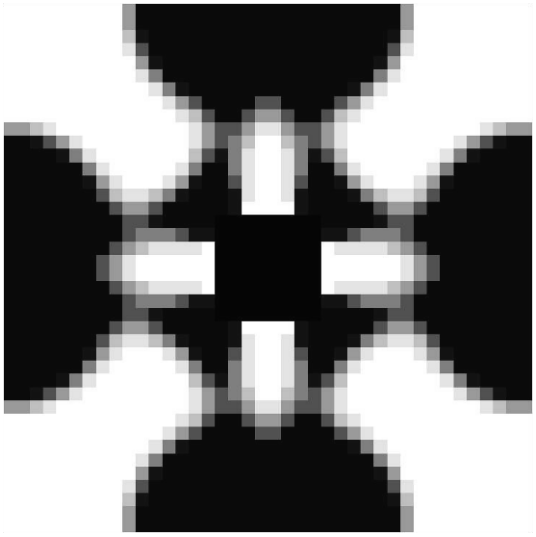

(a) Material layout at 30th Iteration

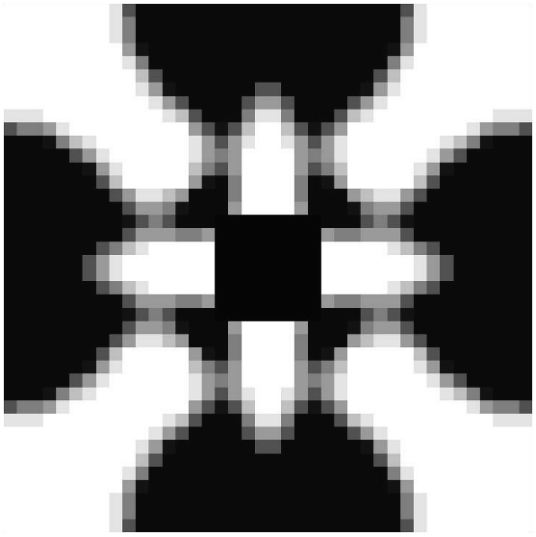

(c) Material layout at 42nd Iteration

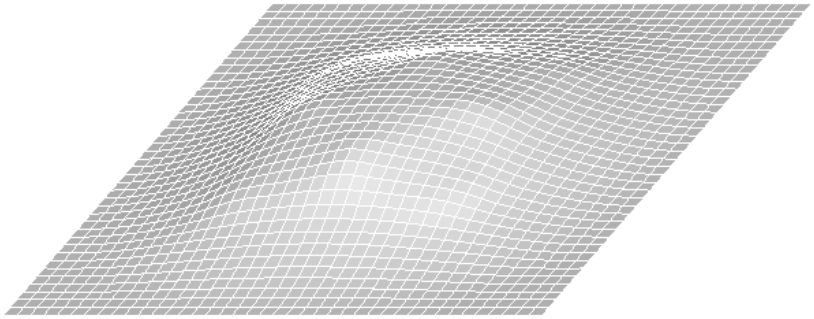

(b) Vibration shape at 30th iteration

Figure 4.22: Layout design of the square plate with the new interpolation model

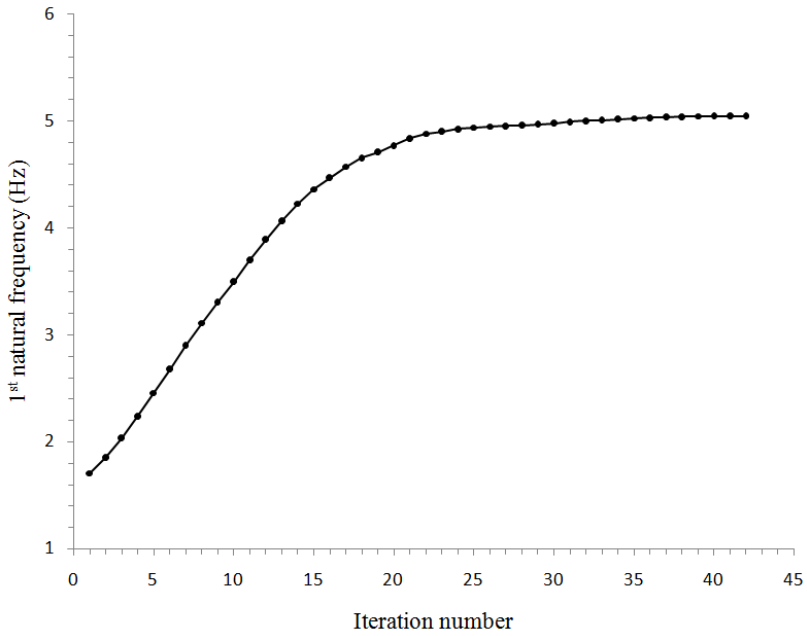

Figure 4.23: Convergence history of the 1st natural frequency

Again, the topology optimization problem with inertial loads is tested here. One

intermediate solution and the corresponding deformation shape are shown in Figures 4.24(a) and (b), respectively. There is no localized deformation found in the design domain. By continuing the design iteration, the final optimal material layout is obtained at the 38th iteration, which is a typical arc. Similar topology optimization problems can be found in Bruyneel and Duysinx (2004).

(a) Material layout at 16th iteration

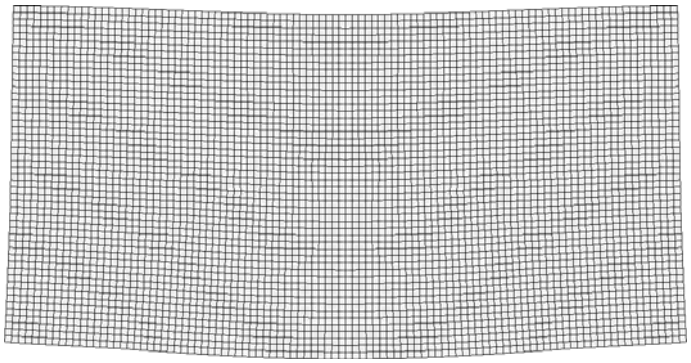

(b) Global deformation at 16th iteration

(c) Material layout at 38th iteration

Figure 4.24: Solutions obtained with new improved interpolation model

The convergence history of the global train energy is shown in Figure 4.25, which is also rather stable.

According to the two new numerical results, the new polynomial interpolation model is effective in avoiding the problems of localized modes and localized deformations, which will benefit the integrated layout design of the multi-component systems with vibrations and design-dependent body loads to be discussed in the following chapters.

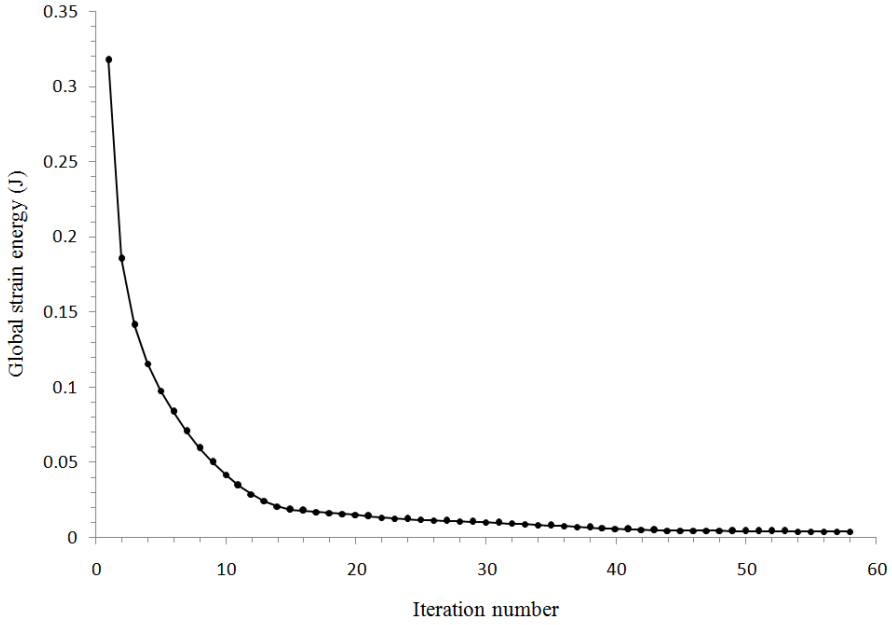

Figure 4.25: Convergence history of the global strain energy

4.4 Break-down in ESO

The topic discussed in this section has no direct relation with the integrated layout optimization. However, it is an interesting numerical problem involved in the family of Evolutionary Structural Optimization (ESO) method which can be discussed from the viewpoint of low-density areas.

The ESO approach is easily understood and implemented with less mathematical rigor. Based on the heuristic engineering concepts and sensitivity results, the optimal structural layout is achieved by removing inefficient elements systematically from the ground structure. Numerical results have shown that a variety of problems, e.g., maximal design of structural stiffness (Xie and Steven 1994a), natural frequency (Xie and Steven 1994b, 1996) and buckling load (Rong and Xie 2001) can be dealt with by this method. However, the breakdown problem of ESO discovered by Zhou and Rozvany (2001) is still a fatal drawback of this method.

4.4.1 Limitations of current ESO/BESO methods

In ESO/BESO method, the problem can be basically expressed as a topology optimization with discrete design variables. With the volume constraint assumed, the design objective is to minimize the global strain energy or maximize the natural frequencies etc.

In the framework of ESO/BESO, element deletions and recoveries are carried out in virtue of the element efficiency which is measured by the sensitivity values or stress level. Conventionally, the commonly used sensitivity value of the global strain energy with respect to the density of *i*th element is approximated by

$$\frac{\Delta C}{\Delta \eta_i} \approx -\frac{1}{2}\boldsymbol{u}_i^T \boldsymbol{K}_i \boldsymbol{u}_i = -C_i \qquad (4\text{-}40)$$

where C_i is the strain energy of the ith element.

For a dynamic problem, the sensitivity value is approximated by

$$\frac{\Delta\omega^2}{\Delta\eta_i} \approx \frac{\boldsymbol{u}_i^T \boldsymbol{K}_i \boldsymbol{u}_i - \omega^2 \boldsymbol{u}_i^T \boldsymbol{M}_i \boldsymbol{u}_i}{\boldsymbol{u}^T \boldsymbol{M} \boldsymbol{u}} \tag{4-41}$$

In both of the sensitivity derivations, $\Delta\eta_i$ is always set to be -1 indicating that element i is completely removed from the design domain.

In fact, the sensitivity values used here are approximated because we cannot directly obtain all the sensitivity values of the finite difference with only one finite element analysis. Sensitivity values of (4-41) and (4-42) used in the hard-killing scheme of ESO/BESO are nothing but the analytical sensitivities.

$$\frac{\partial C}{\partial \eta_i} = -\frac{1}{2} \boldsymbol{u}_i^T \boldsymbol{K}_i \boldsymbol{u}_i = -C_i \tag{4-42}$$

$$\frac{\partial \omega^2}{\partial \eta_i} = \frac{\boldsymbol{u}_i^T \boldsymbol{K}_i \boldsymbol{u}_i - \omega^2 \boldsymbol{u}_i^T \boldsymbol{M}_i \boldsymbol{u}_i}{\boldsymbol{u}^T \boldsymbol{M} \boldsymbol{u}} \tag{4-43}$$

which can be derived by supposing a linear interpolation model for $\boldsymbol{K}_i$ and $\boldsymbol{M}_i$ as a function of η_i with

$$\begin{aligned} \boldsymbol{K}_i &= \eta_i \boldsymbol{K}_{i0} \\ \boldsymbol{M}_i &= \eta_i \boldsymbol{M}_{i0} \end{aligned} \tag{4-44}$$

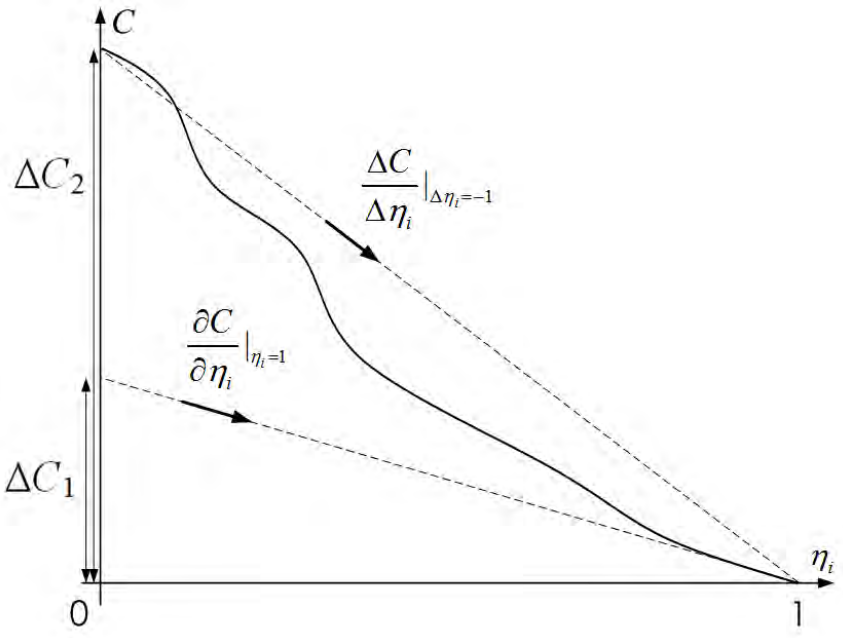

Figure 4.26: Comparison of two kinds of sensitivities

$\boldsymbol{K}_{i0}$ and $\boldsymbol{M}_{i0}$ denote the stiffness and mass matrices of the ith element when it is solid. It is obvious that the analytical sensitivities are unable to represent the real change of the

objective function whenever the inefficient element i is directly removed from the design domain ($\Delta\eta_i$=-1). To figure out the problem, consider two kinds of sensitivities shown in Figure 4.26.

The solid curve in Figure 4.26 represents the objective function versus η_i. This is typically the case for the structural compliance with values of other design variables being invariable. ΔC_1 corresponds to the change of C evaluated with the analytical sensitivity value when the ith element is removed by ESO/BESO from the design domain, whereas ΔC_2 represents the exact change of C after the removal of the ith element. Clearly, both are quite different from each other.

The change of the objective function will be overestimated when $\Delta C_1 > \Delta C_2$. This is a conservative situation so that some inefficient elements are retained in the actual iteration. In contrast, as $\Delta C_1 < \Delta C_2$, particularly when a sharp difference exists, this is the danger if related elements could be erroneously considered to be inefficient, removed and no longer recoverable during the iterations.

Although lots of existing results have shown that the convergence of the iteration procedure is not deteriorated by ESO/BESO, the understanding of the nature of the solid curve in Figure 1 is essential to reveal the underlying trouble of ESO/BESO.

To illustrate the phenomenon and reasons for the failure of ESO, a test example from Zhou and Rozvany (2001) is analyzed here in detail. The FE model shown in Figure 4.27 consists of a 32m×3m horizontal beam and a 1m×4m vertical link meshed with 0.25m×0.25m 4-node quadrangular elements. The material properties are

Elastic modulus E_0=1pa, Poisson's ratio v=0

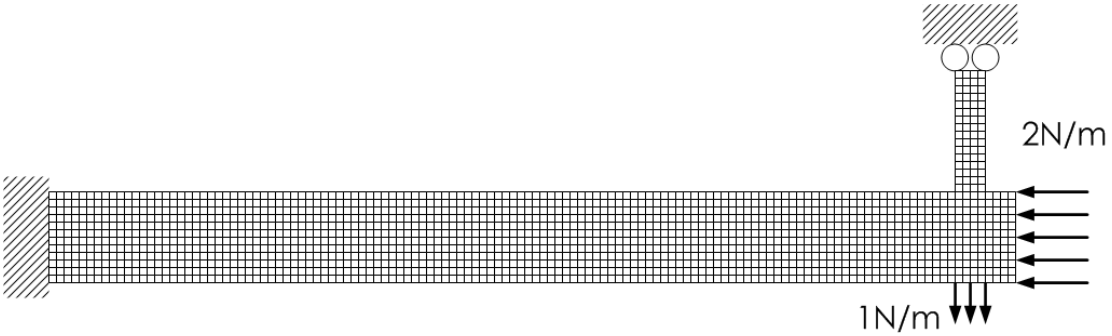

Figure 4.27: A test example for the failure of ESO

To figure out the difficulty, the initial distribution of the element strain energies which indicate the absolute sensitivity values is firstly evaluated and shown in Figure 4.28(a). It is found that the elements on the vertical link take the lowest strain energy and should be removed in the ESO procedure. When the updated model is reanalyzed, a new distribution of the element strain energies is shown in Figure 4.28(b) with a sudden augmentation of the structural compliance C to more than 10 times. This implies that a fatal iteration is generated. Unfortunately, the elements with the maximum strain energies are now relocated at the left bottom corner of the horizontal part so that the erroneously removed elements on the vertical link are no longer recovered by BESO.

(a) Layout of the element strain energy for the full structure (C=194.9J)

(b) Layout of the element strain energy by removing the vertical link (C=2306.1J)

Figure 4.28: Layout of the element strain energy in the design patterns by ESO

To find out the reason for this sudden variation of the objective function, the strain energy of the total structure C is drafted versus the variation of the elastic modulus of elements E on the vertical link from 1pa to 10^{-7}pa in Figure 4.29 where the axis of E is logarithmic.

In Figure 4.29, very small derivatives on the curve are obtained near E=1 and E=0, respectively. This indicates that the elements are not so sensitive when it is solid or void. As a result, these elements are removed firstly in ESO and cannot be recovered by BESO.

Furthermore, a significant change of C can be observed for values of E between 10^{-2}pa to 10^{-5}pa. But as discussed before, the sensitivities used in ESO cannot detect the sharp variation of the global strain energy. Thus, the vertical link is apparently considered to be inefficient and completely removed. This is the fatal error which leads to the design failure.

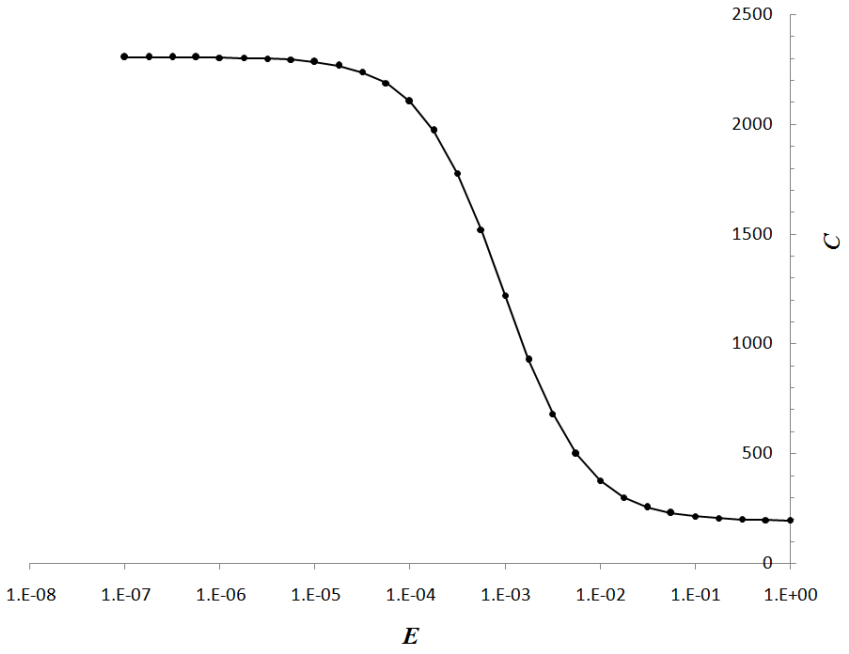

Figure 4.29: Global strain energy versus elastic modulus on the vertical link

4.4.2 Check position

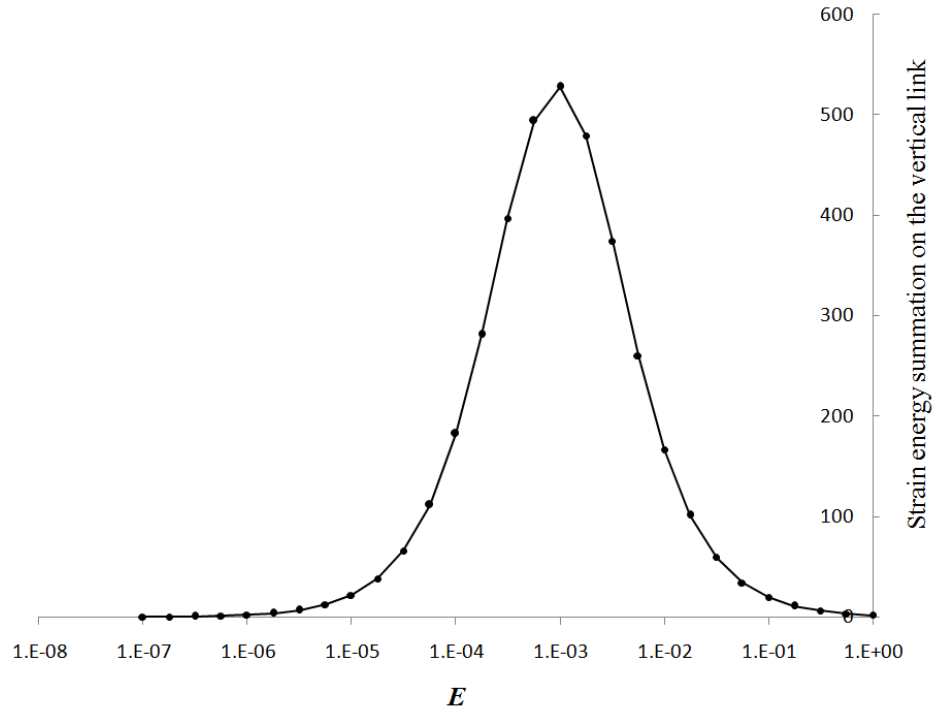

Figure 4.30: Strain energy summation on the vertical link versus its elastic modulus

According to the above discussions, the standard ESO/BESO approach cannot detect the sharp increase of the strain energy that corresponds to high absolute sensitivity values when E varies between 10^{-2}pa and 10^{-5}pa in Figure 4.30. This means that the elements on the vertical link should take the maximum strain energies of all the elements for a wide range of E. To understand well, the variation of the strain energy summation on the vertical link is shown in Figure 4.31 for its elastic modulus varying from 1pa to 10^{-7}pa.

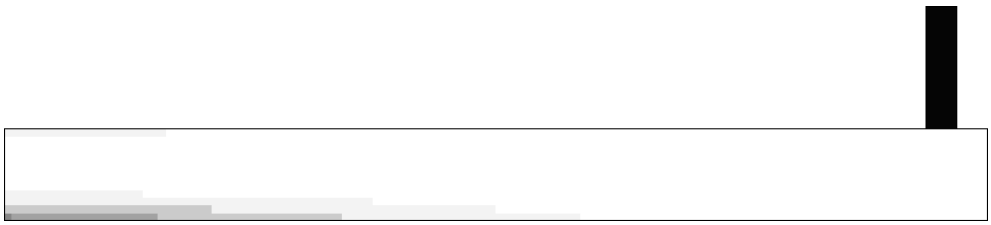

Figure 4.31: Layout of the element strain energy at the check position

Accordingly, the so-called check position method is proposed to identify and remedy the erroneous element deletion. The key idea is to introduce moderate low-density elements with the elastic modulus set to 0.01%-0.1% of the initial value, i.e., 10^{-4}-10^{-3}pa in this problem. These elements are able to capture the sharp variation of the objective function. Compared to solid elements, moderate low-density elements will act as compromising elements between void and solid elements but they are not compliant enough to be treated as removed ones. This makes it possible to pick out the elements that were erroneously removed and to recover them in the design procedure.

In the test example, elements on the vertical link are now replaced with the moderate

low-density elements of equivalent elastic modulus 10^{-3}pa. The corresponding distribution of the element strain energy is shown in Figure 4.30. It is seen that vertical link substituted with the moderate low-density element not only takes an extremely high value but also the maximum value of the element strain energies, which is easily identified in the design domain.

In this way, a modified ESO/BESO design procedure can be resumed as

1) Calculate the design sensitivities and remove the inefficient elements.

2) If a sharp degradation of the objective function is detected against a specified threshold, e.g. the structural compliance increases to more than 5 times or the natural frequency decreases to less than 1/5, the removed elements in the last step will be further recovered with the moderate low-density elements. This is referred to as the check position. Otherwise, a normal ESO/BESO procedure of element removal and growth is carried out.

3) Based on the FE reanalysis of the updated model at the check position, moderate low-density elements having the maximum strain energies will be recovered and marked as non-designable, while the other moderate elements will be removed again. But the mark of non-designable elements only stays for a few steps. These elements will be designable again later on.

4) Standard ESO/BESO element removal and growth procedure is carried out by ignoring the non-designable elements.

Now the test example is carried on with this procedure. With the vertical link recovered and marked as non-designable, the elements removed in the first effective step are presented in Figure 4.32.

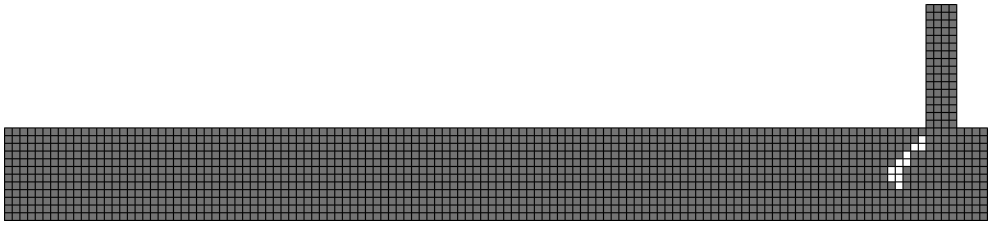

Figure 4.32: Structural topology generated by the first effective iteration

However, after several iterations, when the elements on the vertical link are reclaimed designable, the elements can be removed again. The check position may be reintroduced depending on the objective degradation. After 61 iterations, the final design of the structure is shown in Figure 4.33 with an amount of 40% of the total material.

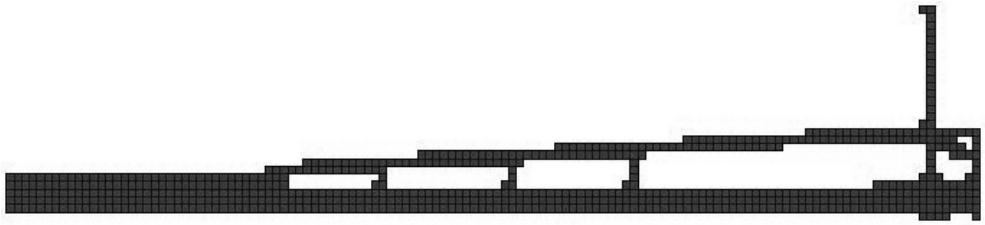

Figure 4.33: Optimal structural topology (C=509.8J)

4.4.3 Dynamic design of a bi-clamped beam

Another topology design is to maximize the 1st natural frequency. As shown in Figure 4.34, a 2m×12m beam supported at both ends is meshed with 20×120 quadratic elements. The non-designable area consists of 2×20 elements at the center. 50% of the total material is allowed. And the material properties are

elastic modulus $E_0=2\times10^{11}$pa, density $\rho_0=7800$kg/m^3 and Poisson's ratio $v=0.3$

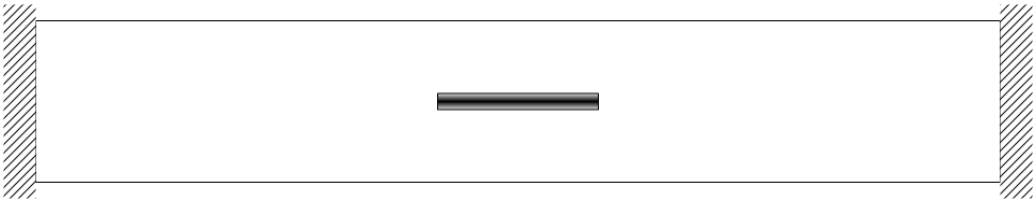

Figure 4.34: Design domain of the bi-clamped beam

Problems are detected at the 4th iteration where the non-designable area is unsupported and the objective function decreases to 0Hz, as shown in Figure 4.35.

(a) Layout of the sensitivities at the 3rd iteration (64.17Hz)

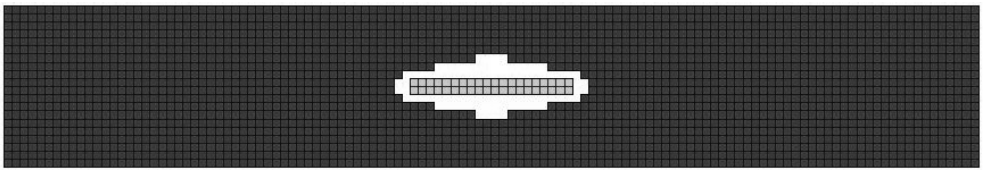

(b) Structural topology at the 4th iteration (0Hz)

Figure 4.35: Erroneous design iteration

The removed elements in the last iteration are then recovered with the moderate low-density elements with 10^{-3} of the solid elastic modulus and density. The updated structure is analyzed again and the layout of sensitivity values is shown in Figure 4.36. It is observed that some of the moderate low-density elements are taking the maximum values and will be recovered as the solid elements as shown in Figure 4.37.

Figure 4.36: Layout of sensitivity values at the check position (59.19Hz)

68 iterations are consumed and the optimal design is shown in Figure 4.38. The proposed ESO/BESO design procedure with check position can be used to avoid some erroneous

design iterations. However, this method is still based on some heuristic rules.

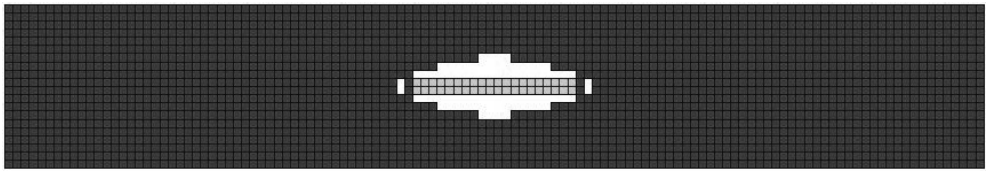

Figure 4.37: The effective structural topology at the 4th iteration (64.27Hz)

Figure 4.38: The final design of the bi-clamped beam (71.18Hz)

4.5 Conclusion

To benefit the extensions of the integrated layout design, some problems involved in the low-density areas in topology optimization are discussed in detail. By observing the phenomena of the localized modes in eigenvalue maximization problems and localized deformations in problems with design dependent body loads, the reasons of these numerical failures are concluded as the improperly defined material properties and their interpolation models. The great difference between mass and stiffness of the low-density elements will be thus limited to avoid these problems. Several existing methods based on different ideas, e.g. limiting the minimum value of the elastic modulus or the derivative of the interpolation, are presented and evaluated. A new proposed polynomial interpolation model is also presented and discussed through numerical tests.

Finally, the break-down of the ESO/BESO family method is discussed. These methods are considering the material layout updating as a discrete procedure by directly removing or adding elements in the design domain. In fact, the design sensitivities used actually cannot correctly describe the practical operations on the elements. This is the reason of the break-down problems. The check position scheme is then proposed by introducing moderate low-density elements into the intermediate design iterations to identify and to recover the erroneously removed elements. Two typical questionable examples can be solved to achieve reasonable results.

Chapter 5

Inertial Forces and Natural Frequencies

Overview

A Multi-component system is actually an integrated system of mass and stiffness. With the new presented material interpolation model for topology optimization in the previous chapter, the integrated layout designs with design-dependent inertial forces and natural frequencies maximization are taken into account in this chapter. More constraints on the location of the center of gravity and moment of inertial are included in the design. The idea is further verified with some numerical tests.

Contents

5.1 Problem statement

5.1.1 Inertial forces

The inertial forces like gravity etc commonly exist in aerospace design. But in Chapter 3 of this thesis, these loads are approximately ignored by assuming that the applied external loads are much stronger than the inertial loads. This is reasonable in some cases e.g. some aircraft or automobile structures are designed to carry heavy loads but the structures are lightweight or in small-dimension and work in low accelerations.

However, the self-weight loadings of some heavy structures commensurate with or are even much greater than the applied loadings. For example, as shown in Figure 5.1, a wheel loader with the rated load 15000N is as heavy as 60000N, which is 4 times of the rated load.

Figure 5.1: A wheel loader
(XGMA Machinery XG916T)

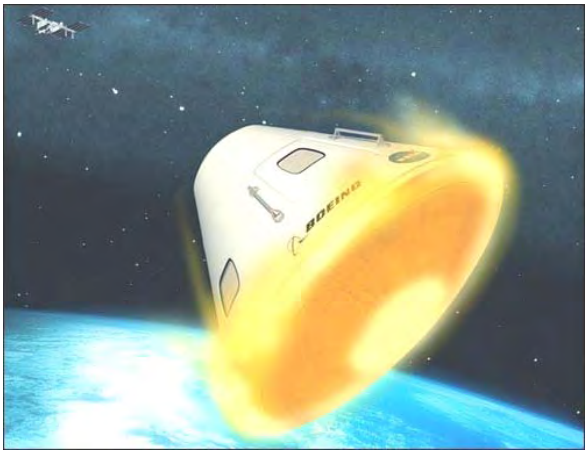

Figure 5.2: Reentry of a spacecraft

There is another possible case when the inertial forces cannot be ignored. For example, during the launch or reentry of the recoverable satellites, the spacecrafts or space shuttles, great acceleration or deceleration are applied on the structural systems, as shown in Figure 5.2. The acceleration rate can be 8*g*~10*g* or ever greater, where *g* is the acceleration of gravity.

The multi-component systems in this thesis are actually integrated systems of mass and stiffness, because both the components and structures are composed of materials with mass and stiffness properties. The integrated layout design will be finally concluded as a coupled mass and stiffness layout design.

When the accelerations are applied to the structural systems, the loading conditions will be composed of two different parts, i.e. the design independent loads and design dependent inertial loads. The equation of finite element can be expressed as

$$\boldsymbol{f} + \boldsymbol{G} = \boldsymbol{K}\boldsymbol{u} \tag{5-1}$$

where $\boldsymbol{f}$ and $\boldsymbol{G}$ indicate the design independent loads and design dependent inertial loads respectively. And the integrated layout optimization problems can be formulated as

$$\begin{aligned} \text{find}: \quad & 0 < \eta_i \le 1,\ i = 1,2,...,n_d; \\ & (x_\varepsilon, y_\varepsilon, \theta_\varepsilon),\ \varepsilon = 1,2,...,n_c. \\ \min: \quad & C = \frac{1}{2}\left(\boldsymbol{f} + \boldsymbol{G}\right)^T \boldsymbol{u} \\ \text{s.t.}: \quad & \text{Eq.(2-10)};\ V \le V^{(U)} \end{aligned} \tag{5-2}$$

The only difference from the problem stated in Chapter 3 is that the effect of the mass layout to the objective function is implied by including the inertial forces. However, during the optimization iteration, the heavy movable components will always try to be located near the boundary fixations to obtain better and stronger supports against the inertial forces. This is reasonable, but to generate more practical solutions, more engineering constraints should be introduced.

5.1.2 Natural frequencies

Besides the compliance minimization, the maximization of natural frequencies is one of the most important applications of topology optimization. In these problems, the natural frequencies are designed away from the solicitation frequency from the external cyclical loads or attached vibrating parts to avoid any structural damage due to the resonance. In some specific cases, the fundamental natural frequency is designed to be 3~5 times of the possible disturbance frequencies.

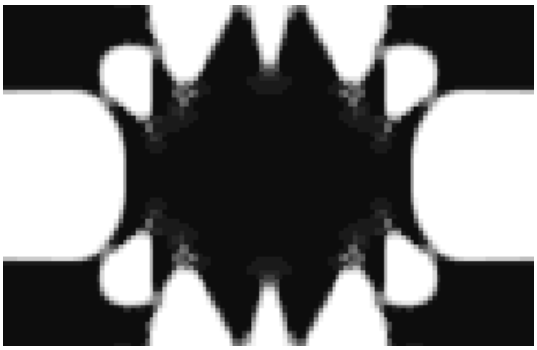

Reinforcement topology design with a concentrated mass at the center (Pedersen 2000)

Engine enclosures of the automobiles are designed with a minimum thickness. (http://www.pcauto.com.cn)

Figure 5.3: Typical reinforcement design

As indicated previously, the layout of mass will be designed simultaneously with the layout of stiffness in the multi-component system design. The eigenvalue equation of the natural frequency problems can be expressed as

$$\left(\boldsymbol{K} - \omega^2 \boldsymbol{M}\right)\boldsymbol{u} = 0 \tag{5-3}$$

The stiffness matrix $\boldsymbol{K}$ and the mass matrix $\boldsymbol{M}$ imply the layout of stiffness and mass respectively.

However, trivial solutions will be obtained in topology optimization of maximizing the natural frequencies. Infinite values of the natural frequencies will be generated by removing all the materials in the design domain. As a result, reinforcement problems are always solved in topology optimization. Some parts of the design domain are chosen as the non-designable areas as described in the previous chapter. Or in some cases a minimum thickness is used as the reinforcement as shown in Figure 5.3.

In the integrated layout design, the components are defined as some movable areas inside the design domain. The optimization problem can be formulated as

$$\begin{aligned} \text{find}: \quad & 0 < \eta_i \le 1,\ i = 1,2,...,n_d; \\ & (x_\varepsilon, y_\varepsilon, \theta_\varepsilon),\ \varepsilon = 1,2,...,n_c. \\ \max: \quad & \omega^2 \\ \text{s.t.}: \quad & \text{Eq.(2-10)}; \\ & V \le V^{(U)} \end{aligned} \tag{5-4}$$

Likewise, the integrated layout optimization of maximizing the natural frequencies will be defined as a reinforcement design as well. Similarly to those with inertial forces, the components are found to move always towards the boundary fixations and more additional constraints will be introduced.

5.1.3 Physical constraints

Space mission Shengzhou-VI, China

Figure 5.4: Physical constraints are introduced in the spacecraft design to ensure the stability of the flight

Since the layout of mass is taken into account in the integrated layout design, some other important properties of the multi-component systems have to be considered, e.g. the location of the center of gravity and the moment of inertia. In most of the industrial applications especially in aeronautics and aerospace engineering, as shown in Figure 5.4, it is critical to ensure proper positions of the gravity center for the structural systems of the products or even single parts. Moreover, to guarantee the stability of the flight, more benefits are obtained when minimizing the moment of inertia during the aerospace structures design.

For a normal 2D structural system with regular size, the center of gravity is located

identically with the centroid, which can be calculated as

$$\begin{bmatrix} x_G \\ y_G \end{bmatrix} = \frac{1}{\iint \rho(x,y)\,t dx dy} \cdot \begin{bmatrix} \iint x \cdot \rho(x,y)\,t dx dy \\ \iint y \cdot \rho(x,y)\,t dx dy \end{bmatrix} \tag{5-5}$$

where $\rho(x, y)$ denotes the material density at the position (x, y), t is the thickness of the plate. While in a multi-component system with finite element mesh, the center of the gravity of the system can be calculated as

$$\begin{aligned} &\left(\sum_i \sum_{j=n_{e(i-1)}+1}^{n_{ei}} \eta_i \rho_{i0} g V_{ij} + \sum_\varepsilon \sum_{j=n_{c(\varepsilon-1)}+1}^{n_{c\varepsilon}} \rho_\varepsilon g V_{\varepsilon j} \right) \cdot \begin{bmatrix} x_G \\ y_G \end{bmatrix} \\ &= \sum_i \sum_{j=n_{e(i-1)}+1}^{n_{ei}} \eta_i \rho_{i0} g V_{ij} \begin{bmatrix} x_{Gij} \\ y_{Gij} \end{bmatrix} + \sum_\varepsilon \sum_{j=n_{c(\varepsilon-1)}+1}^{n_{c\varepsilon}} \rho_\varepsilon g V_{\varepsilon j} \begin{bmatrix} x_{G\varepsilon j} \\ y_{G\varepsilon j} \end{bmatrix} \end{aligned} \tag{5-6}$$

where $j \in \left\{ (1,2,...,n_{e1}),...,(n_{e(i-1)}+1,...,n_{ei})...(n_{c(\varepsilon-1)}+1,...,n_{c\varepsilon})... \right\}$ $n_{e0}=0; n_{c0}=n_{en_d}; i=1,2,...,n_d; \varepsilon=1,2,...,n_c$ indicate the elements of supporting structure and the components. (x_{Gij}, y_{Gij}) and $(x_{G\varepsilon j}, y_{G\varepsilon j})$ are the gravity centers of the corresponding element belonging to the ith density point or the εth component, respectively. Then the moment of inertia is calculated as

$$J = \iint (\Delta d)^2 \cdot \rho(x,y)\,t dx dy \tag{5-7}$$

where Δd indicates the distances between the current positions and the reference rotation axis. According to the parallel axis theorem, the moment of inertia of the global multi-component system can be calculated by summating the moments of inertia of all elements, which can be expressed as

$$J = \sum_i \sum_{j=n_{e(i-1)}+1}^{n_{ei}} \left[\eta_i \rho_{i0} V_{ij} \left(\Delta d_{ij} \right)^2 + \eta_i J_{ij0} \right] + \sum_\varepsilon \sum_{j=n_{c(\varepsilon-1)}}^{n_{c\varepsilon}} \left[\rho_\varepsilon V_{\varepsilon j} \left(\Delta d_{\varepsilon j} \right)^2 + J_{\varepsilon j} \right] \tag{5-8}$$

where $\eta_i J_{ij0}$ and $J_{\varepsilon j}$ are the moment of inertia of the jth element belonging to the ith density point and εth component, respectively. Note that the corresponding rotation axis goes through the centroid of each element and is parallel to the global rotation axis.

Furthermore, since the structural materials and the components tend to be located near the boundary fixations for maximizing the natural frequencies or problems with inertial forces, additional constraints on the center of gravity and moment of inertia will be helpful to relocate the materials and components.

5.2 Sensitivity analysis

The design sensitivities of the strain energy with inertial forces, natural frequency, location

of the center of gravity and the moment of inertia with respect to the pseudo-density variables are derived here. While the finite difference scheme is used to calculate approximately the derivatives of the functions with respect to the location and orientation of the components.

Besides, we use the following polynomial interpolation model for pseudo-density variables.

$$\begin{aligned} \rho_i &= \eta_i \rho_{i0} \\ E_i &= P(\eta_i) E_{i0} = \left(\frac{\alpha - 1}{\alpha} \eta_i^p + \frac{1}{\alpha} \eta_i \right) E_{i0} \end{aligned} \tag{5-9}$$

where E_{i0} and ρ_{i0} are the elastic modulus and density, respectively when the elements controlled by the ith density point are solid, i.e. η_i =1. In $P(\eta_i)$, α and p are usually set to be 16 and 3, respectively.

5.2.1 Strain energy with inertial forces

Compared with the original standard topology optimization, the derivative of the nodal load vector with respect to the pseudo-densities is no longer zero here. The design dependency of the inertial forces will be revealed in the derivation.

The derivative of the strain energy can be written as

$$\frac{\partial C}{\partial \eta_i} = \frac{1}{2} \left[\left(\boldsymbol{f} + \boldsymbol{G} \right)^T \cdot \frac{\partial \boldsymbol{u}}{\partial \eta_i} + \frac{\partial \boldsymbol{G}^T}{\partial \eta_i} \cdot \boldsymbol{u} \right] \tag{5-10}$$

Then the both side of the finite element equation are differentiated and written as

$$\frac{\partial \boldsymbol{G}}{\partial \eta_i} = \frac{\partial \boldsymbol{K}}{\partial \eta_i} \cdot \boldsymbol{u} + \boldsymbol{K} \cdot \frac{\partial \boldsymbol{u}}{\partial \eta_i} \tag{5-11}$$

Then we have

$$\frac{\partial \boldsymbol{u}}{\partial \eta_i} = \boldsymbol{K}^{-1} \left(\frac{\partial \boldsymbol{G}}{\partial \eta_i} - \frac{\partial \boldsymbol{K}}{\partial \eta_i} \cdot \boldsymbol{u} \right) \tag{5-12}$$

With the substitution of Equation (5-12) into (5-10), now the derivative of the strain energy is derived as

$$\begin{aligned} \frac{\partial C}{\partial \eta_i} &= \frac{1}{2} \left[\left(\boldsymbol{f} + \boldsymbol{G} \right)^T \cdot \boldsymbol{K}^{-1} \left(\frac{\partial \boldsymbol{G}}{\partial \eta_i} - \frac{\partial \boldsymbol{K}}{\partial \eta_i} \cdot \boldsymbol{u} \right) + \frac{\partial \boldsymbol{G}^T}{\partial \eta_i} \cdot \boldsymbol{u} \right] \\ &= \frac{1}{2} \left[\boldsymbol{u}^T \cdot \frac{\partial \boldsymbol{G}}{\partial \eta_i} - \boldsymbol{u}^T \cdot \frac{\partial \boldsymbol{K}}{\partial \eta_i} \cdot \boldsymbol{u} + \frac{\partial \boldsymbol{G}^T}{\partial \eta_i} \cdot \boldsymbol{u} \right] = \frac{\partial \boldsymbol{G}^T}{\partial \eta_i} \cdot \boldsymbol{u} - \frac{1}{2} \boldsymbol{u}^T \cdot \frac{\partial \boldsymbol{K}}{\partial \eta_i} \cdot \boldsymbol{u} \end{aligned} \tag{5-13}$$

According to the linear interpolation model for the densities, the gravity of each element is calculated by

$$\boldsymbol{G}_j = \begin{cases} \boldsymbol{G}_{ij} = \begin{bmatrix} 0 \\ -\eta_i \rho_{i0} g V_{ij} \end{bmatrix} & \text{(structure elements)} \\ \boldsymbol{G}_{\varepsilon j} = \begin{bmatrix} 0 \\ -\rho_\varepsilon g V_{\varepsilon j} \end{bmatrix} & \text{(component elements)} \end{cases} \tag{5-14}$$

The corresponding element is the *j*th element either dominated by the *i*th density point or the *j*th element that belongs to the εth component. At node *I*, the gravity force vector, $\boldsymbol{G}_j^{(I)}$, contributed from element *j* is then expressed as

$$\boldsymbol{G}_j^{(I)} = \iint N_I \cdot \frac{\boldsymbol{G}_j}{S_j} \cdot dxdy = N_I \boldsymbol{G}_j \tag{5-15}$$

$$\boldsymbol{G} = \sum_j \sum_I \boldsymbol{G}_j^{(I)} \tag{5-16}$$

where N_I is the value of the shape function at the node *I*. S_j is the area of the element. As a result, for a specified design variable η_i, only a few of the nodal items of $\boldsymbol{G}$ are related to the *i*th density point. And the derivative of $\boldsymbol{G}$ with respect to each pseudo-density is easily calculated with the derivative of $\boldsymbol{G}_{ij}$.

$$\frac{\partial \boldsymbol{G}_{ij}}{\partial \eta_i} = \begin{bmatrix} 0 \\ -\rho_{i0} g V_{ij} \end{bmatrix} \tag{5-17}$$

The global stiffness matrix is assembled with the elements' stiffness matrices, which can be further expressed as

$$\boldsymbol{K} = \sum_i \sum_{j=n_{e(i-1)}+1}^{n_{ei}} P(\eta_i) \boldsymbol{K}_{ij0} + \sum_\varepsilon \sum_{j=n_{c(\varepsilon-1)}+1}^{n_{c\varepsilon}} \boldsymbol{K}_{\varepsilon j} \tag{5-18}$$

where $\boldsymbol{K}_{ij}$ is the stiffness matrix of the *j*th element dominated by the *i*th density point, $\boldsymbol{K}_{ij0}$ is its stiffness matrix when it is solid. $\boldsymbol{K}_{\varepsilon j}$ is the stiffness matrix of the *j*th element belonging to the εth component. We have then

$$\frac{\partial \boldsymbol{K}_{ij}}{\partial \eta_i} = P'(\eta_i) \boldsymbol{K}_{ij0} \tag{5-19}$$

The derivative of $\boldsymbol{K}$ with respect to η_i can be finally evaluated by summing derivatives of $\boldsymbol{K}_{ij}$ from all elements dominated by the *i*th density point.

5.2.2 Natural frequency

By differentiating the eigenequation of the free vibration problems, the sensitivities are derived as

$$\left(\frac{\partial \boldsymbol{K}}{\partial \eta_i} - \frac{\partial \omega^2}{\partial \eta_i} \boldsymbol{M} - \omega^2 \frac{\partial \boldsymbol{M}}{\partial \eta_i} \right) \boldsymbol{u} + \left(\boldsymbol{K} - \omega^2 \boldsymbol{M} \right) \frac{\partial \boldsymbol{u}}{\partial \eta_i} = 0 \tag{5-20}$$

$$\boldsymbol{u}^T\left(\frac{\partial \boldsymbol{K}}{\partial \eta_i}-\frac{\partial \omega^2}{\partial \eta_i}\boldsymbol{M}-\omega^2\frac{\partial \boldsymbol{M}}{\partial \eta_i}\right)\boldsymbol{u}+\boldsymbol{u}^T\left(\boldsymbol{K}-\omega^2\boldsymbol{M}\right)\frac{\partial \boldsymbol{u}}{\partial \eta_i}=0 \tag{5-21}$$

Note that the second term of Equation (5-21) is zero. With the definition of the interpolation model, the sensitivities can be further derived as

$$\frac{\partial \omega^2}{\partial \eta_i}=\frac{\boldsymbol{u}^T\dfrac{\partial \boldsymbol{K}}{\partial \eta_i}\boldsymbol{u}-\omega^2\boldsymbol{u}^T\dfrac{\partial \boldsymbol{M}}{\partial \eta_i}\boldsymbol{u}}{\boldsymbol{u}^T\boldsymbol{M}\boldsymbol{u}} \tag{5-22}$$

where the stiffness and mss matrices related to the *i*th density points can be further derived as

$$\frac{\partial \boldsymbol{K}}{\partial \eta_i}=\frac{\partial\left(\sum_{j=n_{e(i-1)}+1}^{n_{ei}}\boldsymbol{K}_{ij}\right)}{\partial \eta_i}=\frac{P'(\eta_i)}{P(\eta_i)}\sum_{j=n_{e(i-1)}+1}^{n_{ei}}\boldsymbol{K}_{ij} \tag{5-23}$$

$$\frac{\partial \boldsymbol{M}}{\partial \eta_i}=\frac{\partial\left(\sum_{j=n_{e(i-1)}+1}^{n_{ei}}\boldsymbol{M}_{ij}\right)}{\partial \eta_i}=\frac{1}{\eta_i}\sum_{j=n_{e(i-1)}+1}^{n_{ei}}\boldsymbol{M}_{ij} \tag{5-24}$$

The derivative of the mass matrix is substituted back into Equation (5-22). The design sensitivity is finally expressed as

$$\frac{\partial \omega^2}{\partial \eta_i}=\frac{1}{\boldsymbol{u}^T\boldsymbol{M}\boldsymbol{u}}\left(\frac{P'(\eta_i)}{P(\eta_i)}\sum_{j=n_{e(i-1)}+1}^{n_{ei}}\boldsymbol{u}^T\boldsymbol{K}_{ij}\boldsymbol{u}-\frac{\omega^2}{\eta_i}\sum_{j=n_{e(i-1)}+1}^{n_{ei}}\boldsymbol{u}^T\boldsymbol{M}_{ij}\boldsymbol{u}\right) \tag{5-25}$$

which is composed of the strain energy and the kinetic energy of the elements.

5.2.3 Center of gravity and moment of inertia

Here the design sensitivities of the physical properties of the structural system, i.e. the center of gravity and the moment of inertia are derived with respect to the pseudo-densities.

The differentiation of the both sides of Equation (5-6) is written as

$$\left(\sum_i\sum_{j=n_{e(i-1)}+1}^{n_{ei}}\eta_i\rho_{i0}gV_{ij}+\sum_{\varepsilon}\sum_{j=n_{c(\varepsilon-1)}+1}^{n_{c\varepsilon}}\rho_{\varepsilon}gV_{\varepsilon j}\right)\cdot\begin{bmatrix}\dfrac{\partial x_G}{\partial \eta_i}\\ \dfrac{\partial y_G}{\partial \eta_i}\end{bmatrix}+\left(\sum_{j=n_{e(i-1)}+1}^{n_{ei}}\rho_{i0}gV_{ij}\right)\cdot\begin{bmatrix}x_G\\ y_G\end{bmatrix} \tag{5-26}$$
$$=\sum_{j=n_{e(i-1)}+1}^{n_{ei}}\rho_{i0}gV_{ij}\begin{bmatrix}x_{Gij}\\ y_{Gij}\end{bmatrix}$$

The design sensitivities of the center of gravity with respect to a certain pseudo-density can be derived as

$$\begin{bmatrix} \frac{\partial x_G}{\partial \eta_i} \\ \frac{\partial y_G}{\partial \eta_i} \end{bmatrix} = \frac{\sum_{j=n_{e(i-1)}+1}^{n_{ei}} \rho_{i0} g V_{ij} \left(\begin{bmatrix} x_{Gij} \\ y_{Gij} \end{bmatrix} - \begin{bmatrix} x_G \\ y_G \end{bmatrix} \right)}{\sum_i \sum_{j=n_{e(i-1)}+1}^{n_{ei}} \eta_i \rho_{i0} g V_{ij} + \sum_\varepsilon \sum_{j=n_{c(\varepsilon-1)}+1}^{n_{c\varepsilon}} \rho_\varepsilon g V_{\varepsilon j}} \tag{5-27}$$

Then the moment of inertia is differentiated and the design sensitivities are easily obtained as

$$\frac{\partial J}{\partial \eta_i} = \sum_{j=n_{e(i-1)}+1}^{n_{ei}} \left[\rho_{i0} V_{ij} \left(\Delta x_{ij} \right)^2 + J_{ij0} \right] \tag{5-28}$$

5.3 Numerical examples

Several related examples are tested here. For all the examples, the material properties are as follows

for the components:

elastic modulus, $E_0=2\times10^{11}$pa, density $\rho_0=7800$kg/m^3 and Poisson's ratio $v=0.3$;

and for the structures:

elastic modulus, $E_0=7\times10^{10}$pa, density $\rho_0=2700$kg/m^3 and Poisson's ratio $v=0.3$.

5.3.1 Pylon with gravity

The pylon presented in Chapter 3 is further designed here including the self-weight loading. An acceleration of 10m/s^2 is applied vertically to the global structural system. Meanwhile, the rest of the loads and boundary conditions remain identical as shown in Figure 5.5.

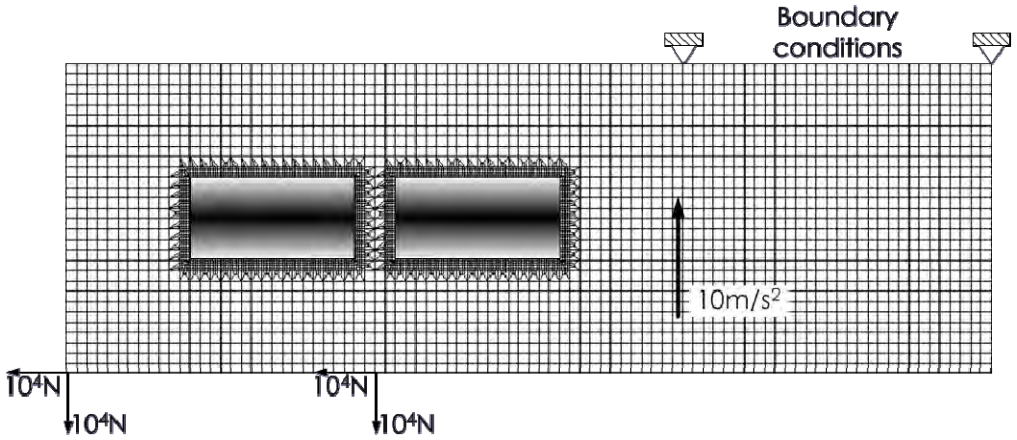

Figure 5.5: Design domain of the pylon with self-weight loading

The optimization is implemented with 50% of the material removed. At the beginning of

the optimization, the two components move towards the fixations very quickly. Because of the topology optimization with design dependent loads, the total weight of the system decreases from 34382.4N to 19802.4N. And the layout of the inertial forces is also changed along with the material layout.

However, the strain energy obtained here is much higher than those obtained in Chapter 3 because of the gravity force. Several design patterns from the design iteration are presented in Figure 5.6. The optimization converges at the 82nd iteration. The objective function converges in a rather stable way as shown in Figure 5.7.

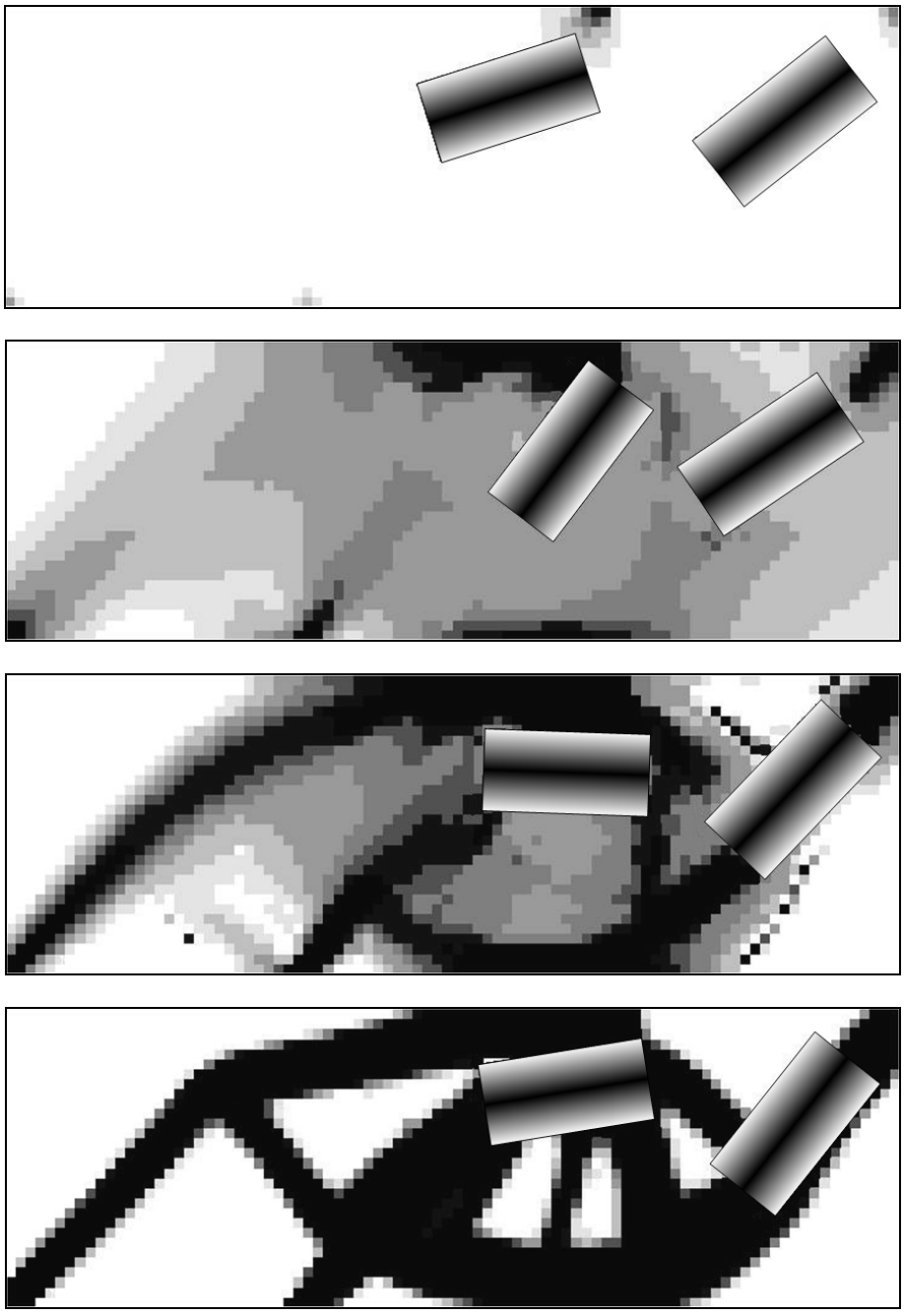

(a) 5th iteration

(b) 15th iteration

(c) 25th iteration

(d) The final design C=0.146J

Figure 5.6: Iteration history of the design patterns

In Figure 5.8, comparisons are made with the design pattern obtained in Figure 3.20 of Chapter 3. It is obvious that the two components are located close to the two fixations

because they are much heavier than the surrounding structures. Although the loading structures are generally similar, most materials are distributed on the right side. The structure on the left side that transfers the concentrated loads becomes much weaker than before.

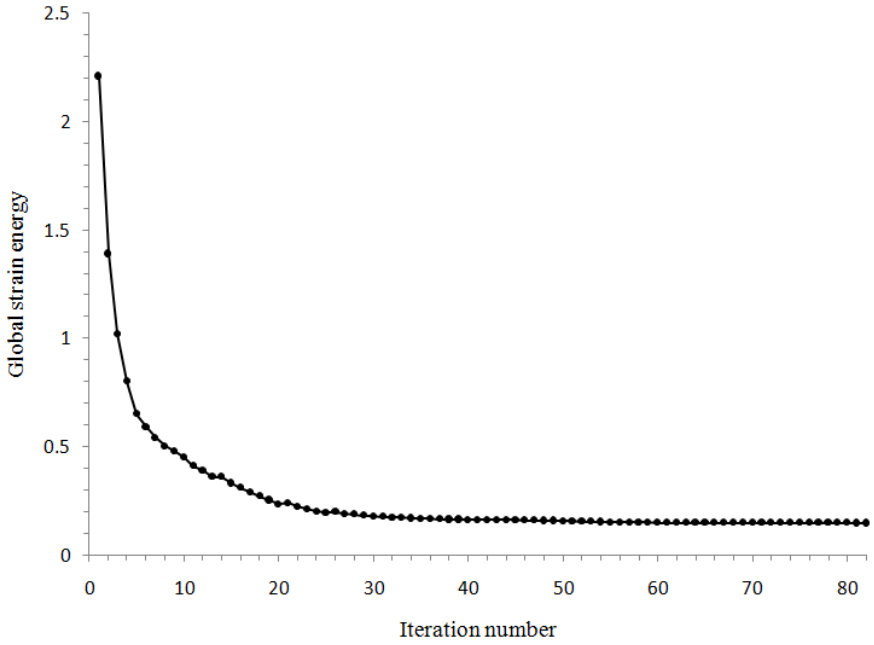

Figure 5.7: The convergence history of the global strain energy

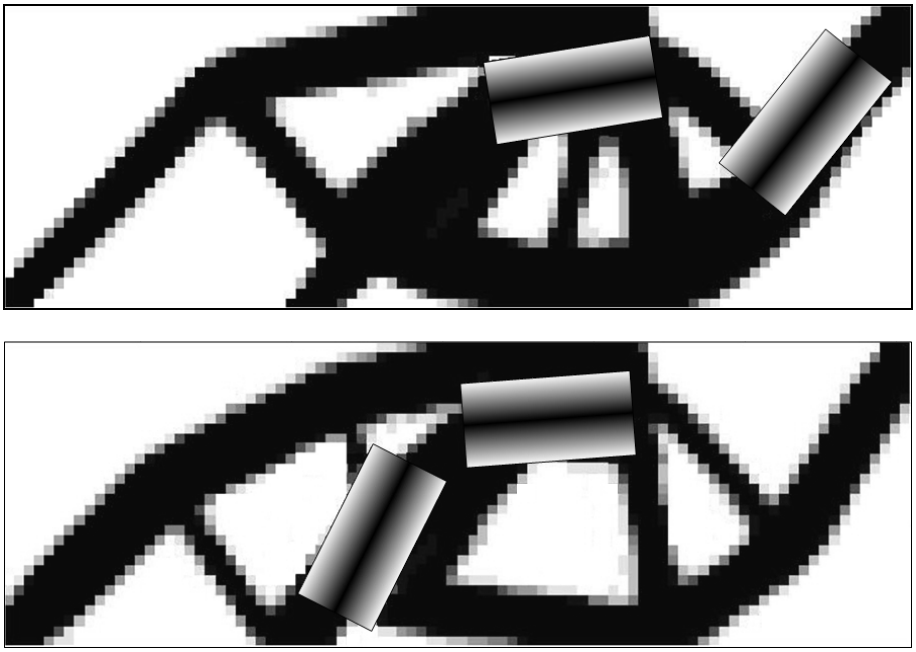

Figure 5.8: Comparisons of the two optimal designs with and without gravity

The constraints on the location of the gravity center are applied to the global system as

$$\begin{bmatrix} 0.8 \\ 0.29 \end{bmatrix} \leq \begin{bmatrix} x_G \\ y_G \end{bmatrix} \leq \begin{bmatrix} 0.95 \\ 0.31 \end{bmatrix} \tag{5-29}$$

which is only a narrow area located at the center of the design domain as shown in Figure 5.9.

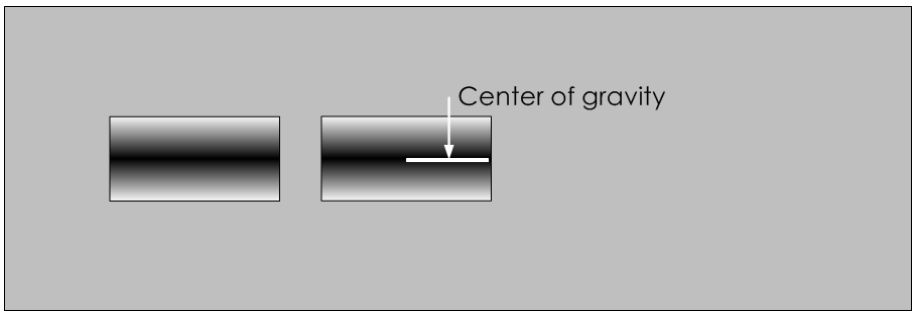

Figure 5.9: Initial design and the location of the center of gravity

The optimization stops at the 102nd iteration. Several design patterns are selected and presented as shown in Figure 5.10. The components are no longer found to move directly towards the fixations but stay at the center of the design domain to satisfy the constraint on the center of gravity. Thus, the structural layout changes a lot. However, most of the structural material is still located on the right side of the design domain.

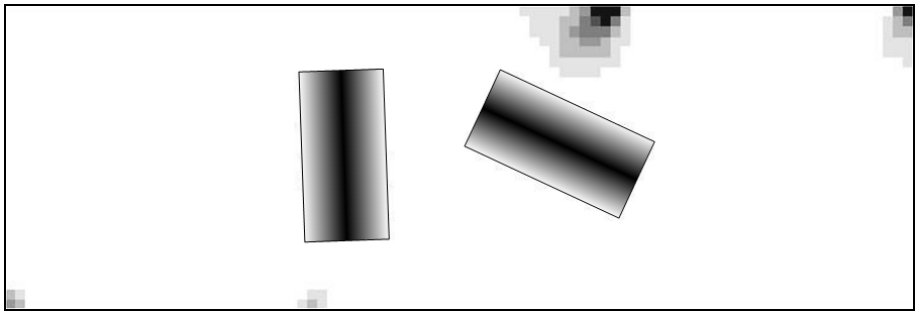

(a) 4th iteration

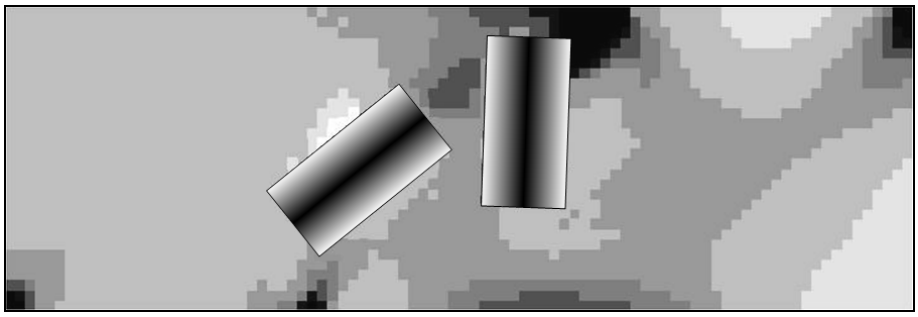

(b) 15th iteration

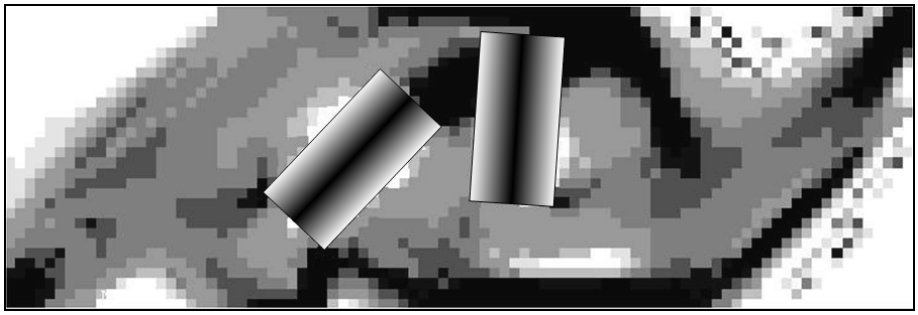

(c) 25th iteration

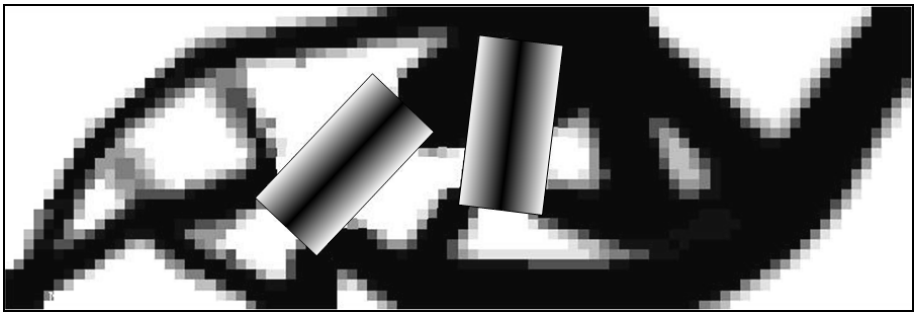

(d) The final design C=0.201J

Figure 5.10: Iteration history of the design patterns

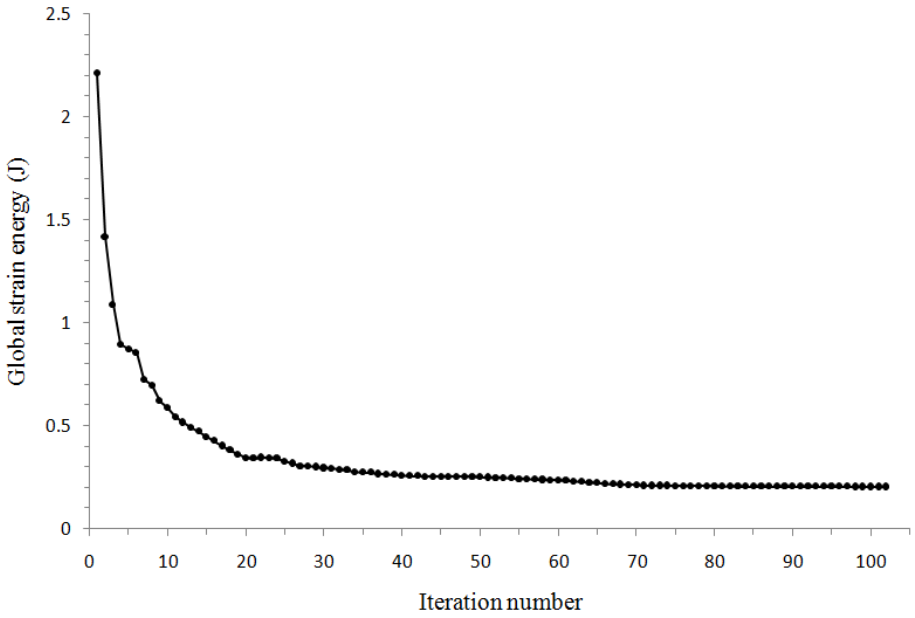

Figure 5.11: Convergence history of the objective function

The iteration history of the objective function is shown in Figure 5.11. The locations of centers of gravity obtained without and with constraints are presented in 5.12. The center of gravity moves leftwards by more than 0.101m horizontally and downwards 0.029m vertically with the cost of the strain energy increasing by 37.7%.

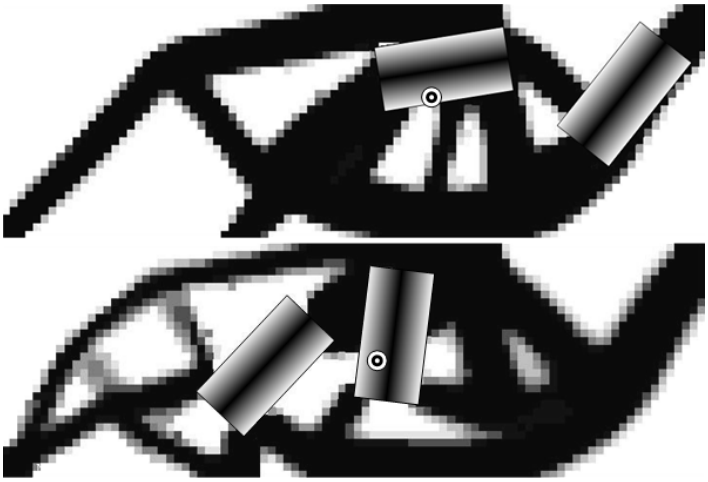

Figure 5.12: Comparison of the locations of centers of gravity

With respect to the bottom left corner of the design domain, the two centers of gravity are (1.050m, 0.326m) and (0.949m, 0.297m), respectively

5.3.2 An aerospace structural system

A test example of an aerospace structural system is designed here with different definitions to verify the proposed ideas. As shown in Figure 5.13, the structural system is to support a heavy device located at the center. Three identical plates with two components are placed symmetrically around the center and supported at the corner. Globally, an acceleration rate 100m/s^2 (10g) is applied to the whole system.

The system is simplified as shown in Figure 5.13. Only one of the plates is designed due to the symmetry and the supported equipment is equivalently defined as a vertical force of 18000N applied at the top right corner. Suppose the two components are initially located in the design domain. To avoid the possible overlap during the iteration, each component is described with 5 circles.

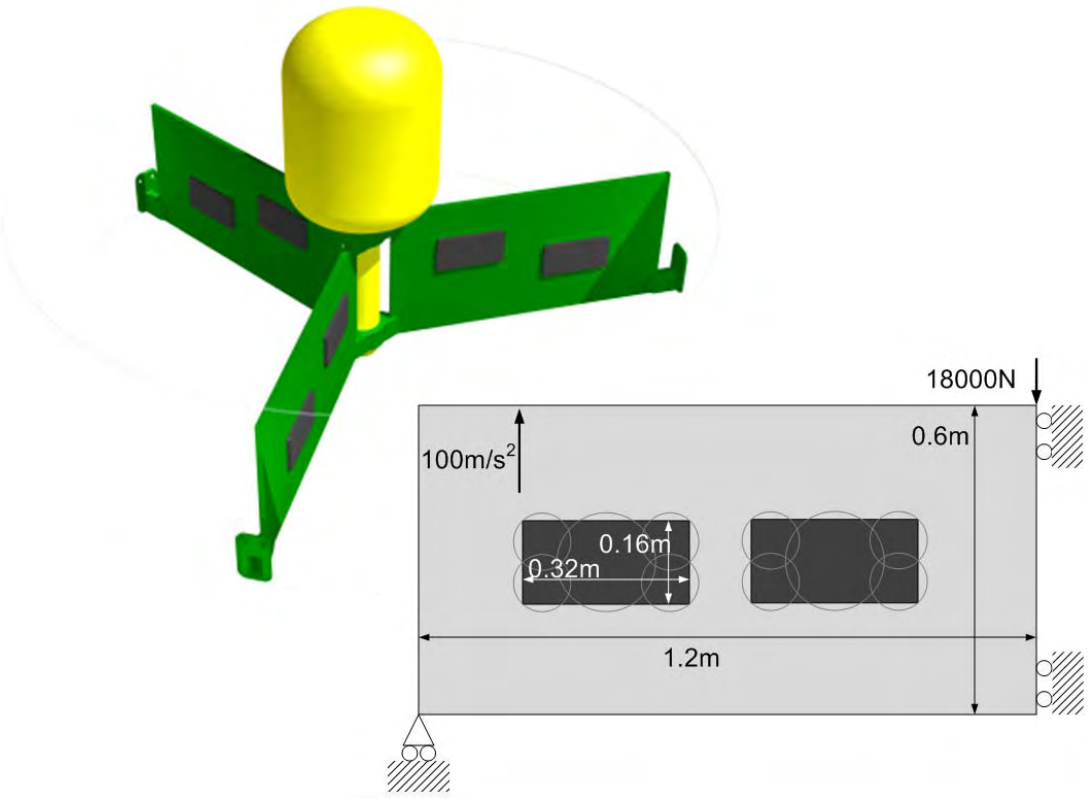

Figure 5.13: Structural system illustration with the design domain and the components

35% of the total material cost for the structure will be assumed to the topology optimization problem. As a result, the system weight is equal to 35% of the total structural weight in the design domain plus the weight of two components, where all the weights are evaluated with the current acceleration 100m/s^2. The concentrated force 18000N related to the weight of the central equipment is about 15% of the system weight. A nodal vertical fixation is assumed at the left bottom corner and more horizontal fixations are assumed at the right edge of the plate.

For the purpose of comparison, suppose the plate and the layout of the components are firstly designed without acceleration applied to the system. This means that an acceleration of g=0 is simply assigned in the model just like that presented in Chapter 3. This problem is presently like a standard MBB beam.

Initial values are set to be 0.35 for the pseudo-densities of the density points. The objective is to minimize the global strain energy. As shown in Figure 5.14, the positions of the components and the layout of the structure update simultaneously during the optimization. Since the components' material is much stronger than the structural material and no clear structural patterns are figured out to support the components at the beginning, the components firstly move around the design domain in a large range to find a proper position. Thereafter, the supporting structure becomes clearer and clearer. The components reach the optimal positions and are integrated as a part of the loading structure at the 82nd iteration.

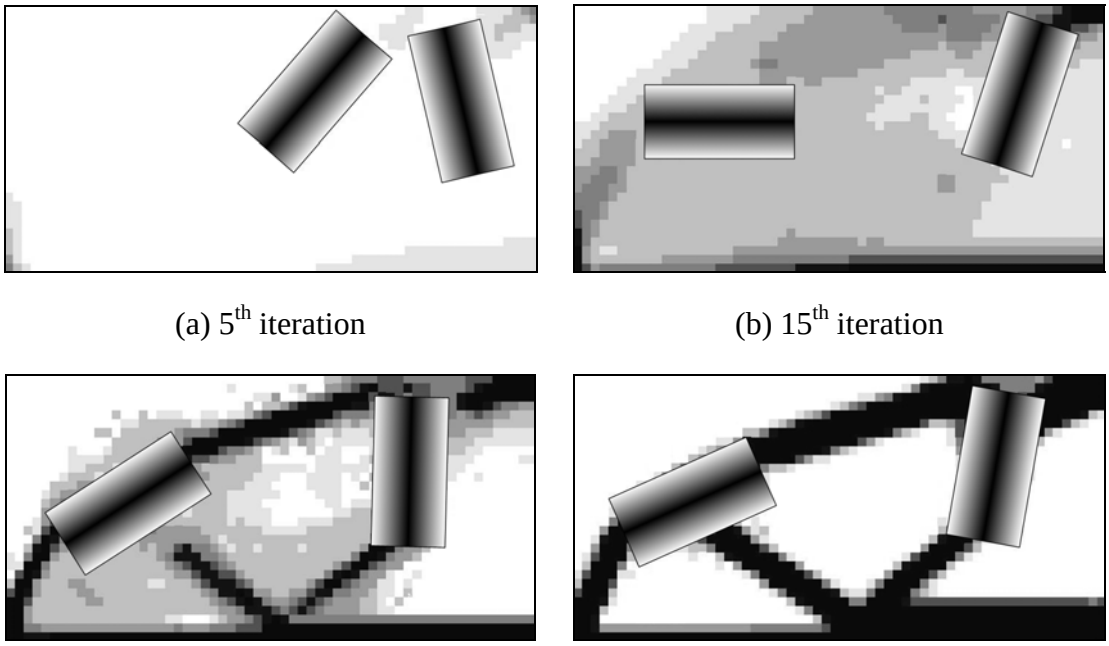

(a) 5th iteration (b) 15th iteration

(c) 25th iteration (d) The final design C=0.231J

Figure 5.14: Iteration history of the design patterns without inertial forces

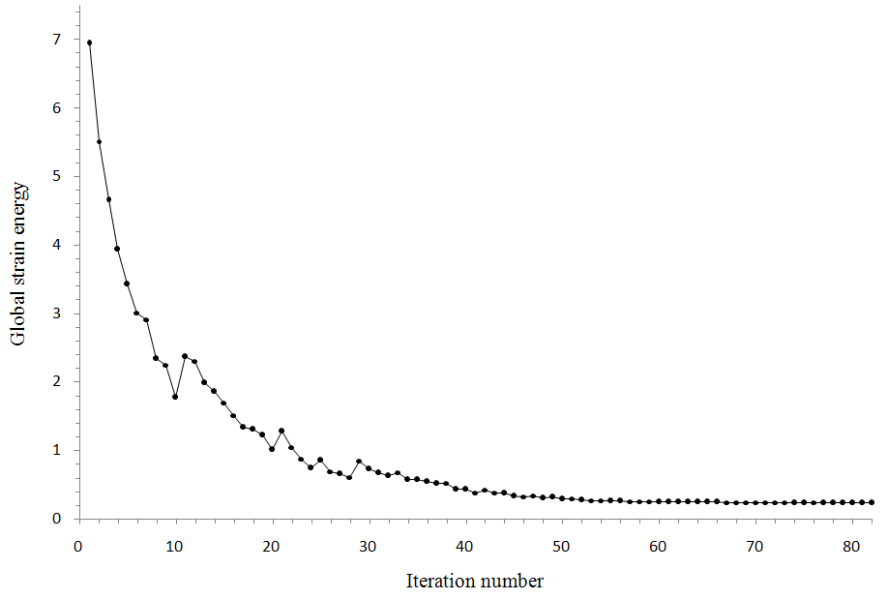

Figure 5.15: Convergence history of the global strain energy

As shown in the final design pattern, the two components are embedded in two crucial positions of the structure. The iteration history of the global strain energy is shown in Figure 5.15.

Comparatively, the problem without component is carried out here. The same design domain, load and boundary conditions are used. The material cost is limited to 50%, which is 15% higher than previous, to compensate the difference of the material cost when the components are removed.

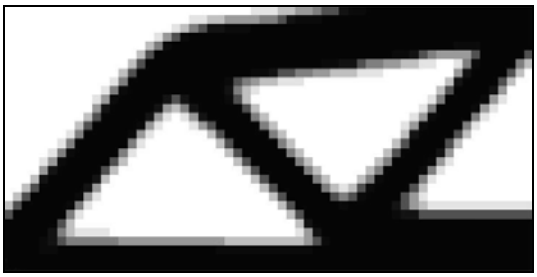

Figure 5.16: Topology design without component

As shown in Figure 5.16, the optimal structure is a typical topology optimization design. Differences between the two structural patterns are found in Figure 5.14 and Figure 5.16. It is sure that the stronger material introduced with the components has a great effect on the mechanical performances of the structure.

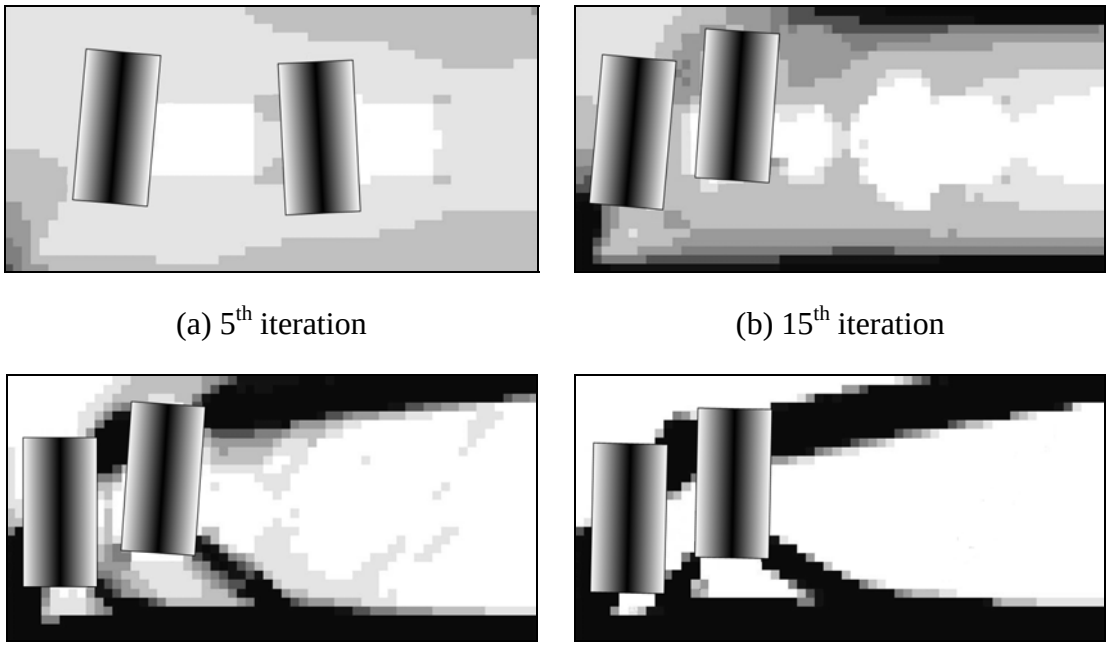

(a) 5^{th} iteration (b) 15^{th} iteration

(c) 25^{th} iteration (d) The final design C =4.698J

Figure 5.17: Iteration history of the design patterns

Instead, the next test is to take an acceleration rate 100m/s^2. The optimization starts with an initial design and a volume fraction of 35% is used. The loads consisting of the design-independent concentrated force and the design-dependent inertial forces are applied to the system. Now the components have material properties that are not only much stronger but also much heavier than the structure. Thus, the two components try to

locate as close as possible to the vertical support at the bottom left corner and reach the proper positions in a few iterations. Later, a clearer structural topology will be generated against the gravity.

As shown in Figure 5.17, the iteration history reaches the convergence at 86 iterations. Because the total weight of the system is much greater than the concentrated force, the structural has a much higher value of strain energy. In Figure 5.18, it is seen that the two components find their locations very quickly at the beginning. The convergence is rather stable. In contrast, the problem without component is also tested here. The optimal structure is shown in Figure 5.19 where 50% of the total material is used.

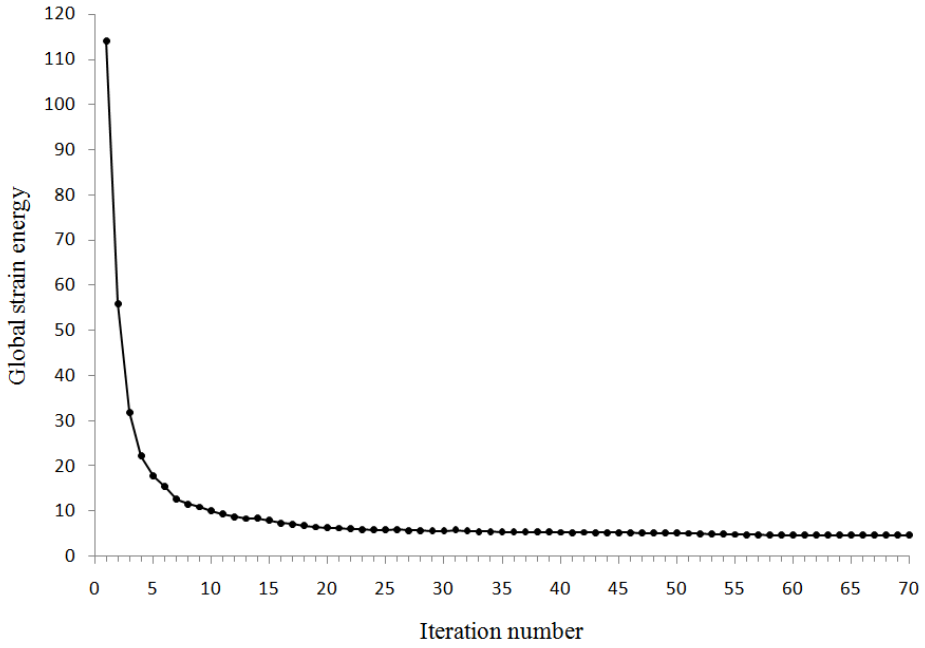

Figure 5.18: Convergence history of the global strain energy

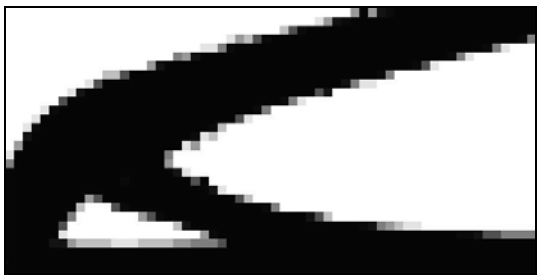

Figure 5.19: Topology design without component

As expected, most of the structural materials are distributed on the left side in Figure 5.17 and Figure 5.19 because of the existence of self-weight load. Significant differences from the results without gravity can be found. Therefore, the self-weight loading is essential for topology optimization design of heavy structures.

Now, suppose rigorous constraints are introduced to make sure that the center of gravity is located at the center of the plate.

$$\begin{bmatrix} x_G \\ y_G \end{bmatrix} = \begin{bmatrix} 0.6 \\ 0.3 \end{bmatrix} \tag{5-30}$$

Numerically, both conditions are little relaxed to transform the equality constraints into inequalities

$$\begin{bmatrix} 0.6 \\ 0.3 \end{bmatrix} \leq \begin{bmatrix} x_G \\ y_G \end{bmatrix} \leq \begin{bmatrix} 0.601 \\ 0.301 \end{bmatrix} \tag{5-31}$$

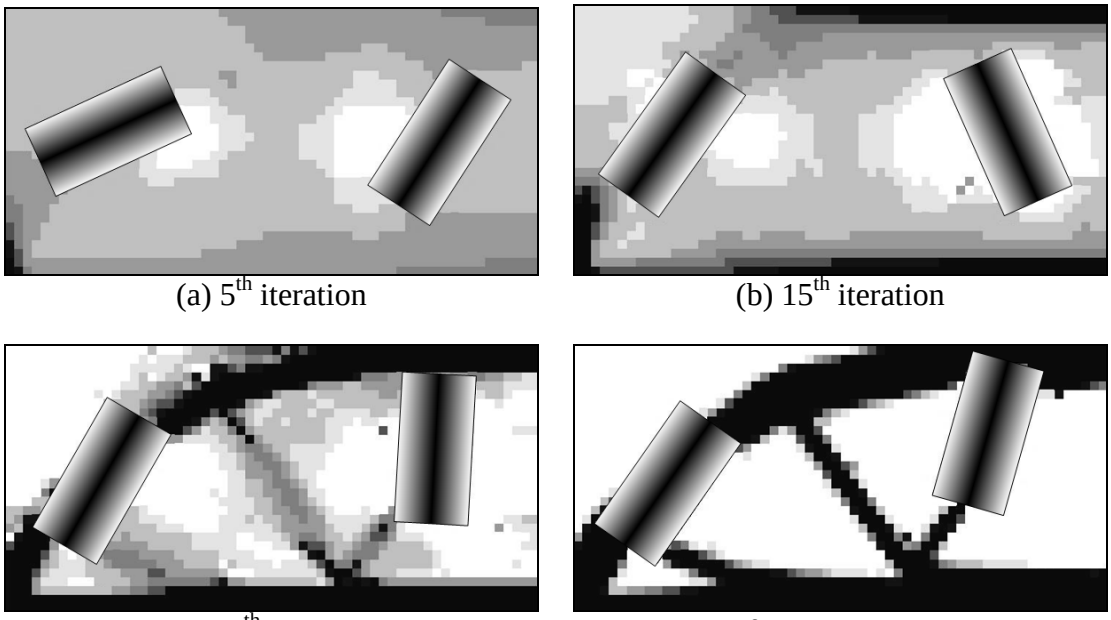

(a) 5th iteration (b) 15th iteration

(c) 30th iteration (d) The final design C =6.928J

Figure 5.20: Iteration history of the design patterns

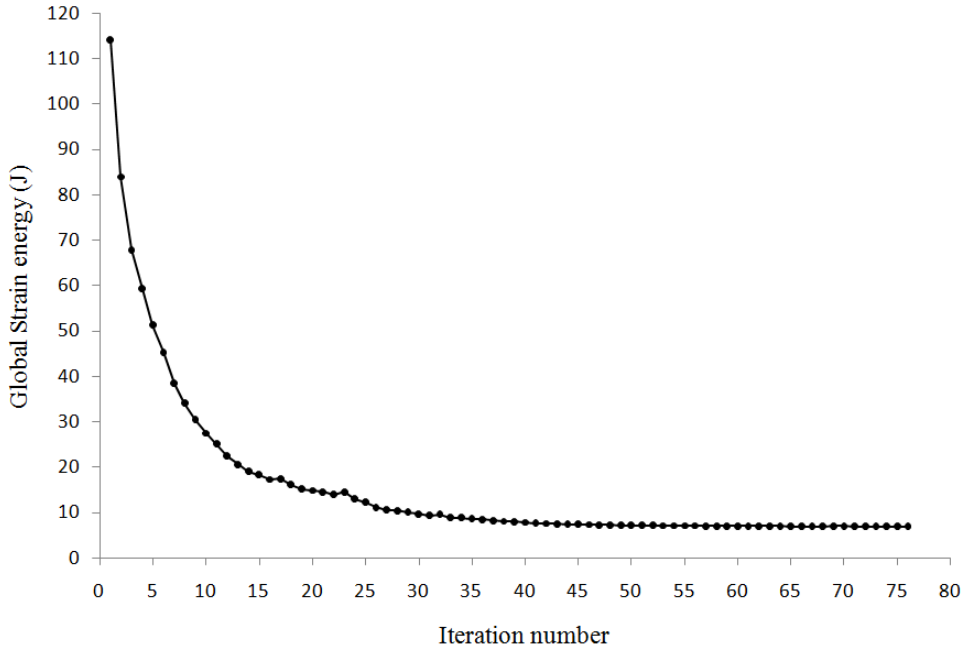

Figure 5.21: Convergence history of the global strain energy

As shown in Figure 5.20, the movements of the components and the layout of the structure are totally different from the previous one in order that the new added constraints are always satisfied. In the final design, although the two components are still embedded into the structure, they are separated to the two sides of the plate to keep the center of gravity unmovable. The convergence history of the design objective is shown in Figure 5.21. Besides, centers of gravity of both results given in Figures 5.17(d) and 5.20(d) are indicated by the arrows and compared in Figure 5.22. The center of gravity now locates at the center of the plate at the cost of increasing the strain energy by 34%.

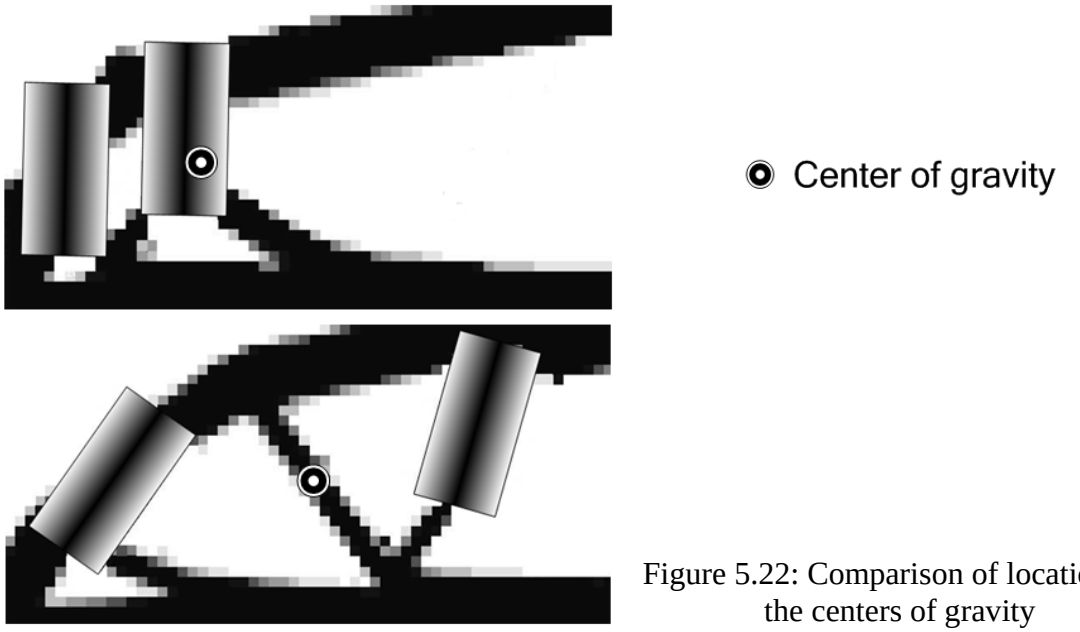

Figure 5.22: Comparison of locations of the centers of gravity

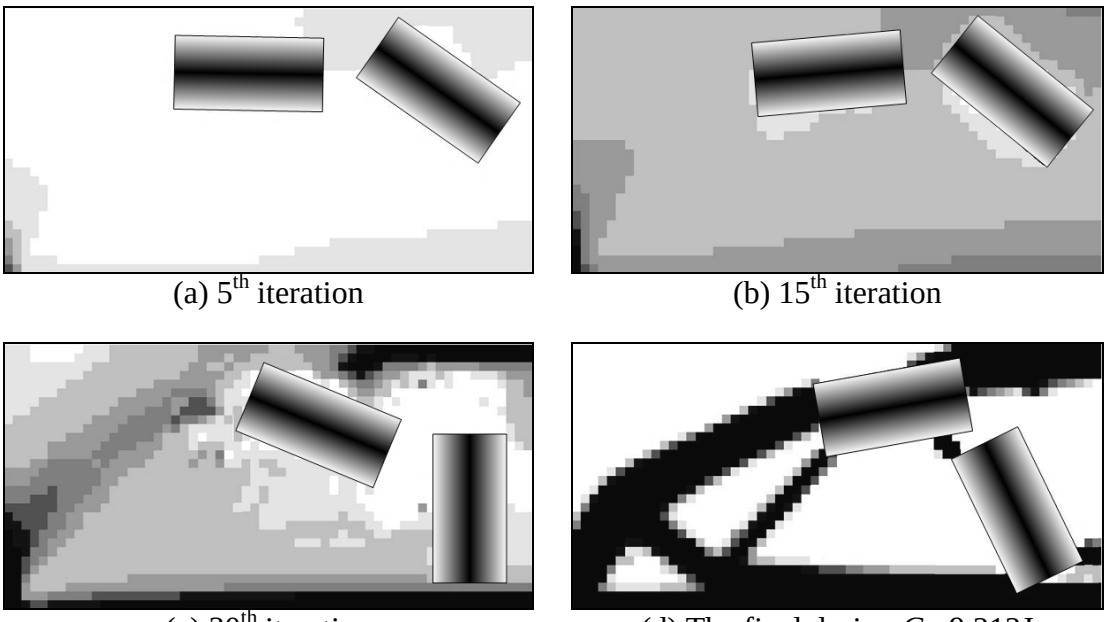

(a) 5th iteration (b) 15th iteration

(c) 30th iteration (d) The final design C =9.212J

Figure 5.23: Iteration history of the design patterns

Note that the moment of inertia of the initial design with a uniform structural material layout is 616.98kg·m^2 while in the final design shown in Figures 5.17 and 5.20, the moments of inertia are 1049.59 kg·m^2 and 703.88 kg·m^2, respectively. If the design

optimization is to constrain the moment of inertia to be less than 500kg·m^2 instead of the constraints on the center of gravity, four intermediate design patterns are presented in Figure 5.23. It costs much more iterations to reach the convergence. The final moment of inertia is 499.6 kg·m^2 that is significantly less than the previous designs. The two components are now located on the right side near the rotation axis. The convergence history is plotted in Figure 5.24.

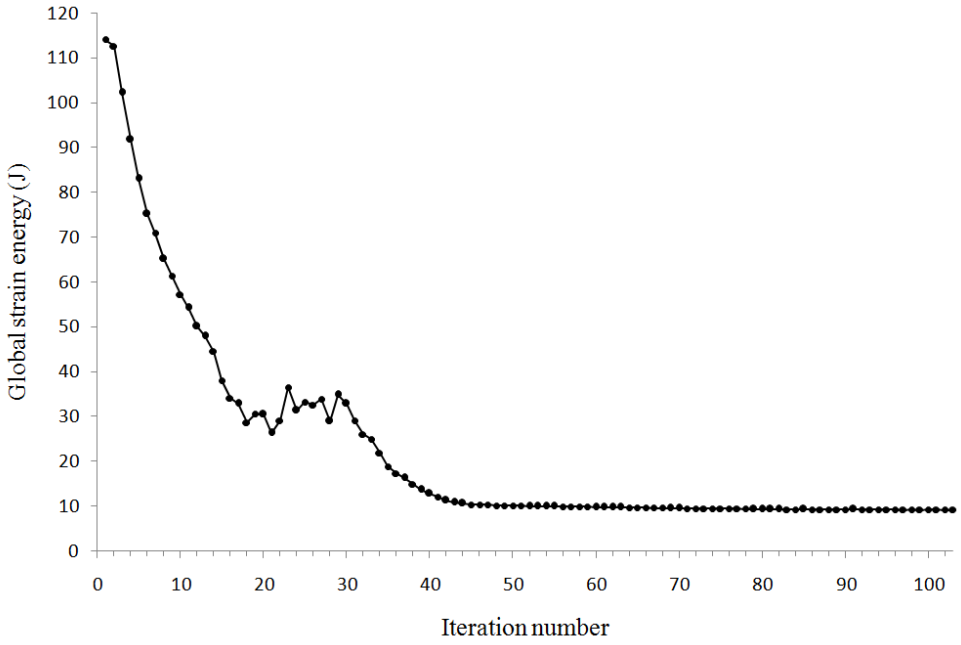

Figure 5.24: Convergence history of the global strain energy

5.3.3 Vibrating cantilever

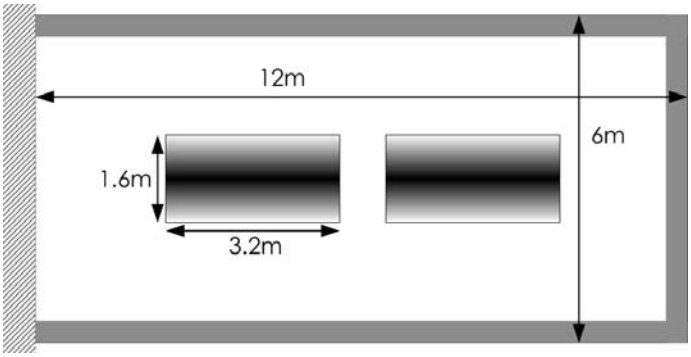

Figure 5.25: Design domain and the two components

Consider here the natural frequency maximization problems. As shown in Figure 5.25, a cantilever beam is fixed at the left side and discretized with 30×60 quadrangular elements. Suppose areas with 2 layer element thickness on the other three edges are non-designable parts to be reinforced by the inner structure. Two rectangle components will be located in the design domain.

Firstly, topology optimization is performed to maximize the 1st natural frequency without component. A 50% of the total material cost is used. The final structural layout and the

convergence history of the objective function are shown in Figure 5.26.

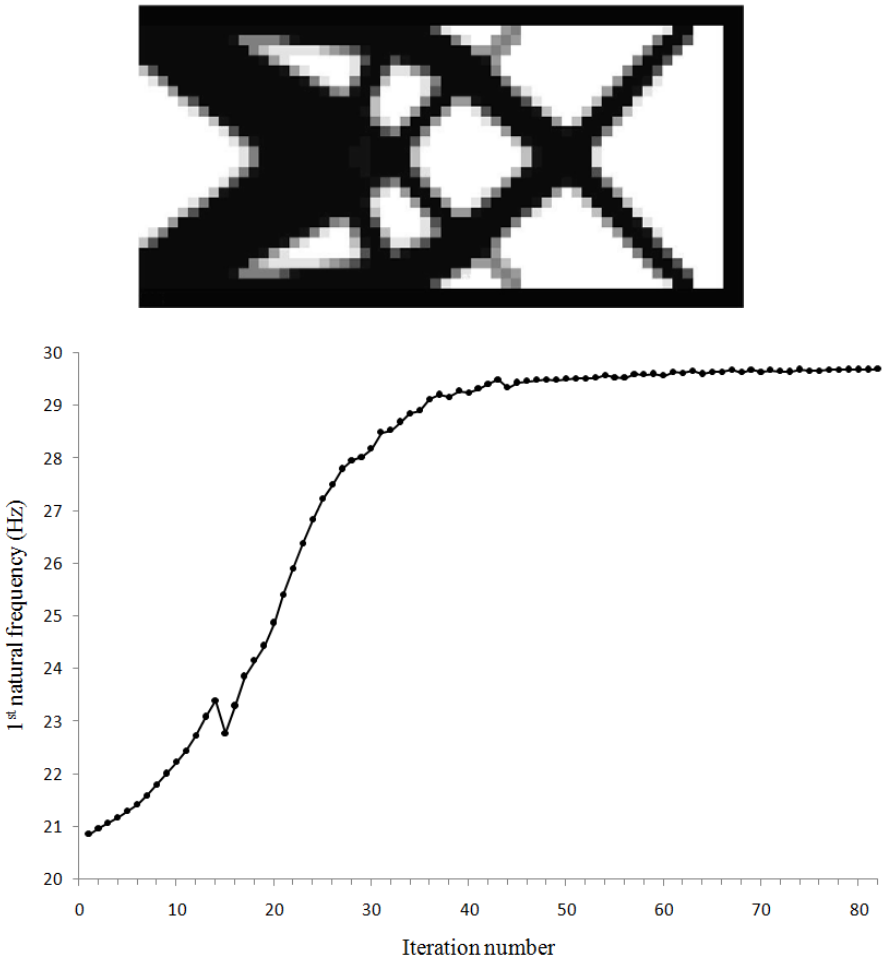

Figure 5.26: Topology optimization without component.
The 1st natural frequency is 29.69Hz

Then the two components are located at the center of the design domain initially. The integrated layout design is processed to maximize the 1st natural frequency as well. 45% of the structural material is used here. The two components move towards the fixation on the left side. When the components occupy the proper positions after dozens of iterations, the structural layout converges steadily as shown in Figure 5.27. However, due to the finite difference calculation of the sensitivities with respect to the geometrical design variables, we cannot ensure the symmetry of the layout design until now even we have symmetrical design domain and boundary conditions. The convergence history of the 1st natural frequency is plotted in Figure 5.28. 104 iterations are used in total.

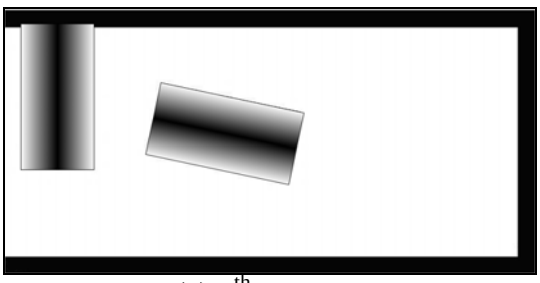

(a) 5th iteration

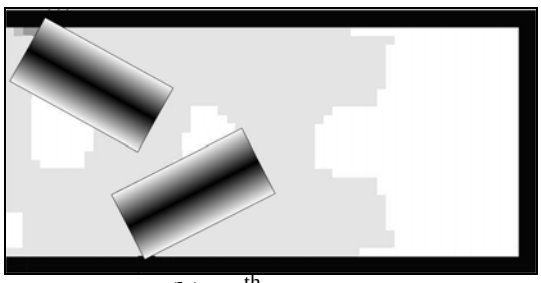

(b) 15th iteration

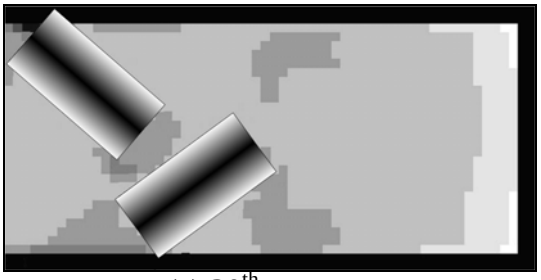

(c) 30th iteration

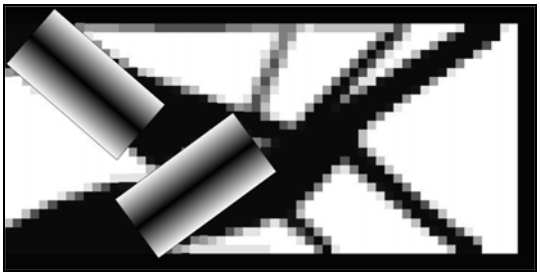

(d) The final design

Figure 5.27: Iteration history of the design patterns,
The 1st natural frequency is 29.71Hz finally

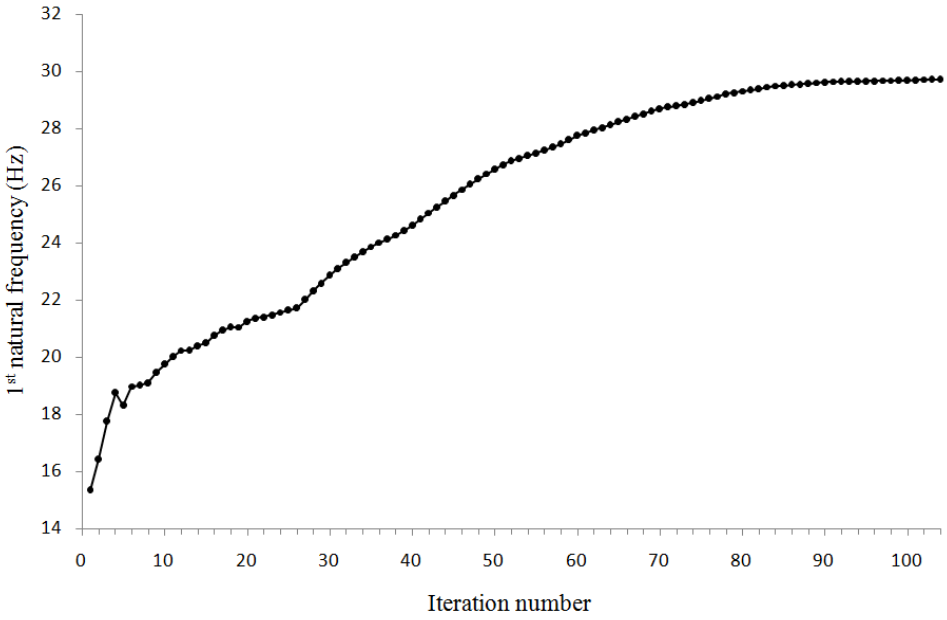

Figure 5.28: The convergence history of the 1st natural frequency

Then, the constraints are imposed to locate the center of gravity at the center of the design domain.

$$\begin{bmatrix} 6 \\ 3 \end{bmatrix} \leq \begin{bmatrix} x_G \\ y_G \end{bmatrix} \leq \begin{bmatrix} 6.01 \\ 3.01 \end{bmatrix} \tag{5-32}$$

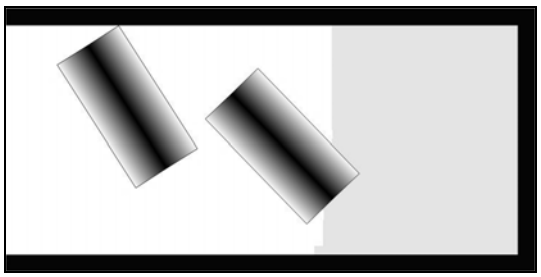

(a) 5th iteration

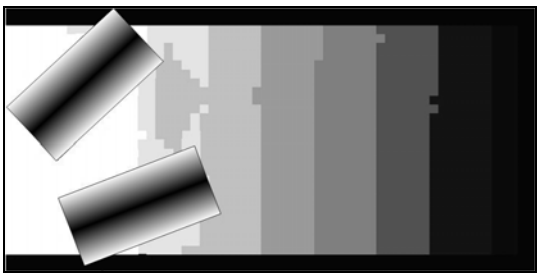

(b) 15th iteration

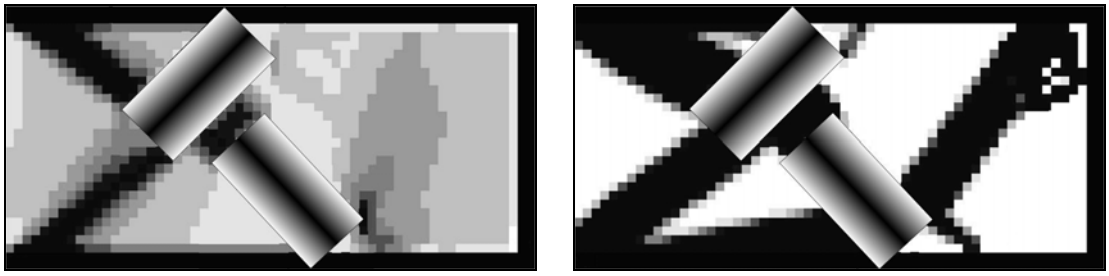

(c) 45th iteration (d) The final design

Figure 5.29: Iteration history of the design patterns,
The 1st natural frequency is 28.19Hz finally

Several structural patterns of the intermediate designs are presented as shown in Figure 5.29. At the beginning of the design procedure, the two components have the tendency of moving on the left side of the design domain just like in the previous one. But the structural materials have to be located on the right side to satisfy the constraints to the center of gravity. Later, the two components are push rightwards by the constraints. They are finally located near the center of the design domain and a clear structural configuration is obtained.

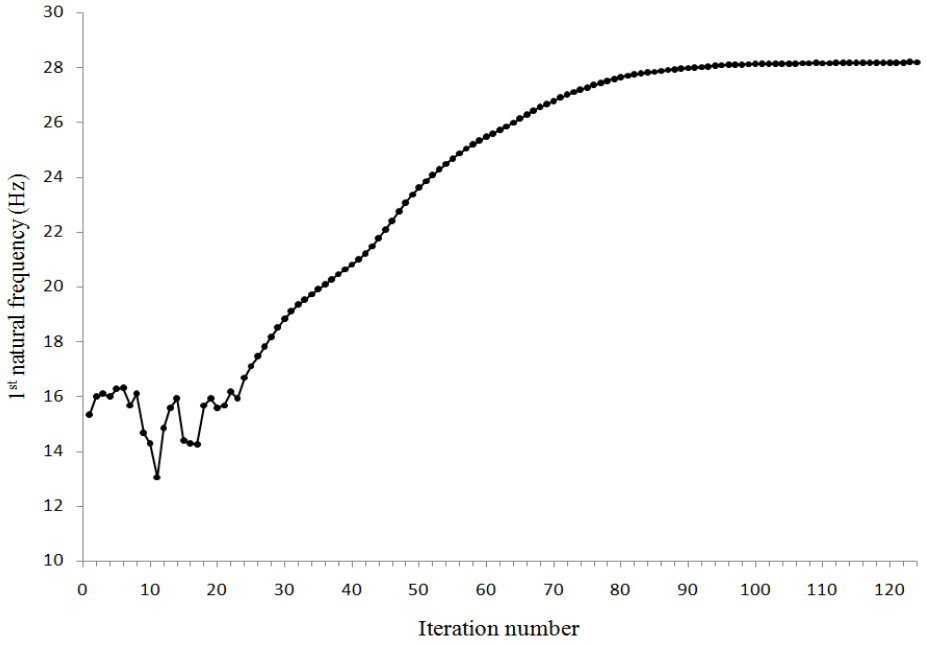

Figure 5.30: The convergence history of the 1st natural frequency

The optimization procedure costs 124 iterations and the convergence history of the 1st natural frequency is shown in Figure 5.30. In reference to the bottom left corner of the design domain, the center of gravity of the final design is located at (6.00, 3.01) whereas the optimal design without constraint on the center of gravity has the center of gravity located at (5.30, 2.98), Thus, the center of gravity moves rightwards by 0.7m with the cost of a reduction in the 1st natural frequency by 1.52Hz.

5.4 Conclusion

In this chapter, design dependent body loads and natural frequency maximization are addressed for multi-component systems. The polynomial material interpolation model proposed in Chapter 4 is used to avoid the localized deformations and localized modes in the low-density area.

Although reasonable results can be obtained with the presented methods, the heavy components are always located as close to the fixations as possible, which restricts the layout of the components in a limited area. To solve this problem, more practical physical constraints i.e. the center of gravity and moment of inertia are introduced.

Several tests are carried out and some results are obtained as expected. Compared with the examples given in Chapter 3, more complexities are included here because of the problems definition and the new introduced constraints. As a result, much more computing time is usually needed to reach the convergence.

Chapter 6

Design-dependent Boundary conditions

Overview

More flexibilities on the boundary definition of topology optimization problems are addressed in this chapter. The different boundary conditions, i.e. surface loads and fixations are considered to be designable. Integrated layout design techniques are utilized here to find proper configurations of the boundary conditions. Moreover, the simultaneous design of the structural layout and boundary conditions are successfully carried out.

Contents

6.1 Problem statement

In practice, the designs of structural supports or fixations are of great importance for the structural mechanical properties. This may arise in most structural engineering designs, as shown in Figure 6.1, especially in building constructions, workpiece machining fixture, welding or rivet joints of marine and aircraft structures. It is well-known that the support conditions play a crucial role in structural analysis. A small amount of adjustments in support positions can influence the structural performance significantly and should be designed carefully in favor of structural performances.

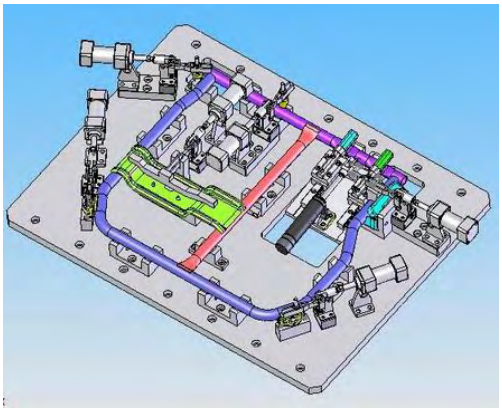

Fixtures in machining http://www.kefanjidian.com/

Figure 6.1: Typical structural supports and fixations

Previously, Rozvany (1974), Mroz and Rozvany (1975), Prager and Rozvany (1975), Szelag and Mroz (1979) discussed the issue of optimal support locations for elastic and plastic responses of beams. Rozvany and Mroz (1977), Olhoff and Taylor (1978), Olhoff and Akesson (1991) discussed the column support optimization for buckling load maximization. Akesson and Olhoff (1988) investigated the minimum stiffness design of the accessional supports to maximize the fundamental natural frequency. Hou and Chuang (1990) derived the sensitivity of the natural frequency to support positions where the concept of material derivative was used to find the optimal support position of a cantilever beam. Later, Wang (1993) derived the frequency sensitivity of closed-form to a support position by means of the classical normal modal method for an Euler-Bernoulli beam. A support force is treated as an external excitation imposed on a restrained structure. Wang and Chen (1996) employed the genetic algorithm to determine optimal support positions of beam structures for a wide variety of boundary conditions. Liu et al. (1996, 2000) derived the frequency sensitivity of closed-form by using the Rayleigh quotient in conjunction with the Lagrange multiplier based on Rayleigh's principle of stationary values. Bojczuk and Mroz (1998) provided an optimization procedure dealing with the number, position and stiffness of the supports. Sinha and Friswell (2001) applied the element shape function to formulate the global stiffness matrix of the beam including a support located on the beam element. Won and Park (1998) illustrated that the optimal support position relies greatly on the support stiffness. In many cases, it was found that the optimal support position is not unique for plate structures when supports are stiff enough. Recently, Wang (2003) developed an evolutionary shift method for support position

optimization in both static and dynamic applications.

In fact, the idea of topology optimization can also be extended to the support position design. Pedersen (1993) dealt with topology optimization of 3D truss structures with support variables involved in the optimization problems. Similarly, Jiang and Chirehdast (1997) designed the structural connections simulated with spring elements. Buhl (2001) designed the structure and supports simultaneously to find the efficient compliant mechanism or to maximize the global stiffness. Meanwhile, spring elements are used to fix the nodes in supported areas.

In this chapter, the structural boundary conditions are defined as some movable components along the boundary of the design domain, which generates a quasi-shape optimization problem. The idea will be verified first by comparing the optimization of support positions with topology optimization. Later the quasi-shape optimization is integrated with the topology optimization similar to the integrated layout design discussed previously. The structural layout and the layout of the boundary conditions are then designed simultaneously. Finally, coupled shape and topology optimization problems are dealt with on account of design dependent surface loads on the moving boundary.

6.2 Support positions

The pure support design problems are firstly discussed here. As shown in Figure 6.2, support component is defined on the boundary and fixations are assigned to the component.

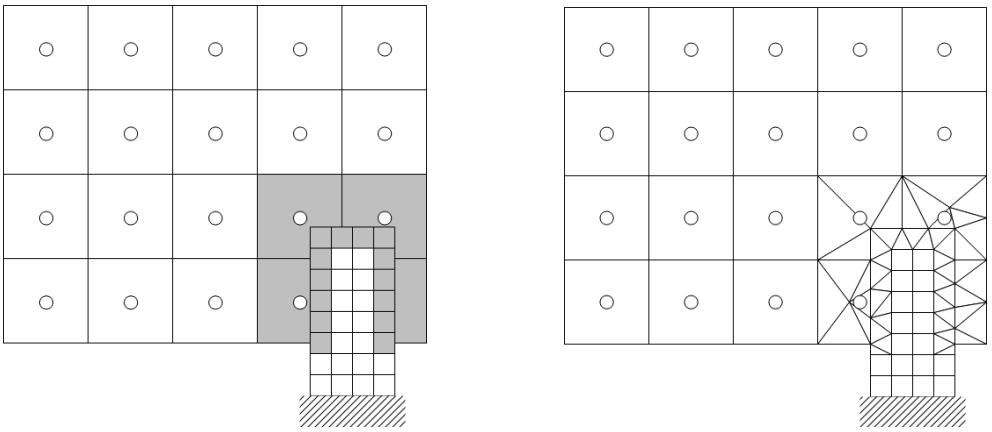

Figure 6.2: Illustration of embedded meshing in the support design

The component is embedded using the embedded meshing technique proposed in Chapter 3. The positions of the components are assigned as the geometrical design variables. During the optimization procedure, the design sensitivities of the objective functions with respect to the support positions are calculated with the finite difference. The layout of the boundary conditions as well as the positions of the components is updated.

The first example is a cantilever beam with one single designable support which will be compared with the existing design obtained by the topology optimization. The problem is illustrated in Figure 6.3. The optimal support position is to maximize the fundamental natural frequency of the structure.

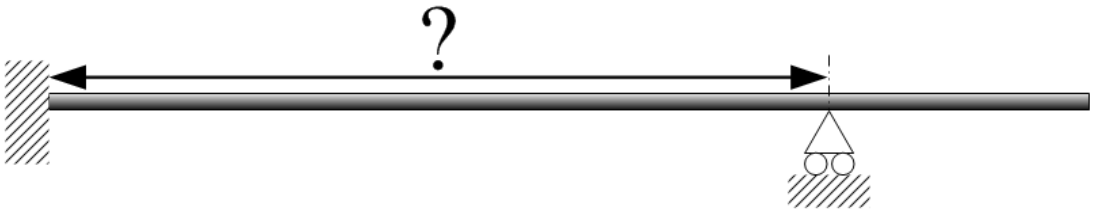

Figure 6.3: Problem definition of the cantilever beam

6.2.1 Simplified model with spring supports

A simplified model is shown in Figure 6.4. The cantilever beam has a length of 10m and a square cross section 0.2m×0.2m. It is modeled with 24 beam elements. 24 springs are attached to the nodes of the beam except the one which has been clamped on the left end. A non-structural mass 100kg is attached at the center of the beam. The material properties of the beam is set to be

elastic modulus, E_0=2×10^{11}pa, density ρ_0=7800kg/m^3.

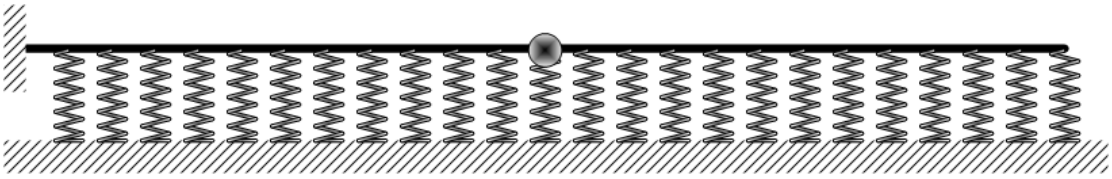

Figure 6.4: Full structural system of the cantilever beam in topology optimization

The pseudo-densities related to the stiffness factors of the springs are assigned as the design variables. Only the nodes that are connected to strong springs can be equivalently considered as fixed. A power-law penalty of SIMP is used approximately to yield a pure 0-1design.

$$k_i = \eta_i^p k_{i0} \tag{6-1}$$

where k_i and k_{i0} denote the current stiffness factor of the *i*th spring and the stiffness factor when it is of full stiffness. The penalty factor here is set to be 3. Because there is no mass property defined for the springs, no problem of localized modes occurs in natural frequency maximization design.

The design sensitivities with respect to the spring stiffness are easily obtained by simply setting the mass properties of the elements derived in Chapter 4 to be 0, which can be expressed as

$$\frac{\partial \omega^2}{\partial \eta_i} = \frac{\boldsymbol{u}^T \dfrac{\partial \boldsymbol{K}}{\partial \eta_i} \boldsymbol{u}}{\boldsymbol{u}^T \boldsymbol{M} \boldsymbol{u}} = \frac{P'(\eta_i)}{P(\eta_i)} \frac{\boldsymbol{u}^T \boldsymbol{K}_i \boldsymbol{u}}{\boldsymbol{u}^T \boldsymbol{M} \boldsymbol{u}} \tag{6-2}$$

The maximum stiffness factors of the springs are set to be k_{i0}=2.8×10^{6}N/m. Only one spring will be retained to support the beam. After 6 iterations, the optimal result is that the 20th spring is retained as shown in Figure 6.5. This can be easily confirmed to be the global optimum.

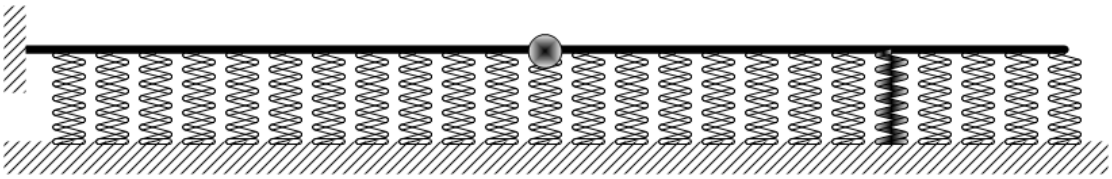

Figure 6.5: The final optimal design, the 1st natural frequency is 7.1092Hz

Besides, it is interesting to understand the effects of spring stiffness upon the support design. By changing the stiffness value of k_0 between 5×10^5N/m and 2.5×10^7N/m, optimal positions and the 1st natural frequencies are shown in Table 6.1.

Table 6.1 Optimal results with different support stiffness factors

Support stiffness (10^6N/m)	Optimal support position 1st natural frequency (Hz)					
	19	20	21	22	23	24
0.50						3.9930
0.89						4.7935
1.20					5.2779	
1.70				5.9376		
2.00			6.3059			
2.80		7.1092				
4.00		8.0832				
8.00	9.9975					
15.0	10.115					
25.0	10.129					

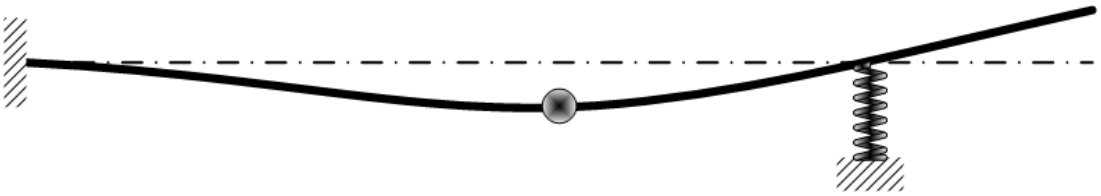

(a) 1st natural frequency 10.129Hz

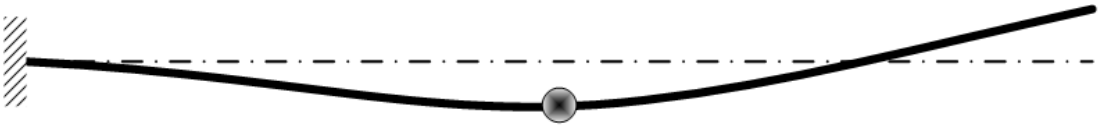

(b) 2nd natural frequency 10.177Hz

Figure 6.6: Comparison between the 1st vibration shape with spring support and 2nd vibration shape without spring support

It is found that the spring stays at position numbered 24 only if the support is compliant enough. When the spring is stiffened, the optimal position will move towards the clamped edge and stop at position numbered 19 as long as the spring reaches the so-called critical stiffness. Similar discussions can be found in the work of Akesson and Olhoff (1988) and

Won and Park (1998).

According to Courant's maximum-minimum principle, a structure with n additional supports will raise its jth natural frequency whose value is between the jth and the (j+n)th frequencies of the original strucutre. Similarly, once the elastic support becomes a rigid one in this example, the optimal support position that maximizes the 1st natural frequency (see Figure 6.6(a)) turns out to be the nodal position of the 2nd mode (Figure 6.6(b)) of the unsupported beam where the vibration displacement is zero. And the optimal 1st frequency shifts to the 2nd frequency of the unsupported beam. This phenomenon can be illustrated with following figures and we can also refer to the work by Akesson and Olhoff (1988), Olhoff (1976) and Szelag and Mroz (1979).

In Figures 6.6, the 1st vibration mode of the optimal design with k_0=2.5×10^{7}N/m and the 2nd vibration mode of the clamped beam without spring support are compared.

6.2.2 Support component

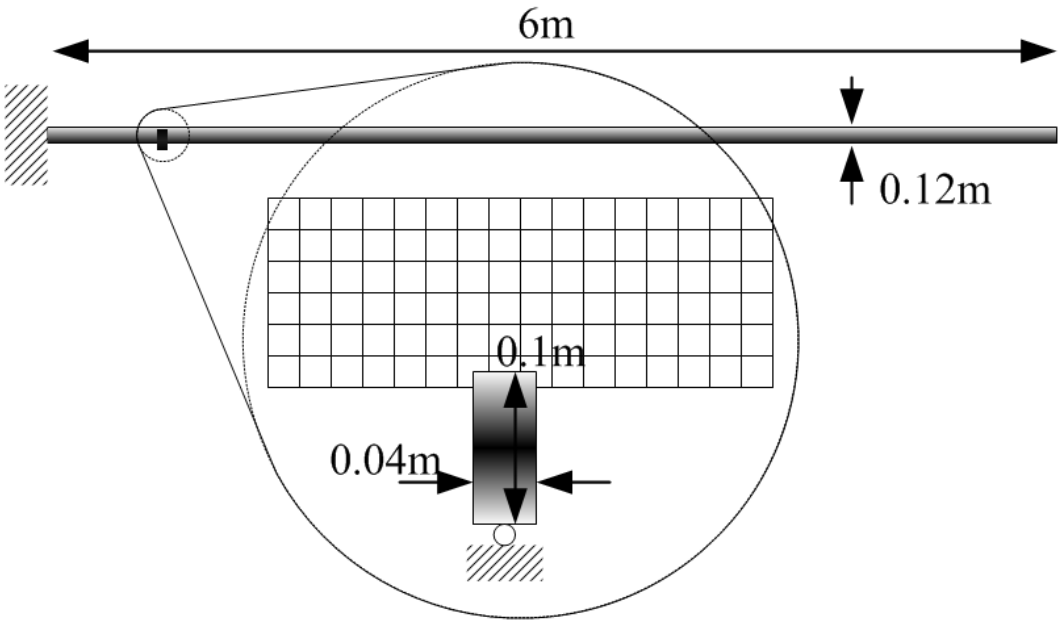

Figure 6.7: Cantilever beam with a support defined as a component

Here, the cantilever is built as a refined model meshed with 6×300 2D quadrangular elements. As shown in Figure 6.7, a small component is defined with its bottom edge fixed. It is partially embedded into the beam where the surrounded elements are modified to ensure the connection.

The material properties of the beam are set to be

elastic modulus, E_0=7×10^{10}pa, density ρ_0=2700kg/m^3 and Poisson's ratio v=0.3

No mass property is defined for the material of the component. Its elastic modulus is 100 times of that of the beam to simulate a rigid support.

In this example, only one design variable, i.e., the horizontal position of the support component exists. It is initially located at the left end of the beam. The final position is obtained at the 8th iteration. The fixation is located 4.71m far from the left end as shown in Figure 6.8(a), which is almost identical with the nodal position of the 2nd order

vibration shape of the unsupported beam as shown in Figure 6.8(b). Although the component is not an ideal nodal fixation, the final 1st natural frequency is very close to the 2nd one of the unsupported beam.

(a) 1st natural frequency 17.15Hz

(b) 2nd natural frequency 17.17Hz

Figure 6.8: 1st vibration shape with optimal support position and 2nd unsupported vibration shape

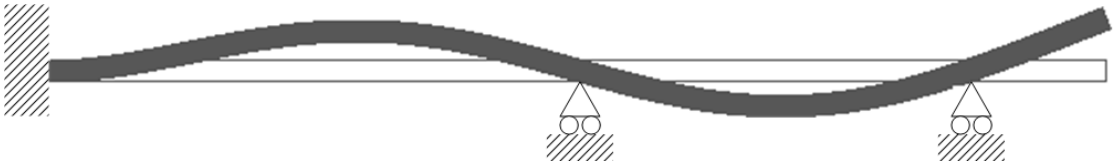

(c) 1st natural frequency 47.84Hz

(b) 3rd natural frequency 47.89Hz

Figure 6.9: 1st vibration shape with two optimal support positions and 3rd unsupported vibration shape

The cantilever beam is further designed by introducing two identical support components, as shown in Figure 6.7. Meanwhile, one simple geometrical constraint is introduced to avoid the overlap between the two components. However, FCM is not needed here since both the components are only allowed to move horizontally.

The two components are located initially at the two ends of the beam. By carrying out the optimization, the optimization converges at the 20th iteration and the components are located at 3.01m and 5.18m, respectively.

In Figure 6.9, the vibration shape with the optimal support positions and the 3rd vibration shape of the unsupported cantilever are compared. The two support components are now located near the two nodal positions of the unsupported cantilever shown in Figure 6.9(b). The obtained optimal 1st natural frequency is still very close to the 3rd natural frequency of the unsupported cantilever.

In fact, the optimization of the support locations presented here is a quasi-shape optimization problem. Compared with the topology optimization of the support design, the actual strategy is not to find a support layout from a great quantity of candidate support positions. This is the case when the number of fixations on each supported boundary and detailed shapes of the support components are prescribed a priori.

6.3 Coupled support and structural layout design

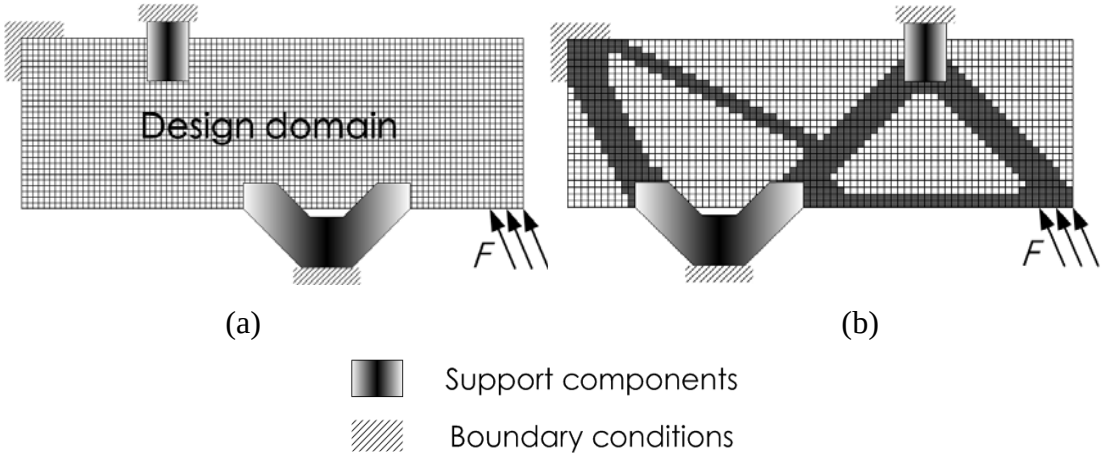

Figure 6.10: Concept of the coupled support and structural layout design

Inspired by the simultaneous topology design presented by Buhl (2001), the proposed integrated layout design techniques are used to solve the coupled support and structural layout optimization. Unlike the topology optimization used in Buhl (2001), the fixations are defined as movable support components that are partially embedded into the design domain. Meanwhile, the material layout of the design domain is described with density points. And the structural layout is designed with topology optimization. The problem can be illustrated in Figure 6.10.

Several examples are discussed here to show the effect of the coupled design. The material properties are as follows
for the components and non-designable areas:

elastic modulus, $E_0=2\times10^{11}$pa, density $\rho_0=7800$kg/m^3 and Poisson's ratio $v=0.3$;

and for the structures:

elastic modulus, $E_0=7\times10^{10}$pa, density $\rho_0=2700$kg/m^3 and Poisson's ratio $v=0.3$.

6.3.1 Bridge problem 1

The design domain of the first example is shown in Figure 6. The basic mesh is composed of 30×120 quadrangular finite elements. The road on the bridge is the non-designable area. As the movable fixations, four support components with the size 0.6m×1m will be located symmetrically on the boundary of the design domain. Considering the symmetry, only two geometrical design variables are involved for the four components.

A uniform surface load 10000N/m is applied on the top of the road. The final volume fraction for the topology optimization of the structure in the design domain is set to be

40%. Several intermediate layout design patterns are presented in Figure 6.12. The material layout and the locations of the components are updated simultaneously. But when a clear structural layout is obtained e.g. at the 25th iteration as shown in Figure 6.12(c), the components are still moving slightly and the structure pattern are modified accordingly in the following iterations. The optimization converges at the 138th iteration.

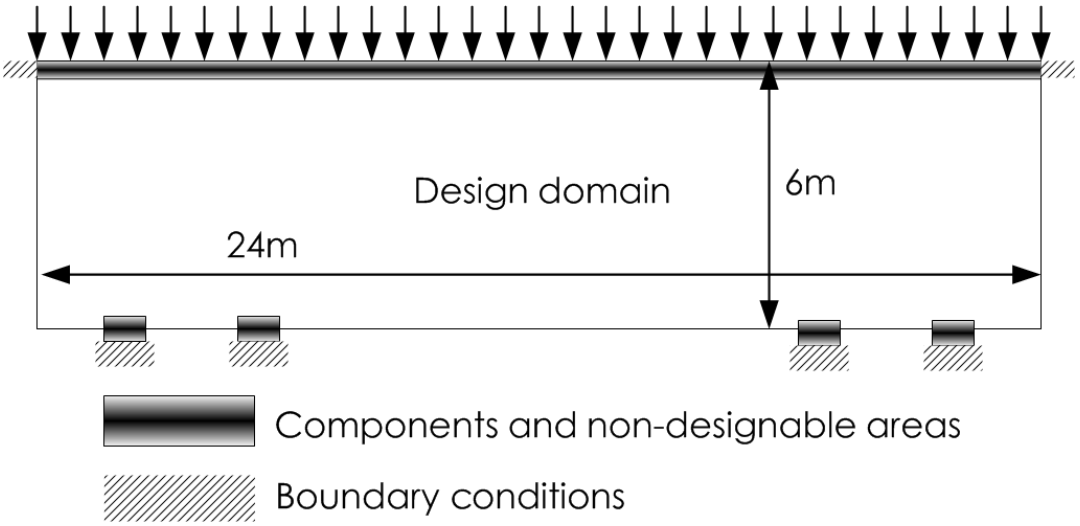

Figure 6.11: The design domain and the support components of the bridge problem

(a) 5th iteration

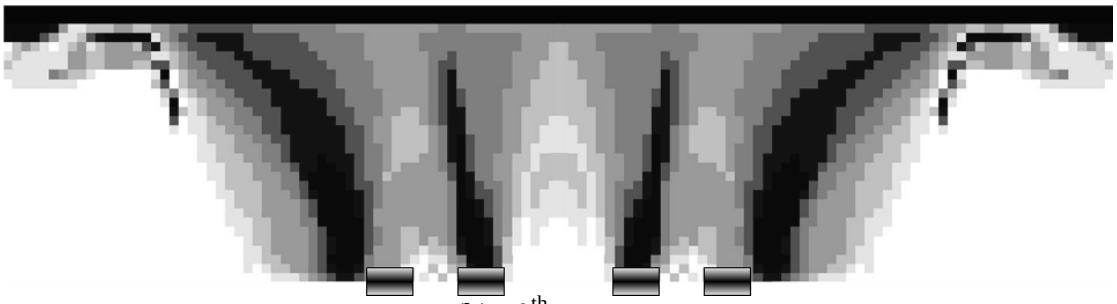

(b) 10th iteration

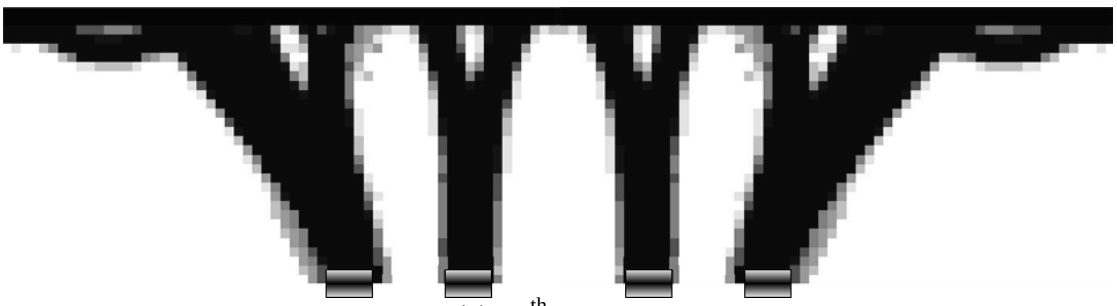

(c) 25th iteration

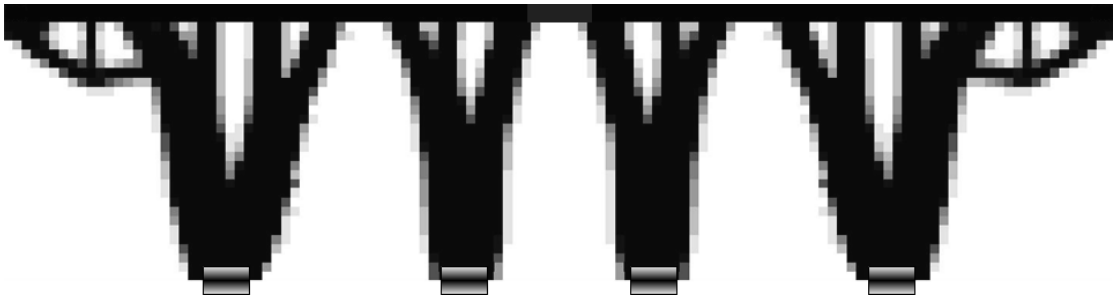

(d) The final design C =0.1298J

Figure 6.12: Iteration history of the design patterns

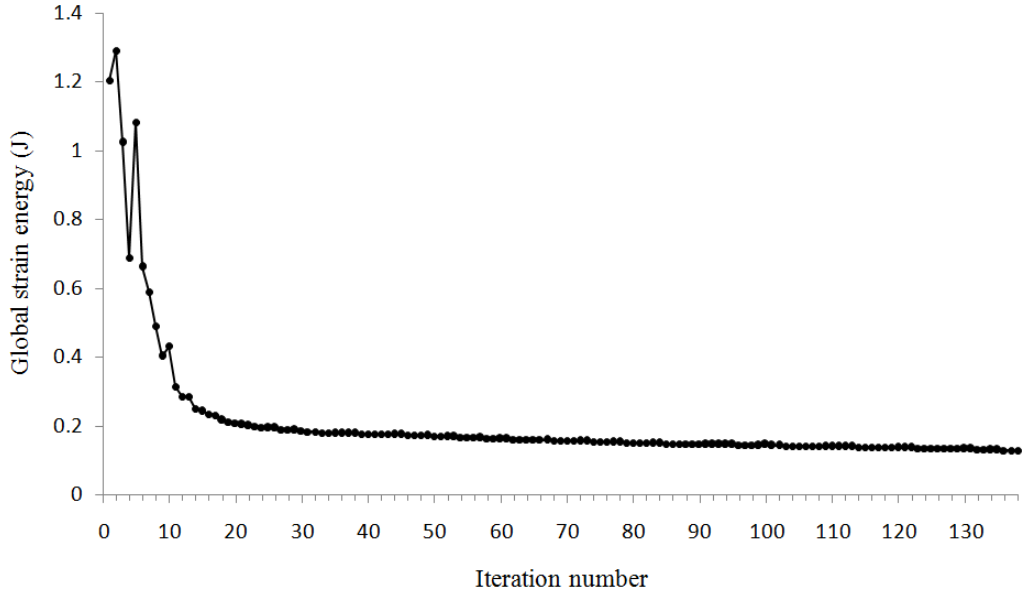

Figure 6.13: The convergence history of the global strain energy

In fact, the design is very sensitive to the support components. A slight change of the support locations will lead to significant variation of the structural configuration.

The convergence history of the objective function is shown in Figure 6.13. At the beginning, the supporting components may be located away from the main loading structure. As a result, some instability is found in the convergence of the objective function. In the final design, the four components find their proper positions and structures are generated to interconnect the components and the road.

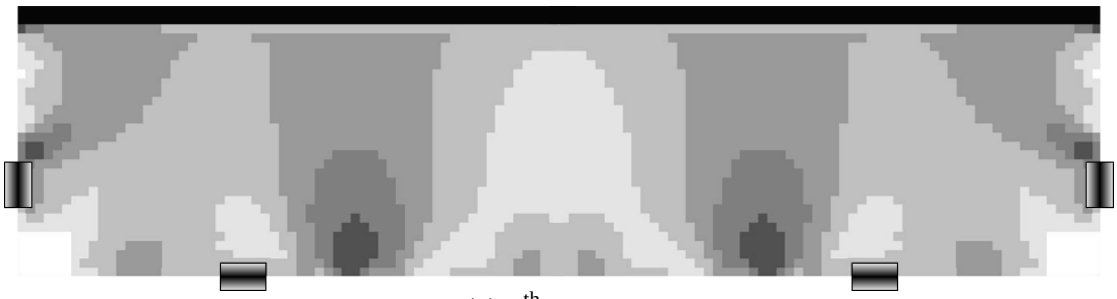

(a) 5th iteration

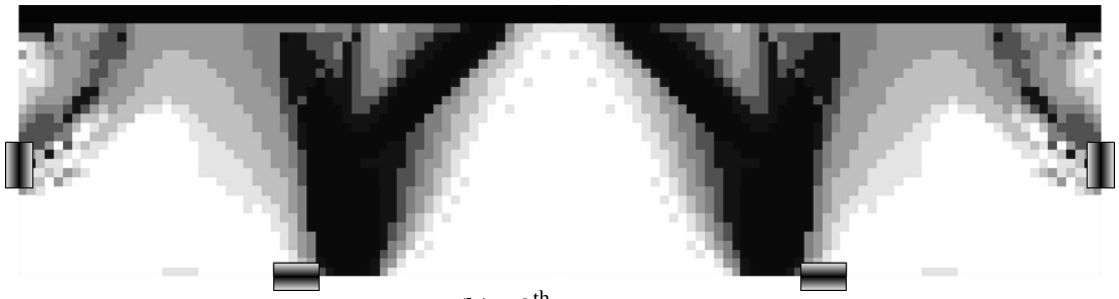

(b) 10th iteration

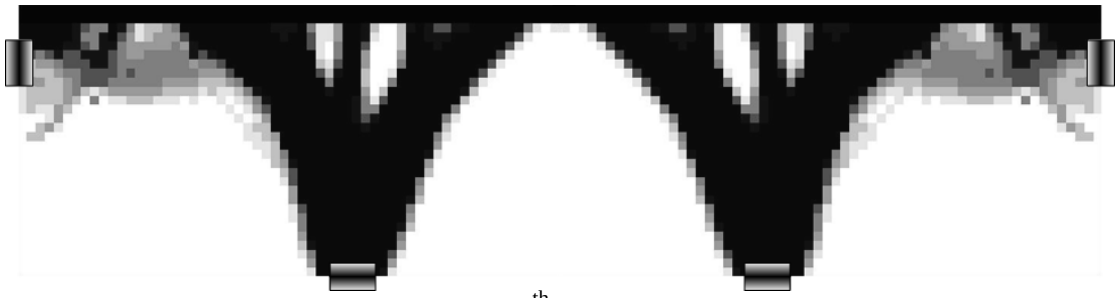

(c) 25th iteration

(d) The final design C =0.1467J

Figure 6.14: Iteration history of the design patterns

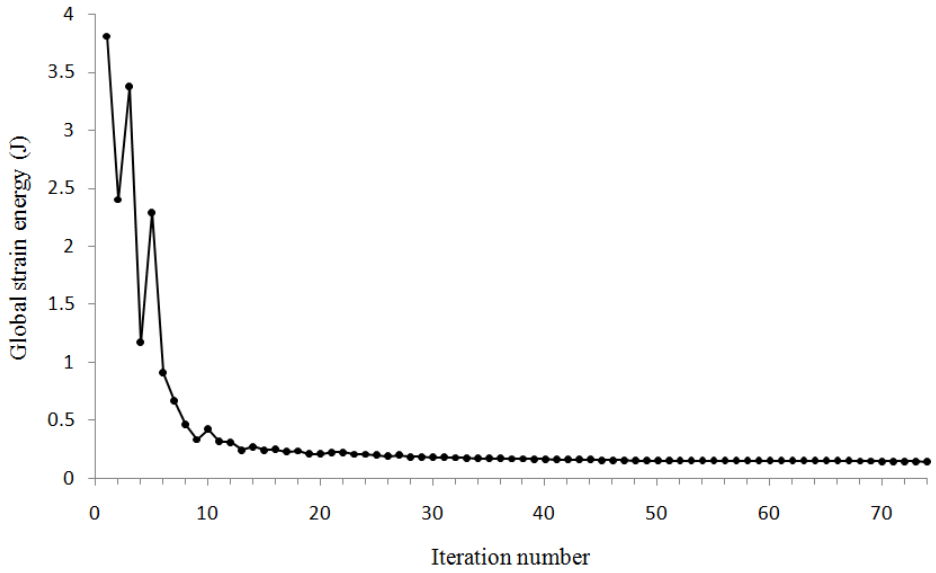

Figure 6.15: The convergence history of the global strain energy

Now, the example is further tested with only two of the components allowed on the bottom edge, while the other two have to be located on the left and right sides of the

design domain. With the structural volume fraction constrained to 40%, several structural patterns are shown in Figure 6.14. The structural layout becomes clear very quickly. But it costs much more iterations to find proper positions for the support components. The final optimal design is obtained at the 74^{th} iteration. The convergence history of the objective function is shown in Figure 6.15.

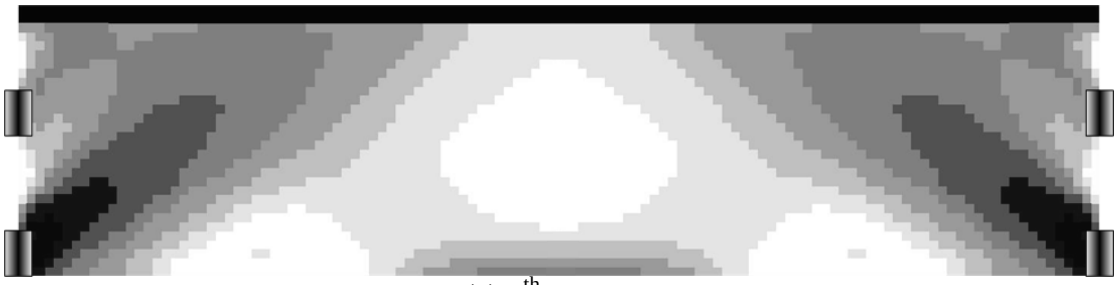

(a) 5^{th} iteration

(b) 10^{th} iteration

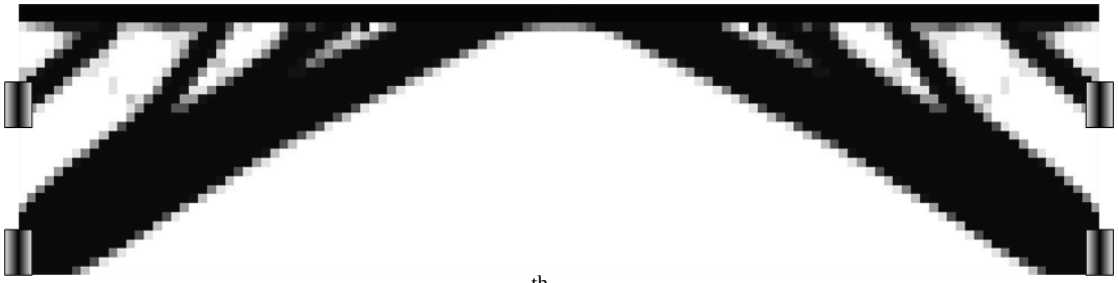

(c) 25^{th} iteration

(d) The final design C =0.8781J

Figure 6.16: Iteration history of the design patterns

Sometimes the supports are only allowed on the two ends of the bridge. With the same definition as previous one, the problem is further designed by locating all the four support components on the left and right sides of the design domain.

By using 40% of the total material, several iterations are presented as shown in Figure 6.16. Similarly, the structural pattern evolves quickly but the locations of the support

components move rather slowly during the design procedure. 124 iterations are used to reach the final convergence.

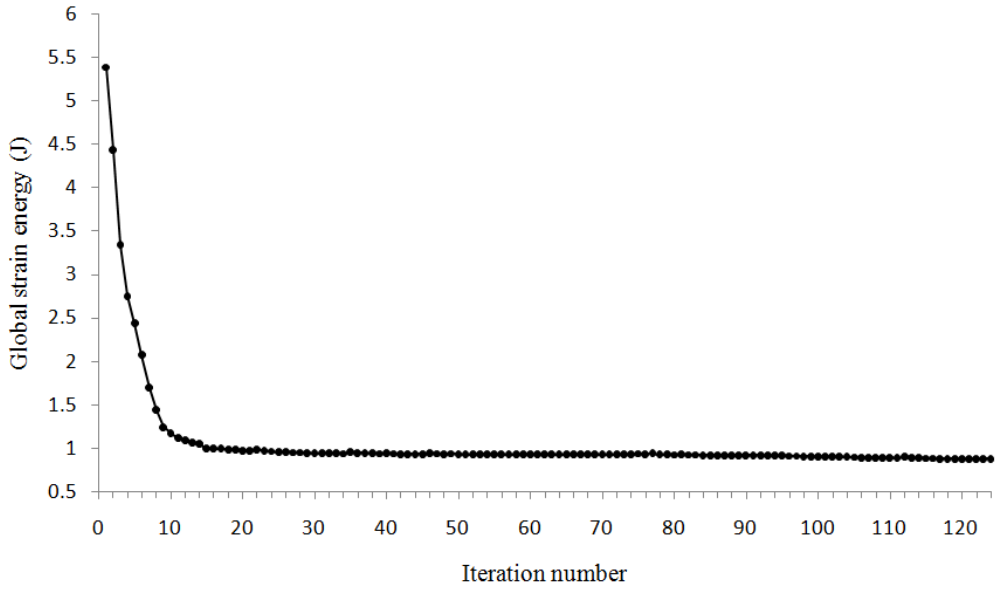

Figure 6.17: The convergence history of the global strain energy

Two support components are always located at the two bottom corners, which provide strong supports for the global structure from the beginning to the end, no instability is found during the iteration history.

6.3.2 Bridge problem 2

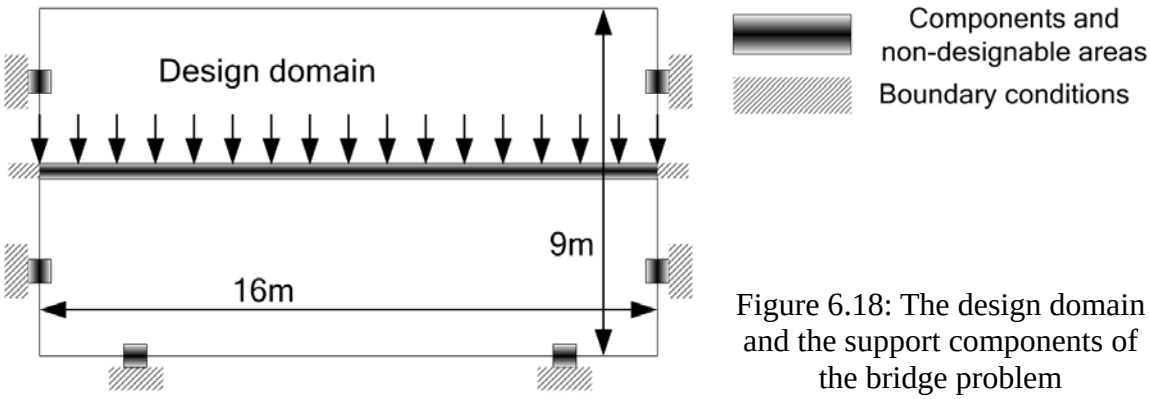

Figure 6.18: The design domain and the support components of the bridge problem

Another bridge problem is tested here with the design domain shown in Figure 6.18, where the six support components and the structures are allowed both below and above the road. The basic mesh consists of 45×80 quadrangular finite elements. The components with the size 0.6m×0.6m are located symmetrically on the boundary of the design domain. A uniform surface load 10000N/m is applied on the road, which is located at the 5m height from the bottom.

Firstly, two of the support components are located on the bottom, the rest four of them are located on the left and right sides, above and below the road, respectively. Only 30% of the total material cost is allowed for the structure. During the optimization procedure, the

structure is growing up from each support component to support different sections of the road. The components find their locations rapidly. As a result, the final design is obtained at the 62nd iteration which converged rather faster than the previous designs. The convergence history is shown in Figure 6.20.

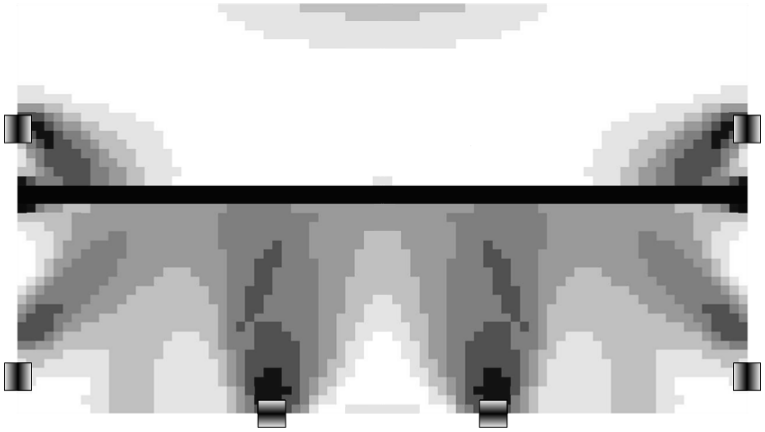

(a) 5th iteration

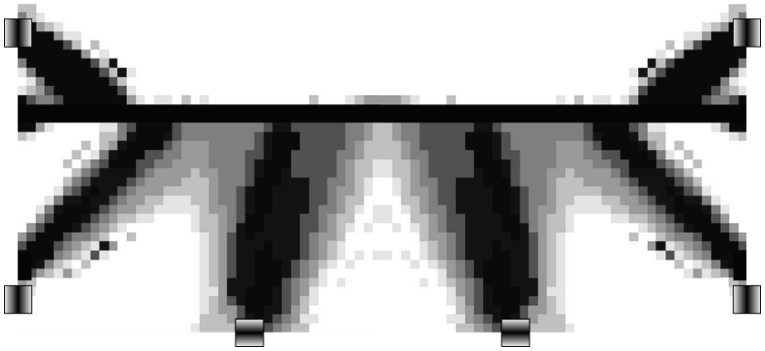

(b) 10th iteration

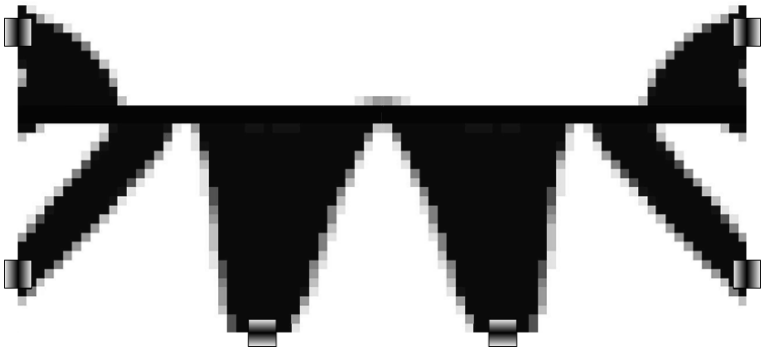

(c) 25th iteration

(d) The final design
C =0.0511J

Figure 6.19: Iteration history of the design patterns

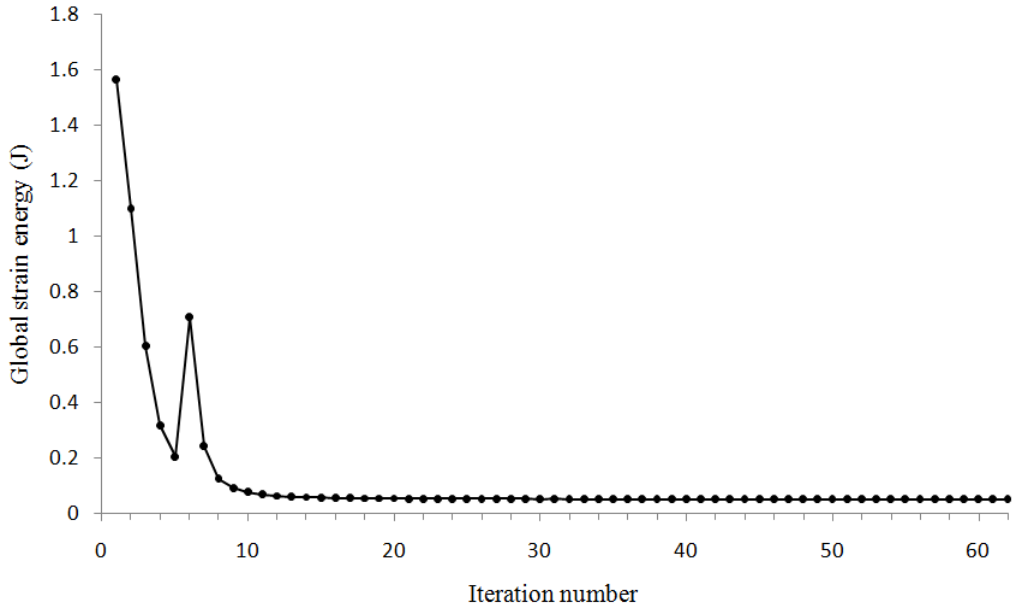

Figure 6.20: The convergence history of the global strain energy

Similarly, another test is carried out without component allowed on the bottom of the design domain. The material cost is also restricted to 30%. Several structural patterns are presented in Figure 6.21. Because the design space for the components is rater limited in this example, they move slightly until they find their proper locations. Finally, the optimal structure connecting the different sections of the road and the support components is obtained. The convergence is achieved at the 45th iteration as shown in Figure 6.22.

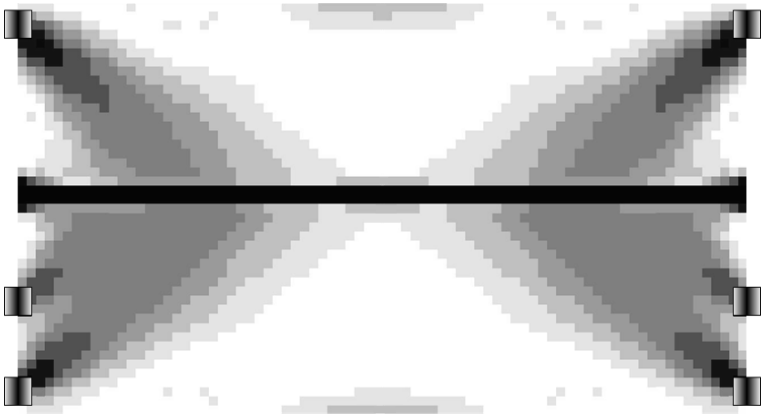

(a) 5th iteration

(b) 10th iteration

(c) 25th iteration

(d) The final design

Figure 6.21: Iteration history of the design patterns, C =0.1774J finally

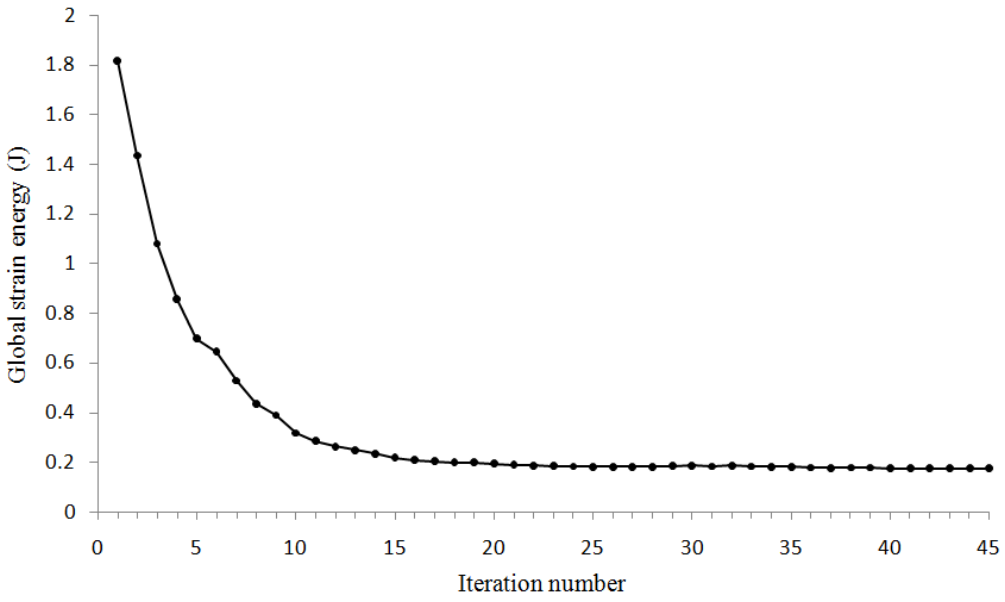

Figure 6.22: The convergence history of the global strain energy

6.3.3 Conclusion

Since the components are limited on the boundary of the design domain, the distance constraints avoiding the overlaps can be easily defined. As a result, the global definition

of these problems is actually less complex than the integrated layout design discussed in the previous chapters. Although all the tested examples with support components generate reasonable structural designs, the introduction of the movable support positions brings more difficulties in the optimization procedure, especially when we have a relatively large design space, e.g. the bridge examples in section 6.3.1.

6.4 Coupled shape and topology optimization

Besides the design dependent body loads as discussed in Chapter 4 and 5, another kind of design dependent loads involved in topology optimization is the pressure load on the variable surface, as shown in Figure 6.23.

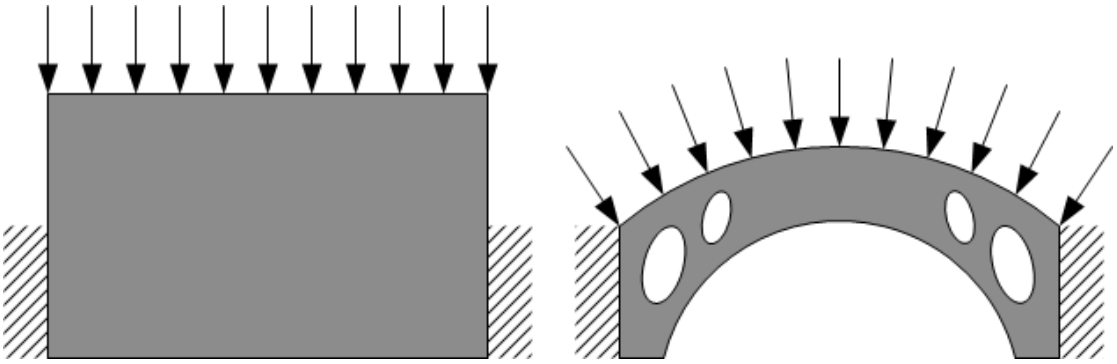

Figure 6.23: Illustration of the topology optimization with design dependent surface load

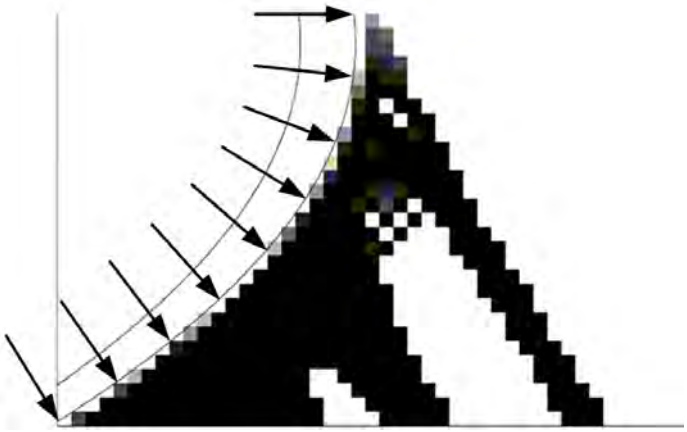

Figure 6.24: The pressure loads on the interface between the solid and void elements
Fuchs and Shemesh (2004)

Similar problems are discussed in detail by Hammer and Olhoff (1999 and 2000), Chen and Kikuchi (2001), Du and Olhoff (2004a and b), Fuchs and Shemesh (2004), Gao and Zhang (2007), Sigmund and Clausen (2007). In all of these previous works, the variable boundaries are still described by the interfaces between the solid and void elements as shown in Figure 6.24. Normally it is complex to identify the interface especially when there are a lot of elements with intermediate pseudo-densities nearby. Since the interface is not a real line (2D) or a real surface (3D) in the structure, the pressure should be equivalently applied on the neighboring nodes. In this way, the shape of the design domain as well as its element mesh can remain unchanged.

An alternative method is presented here by using the proposed techniques of density points and embedded meshing. As shown in Figure 6.25, the pressure is applied on a curved surface which may be built as a spline with several interpolation points to be optimized. The embedded meshing is employed by subtracting the white area using the Boolean operation and the elements around the spline are modified. The rest dark area denotes the actual design domain, where the structural layout will be designed with topology optimization. As the density points fully located in the white area will lose their controlled elements, they are actually useless and the corresponding pseudo-densities will take zero values. Besides, since the shape and the topology of the design domain are optimized simultaneously, this is a kind of coupled shape and topology optimization problems.

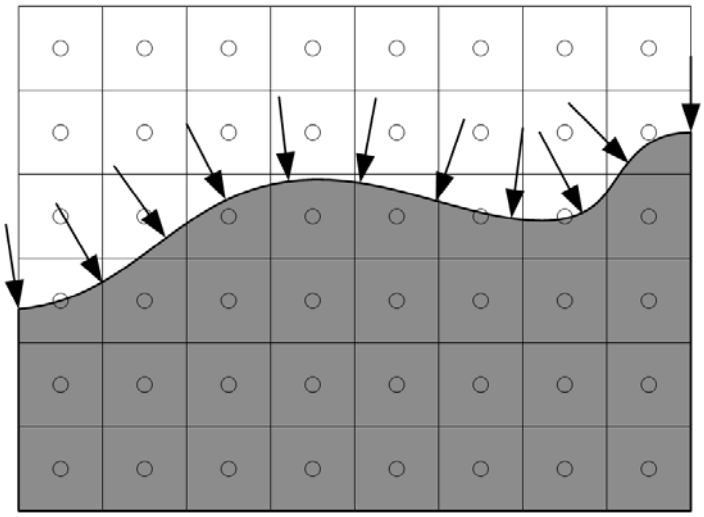

Figure 6.25: Illustration of the curve loading surface and the basic mesh

Consider the test shown in Figure 6.26 to illustrate the coupled shape and topology optimization. The design domain is a 6m×24m rectangle plate with the basic mesh consisting of 30×120 quadrangular elements. The top surface is considered as a thin band modeled by 2 symmetrical spline segments with 11 interpolation points altogether. 6 vertical coordinates of these interpolation points are thus assigned as the geometrical design variables because of the symmetry. The material properties are defined as

elastic modulus, $E_0=7\times10^{10}$pa, density $\rho_0=2700$kg/m^3 and Poisson's ratio $v=0.3$.

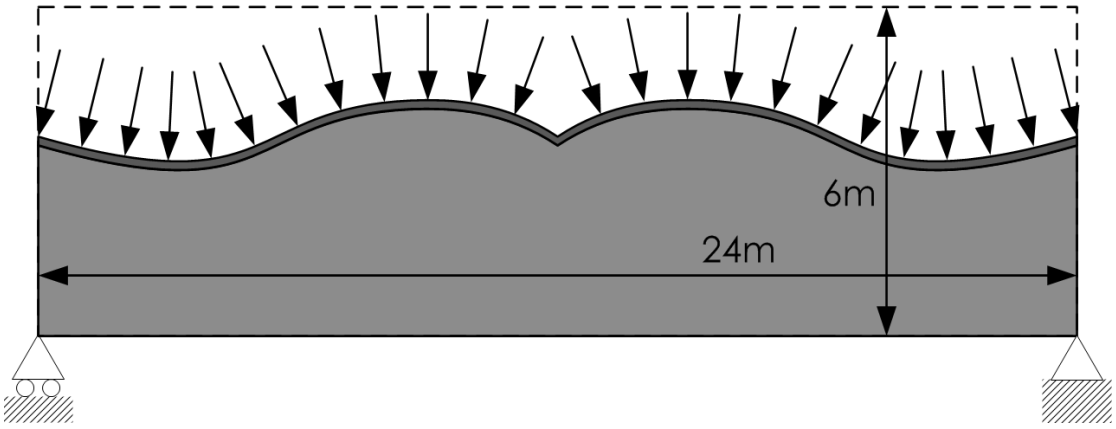

Figure 6.26: Design domain of the simply supported beam

Suppose a pressure of 10000N/m is applied on the top surface. 50% of the total material cost is allowed in the design domain. The iteration history is shown in Figure 6.27. After 15th iteration, the loaded surface evolves to a smooth arch like a MBB beam. Although the shape of the loaded surface reaches the optimum very quickly, but the structural layout converges rather slowly. Therefore, when the global structural pattern is almost clear at the 66th iteration, the sensitivity filter is manually shut down to accelerate the convergence process. Consequently, the elements with intermediate pseudo-densities vanish very quickly. Two new structural branches are generated near the center of the design domain.

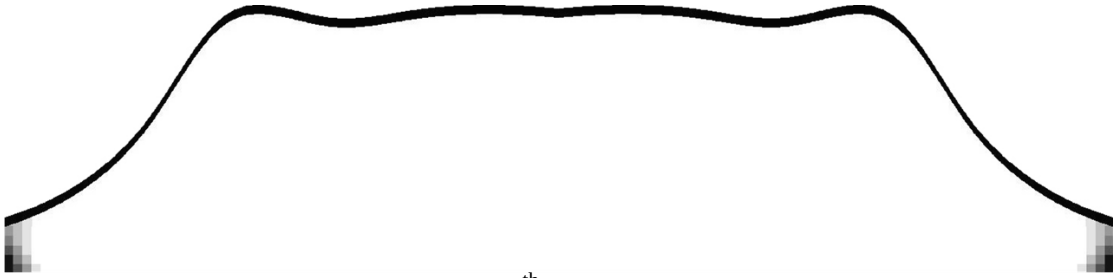

(a) 5th iteration

(b) 12th iteration

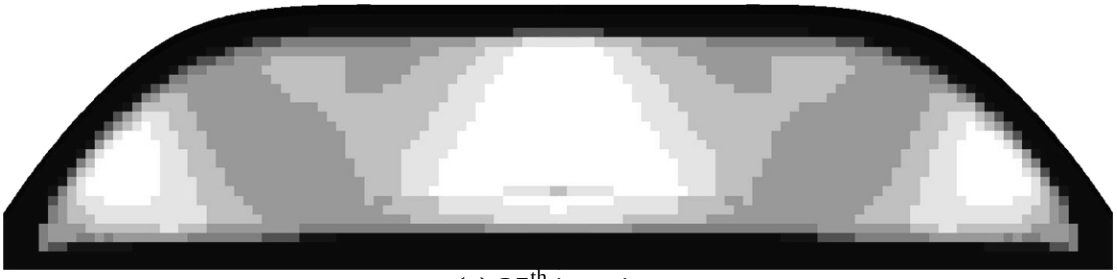

(c) 25th iteration

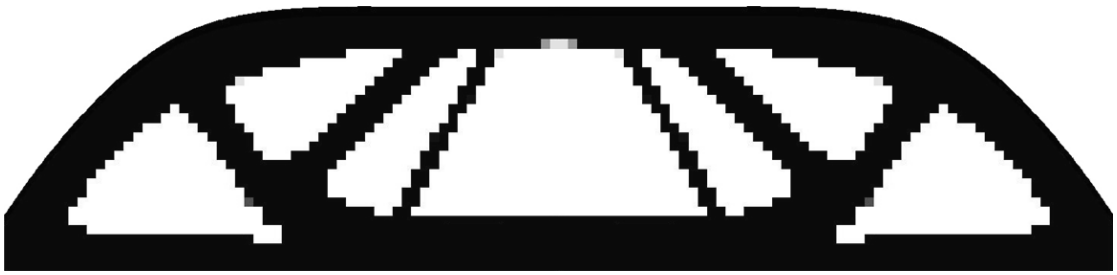

(d) The final design

Figure 6.27: Iteration history of the design patterns, C =3.494J finally

The optimization totally takes 102 iterations. The convergence history of the objective function is shown in Figure 6.28.

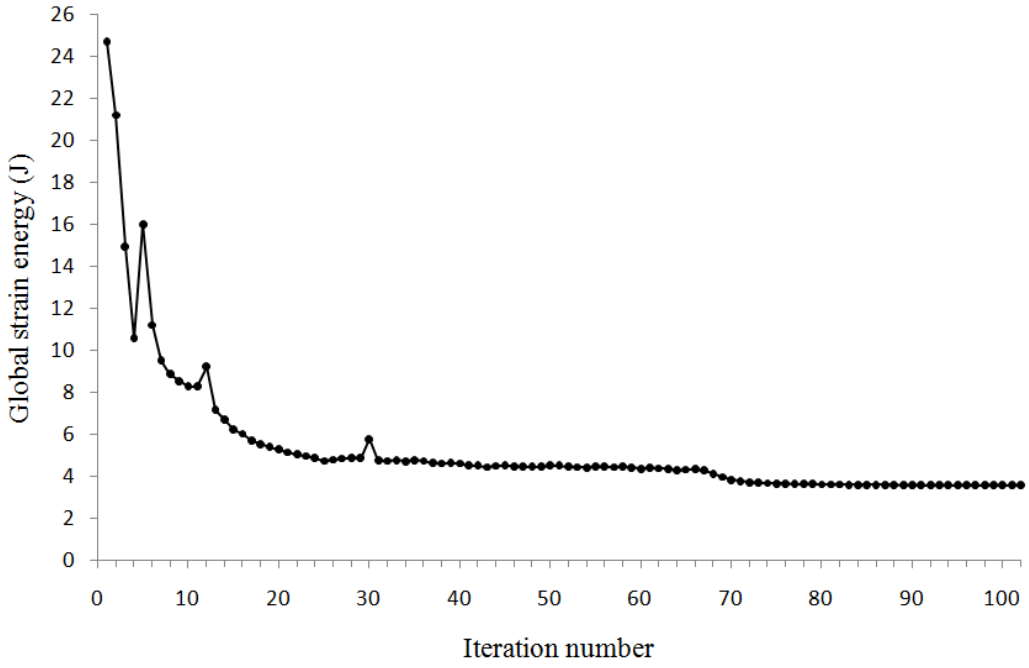

Figure 6.28: The convergence history of the global strain energy

6.5 Conclusion

Different problems with design dependent boundary conditions are considered in this chapter. The fixations are firstly defined as the support components, which are partially embedded into the design domain. The layout of the fixations is to determine the positions of these components on the boundary. Firstly, spring elements are used to perform the supports layout design for vibration problems. Secondly, the positions of the support components and the structural layout are optimized simultaneously. Several bridge problems are designed and reasonable numerical results are obtained.

Then the topology design with pressure loads on the movable surface is considered. The shape of the loaded surface and the structural layout are designed simultaneously without component. But the techniques of density points and the embedded meshing are used as well. The loaded surface is modeled as a spline and the neighboring elements are modified and adapted to the spline. Numerical example is carried out. The loaded surface quickly evolved to a reasonable shape and finally a clear structural layout is obtained.

Chapter 7

Conclusion

Overview

The final conclusion of this thesis is provided in this chapter. In addition, more technical extensions and perspectives of the related ideas and methods are discussed.

Contents

7.1 Achievements

This work was started in the spring festival of 2006 in China, when engineers from Chinese Academy of Engineering Physics (CAEP) were interested in our research on structural topology optimization. The potential applications of the related techniques in aerospace structural systems were discussed in detail. Thus such subject was proposed accordingly. The aim was to develop a systematic method for the topology design of structural and support layout of the multi-component systems based on my work.

With the academic supports from the cooperative platform between the Northwestern Polytechnical University (NPU) and the University of Liège (Ulg), and the technical suggestions received from the CAEP, the achievements and accomplishments of this work are fruitful.

1) The method of FCM is developed based on the idea of the sphere-trees to solve the packing problems.

    a) Using certain numbers of circum-circles to describe the contour of the components and the design domain approximately, the complex geometry constraints are transformed into some distance functions of explicit form, the gradient-based algorithms can be applied accordingly.

    b) Normally in FCM, great quantities of circles are needed to generate fine approximations for the contours of the components and the design domain, which will lead to huge numbers of design constraints in the optimization and unaffordable computing time. Semi-heuristic rules using relocated circles of variant radii are proposed to improve the approximation.

2) The idea of integrating the packing and topology optimization is proposed.

    a) The location and orientation of the components defined as the geometrical design variables, proper layout of the components are found by the optimization procedure and FCM is used to avoid the overlap. Simultaneously, the topology optimization is carried out to generate structural layout supporting the components.

    b) Due to the updating of the geometry variables as well as the element mesh, the pseudo-densities describing the material layout in topology optimization can be no longer defined with respect to the elements. The density points are predefined and located in the design domain with fixed positions. Each element is supposed to receive its value of the pseudo-density from the nearest density point.

3) By means of the derived design sensitivities, the integrated layout design is carried out for the multi-component systems with self-weight loadings and problems of maximizing the fundamental natural frequencies.

    a) SIMP-like material interpolation models may lead to the phenomena of localized modes and localized deformations, which are the key difficulties involved in

topology optimization of maximizing natural frequencies and those with design dependent body loads. These problems are effectively avoided by applying a new interpolation model of polynomial function.

b) Physical constraints such as the limitation to the center of gravity and the moment of inertia are further introduced in the layout design to satisfy practical requirements of the aerospace systems.

4) The break-down problem of the ESO family methods is revealed by treating it as some phenomena appearing in low density areas. Meanwhile, the technique of check position is proposed with a certain intermediate material property defined to replace the removed elements. Thus, the erroneously removed elements will be identified and then recovered back into the design domain.

5) The simultaneous layout design of the designable boundary conditions and supporting structures are implemented with the proposed techniques.

   a) The layout of the fixations is designed by introducing the support components where the fixations are defined. These components are partially embedded into the design domain and movable on the boundary. The simultaneous optimization is carried out to find proper layout of the support components and the material layout of the design domain.

   b) Topology optimization is carried out for the problem with pressure loads on the movable design domain. In view of the shape variation of the loaded surface, the embedded meshing is implemented to remesh the area locally and the material layout is described with the technique of density points. In this way, the shape of the loaded surface as well as the optimal layout of the design domain can be designed in a reasonable way.

7.2 Additional discussions

Before the closure of the thesis, it is important to notice that this does not imply the end of the work on this subject. Much more complexities are actually involved in a practical application of the aerospace structural system design. On the one hand, we can foresee some possible technical extensions or more applications. On the other hand, the multi-component system layout design may be achieved alternatively. Therefore, some additional technical discussions are presented here.

7.2.1 Computing time

In Chapter 3 we have mentioned the problem of computing time when the software platforms using in this work are introduced. Although the program code was optimized as much as possible, the optimization procedure still costs tremendous computing time when relatively complex multi-component systems are designed, Therefore, it should be emphasized once more.

As indicated before, for the purpose of developing new ideas rapidly and conveniently, the problem definitions and the iteration control are mainly programmed in the ANSYS

APDL language. However, it is a programming language skilled in operating the command lines of ANSYS rather than numerical computation. A single design loop of the optimization design is detailed as a flowchart in Figure 7.1, where the white box and the gray box indicate the operations of ANSYS command lines and numerical computing, respectively. The most time consuming parts are also indicated with dashed boxes.

In the embedded meshing, although this procedure costs less time than regenerating the element mesh, there is still much of the computing time consumed in the Boolean operations. This is due to the low efficiency of the geometrical operation in ANSYS, as well as large numbers of elements are involved. So far, there is no better and convenient way to improve the situation. Fortunately, the computing time consumed in the embedded meshing does not increase significantly whenever the complexity of the problem rises.

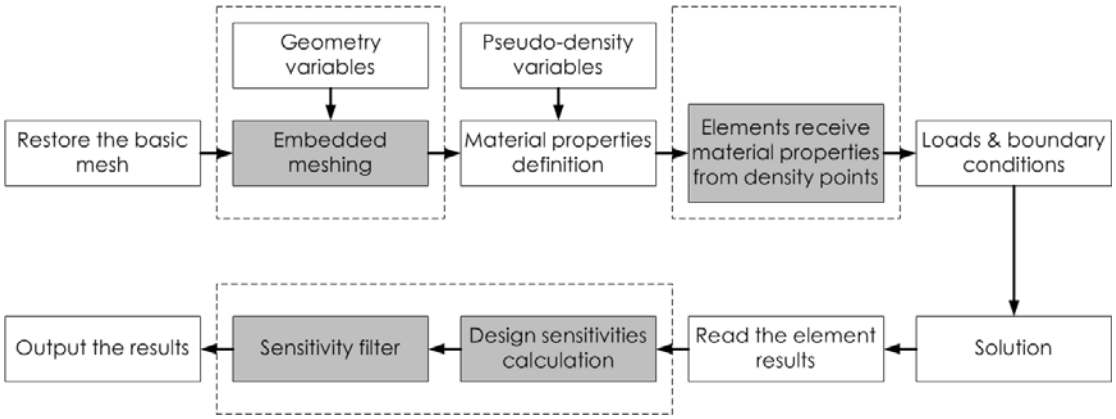

Figure 7.1: A single design loop of the integrated layout design

The rest parts consuming a lot of computing time depend greatly upon the number of the density points and the element number. The remedy is to use high efficient programming languages, e.g. C/C++ or Fortran instead of APDL to calculate the results.

This idea is partially implemented in the sensitivity filter. The calculated sensitivities as well as the pseudo-densities, the coordinate of the density points are written into a text file which will be read into the filter process programmed with C++. Later, the filtered sensitivities are written into another text file. The APDL main process will read the file and receive the updated sensitivities. Compared with the purely APDL programming, the computing time is reduced from 2 minutes to less than 2 seconds for 2500 sensitivities including reading and writing the text files.

7.2.2 Note on the 3D problems

As a single 3D component has 6 geometrical design variables to describe the location and orientation, a 3D multi-component system may have much larger quantities of elements and design variables. Besides, the technique of 3D embedded meshing becomes also complicated. Consider a meshing example of a small part near one component. As shown in Figure 7.2, the basic mesh consists of 125 (5×5×5) hexahedral elements and each density point is assigned at the center of each element. A big cubic component intersects with the basic mesh.

If the intersection part of the basic mesh is subtracted through Boolean operation, some irregular volumes are created and some tetrahedral elements have to be used to modify

the elements around the component. Likewise, the added elements are also restricted inside each cube of the basic mesh.

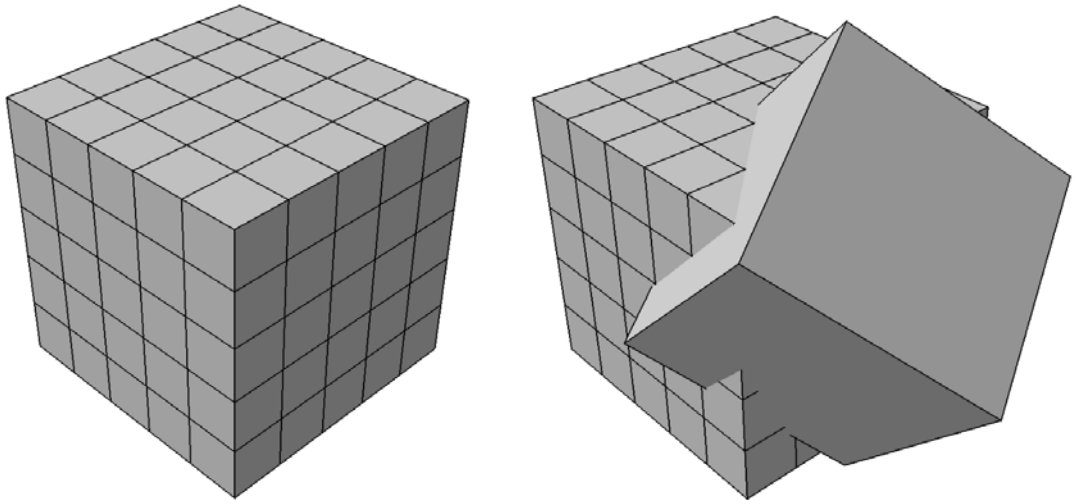

Figure 7.2: The basic mesh and the component

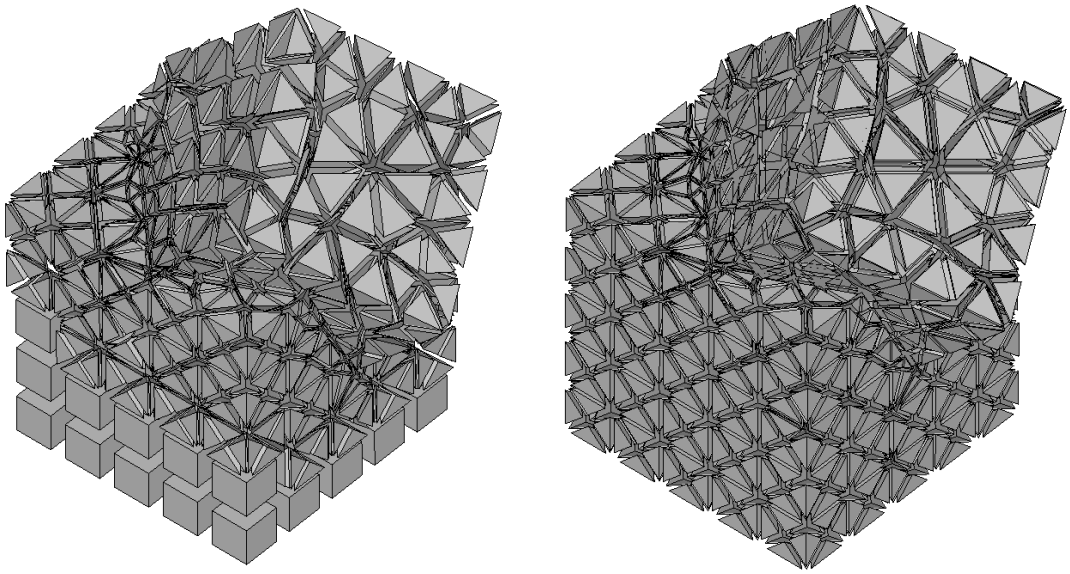

(a) (b)

Figure 7.3: Different element mesh of the structure

The difficulties are however encountered when hexahedral elements and tetrahedral elements are uses together. As shown in Figure 7.3(a), the final finite element mesh consists of 5056 elements and is manually generated. To ensure the quality of the element mesh, we have to use some pyramid elements as the transition interface between the hexahedrons and tetrahedrons in the structure (See Owen and Saigal 2001). However, the elements In Figure 7.3(a) are generated by picking and inputting parameters interactively in the graphic user's interface whereas an automatic approach is needed during the design iteration.

The problem can be solved if the tetrahedral elements are used uniformly for both basic mesh and the component mesh, as shown in Figure 7.3(b). Here, 6690 elements exist. There are no pyramid elements for the interface and the free mesh is generated

automatically by ANSYS. However, this is only a small part of the structure. The total number of the elements will be tremendously large if the hexahedral elements are not used for the basic mesh.

7.2.3 Note on the gradient free algorithms

Considering the fact that local optima exist in the integrated layout design of the multi-component systems, an alternative approach may use the gradient free methods e.g. Genetic Algorithm to solve the problems. However, it seems not to be a very practical approach so far. As is known, the gradient free algorithms are mostly employed to problems for which it is difficult or impossible to derive the design sensitivities. This is not the case for topology optimization using structural compliance as objective function. Besides, due to the random search strategy, there is no way to verify rigorously the optimality and the iteration may lead to strange design patterns. Furthermore, such an optimization procedure has a low efficiency when solving large-scale problems. Therefore, even in a simple topology optimization problem with only hundreds of elements, thousands of finite element analyses are normally needed.

Finally, the random search strategies cannot guarantee the feasibility of intermediate designs, e.g., the appearance of the overlap between components. This is still tolerable in the pure packing optimization since the computing is purely geometrical. But in the integrated design, the overlap of the components will become fatal for finite element analysis.

In topology optimization, applications of gradient free methods can refer to the works of Missoum et al. (2000), Aguilar Madeira (2002), Kim and De Weck (2004) and Tai and Akhtar (2005).

7.2.4 The level set method

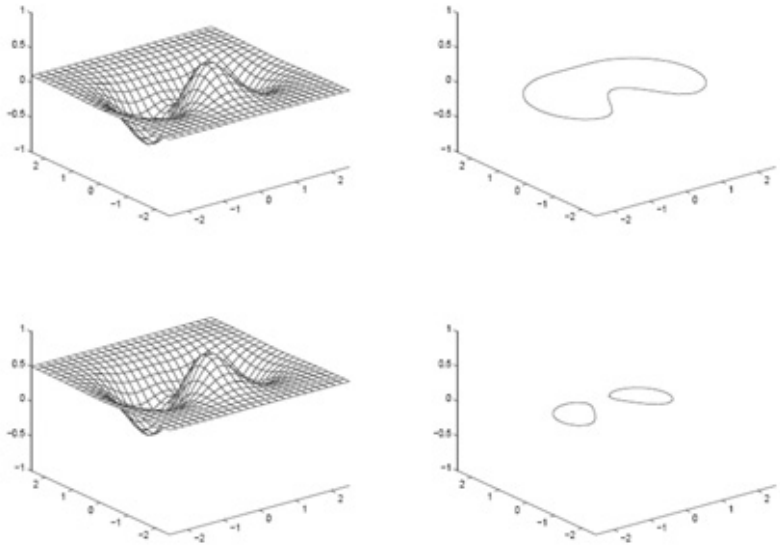

http://www.ariser.info/img/levelset.jpg

Figure 7.4: Topology description of the level set method

The level set method was proposed recently for structural topology optimization (Sethian 1999). As shown in Figure 7.4, the contour of the topology is described as the curve

where the level set function equals 0. The topology optimization with level set method is more like a generalized shape optimization (Duysinx et al 2006, Wang and Wang 2004). It is basically a steepest descent method by combining the shape sensitivity analysis with the Hamilton-Jacobi equation for modifying the level-set function, as show in Figure 7.5.

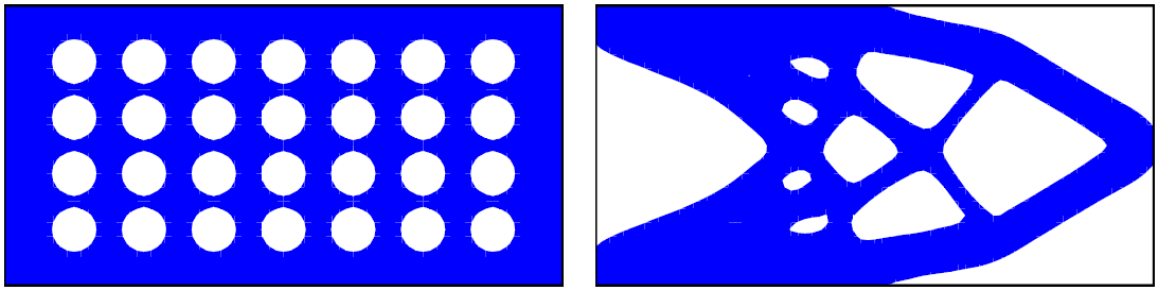

Figure 7.5: Typical topology design with level set method (Park and Youn 2008)

Here, we just discuss the possibility of using level set method to deal with the integrated layout optimization of the multi-component systems. Firstly, the different components and the structural layout have to be modeled with multiple level set functions. Although two level set functions can describe four material phases in the design domain as indicated by Wang and Wang (2004), it would be better to describe each component and the structural layout by means of respective level set functions to maintain the exact form and the free movement of the components. Secondly, level set functions of priority have to be used for the components in order that the intersection areas should be applied as the material properties of the components when the supporting structure and the components are overlapping with each other.

Finally, the overlap will be avoided as well. One possibility is to obtain the minimum distances between different contours described by the level set functions. There will be only one design constraint for each pair of the components. But complex computing of the level set functions will be involved. And the constraints would be highly non-linear. Another way of avoiding the overlap is to use the proposed FCM. Similarly, a pure geometrical model is defined with FCM. Meanwhile, the finite element model will be defined by the level set function instead of the techniques of density points and the embedded meshing.

7.3 Conclusion

Many significant contributions to the layout optimization of multi-component systems have been provided in this thesis. In view of the achievements outlined in Section 7.1, a number of conclusions can be made on the techniques involved, their applicability and on the work presented.

1) In packing optimization with FCM

   a) The complex overlap detection and evaluation can be transformed into a simple and explicit formulation of the FCM. The definition of the circum-circles for each component is essential in reducing the approximation error and saving the computing time. With the proposed semi-heuristic rules, the circle approximation

can be improved significantly.

b) Both 2D and 3D packing optimization problems can be solved by FCM. Although local minima are always obtained in the optimization of complex packing problems, the FCM is suitable to the integrated layout design.

2) In integrated layout design for components and supporting structure

a) The technique of density points is actually an extension of the traditional element-based material layout description. Identical topology patterns can be mapped between different element meshes of the structure. The remeshing of the design domain with embedded components is carried out with the technique of embedded meshing. Since only the elements in a small part of the global system have to be modified, the computing time is saved.

b) The integrated layout design strategy consisting of the FCM, the techniques of density points and embedded meshing makes it possible to find proper positions of the components. Meanwhile, the optimal positions of the components depend upon the relative material properties of the components and the supporting structure.

c) Components with complex shapes and multiple material properties can be employed in the integrated layout design. Similarly, partially supported components are defined and the corresponding optimal supporting structure is adapted to the components.

d) In the integrated layout design with inertial forces and natural frequency maximization, the components and the structural materials always trend towards the boundary fixations. Introducing more design constraints on the center of gravity or the moment of inertia can help to relocate the structural layout. Using the proposed material interpolation model can effectively avoid the localized modes and the localized deformations in the topology optimization maximizing natural frequencies and those with design dependent body loads.

3) In the coupled layout design of structures and boundary conditions

a) By utilizing the support components, the layout design of the structures and the boundary conditions can be implemented simultaneously with the proposed techniques of density points and the embedded meshing.

b) The proposed techniques in this thesis provide the possibility of topology optimization with variable element mesh. Therefore, shape optimization can be integrated with the topology optimization. Topology optimization problems with design dependent pressure loads are easily implemented by introducing a variable loading surface.

Published papers during 2004-2008

Zhu JH, Zhang WH, Beckers P (2008) Integrated layout design of the multi-component system. International Journal of Numerical Methods in Engineering (Accepted)

Zhu JH, Zhang WH, Beckers P, Chen YZ, Guo ZZ (2008) Simultaneous design of components layout and supporting structures using coupled shape and topology optimization. Structural and Multidisciplinary Optimization. 36(1): 29-41

Zhu JH, Zhang WH (2006) Maximization of structural natural frequency with optimal support layout. Structural Multidisciplinary Optimization. 31(6): 462-469

Zhu JH, Zhang WH, Qiu KP (2007) Bi-directional evolutionary topology optimization using element replaceable method. Computational Mechanics. 40(1): 97-109

Zhu JH, Zhang WH, Qiu KP (2006) Investigation of localized modes in topology optimization of dynamic structures. Acta Aeronautica et Astronautica Sinica. 27: 619-623 (In Chinese)

Zhu JH, Zhang WH, Tian J (2004) Optimal layout of structural support conditions based upon continuous density variables. Mechanical Science and Technology for Aerospace Engineering. 26(9): 1113-1116 (In Chinese)

Zhang WH, Zhu JH (2006) A new finite-circle family method for optimal multi-component packing design. WCCM VII Conference. Los Angeles, United States

Beckers P, Zhu JH, Zhang WH (2007) Optimal design of complex multi-component layout. WCSMO Conference 2007, Seoul, Korea

Zhu JH, Zhang WH (2005) Evolutionary topology optimization with a replaceable element of orthotropic cellular microstructure. ICMEM Conference 2005. Nanjing China: 822-827

Zhu JH, Zhang WH, Beckers P (2007) Complex system design with multi-component layout optimization. ASMDO Conference 2007. Besançon France

Zhu JH, Beckers P, Zhang WH (2008) Layout design of the multi-component systems with gravity. ASMDO Conference 2008. Gijon, Spain

Zhu JH, Zhang WH, Qiu KP (2005) Design of structural supports layout using topology optimization. HERCMA Conference 2005, Athens Greece

Zhu JH, Zhang WH (2006) Coupled design of components layout and supporting

structures using shape and topology optimization. CJK-OSM IV Conference. Kunming China

Zhu JH, Zhang WH (2005) Structural evolutionary topology optimization based on the element replaceable method. CSTAM Conference 2005. Beijing, China (In Chinese)

Zhu JH, Zhang WH, Beckers P (2007) Layout optimization of complex multi-component system. CSTAM Conference 2007. Beijing, China

Zhu JH, Beckers P, Zhang WH (2008) On the multi-component layout design with inertial force. ACOMEN Conference 2008. Liège, Belgium

Zhu JH, Beckers P, Zhang WH (2007) On the layout design of multi-component systems. International Workshop 2007: Advancements in Design Optimization of Materials, Structures and Mechanical Systems. Xi'an, China

Zhu JH, Zhang WH (2005) Structural topology optimization with evolutionary methods. Intensive Seminar 2005: Optimal design of structures and materials. Xi'an China.

References

Aguilar Madeira JF (2002) Multi-objective topology optimization of structures. Proceedings of the sixth conference on Computational structures technology. 351-352

Akesson B, Olhoff N (1988) Minimum stiffness of optimally located supports for maximum value of beam eigenfrequencies. Journal of Sound and Vibration. 120: 457-463

Aladahalli C, Cagan J, Shimada K (2007) Objective Function Effect Based Pattern Search—Theoretical Framework Inspired by 3D Component Layout, Journal of Mechanical Design, 129: 243-254

Allaire G, Jouve F, Maillot H (2004) Topology optimization for minimum stress design with the homogenization method. Structural and Multidisciplinary Optimization, 28: 87-98

ANSYS Inc. ANSYS Release 9.0 Documentation

Atiqullah MM, Rao SS (1995) Parallel processing in optimal structural design using simulated annealing. AIAA Journal. 33: 2386-2392

Beckers M (1997) Optimisation de structures en variables dicretes. PhD thesis, University of Liège (In French)

Beckers M (1999) Topology optimization using a dual method with discrete variables. Struct. Optim. 17, 14 – 24

Belegundu AD, Rajan SD (1988) A shape optimization approach based on natural design variables and shape functions. Computer Methods in Applied Mechanics and Engineering. 66: 87-106

Bendsøe MP (1989) Optimal shape design as a material distribution problem. Structural Optimization, 10: 193-202

Bendsøe MP (1995) Optimization of structural topology, shape and material. Springer, Berlin, Heidelberg, New York

Bendsøe MP (2002) Recent developments in topology design of materials and mechanisms. ESAIM: Proceedings, 11: 41-60

Bendsøe MP, Kikuchi N (1988) Generating optimal topologies in structural design using homogenization. Comp. Meth. Appl. Mech. Engr. 71: 197-224

Bendsøe MP, Sigmund O (1999) Material interpolation Schemes in topology optimization. Archive of Applied mechanics 69: 635-654

Bendsøe MP, Sigmund O (2003) Topology optimization: theory, method and application. Springer, Berlin, Heidelberg, New York

Bennet JA, Botkin ME (1985) Structural shape optimization with geometric description and adaptive mesh refinement. AIAA Journal. 23: 458-464

Blouin VY, Miao Y, Zhou X, Fadel GM (2004) An assessment of configuration design methodologies. 10th AIAA/ISSMO, New York

Bojczuk D, Mroz Z (1998) On optimal design of supports and frame structures. Structural Multidisciplinary Optimization. 16: 47-57

Bourdin B (2001) Filters in topology optimization. International Journal for Numerical Methods in Engineering. 50: 2143-2158

Bruns TE, Tortorelli DA (2001) Topology optimization of non-linear elastic structures and compliant mechanisms. Computer Methods in Applied Mechanics and Engineering. 190: 3443-3459

Bruyneel M, Duysinx P (2004) Note on topology optimization of continuum structures including self-weight. 29: 245-256

Bruyneel M, Duysinx P, Fleury C (2002) A family of MMA approximations for structural optimization. Structural and Multidisciplinary Optimization. 24: 263-276

Buhl T (2001) Simultaneous topology optimization of structure and supports. Structural and Multidisciplinary Optimization. 23:336-346

Cagan J, Degentesh D, Yin S (1998) A simulated annealing-based algorithm using hierarchical models for general three-dimensional component layout, Computer-Aided Design, 30: 781-790

Cagan J, Shimada K, Yin S (2002) A survey of computational approaches to three-dimensional layout optimization, Computer-Aided Design, 34: 597-611

Cameron S (1991) Approximation hierarchies and s-bounds. Proceedings Symposium on Solid modeling Foundations and CAD/CAM Applications, 129-137

Chen BC, Kikuchi N (2001) Topology optimization with design-dependent loads. Finite Elements in Analysis and Design. 37: 57-70

Chen S, Tortorelli DA (1997) Three-dimensional shape optimization with variational geometry. Structural and Multidisciplinary Optimization. 13: 81-94

Chickermane H, Gea HC (1997) Design of Multi-Component Structural Systems for Optimal Layout Topology and Joint Locations. Engineering with Computers. 13: 235-243

Clautiaux F, Carlier J, Moukrim A (2007) A new exact method for the two-dimensional bin-packing problem with fixed orientation, Operations Research Letters, 35: 357-364

De Bont FMJ, Aarts EHL, Meehan P, O'Brien CG (1988) Placement of shapeable blocks. Philips Journal of Research, 43:1-22

De Ruiter MJ Van Keulen F (2004) Topology optimization using a topology description function, Structural and Multidisciplinary Optimization, 26: 1615-1488

Du J, Olhoff N (2004) Topological optimization of continuum structures with design-dependent surface loading – Part I: new computational approach for 2D problems. Structural and Multidisciplinary Optimization. 27: 151-165

Du J, Olhoff N (2004) Topological optimization of continuum structures with design-dependent surface loading – Part II: algorithm and examples for 3D problems. Structural and Multidisciplinary Optimization. 27: 166-177

Duysinx P, Van Miegroet L, Jacobs T, Fleury C (2006) Generalized shape optimization using X-FEM and level set methods. IUTAM Symposium on Topological Design Optimization of Structures, Machines and Materials: Status and Perspectives. 23-32

Edwards CS, Kim HA, Budd CJ (2007) An evaluative study on ESO and SIMP for optimizing a cantilever tie-beam. Structural and Multidisciplinary Optimization. 34: 403-414

Eschenauer HA, Kobelev HA, Schumacher A (1994) Bubble method for topology and shape optimization of structures. Structural Optimization. 8: 42-51

Eschenauer HA, Olhoff N (2001) Topology optimization of continuum structures: A review. Applied Mechanics Reviews, 54: 331-390

Fang L (2008) Finite circle method based packing and layout optimization design of arbitrarily shaped multi-components. Master thesis, Northwestern Polytechnical University (In Chinese)

Fleury C, Braibant V. (1986) Structural optimization: a new dual method using mixed variables, International Journal of Numerical Methods in Engineering. 23: 409-428

Fleury C. (1989) First and second order convex approximation strategies in structural optimization, Structural Optimization. 1: 3-10

Fuchs MB, Shemesh NNY (2004) Density-based topological design of structures subjected to water pressure using a parametric loading surface. Structural and Multidisciplinary Optimization. 28: 11-19

Fujita K, Akagi S, Hase H (1991) Hybrid approaches to plant layout design using constraint directed search and an optimization technique. Proceedings of 17th ASME Design Automation Conference, 1:131-138

Gao T, Zhang WH (2007) Structural topology optimization of multiple material phases

under design-dependent solid and semi-solid weight pressure. Proceedings of International Workshop 2007: Advancements in Design Optimization of Materials, Structures and Mechanical Systems, Xi'an, China

Gersborg-Hansen A, Bendsøe MP, Haber RB (2005) Topology optimization of Channel flow problems. Structural and Multidisciplinary Optimization. 30: 181-192

Gersborg-Hansen A, Bendsøe MP, Sigmund O (2006) Topology optimization of heat conduction problems using the finite volume method. Structural and Multidisciplinary Optimization. 31: 251-259

Guedes JM, Kikuchi N (1990) Preprocessing and postprocessing for materials based on the homogenization method with adaptive finite element methods. Computer Methods in Applied Mechanics and Engineering. 83: 143-198

Haber RB, Jog CS, Bendsøe MP (1996) A new approach to variable-topology shape design using a constraint on perimeter. Structural and Multidisciplinary Optimization. 11:1-12

Hammer VB, Olhoff N (1999) Topology optimization with design dependent loads. Proceedings of WCSMO-3. New York

Hammer VB, Olhoff N (2000) Topology optimization of continuum structures subjected to pressure loading. Structural and Multidisciplinary Optimization. 19: 85-92

Hinton E, Sienz J (1995) Fully stressed topological design of structures using an evolutionary procedure. Engineering Computational. 12: 229-244

Hori M, Nemat-Nasser S (1999) On two micromechanics theories for determining micro-macro relation in heterogeneous solids. Mechanics of Materials. 31: 667-682

Hou JW, Chuang CH (1990) Design sensitivity analysis and optimization of vibration beams with variable support locations. 16th Automation Conference, ASME transaction. Chicago. 281-290

Huang WQ, Chen DB, Xu RC (2007) A new heuristic algorithm for rectangle packing, Computers & Operations Research, 34: 3270-3280

Huang X, Xie YM (2008) A new look at ESO and BESO optimization methods. Structural and Multidisciplinary Optimization. 35:89–92

Hubbard PM (1993) Interactive collision detection, Proceedings of IEEE Symposium on Research Frontiers in Virtual Reality

Jiang T, Chirehdast M (1997) A system approach to structural topology optimization: designing optimal connections. Journal of Mechanical Design. 119: 40-47

Jiang T, Chirehdast M (1997) A system approach to structural topology optimization: designing optimal connections. Journal Mechanical Design. 119: 40-47

Jog CS, Haber RB (1996) Stability of finite element models for distributed-parameter optimization and topology design. Computer Methods in Applied Mechanics and

Engineering. 130: 203-226

Kim HA, Querin OM, Steven GP (2003) Improving efficiency of evolutionary structural optimization by implementing fixed grid mesh. Structural and Multidisciplinary Optimization. 24: 441-448

Kim IY, De Weck O (2004) Progressive structural topology optimization by variable chromosome length genetic algorithm. Proceedings of CJK-OSM III, Kanazawa, Japan.

Kodiyalam S, Virendra K, Finnigan PM (1992) Constructive solid geometry approach to three-dimensional structural shape optimization. AIAA Journal. 1992, 30: 1408-1415

Landon MD, Balling RJ (1994) Optimal packaging of complex parametric solids according to mass property criteria, Journal of Mechanical Design, 116:375-381

Lemaire E, Rochus V, Fleury C, Golinval JC, Duysinx P (2007) Topology optimization of microbeams including layer deposition manufacturing constraints. 7th World Congress on Structural and Multidisciplinary Optimization. Seoul Korea

Li Q, Steven GP, Xie YM (2001) Evolutionary structural optimization for connection topology design of multi-component systems. Engineering Computations, 18: 460-479

Lin M, Gottschalk S (1998) Collision detection between geometric models: a survey, Proceeding of IMA Conference on Mathematics of Surfaces

Lindby T, Santos JLT (1997) 2-D and 3-D shape optimization using mesh velocities to integrate analytical sensitivities with associative CAD. Structural and Multidisciplinary Optimization. 13: 213-222

Liu ZS, Hu HC, Wang DJ (1996) New method for deriving eigenvalue rate with respect to support location. AIAA Journal. 34: 864-866

Lund E (1994) Finite element based design sensitivity analysis and optimization. Ph.D. Thesis, Institute of Mechanical Engineering, Aalborg University, Denmark.

Luo Z, Cheng LP, Huang YY, Zhang YQ (2004) Topology optimization design for continuum structures. Advances in Mechanics. 34: 463-476

Ma ZD, Kikuchi N, Pierre C, Raju B (2006) Multidomain topology optimization for structural and material designs. Journal of Applied Mechanics. 73: 565-573

Mattheck C (1997) Design in nature: Learning from trees. Springer-Verlag, Berlin

Meagher D (1982) Geometric modeling using octree encoding, Computer Graphics and Image Processing, 19:129-147

Mei YL, Wang XM (2004) A level set method for structural topology optimization and its applications. Advances in Engineering Software. 35: 415 – 441

Missoum S, Gürdal Z, Hernandez P (2000) A Genetic Algorithm Based Topology Tool

for Continuum Structures. 8th Symposium AIAA/USAF/NASA/ISSMO on Multidisciplinary Analysis and Optimization

Miyazawa FK, Wakabayashi Y (2007) Two- and three-dimensional parametric packing, Computers & Operations Research, 34: 2589-2603

Moore A (2002) The circle tree – a hierarchical structure for efficient storage, access and multi-scale representation of spatial data, SIRC 2002 Dunedin, New Zealand

Moore A, Mason C, Whigham P, Thompson-Fawcett M (2003) The Use of the Circle Tree for the Efficient Storage of Polygons. Proceedings of GeoComputation, University of Southampton

Mroz Z, Rozvany GIN (1975) Optimal design of structures with variable support positions. Journal of Optimization Theory and Applications. 15: 85-101

Neves MM, Rodrigues H, Guedes JM (1995) Generalized topology design of structures with a buckling load criterion. Structural and Multidisciplinary Optimization. 10: 71-78

Nocedal J, Wright S (1999) Numerical Optimization, Springer, Series in Operations Research

O'Sullivan C, Dingliana J (1999) Real-time collision detection and response using sphere-trees, Spring Conference on Computer Graphics, 83-92

Olhoff N (1976) Optimization of vibrating beams with respect to higher order natural frequencies. Journal of Structural Mechanics. 4: 87-122

Olhoff N, Akesson B (1991) Minimum stiffness of optimally located supports for maximum value of column buckling loads. Structural Optimization. 3: 163-175

Olhoff N, Rasmussen J, Lund E (1993) A method of "exact" numerical differentiation for error elimination in finite-element based semi-analytical shape sensitivity analyses. Mechanics of Structures and Machines. 21: 1-66

Olhoff N, Taylor JE (1978) Designing continuous columns for minimum total cost of material and interior supports. Journal of Structural Mechanics. 6: 367-382

Owen SJ, Saigal S (2001) Formation of pyramid elements for hexahedra to etrahedral transitions. Computer Methods in Applied Mechanics and Engineering. 190: 4505-4518

Pál L (2006) A genetic algorithm for the two-dimensional single large object placement problem, Proceedings of 3rd Romanian-Hungarian Joint Symposium on Applied Computational Intelligence

Park KS, Youn SK (2008) Topology optimization of shell structures using adaptive inner-front (AIF) level set method. Structural and Multidisciplinary Optimization. 36: 43-58

Pedersen NL (2000) Maximization of eigenvalues using topology optimization. Structural

and Multidisciplinary Optimization. 20: 2-11.

Pedersen P (1993) Topology optimization of 3D trusses with cost of supports. Advances in Design Automation. 65: 761-768

Pedersen P, Tortorelli DA (1998) Constitutive parameters and their evolution. Control and Cybernetics. 27: 295-310

Prager W, Rozvany GIN (1975) Plastic design of beams: Optimal locations of supports and steps in yield moment. International Journal of Mechanical Sciences. 17: 627-631

Qian ZY, Ananthasuresh GK (2004) Optimal embedding of rigid objects in the topology design of structures. Mechanics Based Design of Structures and Machines 32: 165-193

Querin OM, Young V (2000) Computational efficiency and validation of bi-directional evolutionary structure optimization. Computer Methods in Applied Mechanics and Engineering. 189: 559-573

Quinlan S (1994) Efficient distance computation between non-convex objects, Proceedings of International Conference on Robotics and Automation, 3324-3329

Radovcic Y, Remouchamps A (2002) BOSS QUATTRO: an open system for parametric design Structural and multidisciplinary optimization. 23:140-152

Rajan SD (1995) Sizing, shape and topology design optimization of trusses using genetic algorithm. ASCE Journal of Structural Engineering. 121: 1480-1487

Remouchamps A, Grihon S, Raick C, Colson B, Bruyneel M (2007) Numerical optimization: a design space odyssey. International Workshop: Advancements in Design Optimization of Materials, Structures and Mechanical Systems. Xi'an, China: 168-185

Rodrigues H, Fernandes P (1995) A material based model for topology optimization of thermoelastic structure. International Journal of Numerical Methods in Engineering. 38: 1951-1965

Rong JH, Xie YM (2001) An improved method for evolutionary structure optimization against buckling. Computer and Structure. 79: 253-263.

Rozvany GIN (1974) Optimization of unspecified generalized forces in structural design. Journal of Applied Mechanics ASME. 41: 1143-1145

Rozvany GIN (2001a) Aims, scope, methods, history and unified terminology of computer-aided topology optimization in structural mechanics. Structural and Multidisciplinary Optimization. 21: 90-108

Rozvany GIN (2001b) Stress ratio and compliance based methods in topology optimization – a critical review. Structural and Multidisciplinary Optimization. 21: 109-119

Rozvany GIN, Mroz Z (1977) Column design: optimization of support conditions and segmentation., 5: 279-290

Rozvany GIN, Querin OM (2002a) Combining ESO with rigorous optimality criteria. International Journal of Vehicle Design. 28:294–299

Rozvany GIN, Querin OM (2002b) Theoretical foundations of sequential element rejections and admissions (SERA) methods and their computational implementations in topology optimization. Proceedings of the 9th AIAA/ISSMO Symposium on Multidisciplinary Analysis and Optimization, AIAA, Reston, VA.

Rozvany GIN, Querin OM (2004) Sequential element rejections and admissions (SERA) method: applications to multiconstraint problems. Proceedings of the 10th AIAA/ISSMO Multidisciplinary Analysis Optimization Conference, Albany, NY

Samet H (1989) Spatial data structures: quadtree, octree and other hierarchical methods, Addison Wesley

Samtech Inc, Boss-Quattro 5.0 Documentation

Sethian J (1999) Level set methods and fast marching methods: evolving interfaces in computational geometry, fluid mechanics. Computer Vision and Materials Science, Cambridge University Press

Seyranian A, Lund E, Olhoff N (1994) Multiple eigenvalues in structural optimization problems. Structural Optimization. 8: 207-227

Sigmund O (2001) A 99 line topology optimization code written in MATLAB. Structural and Multidisciplinary Optimization. 21: 120-127

Sigmund O (2006) On topology optimization with manufacturing constraints. 3rd European Conference on Computational Mechanics Solids, Structures and Coupled Problems in Engineering, Lisbon Portugal

Sigmund O (2007) Morphology-based black and white filters for topology optimization. Structural and Multidisciplinary Optimization. 33: 401-424

Sigmund O, Clausen PM (2007) Topology optimization using a mixed formulation: An alternative way to solve pressure load problems. Computer Methods in Applied Mechanics and Engineering. 196: 1874-1889

Sigmund O, Petersson J (1998) Numerical instabilities in topology optimization: A survey on procedures dealing with checkerboards, mesh-dependencies and local minima. Structural and Multidisciplinary Optimization. 16, 68-75

Sigmund O, Torquato S (1999) Design of smart composite materials using topology optimization. Smart Materials and Structures. 8: 365-379

Sinha JK, Friswell MI (2001) The location of spring supports from measured vibration data. Journal of Sound and Vibration, 244: 137-153

Stolpe M and Svanberg K (2001) An alternative interpolation scheme for minimum compliance topology optimization. Structural and Multidisciplinary Optimization 22: 116-124

Suzuki K, Kikuchi N (1991) A homogenization method for shape and topology optimization. Computer Methods in Applied Mechanics and Engineering. 93: 291-318

Svanberg (2007) On a globally convergent version of MMA. 7th World Congress on Structural and Multidisciplinary Optimization. COEX Seoul , Korea

Svanberg K (1987) The method of moving asymptotes – a new method for structural optimization. International Journal for Numerical Methods in Engineering. 24: 359-373

Svanberg K (1995) A globally convergent version of MMA without linesearch. 1st World Congress of Structural and Multidisciplinary Optimization. Pergamon, New York

Szelag D, Mroz Z (1979) Optimal design of vibrating beams with unspecified support reactions. Computer Methods in Applied Mechanics and Engineering, 19: 333-349

Tai K, Akhtar S (2005) Structural topology optimization using a genetic algorithm with a morphological geometric representation scheme. Structural and Multidisciplinary Optimization. 30: 113-127

Tanskanen P (2002) The evolutionary structural optimization method: theoretical aspects. Computer Methods in Applied Mechanics and Engineering. 191: 5485-5498

Tortorelli DA, Wang Z (1993) A systematic approach to shape sensitivity analysis. International Journal of Solids and Structures. 30: 1181-1212

Wang BP (1993) Eigenvalue sensitivity with respect to location of internal stiffness and mass attachment. AIAA Journal. 31: 791-794

Wang BP, Chen JL (1996) Application of genetic algorithm for the support location optimization of beams. Computers and Structures. 58: 797-800

Wang D (2003) Structural optimization with evolutionary shift method. Ph.D. Thesis, Department of Aircraft Manufacturing Engineering, Northwestern Polytechnical University

Wang MY, Wang SY (2005) Bilateral filtering for structural topology optimization. International Journal for Numerical Methods in Engineering. 63: 1911-1938

Wang XM, Wang MY (2003) “Color” level sets: a multi-phase method for structural topology optimization with multiple materials. Computer Methods in Applied Mechanics and Engineering. 193: 469-496

Won KM, Park YS (1998) Optimal support position for a structure to maximize its fundamental natural frequency. Journal of Sound and Vibration. 213: 801-812

Xie YM, Steven GP (1994a) Optimal design of multiple load case structures using an evolutionary procedure, Engineering Computations. 11: 295-302

Xie YM, Steven GP (1994b) A simple approach to structure frequency optimization, Computer and Structure. 53: 1487-1491.

Xie YM, Steven GP (1996) Evolutionary structure optimization for dynamic problems. Computer and Structure. 58: 1067-1073.

Xie YM, Steven GP (1997) Evolutionary Structural Optimization. Springer-Verlag, Berlin

Yang XY, Xie YM (2003) Perimeter control in the bi-direction evolutionary optimization method. Structural and Multidisciplinary Optimization. 24: 430-440

Yang XY, Xie YM, Steven GP (1999a) Bidirectional evolutionary method for stiffness optimization. AIAA Journal. 37: 1483-1488

Yang XY, Xie YM, Steven GP (1999b) Topology optimization for frequency using an evolutionary method. Journal of Structural Engineering. 125: 1432-1438

Zhang B, Teng HF, Shi YJ (2008) Layout optimization of satellite module using soft computing techniques, Applied Soft Computing, 8: 507–521

Zhang WH (1991) Sensitivity analysis and structural shape optimization by finite element method. Ph.D. Thesis, University of Liège, Belgium (In French)

Zhang WH, Beckers P, Fleury C (1995) A unified parametric design approach to structural shape optimization. International Journal of Numerical Methods in Engineering. 38: 2283-2292

Zhang WH, Duysinx P (2003) Dual approach using a variant perimeter constraint and efficient sub-iteration scheme for topology optimization. Computer and Structure. 81: 2173-2181

Zhang WH, Fleury C (1997) A modification of convex approximation methods for structural optimization. Computers and Structures. 64: 89-95

Zhang WH, Fleury C, Duysinx P, Nguyen VH Laschet I (1996) A generalized method of moving asymptotes (GMMA) including equality constraints. Structural and Multidisciplinary Optimization. 12: 143-146

Zhang WH, Sun SP (2006) Scale-related topology optimization of cellular materials and structures. International Journal for Numerical Methods in Engineering. 68: 993-1011

Zhang WH, Wang FW, Dai GM, Sun SP (2007) Topology optimal design of material microstructures using strain energy-based method. Chinese Journal of Aeronautics. 20: 320-326

Zhou M (2004) Topology optimization for shell structures with linear buckling responses. World Congress of Computational Mechanics, Beijing China

Zhou M, Rozvany GIN (1991) The COC algorithm, part II: topological, geometry and generalized shape optimization. Computer Methods in Applied Mechanics and Engineering. 89: 197-224

Zhou M, Rozvany GIN (2001) On the validity of ESO type methods in topology optimization. Structural and Multidisciplinary Optimization. 2001, 21: 80-83

Zhu JH, Zhang WH (2006) Maximization of structure natural frequency with optimal support layout. Structural and Multidisciplinary Optimization. 31: 462-469

Zhu JH, Zhang WH, Qiu KP (2006) Investigation of localized modes in topology optimization of dynamic structures. Acta Aeronautica et Astronautica Sinica. 27: 619-623 (In Chinese)

Zhu JH, Zhang WH, Qiu KP (2007) Bi-directional evolutionary topology optimization using element replaceable method. Computational Mechanics. 40: 97-109